K Further contributions

articles available on-line: http://www.fz-juelich.de/ikp/DE/Service/Download/download_node.html

- Evidence for excitation of two resonance states in the isovector two-baryon system with a mass of 2.2 GeV/c^2 at ANKE
- Measurement of the spin correlation paramaters in the reaction pd$\rightarrow{}^3$He+π^0 with ANKE
- Deuteron breakup pd$\rightarrow$ppn and the contact d-term in the pN$\rightarrow$ppπ subprocesses at ANKE
- One-loop contribution of the Δ-isobar mechanism to the reaction pp$\rightarrow$pp+π^0 near the Δ-threshold region at ANKE
- Identification of the reaction p+d$\rightarrow$d+η+p$_{sp}$ with ANKE
- High precision study on the η-meson production channel d+p$\rightarrow{}^3$He+η with ANKE
- Identification of deuterons in p+d$\rightarrow$ d+X reactions with ANKE
- Study of the p(pol)n quasi-free elastic scattering with ANKE
- Comparison of COSY-TOF and SATURNE-SPES4 data for the scattering length determination
- Investigation of meson production in proton-deuteron fusion to ^{3}HeX with WASA-at-COSY
- Studies on C-violation at WASA-at-COSY: $\eta \rightarrow \pi^0 e^+ e^-$
- Charge symmetry breaking in the dd $\rightarrow{}^4$Heπ^0 reaction with WASA-at-COSY
- Experimental study of few nucleon interaction dynamics in dp collisions with WASA-at-COSY
- Status of the search for η-mesic Helium in *dd* and *pd* reactions with WASA-at-COSY
- Determination of the analysing power for the $\vec{p}p \rightarrow pp\eta$ reaction using WASA-at-COSY
- Final State Interactions and the Box Anomaly in $\eta \rightarrow \pi^+\pi^-\gamma$ with WASA-at-COSY
- Electromagnetic transition form factor of the η meson with WASA-at-COSY
- Double dilepton decay of the η meson with WASA-at-COSY
- Radiative Decays of the η' meson with CLAS
- Transition form factor of the ω meson with CLAS
- Photoproduction of the π^0 meson up to 5.5 GeV with CLAS
- Measurement of the pp Elastic Scattering Differential Cross Section with the KOALA Recoil Detector at COSY
- Study of Excited Ξ Baryons in $\bar{p}$p-Collisions with the $\bar{P}$ANDA Detector
- Simulated Measurement of the D$_s$ Semileptonic Decay Form Factor with the PANDA Detector
- Search for the $\Delta\Delta$ Component in the Deuteron in $\bar{p}d$ Collisions with PANDA
- Parallel algorithms for online trackfinding at PANDA
- A test system for the electronic components of the PANDA Microvertex Detector
- Measurement of the spatial and energy-loss resolution with a prototype Straw Tube Tracker (STT) for the PANDA experiment
- XYZ rates at PANDA
- genfit2: a general fitting tool
- Search for polarization effects in the antiproton production process

- Commission of a Magnetostatic Beam Position Monitor
- Spin Tune Determination using Fourier Transform
- Development of the electrostatic deflector for JEDI
- Introduction to the quasi-frozen spin (QFS) method
- Preparation of First Beam Tests of LYSO Modules for JEDI polarimetry
- Systematic studies of spin dynamics in preparation for the precursor EDM experiment with the RF Wien filter at COSY
- Closed orbit influencing effects at COSY
- Beam and Spin Dynamics in an RF Wien-Filter
- Extension of COSY Toolbox for the Analysis of the Final Electric Dipole Moment Storage Ring
- A candidate layout for the JEDI polarimeter
- Automation of the Orbit Response Matrix Measurement at COSY
- Systematic Limitations of EDM Measurements at COSY due to Magnet Misalignments
- Automation of Rogowski Coil Test Bench and data Acquisition System
- Differential cross section of the dC$\rightarrow$p+X reaction at Td=270 MeV
- First Results of the Upgraded Low Energy Polarimeter Read-Out
- Improvements in Barrier-Bucket Signal Shaping
- Development of MAD-X based LOCO algorithm for COSY optics measurement as well as model improvement
- Measurement of the Harmonic Contents of the HESR Dipoles with a Single 3D Hall Probe
- Development of an automatic model based adjustment of the beam transport in the 2 MeV electron cooler at COSY
- Comparative numerical study of two BPM designs for the HESR
- Design of a test bench to characterize BPMs for the HESR
- GaN-Based High Power Amplifier for the HESR Main Stochastic Cooling System
- Status of the HESR BPM
- Upgrade of the BPM Readout Electronics at COSY
- Prototype of DAQ for commercial stand-alone devices with Ethernet interface
- Feasibility study on muon production with laser-accelerated protons or ions
- SEU Tests with the STS-XYTER Version 1 ASIC for CBM
- Radiation hardness tests of electronic components for CBM-STS low voltage power supply

Evidence for excitation of two resonance states in the isovector two-baryon system with a mass of 2.2 GeV/c^2*

D. Tsirkov[1], V. Komarov[1], S. Dymov[1,2], A. Kulikov[1] for the ANKE collaboration

The $pp \to \{pp\}_s\pi^0$ reaction has been studied at ANKE in the $\Delta(1232)$ resonance excitation region [1–3]. The forward differential cross section $d\sigma/d\Omega$ and analyzing power A_y were measured at several energies from 353 to 1100 MeV. In assumption of the pion angular momentum ℓ equal to 0 and 2, the data can be parametrized as follows:

$$\frac{d\sigma}{d\Omega} = \frac{d\sigma_0}{d\Omega}\left(1 + \kappa \sin^2\theta_{pp}\right), \qquad A_y = \frac{A_y^{\max}\sqrt{1+\kappa}\sin 2\theta_{pp}}{1+\kappa\sin^2\theta_{pp}}, \tag{1}$$

where $d\sigma_0/d\Omega$ is the differential cross section at the zero angle, κ is a slope parameter of the angular distribution, and $A_y^{\max}$ is the maximal value of A_y acquired when $\sin^2\theta_{pp} = 1/(2+\kappa)$.

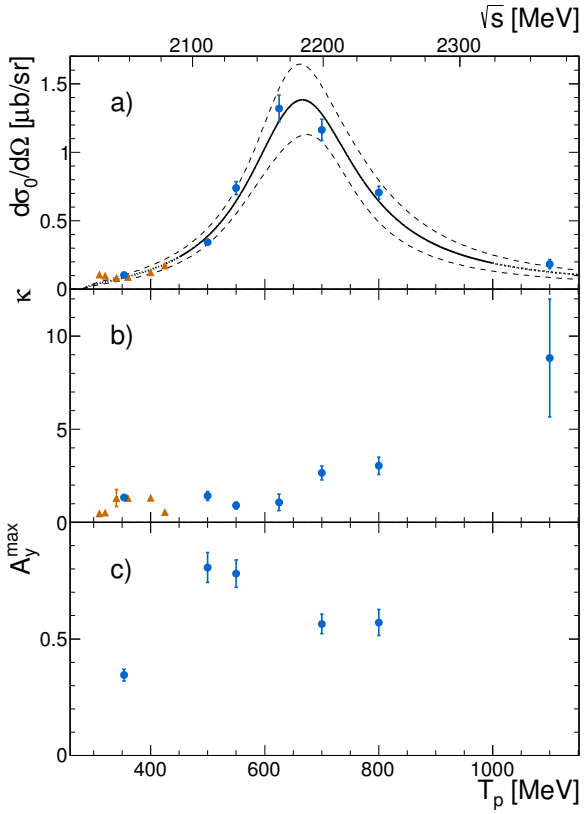

Fig. 1: Energy dependences of $d\sigma_0/d\Omega$ (a), κ (b), and $A_y^{\max}$ (c). • — ANKE data (combined analysis of [1–3]), ▲ — WASA data [4].

Fig. 1 reveals the distinct features of the data: a clean peak at 660 MeV in the $d\sigma_0/d\Omega$ energy dependence, a dip at the zero angle in the angular distribution upon the whole energy region, significant values (0.4–0.8) of the analyzing power. Comparison of the reaction with its spin-isospin partner $pp \to d\pi^+$ confirms a possibility to describe the $pp \to \{pp\}_s\pi^0$ reaction in the Δ excitation region in terms of only two transitions, ^3P_2d and ^3P_0s. Their amplitudes can be unambiguously expressed via $d\sigma_0/d\Omega$, κ, $A_y^{\max}$ and be fitted to the experimental values.

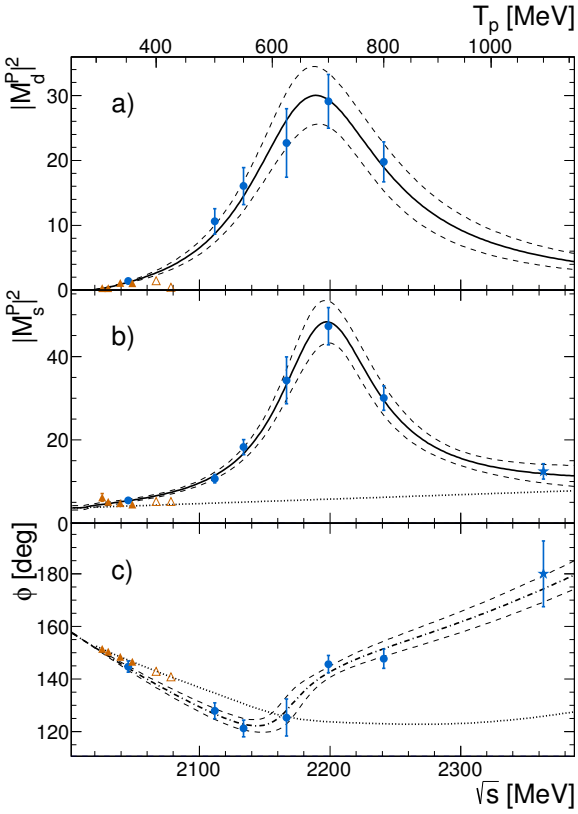

Fig. 2: Energy dependences of the amplitudes squared of the transitions ^3P_2d (a), ^3P_0s (b) and their relative phase ϕ (c). The solid curves show the approximation of $\left|M_d^P\right|^2$ and $\left|M_s^P\right|^2$ by the modified Breit-Wigner.

Result of the fit (Fig. 2) shows that the amplitudes squared of the both transitions are of the resonance kind with a close size and a relative phase variating smoothly in the limited interval of 125°–180°. The corresponding Breit-Wigner resonance parameters are: $E_R(^3P_2d) = 2197 \pm 8$ MeV, $\Gamma_R(^3P_2d) = 130 \pm 21$ MeV, $E_R(^3P_0s) = 2201 \pm 5$ MeV, $\Gamma_R(^3P_0s) = 91 \pm 12$ MeV. The parameters of the ^3P_2d resonance are compatible with those found earlier in the partial amplitude analysis of a vast data set of many experiments [5]. The ^3P_0s one is observed for the first time. Thus, a number of the resonances established in the pp scattering increased at present up to four ones: $^1D_2(2+)$, $^3F_3(3-)$, $^3P_2(2-)$, $^3P_0(0-)$.

References:

[1] V. Kurbatov *et al.*, Phys. Lett. B **661**, 22 (2008).
[2] D. Tsirkov *et al.*, Phys. Lett. B **712**, 370 (2012).
[3] D. Tsirkov *et al.*, talk at EuNPC2015, http://eunpc2015.org (2015).
[4] R. Bilger *et al.*, Nucl. Phys. A **693**, 633 (2001).
[5] SAID interactive code, http://gwdac.phys.gwu.edu

[1] LNP JINR, RU-141980 Dubna, Russia
[2] IKP FZ Jülich, D-52425 Jülich, Germany
* supported by COSY-FFE

Measurement of the spin correlation parameters in the $pd \to {}^3\mathrm{He}\,\pi^0$ reaction*

S. Dymov[1,2], V. Shmakova[1,2] and C. Wilkin[3] for the ANKE collaboration

Two-body pion production in the interaction of protons with few-nucleon systems is of interest, both from the point of view of studying the reaction mechanism, and from that of determining the structure of light nuclei. The success of microscopic models with explicit Δ-excitation for two-nucleon systems suggests that these models should be tested in the three-nucleon case, where production of Δ is intimately linked to 3N forces. The phenomenological approach, using impulse approximation with $pp \to d\pi^+$ cross section, as input was successful near the reaction threshold but only partial progress has been achieved at higher energies [1].

In general six invariant amplitudes are required to describe the $pd \to {}^3\mathrm{He}\,\pi^0$ reaction and these amplitudes will be functions of the angle between the incident proton and outgoing pion in the c.m. frame. The number of independent functions reduce to two at threshold or in the forward/backward directions. These may be written as [2]

$$F(dp \to {}^3\mathrm{He}\pi^0) = \bar{u}_\tau \vec{p}\cdot(A\vec{\varepsilon} + iB\vec{\varepsilon}\times\vec{\sigma})u_p. \qquad (1)$$

Here $\vec{\varepsilon}$ is the deuteron polarisation vector, $\vec{p}$ and $\vec{k}$ the proton and pion centre-of-mass momenta and u_p and u_τ the initial and final fermion spinors. The amplitude should be multiplied by a $\sqrt{2}$ factor if the $pd \to {}^3\mathrm{H}\pi^+$ reaction is being considered.

If only the two amplitudes A and B are retained, the unpolarised c.m. differential cross section, deuteron tensor analysing power, and vector transverse spin correlation become

$$\frac{d\sigma}{d\Omega} = \frac{kp}{3}(|A|^2 + 2|B|^2), \qquad (2)$$

$$T_{20} = \sqrt{2}\frac{|B|^2 - |A|^2}{|A|^2 + 2|B|^2}, \qquad (3)$$

$$C_{y,y} = -\frac{2Re(A^*B)}{|A|^2 + 2|B|^2}, \qquad (4)$$

whereas iT_{11} and T_{22} , as well as the proton analysing power A_y, must all vanish.

The $pd \to {}^3\mathrm{He}\,\pi^0$ and $pd \to {}^3\mathrm{H}\,\pi^+$ reactions have been studied experimentally over many decades and a wealth of data on the differential cross sections and analysing powers has been collected for these processes. However, the double polarisation observables have been explored far less and information on the spin correlations is still very scarce. The ANKE spectrometer equipped with an internal polarised target together with the polarised deuteron beam of COSY offer a unique opportunity to conduct measurements of the transverse spin correlation coefficients in these reactions.

Two double-polarisation experiments have been performed at ANKE with a polarised deuteron beam and a polarised hydrogen target, at the beam energies of 363 and 600 & 1115 MeV per nucleon (COSY proposals #172 and #205). The data at the two lower energies were analysed to obtain the spin correlations in the $pd \to {}^3\mathrm{He}\,\pi^0$ reaction. These results can be used together with the existing data on the differential cross section and the tensor analysing power T_{20} [3] to extract information on the forward amplitudes A and B from eq. 2-4.

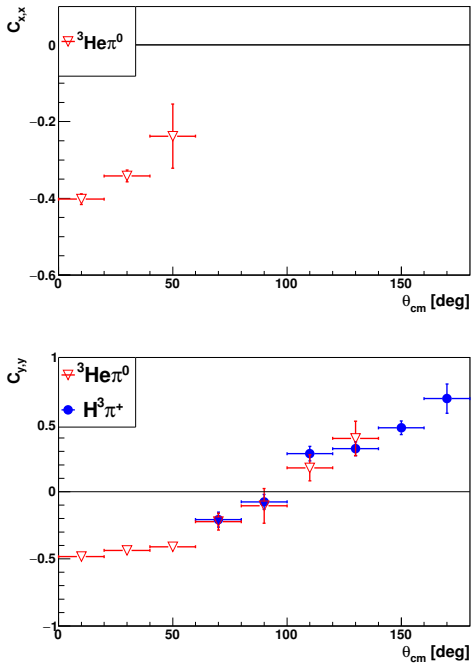

Fig. 1: Transverse spin correlation coefficients $C_{x,x}$ and $C_{y,y}$ in the $\vec{d}\vec{p} \to {}^3\mathrm{He}\,\pi^0$ and $\vec{d}\vec{p} \to {}^3\mathrm{H}\,\pi^+$ reactions at 363 MeV per nucleon.

Preliminary results at 363 MeV are presented in Fig. 1. Both ^{3}He and ^{3}H production processes could be investigated at this energy and the results in the angular range of $60 - 140^o$ covered by the both reactions are completely compatible. The ANKE detector acceptance is limited by the size of the gap in the analysing magnet D2 and is concentrated around $\phi = 0^\circ$ and 180° regions. This leads to a better definition of the $C_{y,y}$ coefficient as compared to $C_{x,x}$.

Since a clean selection of tritium by the energy loss in the scintillation hodoscope is no longer feasible at 600 MeV per nucleon, only data on the $pd \to {}^3\mathrm{He}\,\pi^0$ reaction are shown at this higher energy. The $C_{x,x}$ and $C_{y,y}$ coefficients measured at small angles are presented in Fig. 2. In addition to these spin correlation parameters, the proton and deuteron vector analysing powers can also be extracted from these data. At 363 MeV, A_y^p can be compared to the data of Ref. [4] and to the high statistics ANKE measurement with a polarised proton beam and a deuterium cluster-jet target [5], as it is

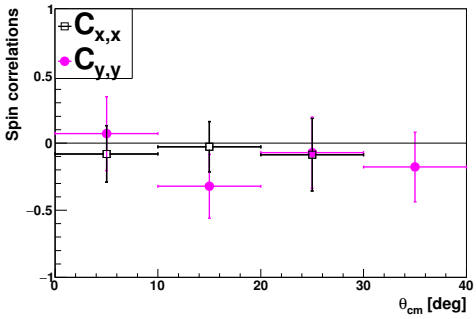

Fig. 2: Transverse spin correlation coefficients $C_{x,x}$ and $C_{y,y}$ in the $\vec{d}\vec{p} \to {}^3\mathrm{He}\,\pi^0$ reaction at 600 MeV per nucleon.

shown in Fig. 3. The new results from the double-polarisation experiment are completely compatible with the existing data.

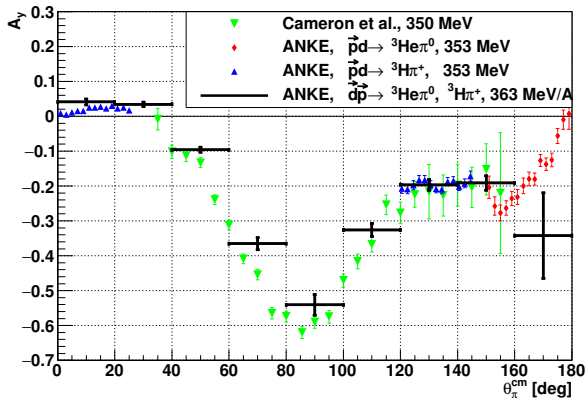

Fig. 3: Proton vector analysing power in the $pd \to {}^3\mathrm{He}\,\pi^0$ and $pd \to {}^3\mathrm{H}\,\pi^+$ reactions at $T_p = 353$ (363) MeV per nucleon. ANKE data with a polarised proton beam and a deuterium cluster-jet target (blue triangles up and red diamonds), and the ANKE double-polarisation data (black line), are compared to the data from Ref. [4] shown with green triangles down.

References:

[1] W.R. Falk *et al.*, Phys. Rev. C 50 (1994) 1574
[2] J.-F. Germond and C. Wilkin, J. Phys. G 16 (1990) 381
[3] C. Kerboul *et al.*, Phys. Lett. B 181 (1986) 28
[4] J.M. Cameron *et al.*, Nucl. Phys. A 472 (1987) 718
[5] V. Shmakova *et al*, IKP Annual report 2010

[1] IKP, Forschungzentrum Jülich, 52425 Jülich, Germany
[2] LNP, JINR, 141980 Dubna, Russia
[3] Physics and Astronomy Department, UCL, London, WC1E 6BT, United Kingdom

* Supported by the COSY-FFE programme.

Deuteron breakup $pd \to \{pp\}_s n$ and the contact d-term in the $pN \to \{pp\}_s \pi$ subprocesses

Yu. N. Uzikov[1] for the ANKE collaboration.

A number of spin observables for the single-pion production reactions $pp \to \{pp\}_s \pi^0$ and $pn \to \{pp\}_s \pi^-$, where $\{pp\}_s$ is the pp pair in the $^1S_0$ state, was measured at ANKE@COSY at 353 MeV [1, 2, 3] including the unpolarized differential cross section $d\sigma/d\Omega$, the vector analyzing power A_y, and the spin correlation coefficient $C_{x,x} = -C_{z,z}$, in the notation of [4]. (Note that $C_{y,y} = 1$.) A partial wave analysis (PWA) of these data was done and as a result three different solutions for the set of five partial-wave amplitudes in the isospin channels $T = 0$ and $T = 1$ were found. The aim of that study was to extract one low-energy constant (LEC), d, associated with a $(N\bar{N})^2\pi$ contact term that arises in the treatment of few-nucleon reactions within chiral effective field theory. This LEC determines the strength of the one-pion exchange three-nucleon force and contributes also to electroweak processes. It means that the amplitudes of the following reactions are connected with each other via this contact term: single-pion production $NN \to NN\pi$, the reaction $\pi^- d \to nn\gamma$, $\nu(\tilde{\nu})d$ breakup, pion absorption on the deuteron $\mu^- d \to nn\nu_\mu$, pp fusion $pp \to d\,e^+\nu_e$, the so called hep process $^3He\,p \to {}^4He\,e^+\nu_e$, the triton β decay, and many others with a larger number of nucleons involved [5, 6, 7]. Once the LEC d is determined from one process, it can be used to calculate observables of any of the other reactions. However, it is important to compare the strength of the contact term, extracted from data at higher energies, i.e. at $T_p = 353$ MeV, with that found at low energies [8] in order to check the applicability of ChEFT in different energy regions.

Unfortunately, the obtained data on the reactions $pp \to \{pp\}_s \pi^0$ and $pn \to \{pp\}_s \pi^-$, are incomplete because the last nontrivial spin-correlation coefficient $C_{x,z}$ was not measured. As a consequence of the incompleteness of the data set it turned out that the obtained PWA solution is ambiguous and several solutions were found as mentioned above.

In order to put further constraints on those solutions, we will study from theory side spin observables of the reaction $pd \to \{pp\}_s n$ measured recently at ANKE-COSY at the same energy in the kinematics of backward elastic pd scattering. The point is that the transition amplitude of the reaction $pd \to \{pp\}_s n$ involves the triangle diagrams with one-pion exchange and the subprocesses $pp \to \{pp\}_s \pi^0$ and $pn \to \{pp\}_s \pi^-$ (see Fig.1), i.e. the amplitudes discussed above, together with other important mechanisms (see Refs. [9],[13]). The study of the deuteron breakup reaction with fast diproton formation was initiated by the theoretical model of Ref. [9], and then continued in Refs. [10, 11]. First data on the reaction were published in Ref. [12]. Previously we studied the deuteron break-up reaction $pd \to \{pp\}_s n$ measured at higher energies 0.5-1.5 GeV [14] within two different complementary approaches based on other set of triangle diagrams of the one-pion-exchange mechanism with the subprocesses $\pi d \to NN$ in Ref. [15] and also on the basis of the SS+Δ+ONE model [9], which includes the Δ-isobar (Δ) explicitly together with the single scattering (SS) mechanism and the one-nucleon exchange (ONE) with rescattering taken into account [13]. Within this approach the energy dependence of the differential cross section $d\sigma/d\Omega$ of the reaction $pd \to \{pp\}_s n$ at the c.m.s. scattering angle of the final neutron $\theta^n_{cm} = 180^\circ$ and its angular depedence were explained.

At lower energies < 0.5 GeV the $pd \to \{pp\}_s n$ reaction was not yet studied. The proposed here calculation of the spin observables of the deuteron break-up at 353 MeV using triangle diagrams in Fig. 1 with the subprocesses $pp \to \{pp\}_s \pi^0$ and $pn \to \{pp\}_s \pi^-$ will allow us to investigate the sensitivity of these observables to the differences in the obtained PWA solutions for the $pN \to \{pp\}_s \pi$ process. Such a sensitivity could be used to discriminate between those solutions by comparison with the date on the reaction $pd \to \{pp\}_s n$. For this aim a new data on the the reaction $pd \to \{pp\}_s n$ is planned to be get out at 353 MeV [16].

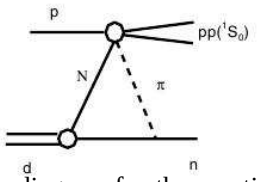

Fig. 1: The tiangle diagram for the reaction $pd \to \{pp\}_s n$ with the subprocess $pN \to \{pp\}_s \pi$.

References:

[1] S. Dymov *et al.*, Phys. Lett. B **712**, 375 (2012).
[2] D. Tsirkov *et al.*, Phys. Lett. B **712**, 370 (2012).
[3] S. Dymov *et al.*, Phys.Rev. C **88**, 014001 (2013).
[4] G. Ohlsen, Rep. Prog. Phys. **35**, 717 (1972).
[5] V. Baru *et al.*, Phys. Rev. C **80**, 044003 (2009).
[6] V. Baru, J. Phys: Conf. Ser. **295**, 012026 (2011).
[7] A. Gårdestig and D.R. Phillips, Phys. Rev. Lett. **96**, 232301 (2006).
[8] D. Gazit, S. Quaglioni, P. Navratil, Phys. Rev. Lett. **103**, 102502 (2009).
[9] O. Imambekov and Yu.N. Uzikov, Yad. Fiz. **52**, 1362 (1990) (Sov. J. Nucl. Phys. **52**, 862 (1990)).
[10] A.V. Smirnov and Yu.N. Uzikov, Phys. At. Nucl. **61**, 361 (1998).
[11] Yu.N. Uzikov, J. Phys. G **28**, B13 (2002).
[12] V.I. Komarov *et al.*, Phys. Lett. B **553**, 179 (2003).
[13] J. Haidenbauer and Yu. N. Uzikov, Phys. Lett. B **562**, 227 (2003).
[14] S. Dymov *et al.*, Phys. Rev. C **81**, 044001 (2010).
[15] Yu.N. Uzikov, J. Haidenbauer, C. Wilkin, Phys. Rev. C **75**, 014008 (2007).
[16] S. Dymov, private communication.

1 JINR, 141980 Dubna, Russia

One-loop contribution of the Δ-isobar mechanism to the reaction $pp \to \{pp\}_s\pi^0$ near the Δ-threshold region

Yu. N. Uzikov[1] for the ANKE collaboration.

Single pion production in NN-collision is the simplest inelastic process in the NN scattering which is used at rather low energies as a testing ground for the chiral perturbation theory of nucleon-nucleon interactions. At higher energies the resonance structure observed in the total cross section of the reaction $pp \to d\pi^+$ with the maximum at about 600 MeV is explained by the $\Delta(1232)$-isobar excitation in the intermediate state via the subprocess $NN \to N\Delta$ (see Ref. [1] and references therein). Within the same approach based on the method of coupled channels differential cross section and several spin observables were explained reasonably [1, 2]. Another channel of this reaction is the process $pp \to \{pp\}_s\pi^0$ with formation of the diproton $\{pp\}_s$ in the final state with small excitation energy $E_{pp} < 3$ MeV providing a dominance of the $^1S_0$ state. It is interesting to consider the reactions $pp \to d\pi^+$ and $pp \to \{pp\}_s\pi^0$ together at similar kinematical conditions. The point is that due to zero spin of the $^1S_0$ diproton $\{pp\}_s$ the reaction $pp \to \{pp\}_s\pi^0$ is described only by two independent spin amplitudes in contrast to six amplitudes for the $pp \to d\pi^+$. This fact allows one to perform a complete polarization experiment for the reaction $pp \to \{pp\}_s\pi^0$ using few differential spin observables. In part this was done at ANKE@COSY for the $pp \to \{pp\}_s\pi^0$ and $pn \to \{pp\}_s\pi^-$ reactions at 353 MeV. Furthermore, the isospin T=1 of the diproton differs from the deuteron isospin T=0. In total, the transitions allowed by the angular-momentum and P-parity conservation are essentially different in the diproton case as compared with the deuteron channel. Therefore, the reaction $pp \to \{pp\}_s\pi^0$ provides a strong test for the models developed for the reaction $pp \to d\pi^+$.

According to [3], the coupled channels approach [1] which explains the reaction $pp \to d\pi^+$ semi-quantitatively, completely fails to describe the data on the reaction $pp \to \{pp\}_s\pi^0$ obtained by ANKE@COSY [4, 5]. A simpler model based on the triangle diagram of the one-pion exchange with the subprocess $\pi N \to \pi N$ turned out to be more successful [6]. In this work we study the reaction $pp \to \{pp\}_s\pi^0$ using (antisymmetrized) on-loop diagrams with the subprocess $\pi N \to \Delta \to p\pi^0$ (Fig.1). For the coupling constants and vertex form factors are used the same parameters as in [7]. The CD Bonn model is used for the $^1S_0$ NN. The penetrate Z-factor is introduced to account the momentum dependence of the Δ-isobar width. The numerical results show (see Fig.2) that the energy dependence of the differential cross section at zero angle of the pion is qualitatively explained in the energy interval 0.4 -1.4 GeV. However, the calculated angular dependence of the differential cross section and A_y is in contradiction with the ANKE data at 0.35 -0.8 GeV [8]. The partial wave amplitude analysis is performed for this mechanism using the Jacob-Wick formalism. The obtained numerical results show that the following three partial waves ^3P_0s, ^3P_2d and ^3F_2d are important in the energy interval 0.35-0.8 GeV, whereas the $^3F_4g - ^3H_4g$ amplitude and other amplitudes with higher orbital momenta are negligible.

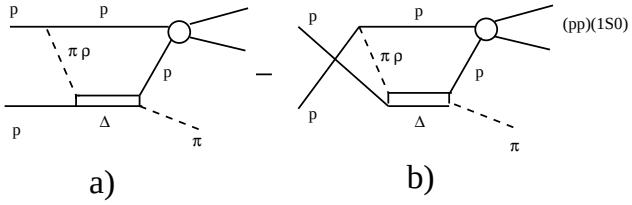

Fig. 1: The one-loop Δ-mechanisms of the $pp \to \{pp\}_s\pi^0$ reaction: a) – direct term, b) – exchange term.

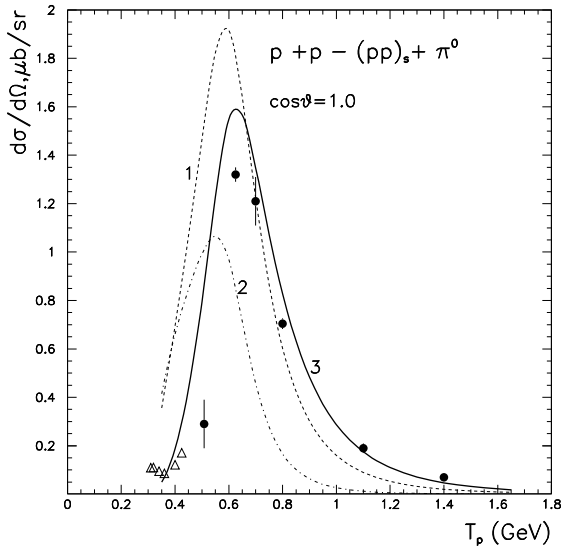

Fig. 2: Differential cross section of the reaction $pp \to \{pp\}_s\pi^0$ at $cos\theta = 1$ versus the proton beam energy. The curves are results of calculations for the one-loop mechanism with the Δ-isobar excitation with the cutoff parameter $\lambda_\pi = 0.65$ GeV/c, $\lambda_\rho = 0.7$ GeV/c, and $Z^{3/2}$ factor in both $\pi N\Delta$-vertexes as defined in Ref. [7]:1 – the direct mechanism with normalization factor $N = 0.55$, 2 – the exchange mechanism (with $N = 1$), 3 – total result with $N = 1$. Experimental data (•) are taken from [4],[5].

References:

[1] J.A. Niskanen, Phys.Lett. **141B**, 301 (1984)
[2] C. Furget *et al.*, Nucl. Phys. A **655**, 495 (1999)
[3] J.A. Niskanen, Phys. Lett. B **642**, 34 (2006)
[4] S. Dymov *et al.*, Phys.Lett. B **635**, 270 (2006)
[5] V. Kurbatov *et al.*, Phys.Lett. B **661**,22 (2008)
[6] Yu.N. Uzikov, arXiv:0803.2342 [nucl-th], arXiv:0812.4661 [nucl-th].
[7] Yu.N. Uzikov, J. Haidenbauer, C. Wilkin, PoS (Baldin ISHEPP XXII) 093 (arXiv:1502.04675 [nucl-th]).
[8] D. Tsirkov, private communication.

1 JINR, 141980 Dubna, Russia

Identification of the reaction $p + d \rightarrow d + \eta + p_{sp}$ *

D. Schröer†, C. Fritzsch, A. Khoukaz, M. Rump for the ANKE-Collaboration

The reaction $p + d \rightarrow d + \eta + p_{sp}$ was measured at the ANKE spectrometer to study the η-nucleus final state interaction (FSI) and to further investigate the question on the possible existence of η-mesic nuclei. Here, the deuteron is used as an effective neutron target with the proton being a spectator particle. The combination of the Fermi motion inside the target with two different beam momenta, $p_1 = 2.09$ GeV/c and $p_2 = 2.25$ GeV/c, allows to extract total and differential cross sections in a region from threshold up to an excess energy of Q = 90 MeV.

For the two-particle $p + n \rightarrow d + \eta$reaction the cross section can be written as

$$\frac{d\sigma}{d\Omega} = \frac{p_f}{p_i} \cdot |f(\vartheta)|^2 \quad (1)$$

with p_f and p_i being the center of mass final/initial state momentum and f the production amplitude. As long as there are no higher partial waves than s-wave, f can be rewritten as a constant term f_{prod} and a term describing the final state interaction between deuteron and η meson

$$|f(\vartheta)|^2 = |\frac{1}{f_{\text{prod}}|^2} \cdot |\text{FSI}|^2 = \frac{|f_{\text{prod}}|^2}{|1 - iap_f|^2} \quad (2)$$

with the complex scattering length a [1].To pin down the range in which this ansatz is valid the onset of higher partial waves has to be identified. Therefore differential cross sections will be determined to identify contributions different from pure s-wave.

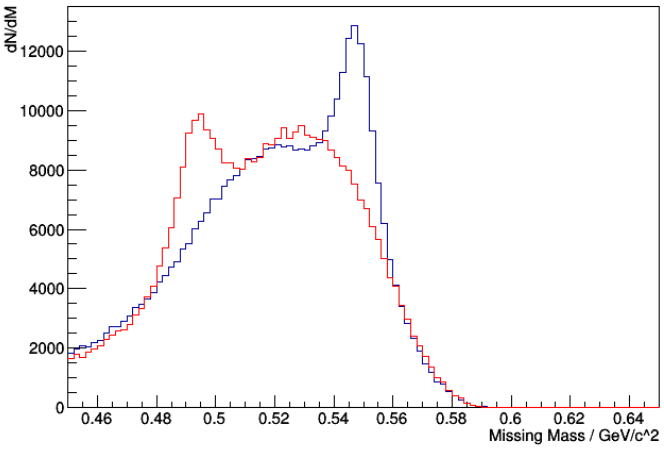

Fig. 1: Missing Mass for both used beam momenta ($p_1 = 2.09$ GeV/c in black and shifted for $p_2 = 2.25$ GeV/c in red) in an excess energy range from 0 MeV up to 5 MeV

As the influence of the FSI term is best seen near the production threshold, it is mandatory to extract a clean signal in its vicinity. To identify the reaction the missing mass technique is used with the spectator proton being detected in one of two Silicon Tracking Telescops ("STT") and the deuteron in the ANKE Forward System ("Fd system"). Due to the huge proton background in the Fd system, great importance was set on the clean separation of the protons and deuterons [2].

As the peak of the η meson is close to the kinematic limit near the threshold a creative solution for background description is necessary.
An elegant way to substract the multi-pion background was developed by the SPESIII Collaboration [3]. The data taken at the second beam energy are analysed as if they were taken at the other energy. By doing this the kinematic limits of both data sets are identical, but the peaks of the investigated reaction are shifted (Fig. 1).

The substraction of these two spectra results in a peak and a dip for the shifted data set (Fig. 2).

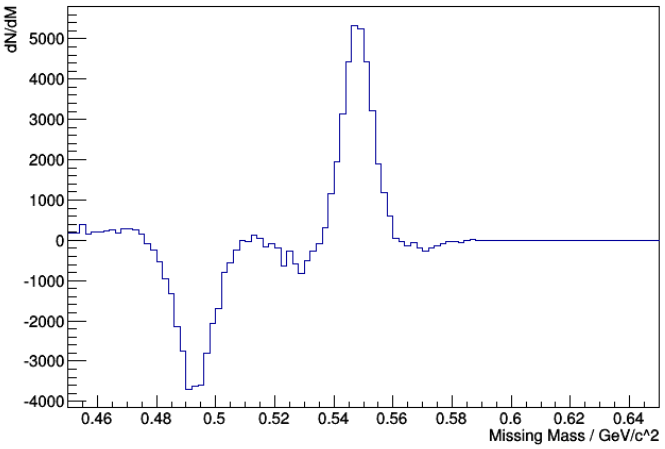

Fig. 2: Difference between the missing mass spectra for both beam momenta in an excess energy range from 0 MeV up to 5 MeV

This allows for a clean and model independent identification of the reaction $p+d \rightarrow d+\eta+p_{sp}$ near threshold. First calculations show that the data are in agreement with the expected count rates. The further analysis of the data is in progress and results on the cross section will be available soon.

References:

[1] C. Wilkin et al., Phys. Lett. B 654, 92-96, 2007
[2] M. Rump et al., Annual report (2015)
[3] F. Hibou et al., Phys. Rev. Lett. 83, (1999) 492.

*Supported by COSY-FFE
†Institut für Kernphysik, Westfälische Wilhelms-Universität, 48149 Münster, Germany

High precision study on the η-meson production channel $d + p \to {}^3\mathrm{He} + \eta^*$

C. Fritzsch†, A. Khoukaz, M. Rump, and D. Schröer for the ANKE-Collaboration

The ANKE collaboration has performed a beam time to determine the η meson mass with high precision using the $d + p \to {}^3\mathrm{He} + \eta$ reaction [1] and to study the two pion production using $d + p \to {}^3\mathrm{He} + \pi^+ + \pi^-$ [2]. In order to determine the η mass, data has been studied at 18 deuteron beam momenta in a range between $3120.17\ \mathrm{MeV}/c \leq p_d \leq 3204.16\ \mathrm{MeV}/c$ which could be extracted very accurately via the resonant depolarization technique with a precision of $\Delta p_d/p_d < 6 \times 10^{-5}$ [1, 3].
Moreover, due to the high statistics of more than 1×10^5 ${}^3\mathrm{He}\eta$ events per energy in combination with full angular coverage these high precision ANKE data allow to investigate the total and differential cross sections of the reaction $d + p \to {}^3\mathrm{He} + \eta$. Such data are of special interest since they differ strongly from a pure phase space behaviour near threshold. Furthermore, analysis of the asymmetry factor

$$\alpha = \frac{d}{d\cos\vartheta_\eta^{\mathrm{CMS}}} \ln\left(\frac{d\sigma}{d\Omega}\right)_{\cos\vartheta_\eta^{\mathrm{CMS}}=0} \qquad (1)$$

of the differential cross sections show a distinct effect of s- and p-wave interference with the η momentum, which can be explained by a rapid variation of the relative phase. These effects are an indication for an unexpected strong final state interaction (FSI) between η mesons and ${}^3\mathrm{He}$ nuclei which could lead to the formation of a quasi-bound state of the $\eta{}^3\mathrm{He}$-system [4, 5].
To extract total and differential cross sections of the η production channel $d + p \to {}^3\mathrm{He} + \eta$ with high precision, a careful luminosity determination was performed for each of the 18 beam momenta of the beam time via dp-elastic scattering [6]. Thereby it was possible to achieve statistical uncertainties of $\Delta_{\mathrm{stat}} = 1\%$ and systematic uncertainties of $\Delta_{\mathrm{sys}} = 6\%$ which leads to an improvement by at least a factor of two compared to previous measurements.

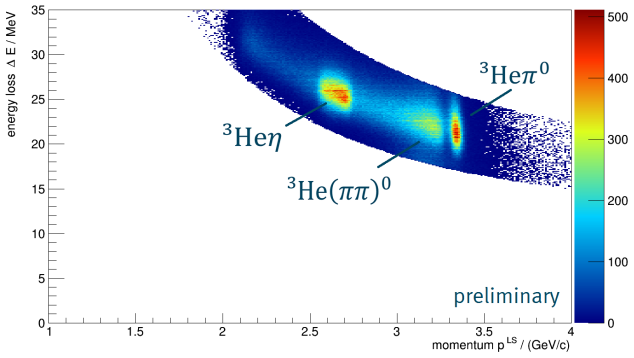

Fig. 1: The two-dimensional distribution of the energy loss information in the forward scintillator hodoscopes of the first layer versus the particles laboratory momentum for a beam momentum of $3158.71\ \mathrm{MeV}/c$. A clear ${}^3\mathrm{He}$ band becomes visible consisting of the single-, multi-pion, and η production.

Identification of the η production channel is achieved by detecting the ${}^3\mathrm{He}$-nuclei in the ANKE Forward Detection system ("FD system") with the calibrated energy loss information [7] in the scintillator hodoscopes. After cutting on the characteristical $\Delta E/p$ band of ${}^3\mathrm{He}$-nuclei (cf. Figure 1), missing mass analyses show a distinct η signal for each beam momentum with more than 10^5 ${}^3\mathrm{He}\eta$ events per energy. The background description is done with data taken below the η production threshold at a beam momentum of $3120.17\ \mathrm{MeV}/c$, therefore allowing a model independent approach. In order to do this, the subthreshold data will be analyzed with the desired laboratory momentum which leads to a shift of the kinematical limit in the missing mass spectra, using

$$\vec{p}_{\mathrm{LS}}^{\,\mathrm{desired}} = \frac{p_{\mathrm{beam}}^{\mathrm{desired}}}{p_{\mathrm{beam}}^{\mathrm{subth.}}} \cdot \vec{p}_{\mathrm{beam}}^{\,\mathrm{subth.}} \quad , \qquad (2)$$

and is then scaled to fit the data. After background subtraction a clear η peak is left (cf. Figure 2).

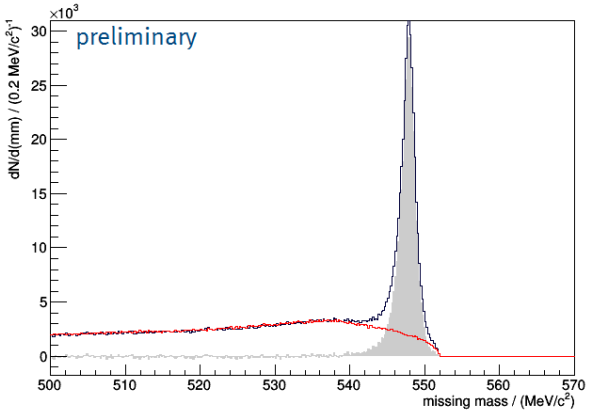

Fig. 2: Missing mass distribution of the events passing the energy loss selection cut for a beam momentum of $3158.71\ \mathrm{MeV}/c$ (blue) and for data taken below the η production threshold (red) as a model independent background description (see text for more detailed information). After background subtraction a clear η peak is left (shaded grey).

Due to the high statistics and the full geometric acceptance of ANKE, this analysis can be performed bin-wise over the entire angular range. An acceptance correction via Monte Carlo simulations is in progress, so that first results will be available soon.

References:

[1] P. Goslawski *et al.*, Phys. Rev.D **85**, 112011 (2012).
[2] M. Mielke *et al.*, Eur. Phys. J. A **50**, 102 (2014).
[3] P. Goslawski *et al.*, Phys. Rev. ST-AB **13**, 022803 (2010).
[4] T. Mersmann *et al.*, Phys. Rev. Lett. **98**, 242301 (2007).
[5] C. Wilkin *et al.*, Phys. Lett. B **654**, 92 (2007).
[6] C. Fritzsch, *"Investigation of different normalization reactions for dp collisions at the ANKE experiment"*, Master thesis , (2014).
[7] C. Fritzsch, *"Energy calibration for the ANKE experiment"*, Bachelor thesis , (2011).

*Supported by the COSY-FFE program of the Forschungszentrum Jülich
†Institut für Kernphysik, WWU Münster, Germany

Identification of deuterons in p + d → d + X reactions *

M. Rump†, C. Fritzsch, A. Khoukaz, D. Schröer for the ANKE-Collaboration

The interaction between η mesons and hadrons is an intensively investigated topic. In order to get further insights and to study the production mechanism of η mesons a measurement of the reaction pd → dηp_{sp} near threshold has been performed at ANKE [1]. Here the deuteron acts as an effective neutron target while the proton is handled as a spectator particle. The Fermi motion of these particles combined with the two different beam momenta (p_1 = 2.09 GeV/c and p_2 = 2.25 GeV/c) allow to study the reaction on a wide excess energy range from threshold up to 90 MeV.

The reconstruction of the η mesons will be accomplished via the missing mass method. Therefore clearly identifying the proton and the deuteron is an essential part of the procedure. The spectator protons are detected in one of two Silicon Tracking Telescopes (”STT”) [2] and can be selected with an almost negligible background from, e.g., deuterons [3].
Contrary, due to a dominant proton background, the identification of the deuterons in the ANKE Forward system (Fd) via the energy loss is more challenging. In ΔE-p spectra the proton and deuteron bands are located very close to each other (Fig. 1 (left)). This is also shown in the projection $\Delta E \cdot \beta^2$ (Fig. 1 (right)) with the relativistic velocity β, where the deuterons appear as a small shoulder on the right tail of the dominant proton peak. As a first step the energy loss in each Fd counter was then calibrated based on Monte Carlo simulations.

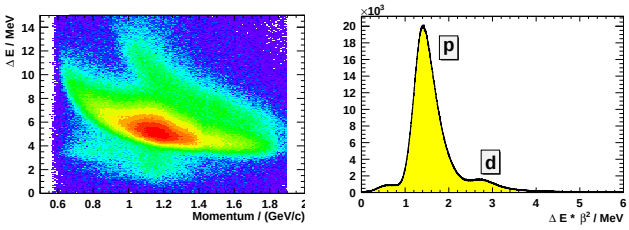

Fig. 1: Left: Energy loss ΔE versus momentum p in the Fd system. The proton band and a deuteron band on top of it are clearly visible. Right: $\Delta E \cdot \beta^2$-spectrum (right) with a dominant proton peak and a small deuteron shoulder on the right-hand side.

In order to allow careful studies on particle identification, an additional trigger was installed during the beam time, combining the Positive detector system (Pd) and the Fd system. By simultaneously detecting a π^+ in the Pd system and another particle in the Fd system one can distinguish protons from deuterons by comparing the Time-of-Flight (ToF) difference between these two particles. The π^+ can be easily identified because of its low energy loss compared to protons. Due to the significant ToF difference the deuteron and proton bands are clearly separated as shown in Fig. 2.
By applying an optimized cut in Fig.2 it is possible to investigate $\Delta E \cdot \beta^2$ spectra individually for deuterons and protons, as can be seen in Fig.3. With this information final

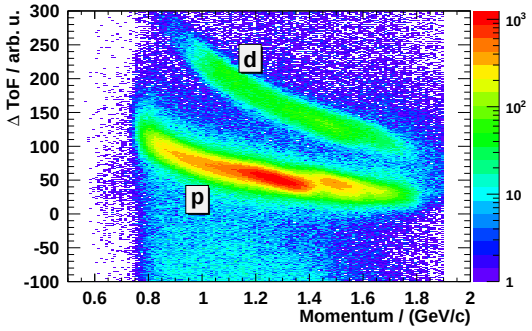

Fig. 2: Time-of-Flight (ToF) difference of the π^+ hit and another particle detected in the Fd system versus the momentum of this particle for one combination of Fd and Pd counter elements. The deuteron band is clearly separated from the proton band.

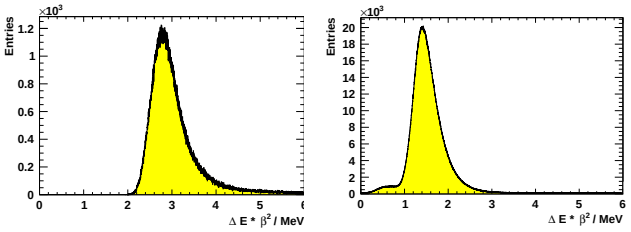

Fig. 3: Left: $\Delta E \cdot \beta^2$-spectrum of the extracted deuteron signal by applying the Time-of-Flight method. Right: Remaining proton background.

cuts will be identified to reduce the proton background in the reaction pd → dηp_{sp} drastically.
Moreover, this method can also be used to identify other reactions that can be studied with the same dataset, e.g. pd → d$\pi^+\pi^-$$p_{sp}$. The wide excess energy range allows to study the low and high-mass enhancement in isoscalar $M_{\pi\pi}$ spectra corresponding to the ABC effect as well as total and differential cross sections [4]. The analysis of this reaction is in progress and first results will be available soon.

References:

[1] A. Khoukaz et al, Measurement of the quasi-free $pn \to d\eta$ cross section at ANKE, 2012 , http://www2.fz-juelich.de/ikp/anke/en/proposals.shtml
[2] A. Mussgiller, Identification and Tracking of Low Energie Spectator Protons, doctoral thesis, Universität Köln, Germany, 2007
[3] D. Schröer et. al., Annual report, 2013
[4] D. Guderian, bachelor thesis, Westfälische Wilhelms-Universität Münster, 2015

*Supported by COSY-FFE
†Institut für Kernphysik, Westfälische Wilhelms-Universität, 48149 Münster, Germany

Study of the $\vec{p}n$ quasi-free elastic scattering at ANKE*

S. Barsov[1], Z. Bagdasarian[2,4], D. Chiladze[3], S. Dymov[3], A. Kacharava[2], G. Macharashvili[3], S. Merzlyakov[2], S. Mikirtychyants[1,2], R. Schleichert[2], S. Trusov[2] for the ANKE collaboration.

As discussed in [1], the nucleon-nucleon interaction amplitudes extracted by the phase-shift analysis are of general importance for study of any hadronic process at intermediate energies. The significant contribution to a small angle domain of the np elastic scattering has been done at ANKE during last years by measuring the interaction of deuteron beam with the hydrogen target [2]. However, in this case the beam energy is limited by 1.15 GeV/nucleon. To approach the higher energy range, where data are very scarce, measurements were performed at ANKE using the polarized proton beam and unpolarized deuterium cluster target.

The data have been taken at 6 proton beam energies of 0.8, 1.6, 1.8, 2.0, 2.2 and 2.4 GeV. The orientation of beam polarization ($\vec{P}_b$) was changing along Y-axis at every beam injection. The polarization value was measured by the EDDA polarimeter. Two Silicon Tracking Telescopes (STT) were installed at 3cm distance to the left and to the right from the deuterium target to detect low energetic particles in coincidence with fast particles going into the ANKE Forward detector (Fd). The missing mass technique and the asymmetric Fd acceptance were exploited for identification of the quasi-free NN elastic scattering as described in [3].

Under the given experimental conditions the ANKE was operating as a single-arm polarimeter. So, the analyzing power (A_y) has to be derived from the asymmetry of counts corresponding to different orientations of $\vec{P}_b$. Such asymmetry is very sensitive to the relative normalization of counts measured in the experiment at different luminosity values. The normalization procedure was verified using the $\vec{p}d$ elastic scattering at all beam energies. In particular, at 0.8 GeV the angular dependence of asymmetry was found to be well coinciding with the dependence of analyzing power measured in [4]. Furthermore, the average beam polarization determined from this asymmetry very well agreed with the polarization measured by the EDDA polarimeter.

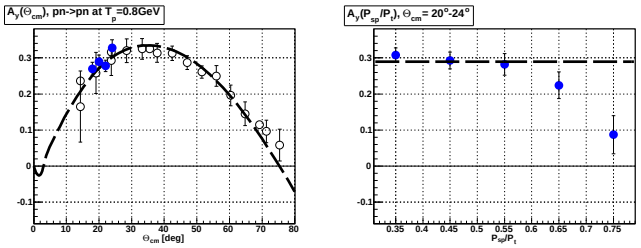

Fig. 1: The quasi-free $\vec{p}n$ elastic scattering at $T_p = 0.8$ GeV. **Left panel.** Open points represent the A_y from [5] versus Θ_{cm} angle. Blue solid points show the $A_y(\Theta_{cm})$ obtained at ANKE under conditions $P_{sp}/P_t < 0.5$ and $P_t > 0.2$ GeV/c. The SAID SP07 solution is shown by the dashed curve.
Right panel demonstrates the A_y measured at ANKE within the $\Theta_{cm} = 20^\circ - 24^\circ$ angular range as a function of the P_{sp}/P_t ratio. The dashed line indicates the $A_y(\Theta_{cm} = 22^\circ)$ predicted by SAID.

The quasi-free scenario is generally assumed to be realized when the momentum transfer from a beam particle to a scattered one (P_t) is large enough as compared with the "spectator" particle momentum (P_{sp}). In contrast to other experiments [5, 6, 7] where the A_y of quasi-free pn elastic scattering was measured detecting both scattered particles, at ANKE the fast scattered proton was detected in coincidence with the "spectator" proton. Due to the STT construction, the proton momentum must be larger than $70 MeV/c$ to be reconstructed. Since this introduced a low threshold on the P_{sp}/P_t ratio, a validity of the "spectator" model was tested. It was found that the model can be used at $P_{sp}/P_t < 0.5$ (Fig. 1) but the additional limitation of $P_t > 0.2 GeV/c$ turned to be necessary. The same restrictions on the P_{sp}/P_t ratio and the momentum transfer were derived from the analysis of quasi-free pp elastic scattering at 0.8 GeV.

Applying the determined limitations, the analyzing power was obtained for all other beam energies. It was found to be smoothly decreasing with increasing of beam energy. The results in Fig. 2 illustrate the scale of the dependence. Despite the different experimental approach, the ANKE results at 2.2 GeV are well consistent with data from [6, 7].

As it was mentioned, the data set on pn elastic scattering above 1.5 GeV beam energy is very poor. Therefore, it is not surprising that the SAID SP07 solution does not fit to experimental data in Fig. 2. But the SAID solution was recently revised involving in the fit new experimental data measured at WASA [8]. The new SAID solution [9] gives the prediction which quite well fits to our data at 1.6 GeV.

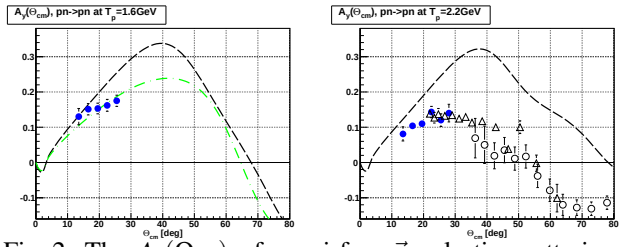

Fig. 2: The $A_y(\Theta_{cm})$ of quasi-free $\vec{p}n$ elastic scattering at 1.6 (left panel) and 2.2 GeV (right panel). Blue solid points show the A_y measured at ANKE. Open points represent results from [6, 7]. The SAID SP07 solutions are shown by dashed curves. The green dot-dashed curve represents the updated SAID solution at 1.6 GeV.

References:

[1] Proposal COSY-212 (2012)
[2] D.Mchedishvili, PhD thesis (2013)
[3] S.Barsov et al., IKP Annual Rep. (2013)
[4] F.Irom et al., Phys.Rev. C 28, 2380 (1983)
[5] M.L.Barlett et al., Phys.Rev. C 27, 682 (1983)
[6] R.Diebold et al., Phys.Rev.Lett 35, 632 (1975)
[7] Y.Mardisi et al., Phys.Rev.Lett 45, 1529 (1980)
[8] P.Adlarson et al., Phys.Rev.Lett 112, 202301 (2014)
[9] R.L.Workmann, private communication

1 PNPI, 188350 Gatchina, Russia
2 IKP, FZ Jülich, 52425 Jülich, Germany
3 JINR, 141980 Dubna, Russia
4 HEPI TSU, 0186 Tbilisi, Georgia

* supported by COSY-FFE

Comparison of COSY-TOF and SATURNE-SPES4 Data for the Scattering Length Determination

Florian Hauenstein

The $\vec{p}p \to pK\Lambda$ reaction has been measured with the COSY-TOF detector at a beam momentum of 2.7 GeV/c. This data has been analyzed to extract the $p\Lambda$ scattering length from the $p\Lambda$ final state interaction by using the method from [1]. However, the obtained result for the spin averaged scattering length shown in [2], $a = (-1.233 \pm 0.014_{\text{stat.}} \pm 0.3_{\text{theo.}} \pm 0.12_{\text{syst.}})$ fm, deviates by more than 1σ away from the results obtained by the HIRES collaboration [3] in a inclusive measurement. They obtain a value of $a = -2.43^{+0.16}_{-0.17}$ fm exploiting the $p\Lambda$ invariant mass spectrum together with measurements of the Λp elastic cross section. Furthermore, their extraction approach was different since they used effective range approximation together with Jost function as described in [4]. Therefore, further studies have been carried out to understand if the difference comes from the measured data or the extraction methods.

Although the measurements of COSY-TOF and HIRES have been done at the same beam momentum, a direct comparison is not possible since HIRES measured the $pp \to KX$ reaction in the very limited kinematic region of Kaon laboratory angles around 0°. This is the region in the laboratory frame where the COSY-TOF detector has no acceptances though the detector has still full phase space acceptance.

To circumvent this problem data from a measurement of $pp \to KX$ at the SATURNE-SPES4 spectrometer can be applied [5]. This data set has a compatible phase space region with COSY-TOF. Furthermore, it has been fitted with both above mentioned methods in the references [1, 4]. The data SPES4 is measured at a beam momentum of 3.5 GeV/c which is 800 MeV/c higher than the COSY-TOF data at 2.7 GeV/c. In addition, the available Kaon angular range is between 8° and 12° in the lab frame. For the comparison the COSY-TOF data is restricted to the same range. Since the SPES4 result is given in units of $\mathrm{d}\sigma/(\mathrm{d}m_{p\Lambda}\mathrm{d}\Omega)$ on the y-axis it has to be scaled by $1/4\pi$ to the COSY-TOF data which has units of $\mathrm{d}\sigma/\mathrm{d}m_{p\Lambda}$.

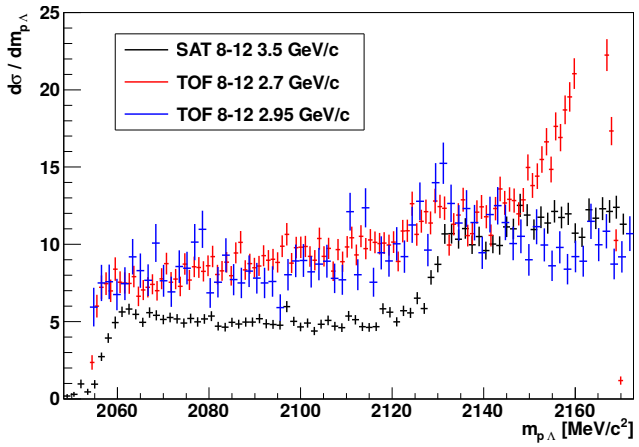

Fig. 1: $m_{p\Lambda}$ invariant mass spectrum obtained by COSY-TOF at 2.7 GeV/c (red) and 2.95 GeV/c (blue) limited to the Kaon angular range $[8°, 12°]$. In black the result from [5] is shown scaled by $1/4\pi$.

In Fig. 1 the comparison of the $m_{p\Lambda}$ invariant mass spectrum from the SPES4 measurement (black, scaled by $1/4\pi$) with the COSY-TOF data at 2.7 GeV/c (red) and 2.95 GeV/c (blue) is shown. No matching between the COSY-TOF and SPES4 data is seen above the $N\Sigma$ threshold at about 2130 MeV/c^2. For higher invariant mass values the data sets could not match since the opening of the $N\Sigma$ channel increases the cross section in the inclusive SPES4 measurement permanently.
Both COSY-TOF data sets matches very well below the $N\Sigma$ threshold. The deviation to the SPES4 measurement might stem from difference in the reaction mechanism at higher energies e.g. other contributions of intermediate N^* resonances. Furthermore, the SPES4 spectrum is systematically shifted by about 2 MeV/c^2 to higher invariant mass values which is already discussed in the fits of this data in the references [1, 4] where a shift of 1.7 MeV/c has been taken into account in their fits.
A clear conclusion can not be drawn by the direct comparison of the spectra and their final state interaction enhancement. Therefore, both COSY-TOF spectra as well as the SPES4 data will be fitted with the methods described in [1] and [4] to distinguish effects from the theoretical models and the measured data.

References:

[1] A. Gasparian, et al., How to extract the ΛN scattering length from production reactions, Phys. Rev. C**69**, 034006 (2004).
[2] F. Hauenstein, PhD Thesis, University Erlangen-Nuernberg, 2014.
[3] HIRES collaboration, A. Budzanowski, et al., High resolution study of the Λp final state interaction in the reaction $p + p \to K^+(\Lambda p)$, Phys. Lett. B**687**, 31-35 (2010).
[4] F. Hinterberger, A. Sibirtsev, Analysis of the Λp Final State Interaction in the Reaction $p + p \to K^+(\Lambda p)$, Eur. Phys. J. A**21**, 313 (2004).
[5] R. Siebert, et al., High-resolution study of hyperon-nucleon interactions by associated strangeness production in pp collisions, Nucl. Phys. A**567**, 819 (1994).
[6] A. Gasparian, et al., Extraction of scattering lengths from final-state interactions, Phys. Rev. C**72**, 034006 (2005).

Investigation of meson production in proton-deuteron fusion to ^{3}HeX with WASA-at-COSY*

N. Hüsken,† F. Bergmann,† K. Demmich,† A. Khoukaz,† D. Lappe,† K. Sitterberg,† J. von Wrangel,† and L. Wölfer†

The production cross section of the pd $\rightarrow$ ^{3}Heη reaction has been studied in great detail in the near threshold region [1, 2, 3, 4, 5], whereas at higher excess energies the amount of available data is limited [6, 7, 8, 9]. Moreover, while the data from ANKE and WASA/PROMICE expose a total cross section plateau away from threshold, recent results from the WASA-at-COSY experiment [10] suggest an unexpected narrow variation of the total cross section at $Q = 50\,\mathrm{MeV}$, as shown in Figure 1.

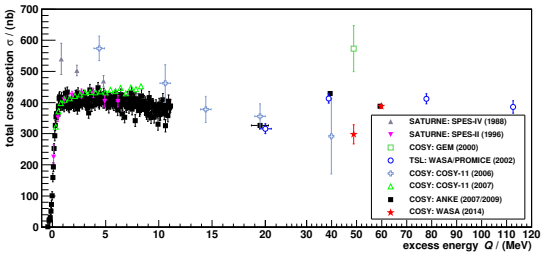

Figure 1: Total cross section data for the reaction pd $\rightarrow$ ^{3}Heη obtained by [1]-[10] as a function of the excess energy Q. Figure taken from [10].

As the WASA-at-COSY experiment is perfectly suited to study the energy dependence of both the total and differential cross sections of the pd $\rightarrow$ ^{3}Heη reaction, a beam time was realized in May 2014 in order to examine the excess energy region of interest. The COSY storage ring provided protons with 15 different beam momenta between $p_p = 1.60\,\mathrm{GeV/c}$ and $p_p = 1.74\,\mathrm{GeV/c}$, which results in a Q-value range from $Q \approx 13.6\,\mathrm{MeV}$ to $Q \approx 80.9\,\mathrm{MeV}$ with a stepsize of $\Delta Q \approx 4.8\,\mathrm{MeV}$.
Identification of the pd $\rightarrow$ ^{3}Heη reaction can be done by means of the missing mass technique. Extracting detailed angular distributions, see Fig.2, will ultimately lead to the precise determination of both total and differential cross sections for the whole energy range studied.

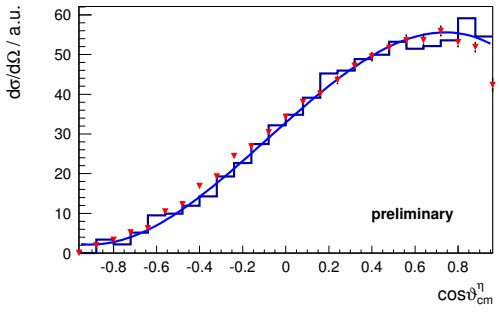

Figure 2: Preliminary pd $\rightarrow$ ^{3}Heη angular distribution for $Q \approx 61.7\,\mathrm{MeV}$ scaled to the data from [10] (shown in red), the blue line is a polynomial fit.

Alongside the investigation of η meson production, the production of pions can also be studied extensively, with the ongoing analysis work featuring studies on one-, two- and three-pion production. While the one-pion production is currently being investigated as a normalization reaction, the two-pion production is of special interest as the famous ABC effect [11] can be observed in this reaction. With this high statistics dataset, the energy dependence of the ABC enhancement can be examined in great detail in both the differential distributions, e.g. the invariant mass of both the $\pi^0\pi^0$-system and the Heπ^0-system (see Fig.3), as well as in the total cross section of the two-pion production.

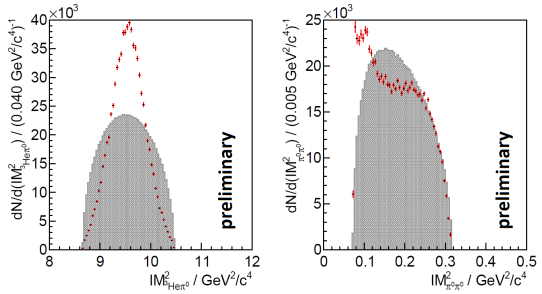

Figure 3: Preliminary invariant mass squared of the Heπ^0- (left) and $\pi^0\pi^0$-system (right) for $p_p = 1.60\,\mathrm{GeV/c}$. Red points correspond to data, the gray shaded histograms correspond to pure phase-space behaviour [12].

These studies will result in precise total and differential cross sections for multiple meson production reactions of the type pd $\rightarrow$ ^{3}HeX. This allows us to not only investigate possible cross section variations in η meson production or the influence of the recently discovered dibaryon $d^*(2380)$ (see [13]-[15]) on two-pion production, but also the one- and three-pion production in great detail, therefore contributing to the development of theoretical models of meson production in proton-deuteron fusion.

References

[1] T. Mersmann *et al.*, Phys. Rev. Lett. **98**, 242301 (2007).
[2] J. Smyrski *et al.*, Phys. Lett. B **649**, 258 (2007).
[3] J. Berger *et al.*, Phys. Rev. Lett. **61**, 919 (1988).
[4] B. Mayer *et al.*, Phys. Rev. C **53**, 2068 (1996).
[5] H.-H. Adam *et al.*, Phys. Rev. C **75**, 014004 (2007).
[6] T. Rausmann *et al.*, Phys. Rev. C **80**, 017001 (2009).
[7] R. Bilger *et al.*, Phys. Rev. C **65**, 044608 (2002).
[8] R. Bilger *et al.*, Phys. Rev. C **69**, 014003 (2004).
[9] M. Betigeri *et al.*, Phys. Lett. B **472**, 267 (2000).
[10] P. Adlarson *et al.*, Eur. Phys. J. A **50:**, 100(2014).
[11] A. Abashian *et al.*, Phys. Rev. Lett. **5:**, 258-260 (1960).
[12] L. Woelfer, BSc Thesis, Westfälische Wilhelms-Universität Münster (2015).
[13] M. Bashkanov *et al.*, Phys. Rev. Lett. **102**, 052301 (2009).
[14] P. Adlarson *et al.*, Phys. Rev. Lett. **106**, 242302 (2011).
[15] P. Adlarson *et al.*, Phys. Lett. B **721**, 229 (2013).

*Supported by COSY-FFE and the European Union Seventh Framework Programme (FP7/2007-2013) under grant agreement n 283286

†Institut für Kernphysik, Westfälische Wilhelms-Universität, 48149 Münster, Germany

Studies on C-violation at WASA-at-COSY: $\eta \to \pi^0 e^+ e^-$ *

K. Demmich†, F. Bergmann†, N. Hüsken†, A. Khoukaz†

Studies on the conservation and violation of symmetries, such as the C-parity, are a convenient way of testing the predictions of the standard model and may give access to particles beyond the standard model. One probe for testing the conservation of the C-parity are decays of the η meson. According to standard model calculations, the decay $\eta \to \pi^0 e^+ e^-$ via two virtual photons is highly suppressed – by approximately eight orders of magnitudes compared to the decay $\eta \to \pi^0 \gamma\gamma$ [1] – resulting in an expected relative branching ratio of $\approx 10^{-12}$. Therefore, the observation of the decay $\eta \to \pi^0 e^+ e^-$ with a significantly higher branching ratio would be a strong evidence for the existence of another decay mechanism. One candidate would be $\eta \to \pi^0 \gamma^* \to \pi^0 e^+ e^-$, which is C-violating and, thus, forbidden within the standard model. The current upper limit of the branching ratio is quoted as 4×10^{-5} [2].

The WASA-at-COSY facility is perfectly suited to perform studies on rare and forbidden meson decays. In the last years, several beam times dedicated for η decay studies were performed resulting in a huge data pool containing about 3×10^7 $pd \to {}^3He\eta$ and about 5×10^8 $pp \to pp\eta$ events.

In order to extract a new upper limit for the rare η decay, the data set taken 2010 in proton-proton-collisions has been preselected on the reaction $pp \to pp\eta$. The protons are selected as two charged forward tracks meeting several energy loss cuts. An additional condition on at least one pair of opposite charge ($\pi^\pm$ and $e^\pm$) and at least two photons (assuming $\pi^0 \to \gamma\gamma$) already produces a clear η signal in the missing mass spectrum of the protons, based on a data sample with $\approx 2 \times 10^8$ $pp\eta$ events (see black line in fig. 1).

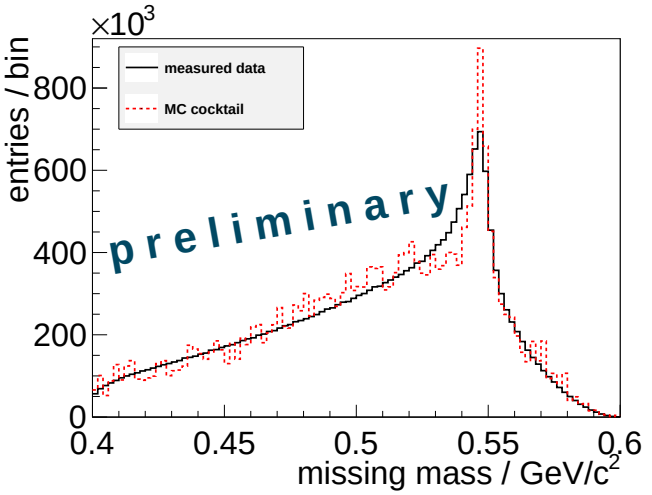

Figure 1: Fit of a Monte Carlo cocktail (red dashed line) to the measured missing mass spectrum (black solid line).

Electrons are distinguished from pions by a particle identification rejecting a large fraction of the dominant pion background. Further cuts are applied including the identification of photon pairs originating from π^0 decays, the suppression of conversion events and cuts on the invariant mass of all decay particles around the η mass.

Further optimizations of these cuts as well as an estimation of the expected background from other reactions will be based on Monte Carlo simulations. Since the decay of interest is a very rare decay only a very small amount of signal events is expected after applying all cuts. Therefore, a very deep understanding of the detector behaviour, an accurate calibration and appropiate adjustments of the Monte Carlo simulations are neccessary. In particular, the detector resolution has a high impact on the shaping of the spectra. Moreover, an additional kinematic fit relies on a careful estimation of the resolution of the measured variables. The red dashed line in fig. 1 shows a first test on fitting a measured missing mass spectrum with a Monte Carlo cocktail.

Fig. 2 shows the invariant mass spectrum of the lepton pairs after applying the mentioned cuts and a probability cut on a preliminary kinematic fit testing the hypothesis $\eta \to e^+ e^- \gamma\gamma$. A very good background suppression could already be achieved, especially at high invariant masses.

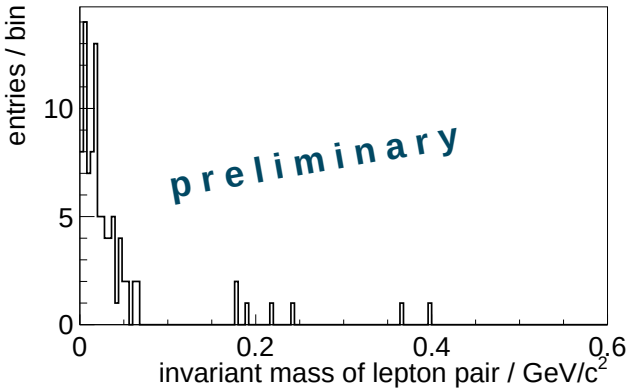

Figure 2: Invariant masses of the lepton pair after all cuts based on the same data sample as fig. 1.

Studies on the angular and energy dependencies of the detector resolution and according adjustments in simulations are essential for the following analysis steps including the optimisation of the cut boundaries and the error parameters for the kinematic fit.

The presented results already show a large step towards a new upper limit for the branching ratio of the decay $\eta \to \pi^0 e^+ e^-$ and reaction models beyond the standard model.

References

[1] J. Smith, Phys. Rev. **166**, 1629 (1968)
[2] M. R. Jane *at al.*, Phys. Lett. B **59**, 99 (1975)

*Supported by COSY-FFE
†Institut für Kernphysik, Westfälische Wilhelms-Universität, 48149 Münster, Germany

Charge symmetry breaking in the dd $\longrightarrow$ ^{4}Heπ^0 reaction with WASA-at-COSY

Maria Żurek

If isospin symmetry was conserved, protons and neutrons would be treated equally by all types of interactions. Since up and down quarks, which are the constituent quarks of the proton and the neutron, have different charges and masses, the isospin symmetry is not an exact one. It is broken both by electromagnetic and strong interactions [1, 2]. Probing elementary symmetry breaking tests our understanding of the theory of strong interactions — Quantum Chromodynamic (QCD). One of the most important static isospin symmetry breaking observable is the proton-neutron mass difference ΔM_{np}. It has electromagnetic origin ΔM_{np}^{em} and strong one ΔM_{np}^{strong} [1].

$$\Delta M_{np} = \Delta M_{np}^{em} + \Delta M_{np}^{strong}$$

Determination of ΔM_{np}^{strong} requires lattice calculations [3] or effective field theory methods. Our approach follows effective field theory, which for low energy QCD is Chiral Perturbation Theory. It links the static isospin symmetry observable ΔM_{np}^{strong} with the dynamic ones, like the πNN production vertex and the πN scattering length [2].

On the hadronic level, isospin breaking observables are dominated by the pion mass difference ($\Delta\pi$), which is an almost purely electromagnetic effect. This makes it difficult to get access to the term linked to the quark mass difference. However, for a special case of isospin symmetry breaking, namely charge symmetry breaking, the $\Delta\pi$ term does not contribute. Charge symmetry is a rotation of 180° angle in isospin space, which exchanges up and down quarks. In our analysis the charge symmetry breaking dd $\longrightarrow$ ^{4}Heπ^0 reaction is investigated to obtain the total cross-section and the angular distribution, especially the contribution of higher partial waves.

In first experiment performed with the WASA-at-COSY detector setup, the total cross section of the dd $\longrightarrow$ ^{4}Heπ^0 reaction at $Q = 60$ MeV has already been obtained [4]. However, for decisive results on higher partial waves, higher statistics and increased sensitivity are needed. Therefore, an 8 week long experimental run dedicated to the dd $\longrightarrow$ ^{4}Heπ^0 reaction at a beam momentum of $p_d = 1.2$ GeV/c was performed in spring 2014. The forward detector of WASA was modified by removing most of the layers of the plastic scintillator detectors. This allows the measurement of the time-of-flight (ToF) of the outgoing ^{4}He and, as a result, a better subtraction of the dd $\longrightarrow$ ^{3}Henπ^0 background.

Both central and forward parts of the WASA detector setup were calibrated. In the forward part, the calibration of time-of-flight (ToF) and energy losses (dE) in first two layers of plastic scintillators were performed. The ToF calibration corrections were studied carefully to obtain the best possible resolution. A run dependent correction was needed, to address a problem of a varying gain of the detector elements and an unstable electronics readout. Additionally, a rate dependent correction had to be applied.

For the full kinematic information of the outgoing particles in the forward detector — apart from the azimuthal and vertical angle from the tracking detector — the kinetic energy E_{kin} is needed. The reconstruction procedure is based on the dependence between E_{kin} and ToF or dE in the forward detector. It was determined as a function of the azimuthal angle and separately for ^{4}He and ^{3}He. An optimization of the method was performed. It included an accurate fit of the E_{kin}(ToF) and E_{kin}(dE) dependence. An azimuthal angle dependence of the ToF and dE resolution was also introduced.

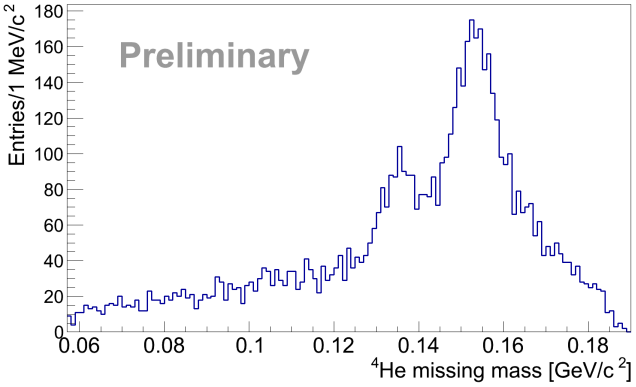

Fig. 1: Preliminary ^{4}He missing mass distribution.

As a next step, a kinematic fit was performed. Two hypothesis were tested — one for dd $\longrightarrow$ ^{3}Hen$\gamma\gamma$, one for dd $\longrightarrow$ ^{4}He$\gamma\gamma$. No constraint on an invariant mass of two gammas was put. A precise error parametrization as a function of the kinetic energy and the azimuthal angle for all outgoing particles was performed. A two dimensional cut on the cumulative probability distribution was applied to subtract the dd $\longrightarrow$ ^{3}Henπ^0 background. The obtained ^{4}He missing mass distribution is presented in Fig. 1. The peak centered of the π^0 mass originating from the dd $\longrightarrow$ ^{4}Heπ^0 reaction is located on the smooth background coming from the dd $\longrightarrow$ ^{4}He$\gamma\gamma$ reaction. The dd $\longrightarrow$ ^{3}Henπ^0 background peak is also visible. It is shifted in respect to the π^0 mass because of the ^{3}He-n binding energy. Roughly estimating, the number of the dd $\longrightarrow$ ^{4}Heπ^0 events is about 3 times bigger then in the previous measurement [4].

A luminosity calculation based on the dd $\longrightarrow$ ^{3}Henπ^0 reaction measurement and the missing mass spectra fitting with a template obtained from Monte Carlo simulations are under the investigation. In a next step, the energy loss information from the last plastic scintillator layer of the forward detector can be introduced to improve the ^{4}He -^{3}He separation. With a clean dd $\longrightarrow$ ^{4}Heπ^0 signal sample, the total and differential cross section will be extracted.

References:

[1] J. Gasser, H. Leutwyler, Phys. Rept. 87 (1982) 77.
[2] S. Weinberg, Trans. N.Y. Acad. Sci. 38 (1977) 185.
[3] Sz. Borsanyi, et al., Science 347 (2015), 1452.
[4] P. Adlarson, et al. (WASA-at-COSY Collaboration), Phys. Lett. B 739 (2014) 4449.

Experimental study of few nucleon interaction dynamics in the dp collisions

B. Kłos[1] and I. Ciepał[2]

An experiment to investigate the ^{1}H(*d,pp*)n breakup reaction using a deuteron beam of 340, 380 and 400 MeV and the WASA detector has been performed at the Cooler Synchrotron COSY-Jülich. The main goal was a detailed study of various aspects of few-nucleon dynamics like the three nucleon force (3NF), the long-range Coulomb interaction or relativistic effects in the medium energy region. The relativistic effects and their interplay with 3NF become more important with increasing available energy in the three nucleon system.

The analysis is continued with the aim to determine the differential cross sections for the deuteron breakup process in the *d*+*p* system at energies of 340, 380 and 400 MeV. The theoretical calculations using modern realistic nucleon-nucleon (NN) interactions, combined with a suitable model of 3N forces [1] and the calculations within the coupled-channel approach with the CD Bonn+Δ potential and with the Coulomb force included [2]. Moreover, the calculations including relativistic effects have been prepared for the ^{1}H(*d,pp*)n breakup reaction at the beam energy of 400 MeV [3], clearly demonstrating importance of relativity for description of breakup reaction at that energy.

Currently, the analysis is focused on obtaining normalized experimental results of the cross sections for different deuteron beam energies. We hit problems, specially prominent at 380 and 400 MeV. After selection of the proton-proton coincidences and having performed the energy calibration, the E_1 vs E_2 kinematical spectra of the two protons registered have revealed very strange structures. The events do not lie on the theoretical line of a three body kinematical curve, calculated for the central values of the experimental angular ranges (Fig. 1, left panel), what indicates incorrect energy reconstruction.

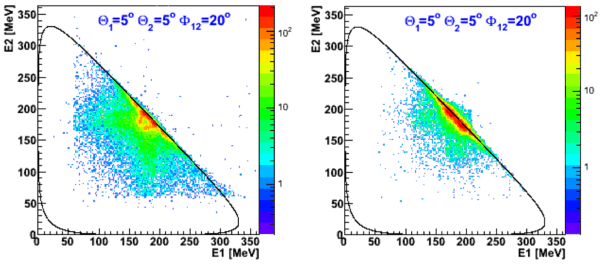

Fig. 1: The E_1 vs E_2 coincidence spectra of the two protons registered at specified kinematical configuration (measurement at 380 MeV beam energy). The solid line shows a three-body kinematical curve. Problems with reconstructed energies of protons (left panel), spectrum after correction of deposited energies (right panel).

We have these problems between of the second (FRH2) and third (FRH3) layers of Forward Range Hodoscope (FRH) there is 5.2 mm of plastic, Forward Range Interleaving Hodoscope (FRI) not included into track reconstruction. We found the angular-dependent functions which allow to reconstruct the energy deposited in FRH2+FRHI together, on the basis of energy deposited in FRH1. The improvement of kinematical spectra is clearly visible (Fig. 1, right panel).

An example of the non-normalized rates of events (obtained for the same configuration) as a function of the arc-length *S* measured along the kinematic curve, before and after correcting deposited energies, are presented in Fig. 2.

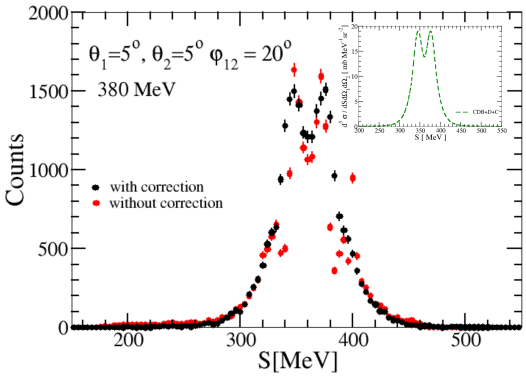

Fig. 2: An example of the preliminary non-normalized experimental breakup event rate obtained for chosen kinematical configurations as a function of the S value. The calculations within the coupled-channel approach with the CD Bonn+Δ potential with the Coulomb force included are shown in the insert figure.

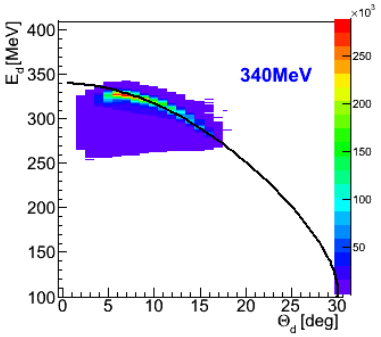

Fig. 3: Preliminary selection of deuterons registered in FD. Solid curve corresponds to kinematics for elastically scattered deuterons.

For the purpose of cross section, the luminosity should be determined on the basis of the number of the elastically-scattered deuterons at a given θ angle. After preliminary selection of deuterons registered in the Forward Detector and similar correction of reconstructed energy, as protons, the correct energy vs angle relation for elastically scattered deuterons was obtained Fig. 3.

We acknowledge support by the Polish National Science Center through grant No. 2012/05/E/ST2/02313 and by the FFE funds of the Forschunszentrum Jülich.

[1]University of Silesia, PL-40007 Katowice, Poland
[2]H. Niewodniczański Inst. of Nuclear Physics PAN, PL-31342 Kraków, Poland

References:

[1] W. Glöckle , H. Witała, D. Hbüer, H. Kamada, J. Golak, Phys. Rep. **274** (1996) 107.
[2] A. Deltuva et al., Phys. Rev. C **72** (2005) 054004.
[3] H. Witała, private communication.

Status of the search for η-mesic Helium in dd and pd reactions

M. Skurzok[a], W. Krzemien[b], P. Moskal[a], O. Rundel[a] and O. Khreptak[a]

In 2010 we performed the measurement dedicated to search for the ^{4}He-η bound states in deuteron-deuteron fusion reaction. In 2015 we have completed analysis of the 2010 data sample with 20 times larger statistics with respect to the 2008 data. The η-mesic nuclei were searched via studying of excitation function for the $dd \to {}^3\mathrm{He}p\pi^-$ [1] and $dd \to {}^3\mathrm{He}n\pi^0$ [1, 4] reactions in the vicinity of the ^{4}Heη threshold. During the experiment the beam momentum was changed slowly around the threshold for the $dd \to {}^4\mathrm{He}\eta$ reaction in each of acceleration cycle. The beam momentum range corresponded to the excess energy region $Q \in$(-70,30) MeV.
The obtained excitation functions determined for $dd \to {}^3\mathrm{He}p\pi^-$ and $dd \to {}^3\mathrm{He}n\pi^0$ processes, do not show any narrow structure which could be interpreted as a signature of the bound state with width less than 50 MeV. Therefore, the preliminary upper limit of the total cross section for the η-mesic ^{4}He formation and decay was estimated for bound state production and decay in $dd \to ({}^4\mathrm{He}\text{-}\eta)_{bound} \to {}^3\mathrm{He}N\pi$ processes. The obtained results are presented in Fig. 1.

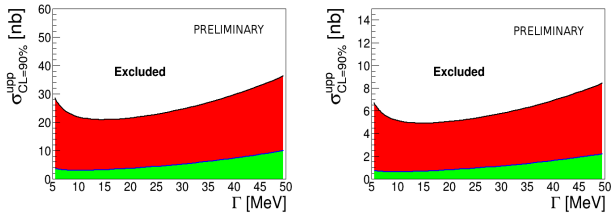

Fig. 1: Preliminary upper limit of the total cross-section for $dd \to ({}^4\mathrm{He}\text{-}\eta)_{bound} \to {}^3\mathrm{He}n\pi^0$ (left panel) and $dd \to ({}^4\mathrm{He}\text{-}\eta)_{bound} \to {}^3\mathrm{He}p\pi^-$ (right panel) reaction as a function of the width of the bound state. The binding energy was set to 30 MeV. The green areas denote the systematic uncertainties [4]. The figure is adapted from Ref. [1].

We achieved a sensitivity of the cross section of the order of few nb for the $dd \to ({}^4\mathrm{He}\text{-}\eta)_{bound} \to {}^3\mathrm{He}p\pi^-$ reaction that is about four times better result in comparison with those obtained from 2008 data [3]. Moreover, the obtained upper limit value does not exclude the cross section σ_{tot} =4.5 nb estimated in Ref. [5]. The excitation function for the $dd \to ({}^4\mathrm{He}\text{-}\eta)_{bound} \to {}^3\mathrm{He}n\pi^0$ reaction was investigated for the first time. The upper limit obtained in this case is by factor of five larger than predicted value therefore, one can conclude, that the measurement does not exclude the existence of bound state in this process either. The theoretical interpretation with respect to very wide $({}^4\mathrm{He}\text{-}\eta)_{bound}$ or ^{3}He-N^* bound system [6] is in progress.
In May 2014 the measurements for searching η-mesic ^{3}He were also performed [7] in processes corresponding to the three mechanisms: (i) absorption of the η meson by one of the nucleons, which subsequently decays into N^*-π pair e.g.: $pd \to ({}^3\mathrm{He}\text{-}\eta)_{bound} \to ppp\pi^-$, (ii) decay of the η -meson while it is still "orbiting" around a nucleus e.g.: $pd \to ({}^3\mathrm{He}\text{-}\eta)_{bound} \to {}^3\mathrm{He}6\gamma$ reactions and (iii) η meson absorption by few nucleons e.g.: $pd \to ({}^3\mathrm{He}\text{-}\eta)_{bound} \to ppn$. The statistics of the data obtained in this experiment is better that is was measured for the same conditions ever before.
Now obtaining luminosity value from $pd \to {}^3\mathrm{He}\eta$ reaction is in progress. The algorithm of ^{3}He kinetic energy reconstruction has been implemented and conditions for identifying the events corresponding to this reactions have been provided.

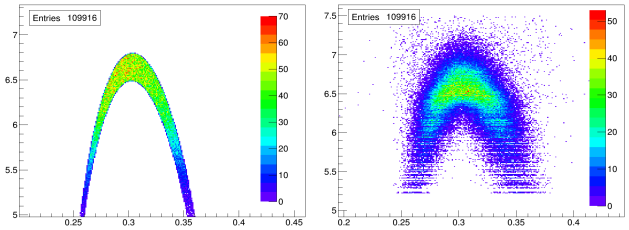

Fig. 2: Kinematic histograms obtained from Monte Carlo simulation for $pd \to {}^3\mathrm{He}\eta$. Horizontal axes: kinetic energy in GeV. Vertical axes: θ in degrees. Left plot: data obtain from vertices. Right plot: reconstruction of parameters from detector signals.

Even if the analysis does not show the existing of the bound state, the upper limit that would be set for the cross section for it's forming will be lower than one obtained in previous measurements for ^{4}He. At present the analysis of this data is going on.

We acknowledge support by the Foundation for Polish Science - MPD program, by the Polish National Science Center through grants No. 2011/01/B/ST2/00431, DEC-2013/11/N/ST2/04152 and by the FFE grants of the Forschungszentrum Jülich.

References:

[1] M. Skurzok, W. Krzemień, O. Rundel and P. Moskal, *Acta Phys. Polon.* **B47**, 1001 (2016).
[2] W. Krzemień, *PhD Thesis, Jagiellonian University, arXiv:nucl-ex/1202.5794* (2011).
[3] P. Adlarson *et al., Phys. Rev.* **C87**, 035204 (2013).
[4] M. Skurzok, *PhD Thesis, Jagiellonian University, arXiv:nucl-ex/1509.01385* (2015).
[5] S. Wycech, W. Krzemień, *Acta Phys. Polon.* **B45**, 745 (2014).
[6] N. G. Kelkar, D. Bedoya Fierro, P. Moskal, *arXiv:1512.01535* (2015).
[7] P. Moskal, W. Krzemień, M. Skurzok, COSY proposal No. 186.3 (2014).

[a] M. Smoluchowski Institute of Physics, Jagiellonian University, 30-059 Cracow, Poland

[b] National Centre for Nuclear Research, 05-400 Otwock-Świerk, Poland,

Determination of the analysing power for the $\vec{p}p \to ppp\eta$ reaction using WASA-at-COSY detector system

I. Ozerianska[a], P. Moskal[a], M. Zieliński[a] for the WASA-at-COSY collaboration

Production mechanism of the η meson and meson-nucleon final state interaction for the $\vec{p}p \to ppp\eta$ reaction can be studied via measurements of the analyzing power, $A_y(\theta)$. Up to now, experiments of the [1–4] investigation A_y have been performed with poor statistics and with large uncertainties. In November 2010 the high statistics sample of $\vec{p}p \to ppp\eta$ reaction has been collected using the azimuthally symmetric WASA-at-COSY detector [5]. Measurements were taken with two beam momentum 2026 MeV/c and 2188 MeV/c, which correspond to 15 MeV and 72 MeV excess energies.

Based on elastic scattering of protons the vertex position of the real experiment were measured with two independent methods [8]. The spin flipping technique of the beam has been used to control the effect caused by potential asymmetries in the detector. Monitoring of the beam polarization was based on the $\vec{p}p \to pp$ reaction. The result shown stable polarization during all experiment [10].

Determination of the analyzing power for the η meson were done separately for spin up and spin down mode. Additionally, analysing power were determined for two neutral reactions $\eta \to \gamma\gamma$ and $\eta \to 3\pi^0$.

After identification of η mesons the number of events corresponding to $\vec{p}p \to ppp\eta$ reaction, have been determined for each angular bin N(θ_η,φ_η) separately. Example of the missing mass distribution for chosen spin mode of the beam momentum 2188 MeV/c shown in the Fig. 1.

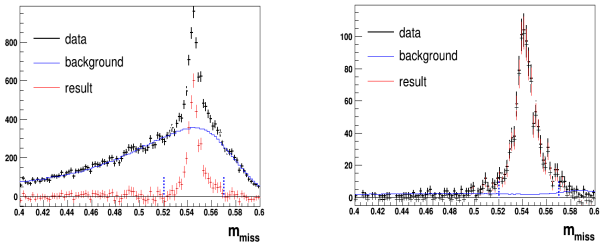

Fig. 1: Missing mass distribution for the chosen range $70° < \theta_\eta < 90°$, $-180° < \varphi_\eta < -170°$ and spin "up" mode. Left: $\eta \to \gamma\gamma$. Right: $\eta \to 3\pi^0 \to 6\gamma$. Beam momentum: $p_{beam} = 2188$ MeV/c. Black crosses denote experimental data. Continuous blue lines show the sum of the simulated background for the $\pi^0, 2\pi^0, 3\pi^0$ and $4\pi^0$ production. Red lines show the result of difference between the experimental data and simulated background. Dashed blue lines show the region of the extraction of the number of produced η meson.

Collected amount of the η events significantly improve the statistical uncertainty of our result of the analyzing power for the η meson compare to the previous COSY-11 experiments.

The result and the predicted theories do not overlap, which required new understanding of the η meson production Fig. 2.

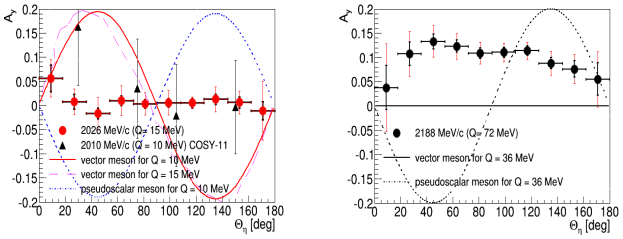

Fig. 2: Analyzing power of the η meson as a function of $cos\theta_\eta$. Comparison of the shape of the angular distribution with the theoretical predictions (see legend) for Q = 15 MeV (upper panel) and Q = 72 MeV (lower panel).The dashed-dotted line shows the prediction of the analyzing power as a function of the η emission angle in the cener-of-mass for vector meson dominance model [11]. The solid line describe vector meson model for [13] and the doted line describe the pseudoscalar model [12].

Fitting the result with the associated Legendre polynomial can give us an answer for the partial wave analysis. Assuming that p and d waves can occur for the η meson production, its analyzing power is given by:

$$A_y = \frac{\Im(A_{Ps}A^*_{Pp})sin\theta_\eta + \Im(A_{Ss}A^*_{Sd})3cos\theta_\eta \sin\theta_\eta}{\frac{d\sigma}{d\Omega}}, \tag{1}$$

where $\Im(A_{Ps}A^*_{Pp})$ is the imaginary part of the interference term between the Ps and Pp waves, and $\Im(A_{Ss}A^*_{Sd})$ is the interference term between the Ss and Sd waves [14]. Figure 3 shows result obtained in this experiment with the results of the fit with the formula

$$A_y \frac{d\sigma}{d\Omega} = C_1 \cdot sin\theta_\eta + C_2 \cdot cos\theta_\eta sin\theta_\eta \tag{2}$$

with C_1 and C_2 treated as free parameters of the fit. One can see in Fig. 3 that the associated Legendre polynomials of order $m = 1$ fully describe the existing data.

Thus analyzing power is zero for the beam momentum 2026 MeV/c, there is no interference between A_{Ss}, A_{Ps}, A_{Pp} and A_{Sd} amplitudes of the partial waves.

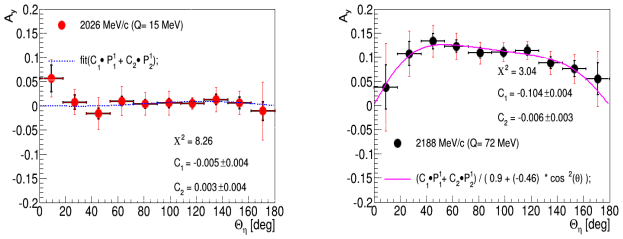

Fig. 3: Analyzing power of the η meson as a function of θ_η. The fit of A_y with the sum of the two associated Legendre polynomials P^1_1 and P^1_2 is shown for the Q = 15 MeV (left) and for Q = 72 MeV (right).

p_{beam}	$C_1^{final} \pm stat \pm syst$	$C_2^{final} \pm stat \pm syst$
2026 MeV/c	0.004 ± 0.003± 0.001	0.004± 0.003± 0.002
2188 MeV/c	-0.102± 0.003± 0.003	-0.003± 0.003± 0.003

Table 1: Coefficients C_1^{final} and C_2^{final} determined for the momenta 2026 MeV/c and 2188 MeV/c for the associated Legandre polynomial fit to analyzing power of the η meson.

For the higher beam momentum 2188 MeV/c, $C_2 = -0.006 \pm 0.003$, which means a very small or maybe still negligible contribution from $SsSd$ so we may claim that even at such a large excess energy Sd is very small or negligible. On the other hand, the contribution of C_1 is equal to -0.104 ± 0.004, so $PsPp$ is large which means that both of these partial waves contribute at Q = 72 MeV (see Fig. 3).

For the systematic studies of the constants C_1 and C_2 the analyzing power of the η meson as a function of the $\cos\theta_\eta$ angular distribution was used. The final results are shown in Tab. 1, where coefficients C_1^{final} and C_2^{final} is average from calculations based on the θ_η and $\cos\theta_\eta$ distributions.

We acknowledge support by the Polish National Science Center through grant No. 2011/03/B/ST2/01847, by the FFE grants of the Research Center Juelich, by the EU Integrated Infrastructure Initiative Hadron-Physics Project under contract number RII3-CT-2004-506078 and by the European Commission under the 7th Framework Programme through the Re- search Infrastructures action of the Capacities Programme, Call: FP7- INFRASTRUCTURES-2008-1, Grant Agreement N. 227431.

References:

[1] R. Czyżykiewicz et al., Phys. Rev. Lett. **98** (2007) 122003.
[2] F. Balestra et al. Phys. Rev. **C 69** (2004) 064003.
[3] P. Winter et al., Eur. Phys. J. **A 18** (2003) 355.
[4] P. Winter et al.,Phys. Lett.**B544** (2002) 251-258.
[5] P. Moskal, M. Hodana, J.Phys.Conf.Ser.295:012080, 2011.
[6] L. Demirors PhD Hamburg University (2005).
[7] M. Altmeier et al., Phys. Rev. Lett. **85** (2000).
[8] M.Hodana et al., Acta Phys.Polon.Supp. 6 (2013) 1041-1052.
[9] D. Prashun private communication (2013).
[10] I. Ozerianska et al., EPJ Web Conf. **81** (2014) 02013.
[11] K. Nakayama et al., Phys. Rev. **C68** (2003) 045201.
[12] K. Nakayama et al., Phys. Rev. **C65** (2002).
[13] G. Fäldt and C. Wilkin, Phys. Scripta **64** (2001) 427.
[14] Saha et al., Phys. Rev. Letter **59** (1983) 759. @articlesaha, author = "Saha et al.", YEAR = "1983", journal = "*Phys. Rev. Letter*", volume = "**51, 9**", pages = "759"

[a] M. Smoluchowski Institute of Physics, Jagiellonian University, 30-059 Cracow, Poland

Final State Interactions and the Box Anomaly in $\eta \to \pi^+\pi^-\gamma$

Daniel Lersch for the WASA-at-COSY collaboration

The decay $\eta \to \pi^+\pi^-\gamma$ allows to study the chiral anomalies of QCD [1, 2]. The decay amplitude is driven by the box anomaly in the chiral limit [1, 2, 3]. When going to physical masses, the triangle anomaly dominates the box anomaly because of final state interactions between the two pions. Thus, a correct description of this decay can only be achieved by including final state interactions [3, 4, 5, 6]. The experimental observables to test interaction models are the relative branching ratio: $\frac{\Gamma(\eta\to\pi^+\pi^-\gamma)}{\Gamma(\eta\to\pi^+\pi^-\pi^0)}$ and the photon energy E_γ distribution [7, 8, 9].

In order to measure both quantities in one experiment, the reaction $pp \to pp\eta[\eta \to \pi^+\pi^-\gamma]$ has been investigated. The data have been acquired during 2008, 2010 and 2012 using the WASA-at-COSY facility [10].

Competing processes to the η production are multi-pion production reactions such as $pp \to pp\pi^+\pi^-\pi^0$ and $pp \to pp\pi^+\pi^-$ which dominate the signal reaction $\eta \to \pi^+\pi^-\gamma$. In order to reduce these background contributions a kinematic fit as well as the rejection of low energetic satellite clusters in the calorimeter have been implemented in the recent analysis.

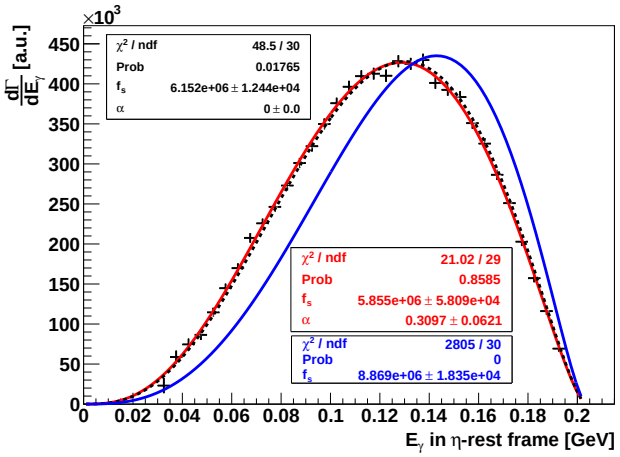

Fig. 1: Single photon energy distribution (black symbols) E_γ obtained from the analysis of the total $pp \to pp\eta$ 2010 data set.

Fig. 1 shows the single photon energy distribution (black symbols) of $\eta \to \pi^+\pi^-\gamma$ after the analysis steps discussed above. The blue curve corresponds to a photon energy distribution assuming no final state interaction bewteen the two pions. The red curve is related to a model independent approach using a single parameter α to describe the shape of the E_γ distribution and account for contributions from final state interactions. The description of the pion-pion interactions is done by using the pion vector form factor, which is independent of the underlying decay mechanism [6], modified by a factor $(1+\alpha s_{\pi\pi})$ [6] such that any decay specific interaction process is related to $\alpha \neq 0$. The dashed black curve in Fig. 1 represents a description of the final state interactions using the pion vector form factor only (e.g. $\alpha = 0$).

The final results for the decay observables of $\eta \to \pi^+\pi^-\gamma$ are given by:

$$\frac{\Gamma(\eta \to \pi^+\pi^-\gamma)}{\Gamma(\eta \to \pi^+\pi^-\pi^0)} = 0.189 \pm 0.001_{stat} \quad (1)$$

and:

$$\alpha = (0.310 \pm 0.062_{stat} \pm 0.02_{theor})\,\mathrm{GeV}^{-2} \quad (2)$$

Both results are in agreement with theoretical models including Vector Meson Dominance to describe the dipion final state interactions [3, 4]. Eq. 1 is also in agreement with the recent PDG value [11].

The investigation of systematic effects related to data analysis is ongoing such that systematic errors will be included in a next step.

References:

[1] J. Wess and B. Zumino. Consequences of anomalous ward identities. *Physics Letters*, **B37**, 95, 1971

[2] E. Witten. Global aspects of current algebra. *Nuclear Physics*, **B223**,422-432, 1983

[3] B. R. Holstein, Allowed Eta-Decay Modes and Chrial Symmetry, *Phys. Scripta*, **T99**, 55-67, 2002

[4] M. Benayoun et al. Anomalous η/η' Decays: The Triangle and Box Anomalies. *European Physics Journal*, **C31**, 525-547, 2003

[5] J. Bijnens et al. Three-Pseudoscalar Photon Interactions in Chiral Pertubation Theory. *Physics Letters*, **B37**, 488-494, 1990

[6] F. Stollenwerk et al. Model independent approach to $\eta \to \pi^+\pi^-\gamma$ and $\eta' \to \pi^+\pi^-\gamma$. *Physics Letters*, **B707**, 184-190, 2012

[7] The CLEO collaboration. Measurement of prominent η branching fractions. *Physics Review Letters*, 99(122001), 2007

[8] The KLOE collaboration. $\Gamma(\eta \to \pi^+\pi^-\gamma)/\Gamma(\eta \to \pi^+\pi^-\pi^0)$ with the KLOE detector. *Physics Letters*, **B718**, 910-914, 2013

[9] The WASA-at-COSY collaboration. Exclusive Measurement of the $\eta \to \pi^+\pi^-\gamma$ Deacy. *Physics Letters*, **B707**, 243-249, 2012

[10] H.-H Adam et al., Proposal for the wide angle shower apparatus WASA-at-COSY, (2004)

[11] K. A. Olive et al. (Particle Data Group). Review of Particle Physics. *Chinese Physics*, **C38**, 2014

Electromagnetic transition form fator of the η meson with WASA-at-COSY

Ankita Goswami

The aim of this work is to measure the electromagnetic transition form factor of the η meson. The study of the transition form factor of the η meson is possible through the $\eta \to \gamma\gamma^* \to \gamma e^+e^-$ Dalitz decay. Here, the transition form factor describes the structure of the meson. The momentum transfer is equal to the invariant mass of the e^+e^- pair. The corresponding decay rate of a point-like particle can be calculated within QED. However, the complex structure of the particle modifies the decay rate. The transition form factor is determined by comparing the experimental lepton-antilepton invariant mass distribution with QED:

$$\frac{d\Gamma}{dq^2} = [\frac{d\Gamma}{dq^2}]_{pointlike}[F(q^2)]^2 \qquad (1)$$

where function $\frac{d\Gamma}{dq^2}$ is the experimently measured transition probability,$[\frac{d\Gamma}{dq^2}]_{pointlike}$ is the theoretically calculated transition probability for a point like particle, $F(q^2)$ is the form factor of the Particle and q^2 is the squared four-momentum of e^+e^-.

Data collected in 2010 for proton-proton reaction at a beam energy of 1.4 GeV has been used in this study. A total of 5×10^8 η mesons have been produced. Particle identification in the forward and central part of the detector has been done in order to identify protons in the forward detector and $e^+e^-\gamma$ in the central detector. The missing mass of incoming and outgoing protons has been derived and ploted in Figure 1.

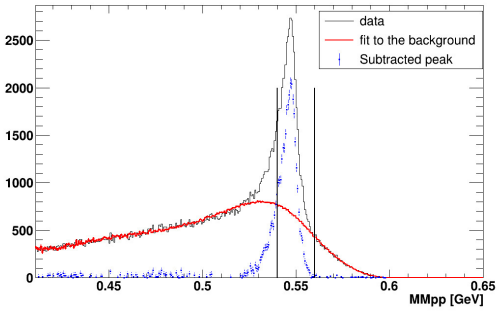

Fig. 1: Missing mass plot of two protons after all kinematic conditions used for obtaining the η signal.

To select good events a cut on total missing energy of ±0.2 GeV and total missing momentum of 0.2 GeV has been implemented . Also kinematic conditions have been implemented in order to reject the conversion and the splitoff background. Then, the background has been estimated by fitting a 4^{th} order polynomial multiplied with the phase space of multipion production pp$\to$pp$\pi^+\pi^-\pi^0$ outside the indicated region in Figure 1. The yield is derived from the subtracted peak. Finally approximately 2.9×10^4 η candidates have been reconstructed from the γe^+e^- channel after background subtraction.

Table 1: Background contribution from competing η decay channels:

Channel	Background contribution (%)
$\eta \to \gamma\gamma$	6.6
$\eta \to \gamma\pi^+\pi^-$	0.63
$\eta \to \pi^0\pi^+\pi^-$	1.2

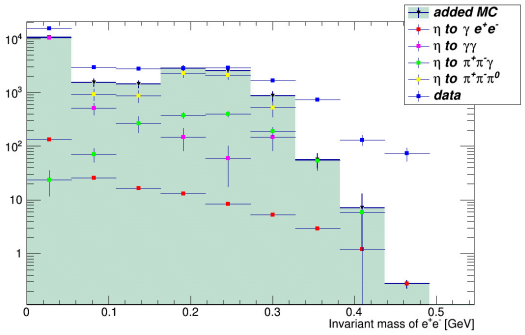

Fig. 2: Cocktail plot of invariant mass e^+e^-.

The major sources of the background for this reaction are $\eta \to \gamma\gamma$, $\eta \to \pi^0\pi^+\pi^-$ and $\eta \to \gamma\pi^+\pi^-$. The $\eta \to \gamma\pi^+\pi^-$ channel is similar to the signal channel therefore it satisfies the selection criteria as there are two oppositely charged tracks and one neutral track in the central detector. In $\eta \to \pi^0\pi^+\pi^-$ channel, π^0 decays into two photons and if one photon fails to register in the detector then this channel also satisfies the selection criteria. It is seen in the simulation studies that 8.4% background still would contribute from the competing decay channels inside the peak region as shown in the Table 1. The resultant invariant mass of the e^+e^- pairs without acceptance correction is shown in the Figure 2. A study of the relative branching ratio of the channel $\eta \to \gamma e^+e^-$ has been performed as a first check. The study has been done relative to $\eta \to \gamma\gamma$ channel which leads to a value of 0.164. We are trying to understood the phase space background. A cut based analysis approach has been used for this study. The phase space background needs to be understand in more details. The kinematic fit (a different approach for the analysis) would be implemented in order to supress the background and sytematic checks has to be done. Then the transition form factor of η meson would be determined.

Double Dilepton Decay of the η Meson with WASA-at-COSY

Susan Schadmand, *for the WASA-at-COSY Collaboration*

At COSY, the pp→ppη reaction at 1.4 GeV beam energy was employed to produce 10^9 η mesons. The data, taken with the WASA detector at COSY from 2008-2012, are being analyzed within the IKP analysis task force for light meson decays. The analysis tools include the WASA analysis software, based on CERN ROOT packages, and simulation software based on the event generator PLUTO and the tracking packages GEANT3 . The task force has developed a standard data analysis routine that is used as foundation for high-level analyses. Data files (in the form of ROOT trees) containing calibrated information about the reconstructed particles as well as a kinematic fit procedure are being prepared for ready-to-go physics analyses. A high-statistics data pool for Monte Carlo simulations, used for acceptance corrections and background studies, is being completed.

One of the physics goals of light meson decay studies is the determination of electromagnetic transition form factors via the momentum transfer to a virtual photon in the final state. The observable is the mass distribution of the emerging dilepton which displays a form factor dominated by intermediate vector meson production. The Dalitz decay η→γee is a candidate that reveals the meson-photon coupling and the structure of the meson itself, see contribution to this annual report by Ankita Goswami. The double dilepton decay, where both final state photons are virtual, has only been observed in the form of an upper limit for the branching ratio.

From the data set discussed above, a first look at the event candidates for η→eeee is performed, on part of the data. The analysis is based on restrictive selections cuts, not yet including kinematic fitting.

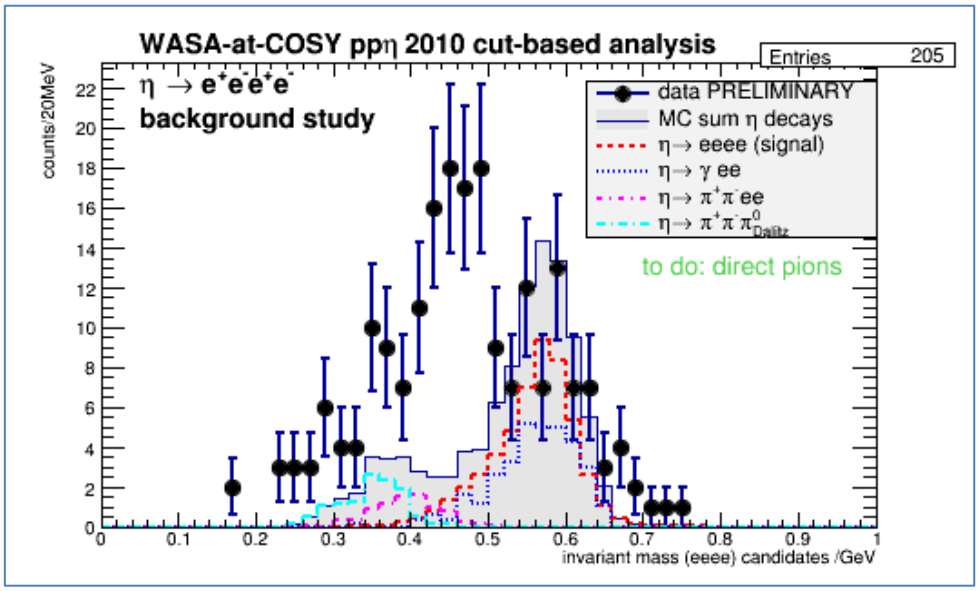

The figure shows the invariant mass of the dilepton pair candidates along with simulations of significantly contributing competing decays. A kinematic fit should provide better charged

pion suppression along with a handle on systematic effects. Note that neutral pions can contribute via their Dalitz decay into γee. Further detailed simulations are necessary, in particular on direct pion production, meaning pions not stemming from the decay of the η mesons. In the extraction of signal counts by background subtraction, systematic effects can be studied by implementing various models for the correlations between final state particles.

Double Dilepton Decay of the η Meson with WASA-at-COSY

Susan Schadmand, *for the WASA-at-COSY Collaboration*

At COSY, the pp→ppη reaction at 1.4 GeV beam energy was employed to produce 10^9 η mesons. The data, taken with the WASA detector at COSY from 2008-2012, are being analyzed within the IKP analysis task force for light meson decays. The analysis tools include the WASA analysis software, based on CERN ROOT packages, and simulation software based on the event generator PLUTO and the tracking packages GEANT3 . The task force has developed a standard data analysis routine that is used as foundation for high-level analyses. Data files (in the form of ROOT trees) containing calibrated information about the reconstructed particles as well as a kinematic fit procedure are being prepared for ready-to-go physics analyses. A high-statistics data pool for Monte Carlo simulations, used for acceptance corrections and background studies, is being completed.

One of the physics goals of light meson decay studies is the determination of electromagnetic transition form factors via the momentum transfer to a virtual photon in the final state. The observable is the mass distribution of the emerging dilepton which displays a form factor dominated by intermediate vector meson production. The Dalitz decay η→γee is a candidate that reveals the meson-photon coupling and the structure of the meson itself, see contribution to this annual report by Ankita Goswami. The double dilepton decay, where both final state photons are virtual, has recently been evaluated by the KLOE collaboration for the branching ratio.

From the data set discussed above, a first look at the event candidates for η→eeee is performed, on part of the data. The analysis is based on restrictive selections cuts, not yet including kinematic fitting.

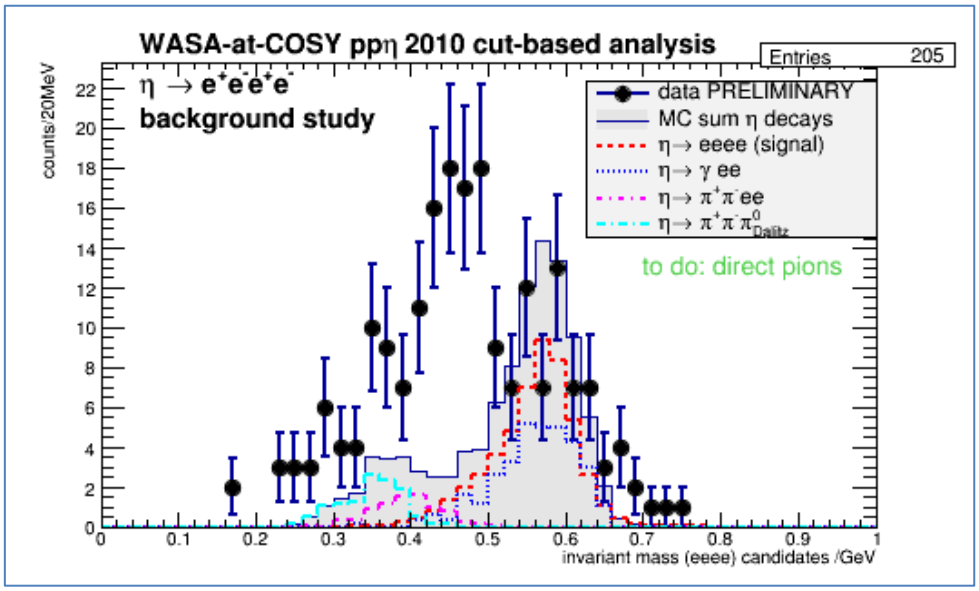

The figure shows the invariant mass of the dilepton pair candidates along with simulations of significantly contributing competing decays. A kinematic fit should provide better charged

pion suppression along with a handle on systematic effects. Note that neutral pions can contribute via their Dalitz decay into γee. Further detailed simulations are necessary, in particular on direct pion production, meaning pions not stemming from the decay of the η mesons. In the extraction of signal counts by background subtraction, systematic effects can be studied by implementing various models for the correlations between final state particles.

Radiative Decays of the η' Meson with CLAS

Susan Schadmand, *for the CLAS Collaboration*

With the IKP analysis task force, light meson decays are being investigated using data from γ+p experiments performed with the CLAS detector at Jefferson Lab.

The radiative decay $\eta^{(\prime)}\to\pi^+\pi^-\gamma$ is used to study the QCD box anomaly which is driving the decay in the chiral limit. At the physical masses, the triangle anomaly dominates the box anomaly due to final state interactions between the two pions. The experimental observable is the photon energy distribution or, equally, the pion pair mass distribution in the meson center-of-momentum. The case of the η meson has been studied with WASA-at-COSY, see contribution to this annual report by Daniel Lersch, and will be under study with CLAS data. The mass distribution shows the signs of the final state interaction between the charged pions which hints at the presence of an intermediate vector meson. The case of the η' meson provides more phase space in the final state and covers the full line shape of the vector meson. Previous measurements were not consistent on the possibly extractable contribution of the box anomaly. Using CLAS data, this decay is being investigated with two analyses, one at Old Dominion University using the g11 experiment, and one at IKP using the g12 experiment. The two experiments differ in the detector setup and other technical details. Both were identified as useful for the analysis of light meson decays.

The g12 experiment is specifically used for conversion decays. The lepton identification is achieved using Cherenkov detectors along with electromagnetic calorimetry, providing a suppression factor of 10^6 for charged pion pairs in favor of dileptons (e^+e^-).

Here, the interest is in the Dalitz decay of the η' meson and the possibility of determining the electromagnetic transition form factor via the momentum transfer to a virtual photon in the final state. The observable is the mass distribution of the emerging dilepton which displays a form factor dominated by intermediate vector meson production. The Dalitz decay $\eta^{(\prime)}\to\gamma ee$ is a candidate that reveals the meson-photon coupling and the structure of the meson itself, see contribution to this annual report by Ankita Goswami. Again, the η' decay provides more phase space in the final state than the η decay, both being dominated by an intermediate vector meson. Thus, it is important to study the dilepton mass distribution for the heavier meson case. The world data provides insufficient statistics for a detailed comparison to theoretical models.

A recent measurement of BESIII reports the branching ratio $\eta'\to\gamma ee$ / $\eta'\to\gamma\gamma$ to be $(2.13\pm0.09(\text{stat.})\pm0.07(\text{sys.}))\cdot10^{-2}$, derived from 864 events. Preliminarily, 89 events are extracted from the CLAS g12 experiment. The corresponding preliminary branching ratio $\eta'\to\gamma ee$ / $\eta'\to\gamma\gamma$ would be consistent with the BESIII measurement. However, the statistics of

either BESIII or CLAS are not sufficient to determine the transition form factor over the entire dilepton mass range.

With the newly built CLAS12 detector, electron/positron identification can be achieved with a pion rejection of 10^6-10^{11} while retaining an acceptance of ~ 1% - 0.1%. Using the GEant4 Monte-Carlo (GEMC) simulation suite for CLAS12, a simulation of an electron-induced experiment $e+p \rightarrow e' \gamma^* p \rightarrow p \eta' \rightarrow p \gamma ee$ was performed and is being analyzed in preparation of the first experiment of several planned proposals for meson decays with CLAS12.

Transition form factor of the ω meson with CLAS

Susan Schadmand, *for the CLAS Collaboration*

With the IKP analysis task force, light meson decays are being investigated using data from γ+p experiments performed with the CLAS detector at Jefferson Lab. The g12 experiment is specifically used for conversion decays. The lepton identification is achieved using Cherenkov detectors along with electromagnetic calorimetry, providing a suppression factor of 10^6 for charged pion pairs in favor of electron-positron pairs.

The transition form factor of the ωπ transition is investigated in the time-like region with the decay $\omega \rightarrow \pi^0 e^+e^-$. The form factor is extracted by dividing the dilepton mass distribution (the momentum transfer) by the QED prediction for simple conversion of the final state photon. The experimental results show a rise at the high-mass end that is inconsistent with measurements in the space-like region by SND and with recent theories going beyond standard vector meson dominance models.

The analysis strategy uses the excellent dilepton detection of the CLAS g12 experiment. The final state pion is left as a missing particle because neutral pions decay into two photons and the photon acceptance of this detector setup is limited. The data have been prepared including calibration and further corrections and a kinematic fitter serving several missing particle scenarios has been made available. The analysis procedure for the g12 experiment has recently been approved by the collaboration and is successfully used in several meson decays analyses.

The figure shows a first missing mass spectrum as derived from the incident kinematics and the detected outgoing proton, under the condition that a dilepton candidate is present and that the fitter scenario of a missing pion was more probable than 10%.

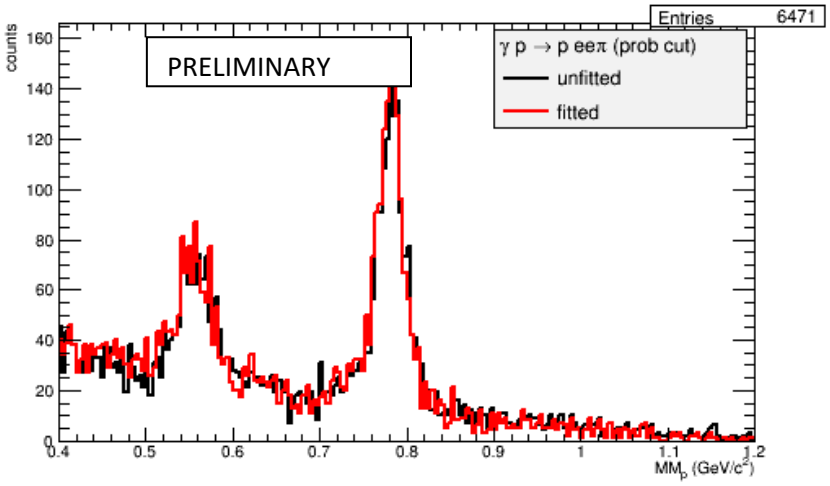

The expected peak at the ω meson mass (0.77 GeV) is prominent. Also, there is a remnant of η meson decays visible between 0.5 and 0.6 GeV. Note that the decay of η into a neutral pion and a (virtual) photon is a rare decay (C-forbidden). Thus, the contribution in the η mass region stems more likely from the decay $\eta \rightarrow \gamma ee$, due to overlap in mass and energy of the supposed missing particle. Similarly, the peak at the ω mass has peaking and non-peaking background contributions from multi-pion production, competing decays, and photon external conversion. The next steps are further analysis for background suppression as well as detailed simulations for background subtraction en route to determining the transition form factor.

Photoproduction of the π^0 meson up to 5.5 GeV with CLAS

Michael C. Kunkel

1 Intro

In hadron physics, photoproduction of single pion is essential to understand the photon-nucleon vertex. At low energies, the photon-nucleon coupling establishes excited nucleon resonances which has been at the forefront of physics "missing resonances" search. At high energies single pion photoproduction can be used to test predictions of Regge theory [1], the hand-bag model [2] and test the validity of the constituent counting rule (CCR) [3, 4].

2 Outlook

Exclusive neutral pion photoproduction ($\gamma p \to p\pi^0$) was measured in the CLAS detector at the Thomas Jefferson National Facility. The experiment employed a 1.1-5.5 GeV bremsstrahlung photon beam from 5.6 GeV electron beam created in the Continuous Electron Beam Accelerator Facility (CEBAF). The photon beam energy was impinged on a liquid hydrogen target. The neutral pions were detected via external conversion, $\pi^0 \to \gamma\gamma \to e^+e^-\gamma$, and subsequent Dalitz decay, $\pi^0 \to \gamma^*\gamma \to e^+e^-\gamma$. The focus of this research is to measured the differential cross-sections, $\frac{d\sigma}{dt}$ and $\frac{d\sigma}{d\cos\theta}$ and compare them to existing data, and also to compare to theoretical predictions were data does not exsist.

References:

[1] Mathieu, V. and others, Phys. Rev. D **92**, 074013 (2015) [arXiv:1505.02321 [hep-ph]].

[2] Huang, Han Wen and Kroll, Peter, Eur. Phys. J. C **17**, 423-435 (2000) [arXiv:hep-ph/0005318]

[3] Brodsky, Stanley J. and Farrar, Glennys R., Phys. Rev. Lett. **31**, 18 (1973)

[4] Lepage, G. Peter and Brodsky, Stanley J., Phys. Rev. D **22**, 9 (1980)

Measurement of the pp Elastic Scattering Differential Cross Section with the KOALA Recoil Detector at COSY

Qiang Hu[1,2], James Ritman[2] and Huagen Xu[2]

The KOALA experiment is being built to measure antiproton-proton elastic scattering differential cross section spectrum in a large range of squared 4-momentum transfer ($|t| \in [0.0008, 0.1]$ (GeV/c)^2) at H-ESR. It will determine the elastic differential parameters σ_T, ρ and b,which are an essential input to enable the $\overline{\mathrm{P}}$ANDA luminosity determination to obtain the desired absolute precision of 3%. The complete KOALA experimental setup will be composed of one forward arm and two recoil arms. One recoil arm consists of two silicon detectors and two germanium detectors, which covers a polar angle range from 71° to 91.5°. In the first stage, one recoil arm has been constructed and commissioned at COSY by measuring the proton-proton elastic scattering. The layout of the KOALA recoil detector in the commissioning experiment is shown in Fig. 1, the beam direction is from left to right.

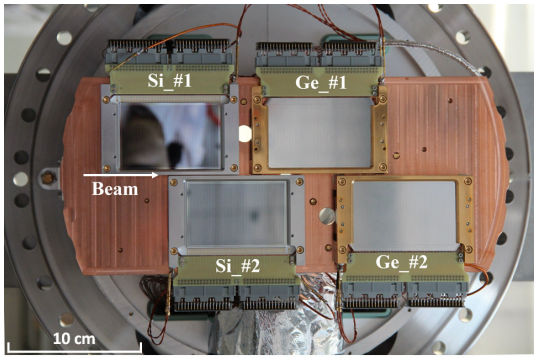

Fig. 1: Photo graph of the KOALA recoil detector for pp elastic scattering experiments at COSY.

Data of proton-proton elastic scattering has been taken at several beam momenta. After energy calibration and clustering, the typical energy spectra at different recoil angles (P_{beam} = 3.2 GeV/c) are shown in Fig. 2. As one can see that with increasing recoil angle, the recoil peak moves away from the background. However, the signal is difficult to separate from the background when the recoil protons' energy is below 600 keV. It is difficult to parameterize the distribution of the background in this region. Therefore, we summed the pure background spectra ($\theta \geq 90°$), scaling and subtracting it from the energy spectrum to determine the signal distribution. An example of background subtraction at recoil angle $\alpha = 1.60°$ with this method is shown in Fig. 3.

After background subtraction, the centroid energy of the recoil peak as well as the elastic scattering yield were obtained. Based on the centroid energy and the yield, the distribution of differential rate dN/dt as a function of $|t|$ ($|t| = 2m_pT_p$) has been reconstructed and efficiency corrected. It is shown in Fig. 4. To determine the elastic scattering differential parameters, one typical method is to analysis the characteristic shape of the $|t|$-spectrum

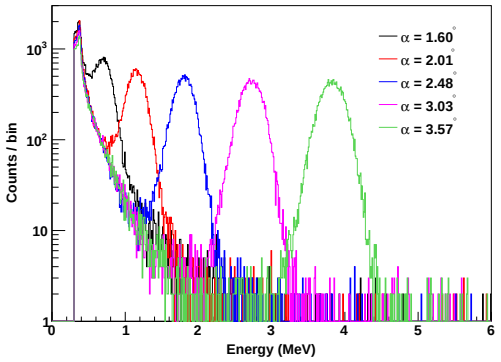

Fig. 2: Energy spectra at different recoil angles (P_{beam} = 3.2 GeV/c).

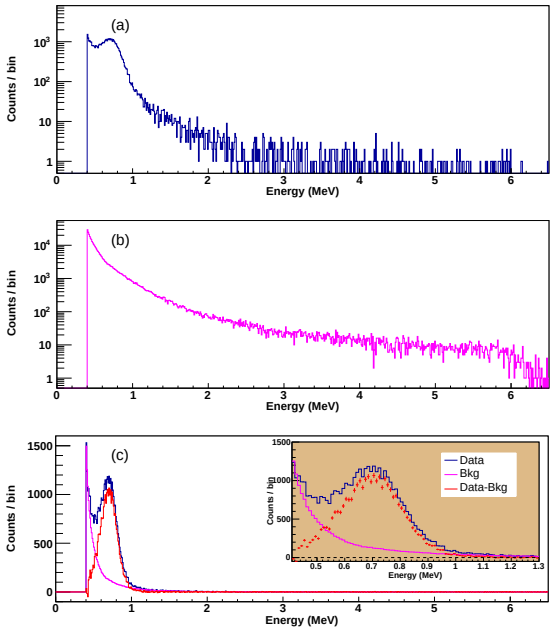

Fig. 3: Demonstration of the background subtraction method. (a) Single energy spectrum at α =1.6°. (b) Summed background spectrum. (c) Background subtraction for recoil angle at α =1.6°.

with the parameterized expressions 1-4[1] and 5.

$$\frac{d\sigma}{dt} = \frac{\pi}{k^2}\left|f_c^{i\delta} + f_n\right|^2 = \frac{d\sigma_c}{dt} - \frac{d\sigma_{int}}{dt} + \frac{d\sigma_n}{dt}, \quad (1)$$

$$\frac{d\sigma_c}{dt} = \frac{4\pi\alpha^2 G^4(t)(\hbar c)^2}{\beta^2 t^2}, \quad (2)$$

$$\frac{d\sigma_{int}}{dt} = \frac{\alpha\sigma_{tot}G^2(t)}{\beta|t|}e^{-\frac{1}{2}b|t|}(\rho\cos\delta + \sin\delta), \quad (3)$$

$$\frac{d\sigma_n}{dt} = \frac{\sigma_{tot}^2(1+\rho^2)e^{-b|t|}}{16\pi(\hbar c)^2}, \quad (4)$$

where $\frac{d\sigma_c}{dt}$ is the Coulomb term, $\frac{d\sigma_{int}}{dt}$ is the nuclear-Coulomb interference term and $\frac{d\sigma_n}{dt}$ is the nuclear term.

α is the fine-structure constant ($\alpha \simeq 1/137$), $G(t)$ is the proton form factor and δ is phase factor.

$$\frac{dN}{dt} = L \cdot \frac{d\sigma}{dt}. \quad (5)$$

where L is the integrated luminosity (or normalization coefficient) to be determined.

Fitting the $|t|$-spectrum with the parameterized formula, the elastic scattering differential parameters and normalization coefficient L have been extracted as shown in Fig. 4. The relative differential cross sections were obtained after normalization. Fig. 5 (a) and (b) illustrate the distribution of relative differential cross section at different beam momenta. As seen in Fig. 5 (a), with increasing beam momentum the differential cross section becomes smaller. In the strong interaction region ($|t| \geq 0.02$ (GeV/c)^2), the differential cross section distribution at P_{beam}=2.5, 2.8 and 3.2 GeV/c are parallel each other and they have a similar behavior as the existing data at 3.0 GeV/c. Furthermore, the measured differential cross sections in this work have smaller uncertainty than the data at 3.0 GeV/c.

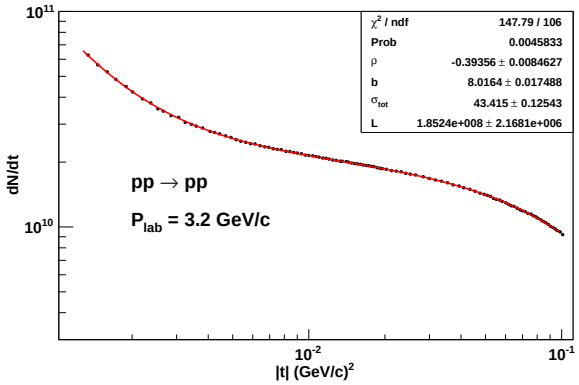

Fig. 4: $|t|$ distribution at $P_{beam} = 3.2$ GeV/c.

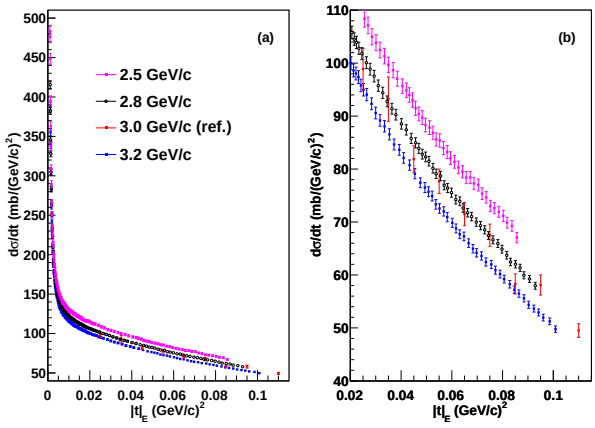

Fig. 5: Differential cross sections of four beam momenta. (a) Complete differential cross section in the measured range. (b) A range of the differential cross section, the data points at 3.0 GeV/c are taken from the reference [2].

In conclusion, the proton-proton elastic scattering at P_{beam} =2.5, 2.8 and 3.2 GeV/c have been measured with the KOALA recoil detector at COSY, the differential parameters as well as the relative differential cross sections were obtained. Our results are in good agreement with the existing data and have higher precision.

[1]Key Laboratory of High Precision Nuclear Spectroscopy and Center for Nuclear Matter Science, Institute of Modern Physics, Chinese Academy of Sciences, Lanzhou 730000, China
[2]Forschungszentrum Juelich, 52425 Juelich, Germany

[1] M. M. Block *High-energy $p\bar{p}$ and pp forward elastic scattering and total cross sections.* Rev. Mod. Phys, 1985, 57(2):563.
[2] I. Ambats, D. S. Ayres and R. Diebold et al., *Systematic study of $\pi^{\pm}p$, $K^{\pm}p$, pp, and $\bar{p}p$ forward elastic scattering from 3 to 6 GeV/c.* Phys. Rev. D, 1974, 9 (5): 1179.

Study of Excited Ξ Baryons in p̄p-Collisions with the P̄ANDA Detector

Jennifer Pütz

Introduction

Understanding the excitation pattern of baryons is indispensable for a deep insight into the mechanism of non-perturbative QCD. Up to now only the nucleon excitation spectrum has been subject to systematic experimental studies while very little is known on excited states of double or triple strange baryons. The P̄ANDA detector is well-suited for a comprehensive baryon spectroscopy program in the multi-strange baryon and meson sector. A large fraction of the p̄p-cross section is associated to final states with a baryon-antibaryon pair together with additional mesons, giving access to excited states in the baryon and antibaryon sector.

Event generation

For the study of excited Ξ^- baryons 1.5 million signal events for the reaction $\bar{p}p \to \Xi(1820)^- \bar{\Xi}^+$; $\Xi(1820)^- \to \Lambda\, K^-$; $\bar{\Xi}^+ \to \bar{\Lambda}\, \pi^+$; $\Lambda \to p\, \pi^-$ were generated with the event generator EvtGen at $p_{\bar{p}} = 4.6\,\mathrm{GeV/c}$. Another 1.5 million events were generated with the same beam momentum for the charge conjugate channel $\bar{p}p \to \bar{\Xi}(1820)^+ \Xi^-$. If not otherwise specified, the charge conjugate process is implicitly included in the following. The simulation was done by using the PandaRoot framework at trunk revision 28555. The $\Xi(1820)^-$ resonance was defined in the file evt.pdl, listing the properties of particles used in EvtGen. The properties of the $\Xi(1820)^-$ resonance are taken from [1].
The production cross section is expected to be of the same order ($\sim \mu$b) as for the ground state Ξ^- production in $\bar{p}p \to \Xi^- \bar{\Xi}^+$ [2].

Vertex fitter extension

For the reconstruction of non-final state particles it is necessary to fit the tracks of all daughter particles to a common vertex point. This is done with the PandaRoot kinematic vertex fitter PndKinVtxFitter. Up to now this vertex fitter has not been able to perform a vertex fit on particles with one or more neutral daughters. An extension for neutral daughter particles was developed to apply the vertex fitter to the reaction chain mentioned above.
The performance of the extension was tested with the so-called "poormantrack" algorithm [3]. This algorithm creates simple particle tracks independent from any detector information. To test for example the vertex fitter for a candidate with a neutral and a charged daughter particle, a Λ hyperon and a π^- meson were generated with the same vertex point. Then a kinematic vertex fit was performed. To show the performance of the vertex fitter for this case, the momentum pull distribution for the x coordinate obtained from the vertex fit is shown in figure 1.
The momentum pull distribution should have a Gaussian shape with mean value zero and a width of one. Performing a Gaussian fit gives the mean value $\mu = -0.0053 \pm 0.0071$ and the width $\sigma = 0.994 \pm 0.005$. These values are in good agreement with the expectation of 0 and 1, respectively.
The same test was also done for two neutral daughter particles.

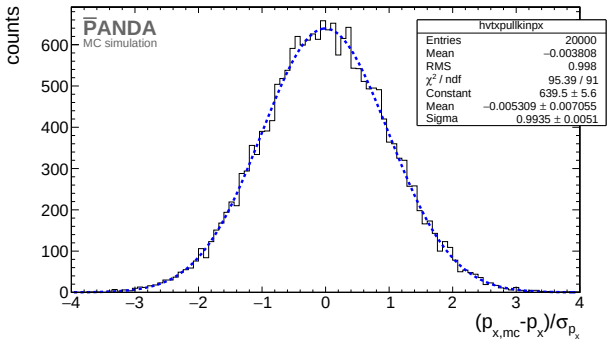

Fig. 1: Momentum pull distribution (black histogram) in the x coordinate for the vertex fit performed on the combination of Λ and π^-. The blue dashed line shows the fitted Gaussian distribution.

Reconstruction

To reconstruct all particles involved in the reaction one starts with the final state particles and proceeds backwards through the reaction chain. The selected final state particles are proton, anti-protons, π^-, π^+ and K^- mesons. Due to the use of an ideal track reconstruction, only particles with at least 3 hits in any inner tracking detector of P̄ANDA are selected. The particle identification is also ideal.
The reconstruction efficiency for the final state particles is shown in table 1.

Table 1: Reconstruction efficiency ε for final state particles for $\bar{p}p \to \Xi(1820)^- \bar{\Xi}^+$ (left) and $\bar{p}p \to \bar{\Xi}(1820)^+ \Xi^-$ (right).The statistical error on the reconstruction efficiency is $\sigma_\varepsilon = 0.1\,\%$ for all particles .

final state	ε/%
π^-	83.5
π^+ ($\bar{\Xi}^+$)	80.9
π^+ ($\bar{\Lambda}$)	83.1
K^-	78.6
p	84.4
$\bar{p}$	78.3

final state	ε/%
π^+	83.0
π^- (Ξ^-)	80.4
π^- (Λ)	82.7
K^+	83.3
p	80.7
$\bar{p}$	80.9

For the reconstruction of a Λ hyperon a proton and a π^- meson are combined and for the reconstruction of $\bar{\Lambda}$ hyperons a $\bar{p}$ and a π^+ is combined. After combining the daughter particles a mass cut is performed on the Λ candidate. Only those candidates are chosen which have a mass within the mass window $0.3\,\mathrm{GeV/c^2}$ symmetric to the nominal Λ mass. Then a vertex fit is performed on the selected candidate. As the next step a mass constraint fit is performed on the fitted candidate using the kinematic fitter PndKinFitter. Only those candidates which have a probability of more than 1% in both fits are selected. If more than one candidate is found, the candidate with the smallest χ^2 is chosen.
In case of a correct selection of π^+ as daughter particle of $\bar{\Lambda}$, only one π^+ meson is left as daughter of the $\bar{\Xi}^+$ baryon. The reconstruction scheme of the $\bar{\Xi}^+$ is similar to the reconstruction of Λ and $\bar{\Lambda}$. After combining the $\bar{\Lambda}$ hyperon and the

π^+ meson a mass cut within a window of $0.3\,\mathrm{GeV/c^2}$ symmetric to the nominal $\bar{\Xi}^+$ mass is performed. A vertex fit is performed on the selected candidate. After the vertex fit a mass constraint fit is performed on the fitted candidate. The candidate which has a probability of more than 1% in both fits and the smallest χ^2 value is selected. The same is done for the Ξ^- in the charge conjugate channel.
For the reconstruction of $\Xi(1820)^-$ baryons a Λ hyperon and a K^- meson are combined. A mass cut within a window with width $0.3\,\mathrm{GeV/c^2}$ symmetric to the nominal $\Xi(1820)^-$ mass is performed after the combination of the daughter particles. On the selected candidate a vertex fit is performed and only the candidate with a probability of more than 1% and the smallest χ^2 value is selected. The reconstruction of $\bar{\Xi}(1820)^+$ is done by combining a $\bar{\Lambda}$ hyperon and a K^+ meson from the charge conjugate channel and using the same cuts.
The vertex resolution for $\Xi(1820)^-$ and $\bar{\Xi}(1820)^+$ is shown in table 2.

Table 2: Vertex resolution for $\Xi(1820)^-$ and $\bar{\Xi}(1820)^+$

Position	$\bar{p}p \to \Xi(1820)^- \bar{\Xi}^+$	$\bar{p}p \to \bar{\Xi}(1820)^+ \Xi^-$
$x/\,\mathrm{cm}$	0.028	0.028
$y/\,\mathrm{cm}$	0.028	0.028
$z/\,\mathrm{cm}$	0.1	0.1

The mass distribution of $\Xi(1820)^-$ after all cuts is shown in figure 2.
The reconstructed mass of the $\Xi(1820)^-$ resonance obtained from a Gaussian fit is about $1.823\,\mathrm{GeV/c^2}$. The width of the distribution is $\sigma = (14.24 \pm 0.05)\,\mathrm{MeV/c^2}$.

To reconstruct the full reaction chain, $\Xi(1820)^-$ and $\bar{\Xi}^+$ are combined. This is also done for $\bar{\Xi}(1820)^+$ and Ξ^- in the charge conjugate channel. The resulting four-momentum vector of both daughter particles are fitted to the initial four-momentum vector $(p_x, p_y, p_z, E) = (0, 0, 4.6, 5.63)\,\mathrm{GeV}$ of the $\bar{p}p$ entrance channel. After the four-momentum fit only those candidates are selected which have a probability of more than 1%. Table 3 shows the reconstruction efficiency of the intermediate state particles.
The different reconstruction efficiencies of Λ and $\bar{\Lambda}$ are caused by the different position of their decay vertices. Λ

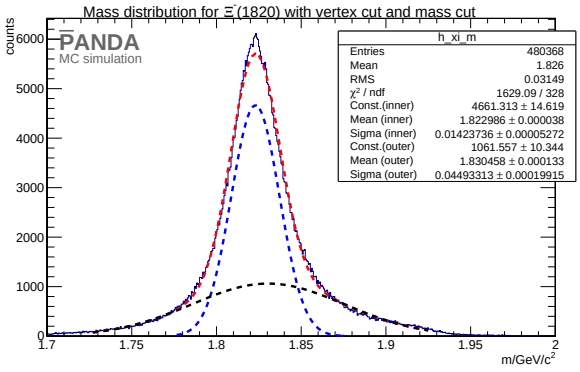

Fig. 2: Mass distribution of $\Xi(1820)^-$ (blue histogram). The double Gaussian Fit is shown as red dashed line, the inner Gaussian fit as blue dashed line and the outer Gaussian fit as black dashed line.

Table 3: Reconstruction efficiency ε for intermediate state particles for $\bar{p}p \to \Xi(1820)^- \bar{\Xi}^+$ (left) and $\bar{p}p \to \bar{\Xi}(1820)^+ \Xi^-$ (right) including the branching ratios $\mathrm{BR}(\Lambda \to p\,\pi^-) = 63.9\,\%$, $\mathrm{BR}(\Xi^- \to \Lambda\,\pi^-) = 99.9\,\%$ and $\mathrm{BR}(\Xi(1820)^- \to \Lambda\,K^-) = 100\,\%$ (assumed).

particle	$\varepsilon/\%$
Λ	40.5
$\bar{\Lambda}$	33.4
$\bar{\Xi}^+$	18.4
$\Xi(1820)^-$	32.0
$\Xi(1820)^- \bar{\Xi}^+$	4.7

particle	$\varepsilon/\%$
Λ	32.8
$\bar{\Lambda}$	40.8
Ξ^-	18.6
$\bar{\Xi}(1820)^+$	33.2
$\bar{\Xi}(1820)^+ \Xi^-$	4.9

is emitted by the $\Xi(1820)^-$ resonance which decays at the primary interaction point while the decay length of $\bar{\Xi}^+$ is $c\tau = 4.91\,\mathrm{cm}$. The decay length of Λ and $\bar{\Lambda}$ is $c\tau = 7.98\,\mathrm{cm}$ so that the final state particles of $\bar{\Lambda}$ are produced more downstream than the final state particles coming from Λ. The final state particles of $\bar{\Lambda}$ are produced close to the edge of the Micro Vertex Detector (MVD) which has a high spatial resolution. The reconstruction efficiency for these particles is reduced. An extension of the MVD with two more discs, the so-called "Lambda Discs", might improve the reconstruction efficiency for Λ and $\bar{\Lambda}$.

Summary and Outlook

The complete reaction chain can be reconstructed with an efficiency of about 5% each for $\bar{p}p \to \Xi(1820)^- \bar{\Xi}^+$ and its charge conjugate channel.
Each final state particle has a reconstruction efficiency of nearly 80%. The reconstruction of Λ and $\bar{\Lambda}$ shows a difference in the efficiencies. This is caused by the different mother particles of the Λ and $\bar{\Lambda}$. The reconstruction efficiency for Λ and $\bar{\Lambda}$ might be improved by using the so so-called "Lambda Discs". However, this requires further studies which will be a part of the future analysis.
The reconstructed mass for $\Xi(1820)^-$ and $\bar{\Xi}(1820)^+$ is in good agreement with the literature value [1].
As a next step background simulation will be done and a partial wave analysis of $\Lambda\,K^-\,\bar{\Xi}^+$ final state and its charge conjugate final state will be explored.

References:

[1] K. A. Olive *et al.* [Particle Data Group Collaboration], Chin. Phys. C **38**, 090001 (2014). doi:10.1088/1674-1137/38/9/090001
[2] W. Erni, I. Keshelashvili, *et al.*, "Physics performance report for PANDA: Strong interaction studies with antiprotons.", arXiv preprint arXiv:0903.3905 (2009)
[3] R. Kliemt, private communication, 2015

Simulated Measurement of the Ds Semileptonic Decay Form Factor with the $\overline{\text{P}}$ANDA Detector

Lu Cao

The semileptonic D_s decays are governed by both weak and strong interactions. The strong interaction dynamics can be described by a form factor $f_+(q^2)$, where q^2 is the invariant mass of the lepton-neutrino system $M^2_{e^+\nu_e}$. Theoretical calculations of the form factor offer increasing precision [1]. Therefore, the experimental validation of the results becomes important. The $\bar{p}p$ interaction has been simulated to evaluate the performance of the $\overline{\text{P}}$ANDA detector to measure the semileptonic decay form factor of $D_s^+ \to e^+\nu_e\eta$. The precision on measuring $f_+(q^2)$ has been studied event-wise. Several developments has been made comparing with the work presented in the annual report of last year: the improvements of software tools e.g. GenFit2 and Monte Carlo (MC) Truth Matching, as well as improvements in the event reconstruction strategy. In addition, the beam momentum dependence of the reconstruction efficiency has been studied for three different $\bar{p}$ momenta above the production threshold, 7.3 GeV/c, 7.685 GeV/c and 8 GeV/c.

Decay chain One million events of the following decay channels are simulated: $\bar{p}p \to D_s^+ D_s^-$; $D_s^+ \to e^+\nu_e\eta$; $\eta \to \pi^+\pi^-\pi^0$; $\pi^0 \to \gamma\gamma$ with two tagging modes for the D_s^-, i.e. $D_s^- \to K^+K^-\pi^-$ and $D_s^- \to \pi^+\pi^-\pi^-$. This simulation is done by using the GEANT4 transport code for the particle tracking through the complete $\overline{\text{P}}$ANDA detector. All the related decay models have been studied in [2].

Neutral particle reconstruction There are two issues on the neutral particle reconstruction. The first is to find the photon candidates among the whole clusters detected by the Electromagnetic Calorimeter (EMC). The algorithm for correlating neutral clusters has been separated from the charged particle correlation, in order to validate the distance parameter of reasonable correlation for the neutral particle directly. The parameter is defined as the squared distance between a cluster and its nearest point of track extrapolation. A efficiency study has been carried out with a particle gun of π^+. In this case, the total number of the EMC clusters N_{all} and the number of the generated charged particles N_{char} are known. Then, the number of reconstructed γ candidates should approximately match the gap between the former two values, i.e. $N_{all} - N_{char}$. It is indicated that an acceptable range of the neutral correlation parameter is from 50 cm^2 to 400 cm^2, when the charged correlation parameter is 2500 cm^2.

The second issue is the pre-selection on photon energy. Low energy photons can be caused by bump split-off and secondary interaction, and leads to a high multiplicity of photon candidates appearing as a combinatoric background in reconstructing π^0 meson. In the decay chain mentioned above, for selecting a reasonable energy threshold and cross checking the neutral correlation parameter, a significancy (sig = # MC truth matched candidates /$\sqrt{\#\text{ all candidates}}$) of the reconstructed π^0 and η has been studied with different energy thresholds for photons with the correlation parameter of 100 cm^2 and 400 cm^2 respectively. This study indicates the best significance can be achieved when the neutral correlation parameter is 100 cm^2 and the energy threshold is 40 MeV.

Reconstruction strategy and event selection To reconstruct the tagged D_s^-, the vertex fitting and mass constraint fitting are performed on the combination of its decay products, where the cut applied on the χ^2 probability is $prob > 0.01$. After mass constraint fitting, only the D_s^- owning the smallest χ^2 is selected as the "best" candidate to ensure the correct multiplicity in the final step of calculating $M^2_{e^+\nu_e}$. Photons above a energy threshold $E_\gamma^{thres} = 40$ MeV are combined to reconstruct π^0. The mass constraint fitting has been performed on the two-photon system and a cut on the χ^2 probability of $prob > 0.01$ is applied. The π^+ and π^- tracks allow the reconstruction of the decay vertex of $\eta \to \pi^+\pi^-\pi^0$. The e^+ is combined in addition to the $\pi^+\pi^-$ pair for determining the decay vertex of the η. Since the decay length of η is very short, it is safe to assume the three charged particles are produced at the same point. This method can imrpove the η vertex resolution by nearly 50% compared to that obtained from $(\pi^+\pi^-)$. The reconstructed η candidates are selected with a χ^2 probability cut on the mass constraint fit of the three-pion system, and the "best" candidate of η is selected, in which the daughters $\pi^+\pi^-$ are used to select the "best" e^+ in the vertex fitted candidates $(\pi^+\pi^-e^+)$. After reconstructing the intermediate particles D_s^- and η, the kinematics of the undetected neutrino can be calculated based on a four-momentum condition as

$$M^2_{\nu_e} = \left(E_{\bar{p}p} - E_{D_s^-} - E_\eta - E_{e^+}\right)^2 - \left|\mathbf{p}_{\bar{p}p} - \mathbf{p}_{D_s^-} - \mathbf{p}_\eta - \mathbf{p}_{e^+}\right|^2, \tag{1}$$

where $E_{\bar{p}p}(\mathbf{p}_{\bar{p}p})$ is the energy (three-momentum) of the initial anti-proton beam and proton target system. A ν_e mass window of $|M^2_{\nu_e}| \leq 0.1$ GeV$^2/c^4$ is applied to select ν_e candidates. The selected ν_e and corresponding e^+ are used to calculate $M^2_{e^+\nu_e}$. Fig. 1 shows the reconstructed $M^2_{e^+\nu_e}$ with a comparison of event-wise MC truth matched data. It is shown that the reconstructed result is consistent with the MC data in the large momentum transfer region $M^2_{e^+\nu_e} > 0.2$ GeV$^2/c^4$. In addition, a bremsstrahlung correction for the e^+ has been tried with a tool developed by $\overline{\text{P}}$ANDA Orsay group for the $\bar{p}p \to e^+e^-$ decay. Unfortunately, the tool did not improve the result of $M^2_{e^+\nu_e}$. It might be due to the complexity of the decay chain. The algorithm of associating the bremsstrahlung photon developed for the $\bar{p}p \to e^+e^-$ is incapable for a much more complicated case, where totally six charged candidates and two neutrals are produced.

Efficiency and resolution With the present software, the decay chain has been reconstructed with two tagging modes. Three different beam momenta have been simulated. It it found the reconstruction efficiencies at 7.3 GeV/c and 7.685 GeV/c are very close, and the highest one is at 8 GeV/c. Table 1 summarizes the preliminary results on reconstruction efficiency and resolutions at a beam momentum of 8 GeV/c. The efficiency of reconstructed $e^+\nu_e$ is 0.6% for the tagging mode A $D_s^- \to K^+K^-\pi^-$ and 0.9% for the mode B $D_s^- \to \pi^+\pi^-\pi^-$. The theoretical calculations bring a wide range of estimates on the cross section of charm production in proton-antiproton interaction [3, 4]. Assuming the cross section on

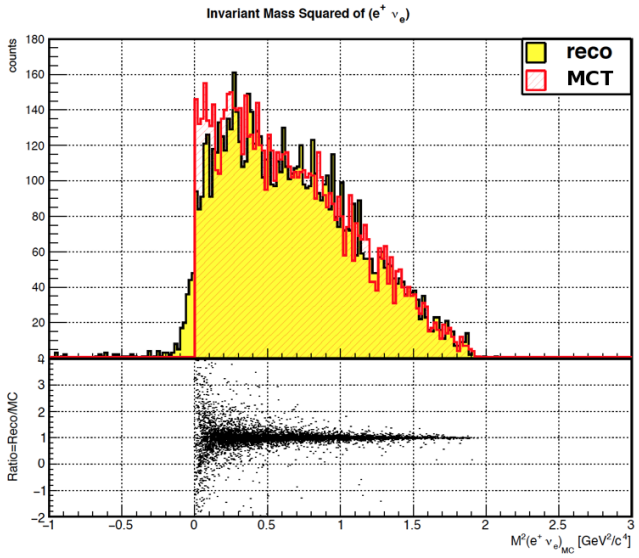

Fig. 1: Invariant mass squared of lepton-neutrino system with tagging mode $D_s^- \to K^+K^-\pi^-$. In the upper frame, the yellow field is the reconstructed result, and the red shadowed area is the result obtained by the MC truth matched particles involved in Eq. 1. Black dots in the lower frame show the ratio between "reco" and "MCT".

Table 1: Resolutions of reconstructed D_s^- and η candidates with tagging mode A: $D_s^- \to K^+K^-\pi^-$ and B: $D_s^- \to \pi^+\pi^-\pi^-$. Only the reconstruction results of neutral particles for mode A are listed since they are same in both modes.

	rec. eff.	σ_{mass}	σ_{vtx} [μm]			σ_{mom} [%]	
	[%]	[MeV/c^2]	x	y	z	p_t	p_z
D_s^-	15.1	13.1	62	61	130	2.2	0.7
π^0	-	4.8				1.9	1.8
η	16.4	5.6	100	97	187	1.6	1.3
D_s^-	23.4	17.2	51	49	89	2.2	0.7

the production of a D_s pair is 20 *nb* with a beam momentum of 8.0 GeV/c [4], it is estimated that the reconstruction rate to be approximately 60 events per month for a luminosity of 2×10^{32} cm^{-2}s^{-1}.

Summary For reconstructing the neutral particles in the decay chain, the photon EMC correlation parameters and energy pre-selections have been tuned for adapting to the physics situation of the decay chain. The kinematics of the neutrino have been reconstructed with two tagging modes of the D_s^-. Comparing with the previous results, the resolution have been improved due to improvements of reconstruction strategy and software tools, in particular the η vertex resolution has been improved from 193 μm to 100 μm on the X direction for instance.

The event-wise precision of q^2 is consistent with the MC data in the large momentum transfer region $M^2_{e^+\nu_e} > 0.2$ GeV$^2/c^4$. The count rate of useful events is estimated to be about 60 events per month for measuring the form factor. The beam momentum of 8 GeV/c is found to produce the best reconstruction efficiency. The next steps will include a modification of the present software to improve the neutral particle reconstruction efficiency and an investigation of the background channels.

References:

[1] K. Azizi *et al.*, J. Phys. G **38**(9), 095001 (2011); N. Offen *et al.*, Phys. Rev. D **88**(3), 034023 (2013), I. Kanamori, arXiv:1302.6087 [hep-lat].

[2] L. Cao and J. Ritman, J. Phys.: Conf. Ser. **503**(1) 12024 (2014).

[3] A. T. Goritschnig *et al.*, J. Phys.: Conf. Ser. **503**(1) 012012 (2014); A. Khodjamirian *et al.*, Eur. Phys. J. A **48**(3), 31 (2012).

[4] J. Haidenbauer and G. Krein, Phys. Rev. D **89**(11), 114003 (2014).

Search for the ΔΔ Component in the Deuteron in $\bar{p}d$ Collisions with $\overline{\text{P}}$ANDA

Albrecht Gillitzer

The deuteron is the lightest nuclear bound system. With its particularly small binding energy of 2.2 MeV it is an extended system, whose constituents spend a considerable part of the time outside of the characteristic range of the binding force between them. On the other hand, it is well known from large momentum transfer reactions on the deuteron, e.g. elastic electron scattering, that its wave function also has a hard component. It has therefore been speculated that also non-nucleonic components such as a compact six-quark configuration could be present. As a sub-component the six constituent quarks could also arrange in a ΔΔ configuration that could be visible in large momentum transfer reactions.

Proposed experiment for $\overline{\text{P}}$ANDA: The only experimental upper limit on the strength of the ΔΔ content in the deuteron we are aware of, has been set by the study of neutrino induced reactions [1] to be 0.2% for a $\Delta^{++}\Delta^{-}$ component. More recently, high-energy photo-induced deuteron break-up into two Δ isobars was discussed [2, 3] related to possible experimental studies at JLab. Complementary studies also delivering a clear ΔΔ signature are possible by using high-energy annihilation reactions of antiprotons on a deuteron target. With the momentum range of the $\bar{p}$ beam at the HESR up to 15 GeV/c and its large acceptance for both low-energy and high-energy particles, $\overline{\text{P}}$ANDA is the ideal tool for this study. Specifically, we propose to use the reaction $\bar{p}d \to (p\pi^+)(\pi^-\pi^-)$ that would be sensitive to a $\Delta^{++}\Delta^{-}$ configuration and deliver a characteristic signature for it (see Fig. 1). The final $p3\pi$ state would consist of a $\pi^-\pi^-$ pair resulting from $\bar{p}\Delta^-$ "annihilation" with large longitudinal momentum approximately given by the incident antiproton projectile, and of a slow $p\pi^+$ pair with invariant mass given by the Δ^{++} spectator. In order to obtain a large longitudinal momentum gap between the $p\pi^+$ pair and the $\pi^-\pi^-$ pair, the $\bar{p}$ beam momentum should be ~ 8 GeV/c or higher. In addition to final states with a $\pi^-\pi^-$ pair also those with additional annihilation pions such as $\pi^-\pi^-\pi^0$ and $\pi^-\pi^-\pi^+\pi^-$ can be considered, however for the time being feasibility studies focus on the subprocess $\bar{p}\Delta^- \to \pi^-\pi^-$.

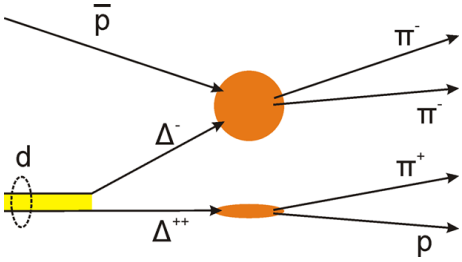

Fig. 1: Reaction proposed for $\overline{\text{P}}$ANDA to study the ΔΔ content in the deuteron.

Ingredients for Monte-Carlo Simulation: Since for the simulation of the $\overline{\text{P}}$ANDA detector response the PandaRoot software package is being used, it is convenient to implement the Monte-Carlo generation of the signal events in the existing event generator EvtGen [4] which is commonly used to generate signal events in $\bar{p}p$ collisions at $\overline{\text{P}}$ANDA. As a first step, the deuteron is assumed to consist of an *on-shell* spectator Δ^{++} and an *off-shell* Δ^- struck by the incident antiproton, that is EvtGen starts from a $\bar{p}d$ system decaying into an *on-shell* Δ^{++} and a $\bar{p}\Delta^-$ system, using the decay model `EvtDeuteronDeltaDelta` developed for this purpose. As ingredients, this decay model uses the internal Δ momentum distribution in the deuteron and the $\sqrt{s}$ dependence of the sub-process $\bar{p}\Delta^- \to \pi^-\pi^-$. The t dependence of this subprocess is taken into account in the next step. The Δ momentum distribution is assumed to be isotropic and its radial part $\mathrm{d}P(p_\Delta)/\mathrm{d}p_\Delta$ parametrized as a scaled Hulthén distribution close to results obtained in a theoretical study [5], as shown in Fig. 2. It peaks at ~ 0.6 GeV/c, roughly a factor 10 higher than the standard nucleon momentum distribution. The momentum vector selected randomly according to this distribution together with the Δ mass according to its spectral distribution define the Δ^{++} 4-momentum vector in the laboratory frame which is identical to the deuteron rest frame. The 4-momentum vector of the $\bar{p}\Delta^-$ system is thus fully determined as well.

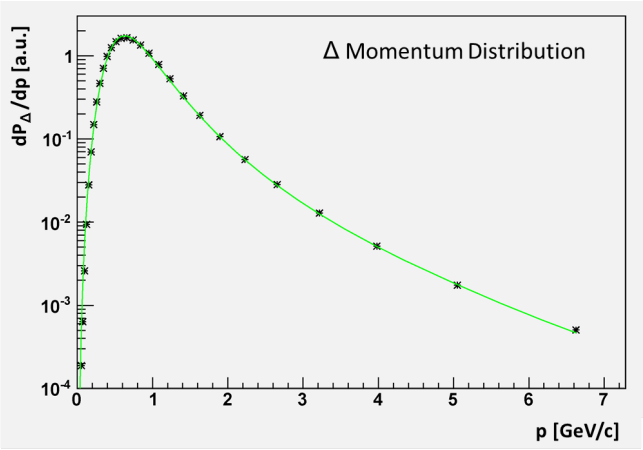

Fig. 2: Parametrized Δ momentum distribution as implemented. The marked positions correspond to values calculated in Ref. [5].

The spectator Δ^{++} is assumed to decay isotropically in its rest frame to a $p\pi^+$ pair. Both the $\sqrt{s}$ dependence and the t dependence of the sub-process $\bar{p}\Delta^- \to \pi^-\pi^-$ are unknown. In order to implement these dependencies in a reasonable way, they are adapted to Fermilab E760 data on $\bar{p}p \to \pi^0\pi^0$ in the $\sqrt{s}$ range between ~ 2.9 GeV and ~ 3.7 GeV [6], which is the most directly related experimental information. The data set consists of differential cross sections $\mathrm{d}\sigma/\mathrm{d}(\cos\theta_{\mathrm{cm}})$ within a $\cos\theta_{\mathrm{cm}}$ range from zero up to a maximum value between 0.5 and 0.6 for 22 values of $\sqrt{s}$. A forward-backward symmetric two-parameter distribution $\mathrm{d}\sigma/\mathrm{d}z = A\left(e^{\beta z} + e^{-\beta z}\right)$ was adapted to the measured angular distributions, with $z = \cos\theta_{\mathrm{cm}}$, A a normalization factor, and $\beta = 2p_1p_3 \cdot \alpha$ where p_1, p_3 are the center-of-mass momenta in the initial and the final state, and

$$\ln\left(\alpha \cdot \mathrm{GeV}^2\right) = 0.7353\, s/\mathrm{GeV}^2 - 6.276\sqrt{s}/\mathrm{GeV} + 12.88.$$

Based on both shape and absolute value of the measured differential cross sections, for the total cross section the $\sqrt{s}$ dependence $\sigma(\bar{p}\Delta^- \to \pi^-\pi^-) \propto s^{-5.7}$ was used for $\sqrt{s} \geq 2M_p$. Due to the $\sqrt{s}$ dependent shape of the angular distribution, the found dependence is less steep than $\frac{d\sigma}{d\cos\theta_{cm}}(\cos\theta_{cm} = 0) \propto s^{-7.2}$ observed by E760. In the far off-shell region the cross section was set to zero for $\sqrt{s} < M_p$, while it was assumed to be constant for $M_p \leq \sqrt{s} < 2M_p$. To avoid discontinuities, the transition between the different regions was smoothened. The $\sqrt{s}$ dependence is taken into account in the decay model `EvtDeuteronDeltaDelta` by accepting or rejecting the selected Δ^{++} 4-momentum according to the cross section calculated in this way for the corresponding mass of the $\bar{p}\Delta^-$ system. The decay $\bar{p}\Delta^- \to \pi^-\pi^-$ with its t dependence is modelled in the decay model `EvtPbarDelta2PiPi`, where θ_{cm} is evaluated relative to the $\bar{p}$ momentum direction in the $\bar{p}\Delta^-$ rest frame. In this frame the π^- emission is strongly forward-backward peaked.

Resulting $p\pi^+\pi^-\pi^-$ final state: Using an antiproton beam momentum of 8.0 GeV/c, 10^5 signal events were created for the signal channel as described above. The final state of $p\pi^+\pi^-\pi^-$ can also be populated in background reactions, with the quasifree sub-process $\bar{p}n \to \pi^+\pi^-\pi^-$ together with a spectator proton, being expected to be the dominant contribution. This process has been modelled both by using the event generator EvtGen with the corresponding decay model `EvtDeuteronSpectator` and by using the event generator FTF based on the FRITIOF quark-gluon string model, with results consistent to each other. With the latter generator $2.5 \cdot 10^5$ events were produced.

The distributions of kinematic variables in signal and background samples exhibit very distinct features. In the signal event sample, the mass distribution of the $p\pi^+$ pair reflects the spectral function of the free Δ isobar. Its longitudinal momentum in the laboratory frame is shifted towards negative (backward) values and peaks at ~ -0.4 GeV/c. This shift is due to the $\sqrt{s}$ dependence of the sub-process $\bar{p}\Delta^- \to \pi^-\pi^-$ which enhances low invariant $\bar{p}\Delta^-$ masses and thus Δ^- with positive (forward) longitudinal momenta. The $\pi^-\pi^-$ system has a mass distribution ranging from ~ 1 GeV to ~ 2.5 GeV and peaks at ~ 1.5 GeV. Its longitudinal momentum peaks at ~ 8.4 GeV/c, as required by the constraint given by the initial beam momentum of 8.0 GeV/c. Thus for the signal events, the distribution of $p_z(\pi^-\pi^-) - p_z(p\pi^+)$ is narrow and peaks close to 9 GeV/c. In contrast, the background events have a wide $p_z(\pi^-\pi^-) - p_z(p\pi^+)$ distribution increasing almost linearly from ~ -8 GeV/c to $\sim +8$ GeV/c. On the other hand, for the three-pion system mass and momentum distributions in the signal sample are wide, whereas in the background sample they are narrow as expected from an antiproton with given beam momentumn hitting a slow almost on-shell neutron. A complete suppression of background in the correlation of only two kinematic variables is not possible, however a particularly good separation has been found by comparing the distributions of the $\bar{p}\pi^-\pi^-$ squared missing mass (which is equivalent to the squared off-shell Δ^- mass in case of the signal) versus the $p\pi^+$ invariant mass for signal and background, as shown in Fig. 3. By using appropriate cuts on the kinematic variables, zero events survive out of 250000 background events, while the number of signal events is reduced only by a factor 0.976. This corresponds to a lower bound for the detection limit of the $\Delta^{++}\Delta^-$ component in the deuteron given by $f_{\Delta^{++}\Delta^-} \cdot \frac{\sigma_{\bar{p}\Delta^- \to \pi^-\pi^-}}{\sigma_{\bar{p}n \to \pi^+\pi^-\pi^-}} \simeq 0.4 \cdot 10^{-5}$, with $f_{\Delta^{++}\Delta^-}$ being the $\Delta^{++}\Delta^-$ content.

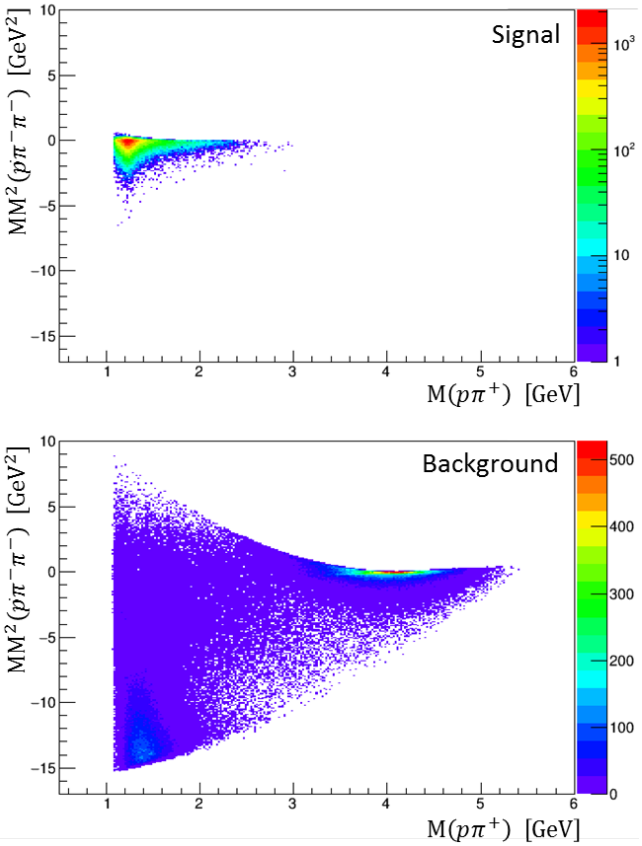

Fig. 3: Squared $\bar{p}\pi^-\pi^-$ missing mass versus $p\pi^+$ invariant mass for signal events (upper panel) and quasifree background events (lower panel).

Outlook: The results obtained on the level of Monte Carlo generated events are promising. However, so far the background due to rescattering on the spectator nucleon of one or more of the pions created in $\bar{p}N$ annihilation has not yet been taken into account. These rescattering processes are expected to be less abundant than the quasi-free three-pion annihilation, however they might have a larger overlap in the kinematic variables with the signal events. It is planned to implement these processes into the Monte Carlo generation of background as well, either in FTF or in a separate generator. A full simulation study of the detector response has been started, and the analysis is in progress. The results of this study will be shown in the following report.

References:

[1] D. Allasia *et al.*, Phys. Lett. **B 174** (1986) 450.
[2] S.J. Brodsky, AIP Conf. Proc. **792** (2005) 279.
[3] C.G. Granados and M.M. Sargsian, Phys. Rev. **C 83** (2011) 054606.
[4] http://www.slac.stanford.edu/ lange/EvtGen/
[5] J. Haidenbauer, priv. comm. (2013).
[6] T.A. Armstrong *et al.*, Phys. Rev. **D 56** (1997) 2509.

Parallel Algorithms for Online Trackfinding at $\overline{\text{P}}$ANDA

Ludovico Bianchi

Online Tracking on GPUs at $\overline{\text{P}}$ANDA The $\overline{\text{P}}$ANDA[1] experiment, one of the four scientific pillars of the FAIR[2] facility currently under construction in Darmstadt, is a next-generation particle detector that will study collisions of antiprotons with beam momenta of 1.5–15 GeV/c on a fixed target. Because of the broad physics scope and the similar signature of signal and background events in the energy region of interest, $\overline{\text{P}}$ANDA's strategy for data acquisition is to continuously record data from the whole detector and use this global information to perform online event reconstruction and filtering. A real-time rejection factor of up to 1000 must be achieved to match the incoming data rate for offline storage, making all components of the data processing system computationally very challenging. Online particle track identification and reconstruction is an essential step, since track information is used as input in all following phases. Online tracking algorithms must ensure a delicate balance between high tracking efficiency and quality, and minimal computational footprint. To fulfill these requirements, a massively parallel solution exploiting multiple Graphic Processing Units (GPUs) is under investigation [2]. The activity of our group is focused on developing algorithms using $\overline{\text{P}}$ANDA's barrel tracking subsystems, the MVD[3] and the STT[4], and their implementations for CPU and GPU using C++, CUDA and OpenACC.

Circle Hough Algorithm The Circle Hough (CH) algorithm is a novel method developed by our group[1, 2]. It is based on the Hough Transform, an image processing algorithm used to find instances of a given shape within an image. The main idea behind the CH is, for each hit, to generate all possible primary tracks (Hough circles) compatible with the hit. The resulting hit parameters are collected in an accumulator array (AA), representing the Hough space. Peak values in the AA correspond to real tracks. The main advantages of the CH is its good trackfinding efficiency even for low-momentum tracks, and the possibility of operating in parallel on single hits. This aspect is particularly important for the application on GPUs, as exposing additional layers of parallelism contributes to exploiting the full capabilities of the GPU programming paradigm.

Locus Circle Hough The AA is a crucial component of the algorithm. In addition to the requirement of high computing performance, once the candidate track is found, the algorithm must be able to associate to it all hits used to perform the hit finding. For this reason, in the current version of the algorithm, the AA filling phase must be supplemented with additional steps to ensure that only one hit is registered in each cell, and that any empty cells, if present, are also filled. The impact of these additional steps on the algorithm performance is not significant on the CPU, but becomes critically important on the GPU, where dependency between data points and branches in the execution are greatly detrimental to performance.
An alternative approach was introduced to bypass these limitations. The main idea behind te hLocus Circle Hough algorithm is that the geomentric locus of the Hough Circle centers can be found analytically. The locus is a straight line for point-like hits, such as the ones coming from the MVD, or two branches of a hyperbola for extended hits, like the hits produced in the STT. Instead of the parametric equation of the hyperbola, a pair of rational degree-2 Bézier curves are used, allowing to represent the hyperbola with arbitrary precision, and less computation, directly from the hit parameters, eliminating the need for direct calculation of the Hough circles. All these operations can be performed in parallel on all hits. A minimal software framework, written in Python with no dependencies from the complex PandaRoot framework, has been developed to assist quick development and programmatically create figures. Currently, two different options are being investigated. In the first, the cells of the AA are filled by rasterizing the Bézier curves. Rasterization is a common computing task, and it's particularly well-suited to Bézier curves and parallel implementations. Once the AA is constructed in this way, a peakfinding procedure is performed. The nature of the rasterization procedure automatically ensures that the AA is filled properly, without the need for additional processing. In addition, the peak structures in the AA contributes to making the peakfinding phase easier. A second possibility is to find the accumulation points by analytically computing the intersection of the locus curves. Selection criteria must be used to reduce the O(n^4) complexity of the naive solution.

Outlook Activity on the Locus Circle Hough algorithm is ongoing. The problem is interesting from a computational point of view, and many different possibilities for the rasterization, peakfinding, and analytical intersection phases are being explored. The current preliminary versions of the algorithm implementation will be replaced by optimized, performance-oriented versions. Systematic testing of the algorithm, both of the computing and the physics performance, will be performed. The adoption and development of software tools to ensure reproducibility of the results and ease of use is considered an important requirement of the testing mechanism.

References:

[1] L. Bianchi, A. Herten, J. Ritman, T. Stockmanns, A. Adinetz, J. Kraus and D. Pleiter, J. Phys. Conf. Ser. **664** (2015) 8, 082006. doi:10.1088/1742-6596/664/8/082006

[2] A. Herten, "GPU-based Online Track Reconstruction for $\bar{P}$ANDA and Application to the Analysis of $D \to K\pi\pi$", PhD Thesis, 2015

[1] Anti-Proton Annihilation at Darmstadt
[2] Facility for Antiproton and Ion Research
[3] Micro-Vertex Detector
[4] Straw Tube Tracker

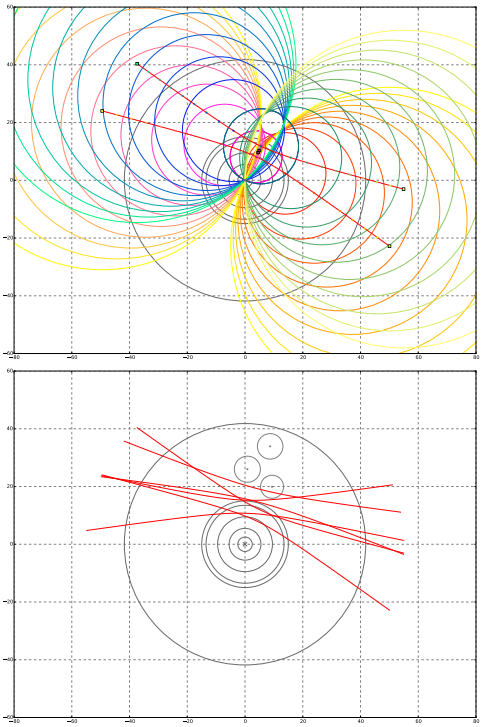

Fig. 1: (Top) Hough circles and geometric locus of their centers, parametrized as a pair of Bézier curve, for a single hit. For each value of the track momentum, up to four distinct candidate tracks are compatible with a set of hit parameters (position, radius). Sizes are exaggerated for clarity. (Bottom) The intersection of Bézier curves for three hits corresponds to the center of the reconstructed track, without explicit calculation of individual Hough circles.

A test system for the electronic components of the PANDA Micro Vertex Detector

Alessandra Lai

Introduction The 'anti-proton annihilation at Darmstadt' (PANDA) experiment is one of the main devices at the upcoming Facility for Antiproton and Ion Research (FAIR), which is under construction in Darmstadt, Germany. This fixed target experiment will study the transition region between perturbative and non-perturbative QCD in the energy regime of the charmonium. The innermost sub-detector system of the target spectrometer of the PANDA experiment is the Micro Vertex Detector (MVD). It consists of four barrel layers in the central part and six disk layers in the forward direction. Two types of silicon detectors will be used: pixel detectors at the inner part and double-sided strip detectors at the outer part. Two different front-end chips are required for the MVD: the Torino Pixel ASIC (ToPix) and the PANDA Strip ASIC (PASTA). The ToPix ASIC is a chip developed for the readout of silicon pixel detectors. The final version of a single chip reads out more than 10,000 pixels with pixel dimensions of 100 μm x 100 μm. In addition to the spatial information, the deposited energy in a pixel and the time when the pixel was hit are measured with a precision better than 10 ns [1]. The PASTA chip is designed to read out silicon strip sensors. Like the ToPix ASIC, it measures the position, the deposited energy and the time of a hit. Both are designed to transmit data at a rate of several hundred Megabits per second and are capable of handling the expected hit rate in hot spots of the detector. One key component in the development of new front-end electronics is a test system that is capable to handle these high rates. It should be flexible enough to test different kinds of front-end electronics and it should be easy to adapt to new prototypes. Therefore, an FPGA-based (field programmable gate array) system is the ideal candidate. For this test system suitable firmware and a software framework are needed. Such a system is under development at the Forschungszentrum Jülich.

The Jülich digital readout system The main components of the Jülich digital readout system (JDRS) are an evaluation board from Xilinx (ML605), hosting a Virtex-6 FPGA and a custom made readout board that hosts the device under test (DUT), i.e. the chip. A network link allows the connection from the evaluation board to a PC. The logic scheme for the FPGA, called firmware, is written in VHDL (Very high speed integrated circuit-Hardware Description Language). Its main duties are to handle the comunication of the DUT with the PC, to generate the clock signals and to handle the data conversion. Different internal modules are responsible for each of these tasks. A software called MVD Readout Framework (MRF) [2] , based on C++ has been developed with the idea of maximum modularity in mind. It is a library that collects functions that allow access to the elements of the readout chain. It is structured in four abstraction layers, that isolate low level function from higher level ones. The first is the physical layer and it is responsible for the connection between the readout board and the PC. In the past it was an optical link but at present it uses an ethernet connection. The second is the generic access layer (GAL), responsible for data transfer and formatting (e.g. open a connection, send and receive data packages,...). Then comes the transport access layer (TAL) providing board specific functions (e.g. clock generation, flush of data buffers,...) and latest the chip access layer (CAL) for DUT specific functions such as configuration and readout.

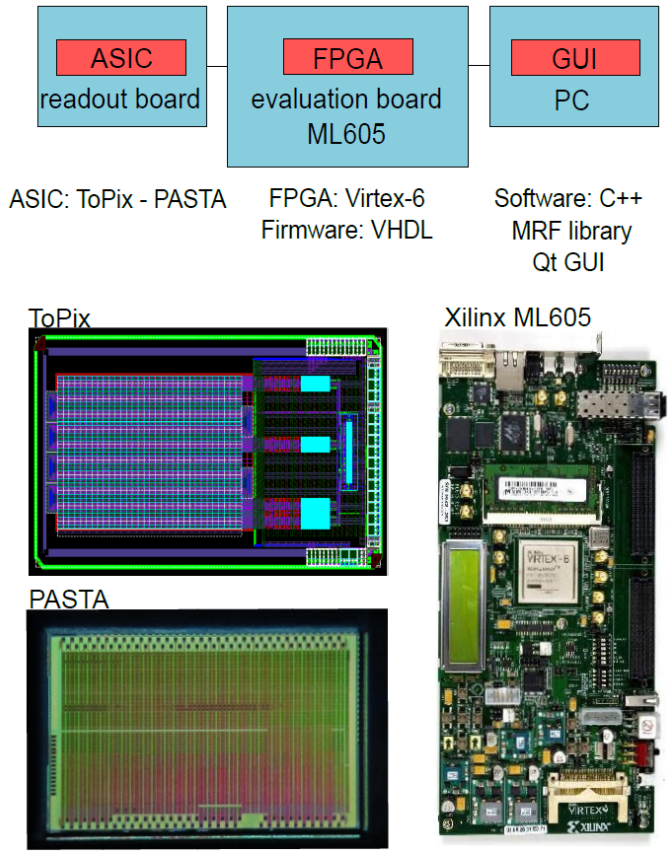

Fig. 1: Main components of the readout chain for the PANDA MVD ASICs [3]

To facilitate the access to the readout elements, a Qt-based graphical user interface (GUI) has been developed. Qt is an open source framework based on C++ which is widely used for the development of applications that require GUIs, as well as command-line tools. Among many features, it offers support for event handling exploting the signals and slots mechanism, allows parallel programming via threads creations and provides a graphical designer for layout operations.

Latest developments The latest developments on the JDRS have their focus on the GUI, which was originally designed for beam test measurements to provide essential functionalities. In fact, at present, the aim is to perform laboratory measurements to fully characterize both the MVD ASICs, ToPix and PASTA, and for that purpose several modifications are required (e.g the data handling can be simplified with respect to the case of in-beam measurements). This new aim has been taken as an opportunity to work on the mantainability and reusability of the code. A refactoring process that involves the structure of the GUI itself has been carried out, strongly exploiting the features that Qt offers. The basic idea is to make the existing framework modular

by separating the functionalities in indipendent projects, which are all sub-parts of a main container. In this way each part can be checked, extended and mantained with minimum effort. Despite the modularity, communication among projects is necessary (i.e. an event that occurs in one part of the GUI might trigger an instructin in another distinct part). At this point the signals and slot mechanism comes in handy, for it allows to connect functionalities belonging to different sub-projects and distribute global information. This approach is adopted not only at the code level, but also in the layout of the GUI itself, grouping logical interaction possibilities together. The advantage of such an approach is double; in fact both the developer and the user are helped in the process of interacting with a complex system.

At the moment, a prototype of the ToPix chip is available. Therefore the present version of the JDRS is adapted to the ToPix structure. Nevertheless, the newly gained modularity of both the firmware and the software guarantees its reusability as interface for the PASTA chip, or another front-end chip.

Outlook As already mentioned, the goal for the next future is the full qualification of the front-end chips designed for the MVD. Therefore a section of the GUI dedicated to laboratory measurements for performance studies is under development and will be completed in the next months.

References:

[1] The PANDA Collaboration, Technical Design Report for the: PANDA Microvertex Detector. (2011) http://arxiv.org/abs/1207.6581

[2] M. Mertens, PhD thesis http://www-brs.ub.ruhr-uni-bochum.de/netahtml/HSS/Diss/MertensMariusC/

[3] Courtesy of Daniela Calvo (INFN Torino) and Tommaso Quagli (Univ. Giessen)

Measurement of the spatial and energy-loss resolution with a prototype Straw Tube Tracker (STT) for the $\bar{P}ANDA$ experiment

A.Apostolou

The Straw Tube Tracker will be one of the tracking sub-detectors of the $\bar{P}ANDA$ experiment. The task of the STT will be the simultaneous measurement of the drift time for the spatial resolution and the deposited charge for the specific energy-loss information. Both of the measurements have to be of high resolution and suitable for the $\bar{P}ANDA$ environment. The development of a new custom-designed electronic readout system for the STT is required. One concept is based on an Application Specific Integrated Circuit (ASIC), which measures the pulse start time and the width of a straw signal (Time-over-Threshold (ToT)). Both time information are readout by a digitized Time-Readout-Board (TRB) [1].

In May 2015 the first pre-series test was carried out in the Big Karl beam area at COSY. A proton beam with two different momenta was used (0.6GeV/c and 2.95GeV/c). The straw prototype setup used for the measurements (Figure 1) consisted of 96 channels (3 separate double layer modules of 16 channels per layer). Several data runs were taken for each momentum and for a wide range of operational settings (amplification factor, peaking time, high voltage, signal threshold).

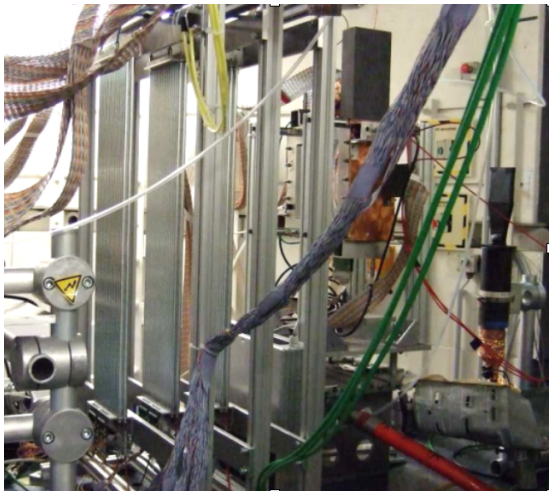

Fig. 1: The straw prototype setup in the Big Karl beam area. The beam is coming from the left.

Figure 2 shows an example of the measured straw drift times and ToT times for the 2.95GeV/c proton beam, after a calibration method of both times for each channel. The maximum drift times are about 160 ns, and the ToT distribution clearly shows a rise towards shorter drift times. A small beam related background is present at drift times greater than 160 ns and smaller than 10 ns.
The next step in the analysis is the calibration of the drift time-isochrone relation and the reconstruction of the tracks to determine the spatial resolution. The ToT information together with the track reconstruction will determine the specific energy-loss for the protons at different momenta. In general, the truncated mean method is applied to the ToT/dx values in order to obtain the specific energy-loss resolution and the separation power for the different momenta.

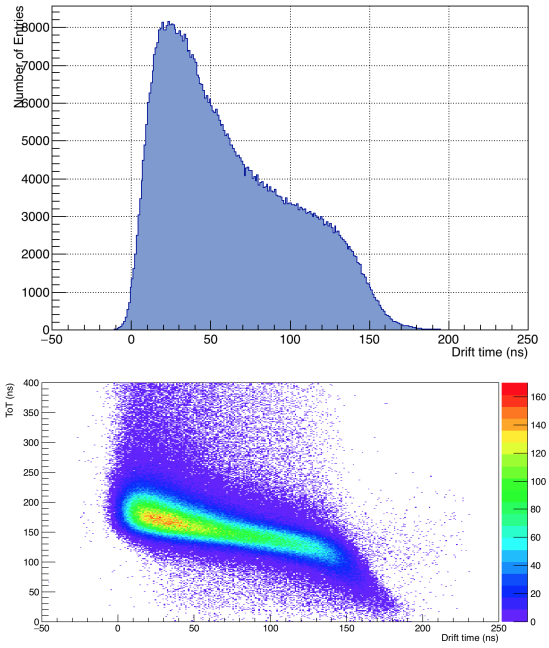

Fig. 2: Upper: Drift time spectrum of selected straws for the 2.95GeV/c proton beam.The maximum drift times observed are about 160 ns.
Lower: Time-over-Threshold versus drift time of selected straws for the 2.95GeV/c proton beam.

For the setup we used for our measurements, this was not possible, since we have only 6 hits per track, and thus, the truncated mean method was not possible to be applied. In figure 3, the residuals plot is being shown, with the obtained spatial resolution taken as the sigma of the distribution to be of the order of 160 μm. As next step, a larger setup with more channels (144 in total) will be tested with a proton beam using four different momenta where both the specific energy-loss resolution and the separation power will be calculated.

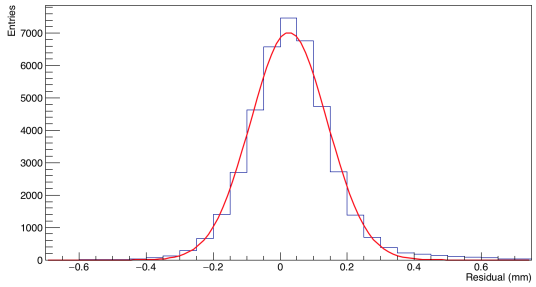

Fig. 3: Residuals calculated from the distance between the reconstructed track and the isochrones. The spatial resolution obtained is of the order of 160 μm.

References:

[1] Technical Design Report for the $\bar{P}ANDA$ Straw Tube Tracker, $\bar{P}ANDA$ collaboration

X, Y, Z rates at $\overline{\text{P}}$ANDA.

E. Prencipe

In the past decade many new, narrow states have been observed in the charmonium and bottomonium mass regions, which do not fit into a spectroscopical scheme as predicted by a static quark-antiquark potential model [1]. Their nature is still unclear.

The transition $Y(4260) \to Z(3900)^-\pi^+$ has been seen by BES III [2]; the transition $Y(4260) \to X(3872)\gamma$ has also been seen [3]. But no experiment until now looked for the transition $X \to Z$, or vice versa. Some Z states are observed decaying to DD^* or $\overline{D^*}D^*$. The mass values of the $Z_c(3885)$, the $Z_c(3900)$, and the $Z_c(4020)$, published by BESIII, are close to the DD^* and $\overline{D^*}D^*$ thresholds, respectively. Assuming that the Z states contain S-wave DD^* and $\overline{D^*}D^*$ components, the spin parity $\text{J}^\text{P}$of the $Z_c(3885)$ and the $Z_c(3900)$ would be $\text{J}^\text{P}= 1^+$, and the spin parity of the $Z_c(4020)$ is expected to be $\text{J}^\text{P}=0^+$, 1^+, or 2^+. The former is confirmed by BESIII experimental data. One can expect also similar S-wave resonances in the $\bar{D}D$ system, with $\text{J}^\text{P}= 0^+$ (C=+1 for the neutral state), and mass values about 3730 MeV/c^2, which are not observed yet.

In this context, the contribution of a $\bar{p}p$ machine has to be considered as essential, because it can either confirm the above BES III measurements, and look for the non-observed 0^+ Z states at the $\bar{D}D$ threshold, as $\bar{p}p$ annihilation is a gluon rich process with direct access to various quantum numbers in production processes.

One of the most striking advantages of the $\overline{\text{P}}$ANDA experiment is the opportunity to search for direct production of exotic resonant states with various quantum numbers, including charged ones in $\bar{p}d$ collisions. In e^+e^- experiments only neutral $J^{PC} = 1^{--}$ resonances can be directly produced, and production of exotic charmed states through other mechanisms is suppressed.

Using the detailed balance method, we can evaluate the cross section as:

$$\sigma[\bar{p}p \to R] \cdot BR(R \to f) = \frac{(2J+1) \cdot 4\pi}{s - 4m_p^2} \cdot \frac{BR(R \to \bar{p}p) \cdot BR(R \to f) \cdot \Gamma_R^2}{4(\sqrt{s} - m_R)^2 + \Gamma_R^2} \qquad (1)$$

where f is the final state of the decay channel, Γ is the total width of a resonance R, and $\sqrt{s}$ the center of mass energy. For example, in order to evaluate the cross section of the process $\bar{p}p \to X(3872)$, we make use of the Eq. (1). When the $BR(R \to \bar{p}p)$ indeed is not known, then we use the scaling method, for instance to evaluate $\bar{p}p \to Y(4260)$, as from a known PDG [4] upper limit, Eq. 1 would lead to unrealitic high estimates for the Y(4260) case. So, at first we use the ansatz that partial width is identical for states R_1, R_2 of the same quantum number.

$$BR(R_1 \to p\overline{p}) = BR(R_2 \to p\overline{p}) \cdot \frac{\Gamma_{total}(R_2)}{\Gamma_{total}(R_1)}. \qquad (2)$$

This method assumes that the partial widths $\Gamma(R \to \bar{p}p)$ of all charmonium states are identical, where R refers to the state. Although we might have indication that the $Y(4260)$ is not a charmonium state, no model exists to evaluate the cross section for exotic states. In absence of any explanation of the $Y(4260)$ nature, thus we perform our calculation

Table 1: Summary of the expected X, Y, and Z production rates per day in $\overline{\text{P}}$ANDA, assuming different operation modes (e.g. different rates $\mathcal{L}$/day). The calculation is performed by multiplying luminosity and cross sections. The cross section upper limits are used in these calculations, and in parenthesis the corresponding lower limit is reported. For the $X(3872)$, only an upper limit was evaluated in this short report, and thus we omit a second number.

Resonance	$\mathcal{L}$ = 8.64 pb^{-1}/day	$\mathcal{L}$= 0.864 pb^{-1}/day	$\mathcal{L}$= 0.432 pb^{-1}/day
$X(3872)$	432000	43200	21600
$Y(4260)$	19000 (665)	1900 (67)	950 (7)
$Z(3900)^+$	4050 (140)	405 (14)	202 (7)

under the naive assumption that it is a charmonium state. In such a case, the $\psi(3770)$ is assumed to be the reference state. To estimate lower and upper limit we use the partial width $\Gamma_{ee}(Y(4260))$ and Γ_{total} from PDG [4], respectively, and $BR(\psi(3770) \to \bar{p}p)$ from Ref. [5]. Results are summarized in Tab. 1.

The number of expected $Z_c(3900)$ events in $\overline{\text{P}}$ANDA can be indeed estimated from Refs. [2], [6], and [7]: in the decay $e^+e^- \to J/\psi\pi^+\pi^-$ the BESIII experiment observed the $Z_c(3900)$ [2], using the full dataset collected near the $Y(4260)$ energy. The observed $Z_c(3900)$ yield is 307, and the ratio: $R = \frac{\sigma(e^+e^- \to Z_c(3900)^+\pi^- \to J/\psi\pi^+\pi^-)}{\sigma(e^+e^- \to J/\psi\pi^+\pi^-)} = 21.5\%$. Estimates are reported in Tab. 1.

Observations of X, Y and Z transitions are very important for understanding the spectroscopical pattern, and possibly conclude similarities in the nature of these states. Two recent BESIII publications connect the $X(3872)$ to the $Y(4260)$ [3], and the $Y(4260)$ to the $Z_c(3900)$ [2]. However, up to now, no experimental measurement connects the $X(3872)$ to the Z structures. Thus, $\overline{\text{P}}$ANDA would be unique to search for $X \to Z\pi$ transitions involving yet unobserved neutral and charged $Z(3730)$ states in the processes:

- $\bar{p}p \to Z(3730)^0\pi^0$, $Z(3730)^0 \to J/\psi\gamma$, with $J/\psi \to$ leptons and $\pi^0 \to \gamma\gamma$;
- $\bar{p}p \to Z(3730)^0\pi^0$, $Z(3730)^0 \to \chi_{c1}\pi^0$, with $\pi^0 \to \gamma\gamma$, $\chi_{c1} \to J/\psi\gamma$ and $J/\psi \to$ leptons;
- $\bar{p}p \to Z(3730)^\pm\pi^\mp$, $Z(3730)^\pm \to \chi_{c1}\pi^\mp$, with $\chi_{c1} \to J/\psi\gamma$ and $J/\psi \to$ leptons.

We also note, that the $Z_c(3900)$ and the $Z_c(4020)$ have not been observed in B decays, yet. Thus, we expect high discovery potential for $\overline{\text{P}}$ANDA.

References

[1] N. Brambilla *et al.*, *CERN Yellow Report*, hep-ph/0412158 (2005); N. Brambilla *et al.*, Eur. Phys. J. C 71 (2011) 1534 [arXiV:1010.5827 [hep-ph]]; N. Brambilla *et al.*, arXiv:1404.3723 (2014) [hep-ph].

[2] M. Ablikim *et al.* (BESIII), Phys. Rev. Lett. 110 (2013) 252001.

[3] M. Ablikim *et al.* (BESIII), Phys. Rev. Lett. 112 (2014) 092001.

[4] K.A. Olive *et al.* (Particle Data Group), Chin. Phys. C, 38 (2014) 090001.

[5] M. Ablikim *et al.* (BES III), Phys. Lett. B 735 (2014) 101.

[6] J. S. Lange *et al.*, arXiV:1311.7597 (2013) [hep-ex].

[7] E. Prencipe *et al.*, arXiv:1410.5201 (2014) [hep-ex].

genfit2: a general tracking fitting tool.

E. Prencipe

*genfit*2 is a track-fitting tool, providing the Kalman filter equations and the track representation. It was developed for high energy physics experiments, and it can run a test demonstration by producing a default geometry and a constant magnetic field [1]. Indeed, *genfit*2 is suited to run as input any kind of geometry file, and it is independent on the specific magnetic field map. This tool represents an extension of the previous *genfit* package, developed inside the PandaRoot framework in 2007 [2]. Then, a more modern development of the tool has been implemented and extended.

In general, *genfit*2 can handle as input whatever detector geometry, as it is furnished of flexible classes; it accepts as input track candidates, which implementation is new in *genfit*2, and builds interfaces between tracks, hits, and alignment information. It processes an extrapolation code and fitting algorithms, and can handle flexible convergence criteria, which are mostly user-ajustable. It creates root files as output, where information about fitted tracks are stored. An interface between Millepede II (for alignment purposes) and RAVE (the vertex finder) is available, now. *genfit*2 also provides a performant event-Display.

The design of *genfit*2 is based on three pillars: measurements, track representations, and fitting algorithms. The main improvements compared to the old *genfit* is due to a new implementation of the Runge-Kutta representation. It handles informations such as track parameterization, through 3 different sets of coordinates; energy loss, bremmstrahlung, particle hypothesis are also information available. Four different fitting algorithms are available in *genfit*2: a standard Kalman fitter. e.g. a linear estimator that linearizes the transport. It works in both directions, forward and backward. When linearizing arorund the prediction, indeed problems can occur, due to the fact that the state prediction can be far off the actual trajectory. As consequence, the linearization does not make sense. *genfit*2 proposes a solution: it makes use of the reference track. The estimated track parameters are estimated from pattern recognition or the previous fit as exansion point for linear approximation. Then, *genfit*2 proposes to linearize around the reference track instead of the state prediction, in these cases. This is the new "reference Kalman fitter" available in *genfit*2.

After the user (or *genfit*2) chooses which Kalman fitter has to run, a robust track fitter can run: the DAF (deterministic annealing filter). It produces assigned probabilities to measurements (so called *weights*). It is useful to reject outliers or resolve the left/right ambiguities. Actually *genfit*2 implements a novel technique to assign weights and solve the left/right ambguities, that is totally new in this track fitting tool.

The generalized broken line fitter (GBL) is indeed useful for Millepede II.

To quantify the performance of *genfit*2 vs *genfit*, the plots of Fig. 1 and 2 are provided.

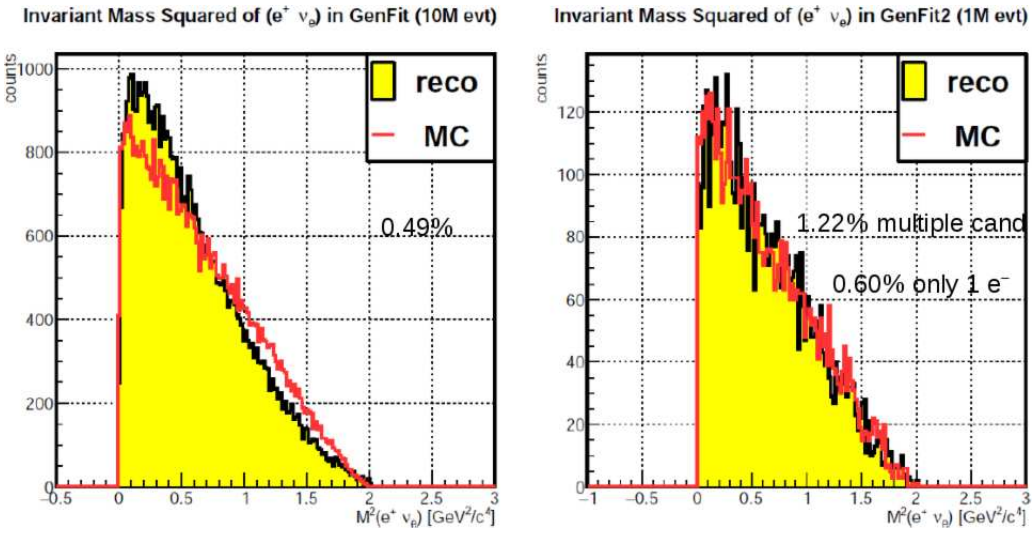

(a)

Figure 1: The left plot represents the invariant mass of $(e^+\nu_e)$, in the chain $\bar{p}p \to D_s^+ D_s^-$, with $D_s^- \to K^+K^-\pi^-$ and $D_s^+ \to \eta\nu_e e^+$, and it is obtained using a standard PandaRoot release tracking tool; the right plots represents the same distribution, but using the $genfit2$ Runge-Kutta track representation, indeed: it is proven that the reconstruction efficiency of electrons improves, and the reconstructed distribution (yellow area) matches better with true values (red line).

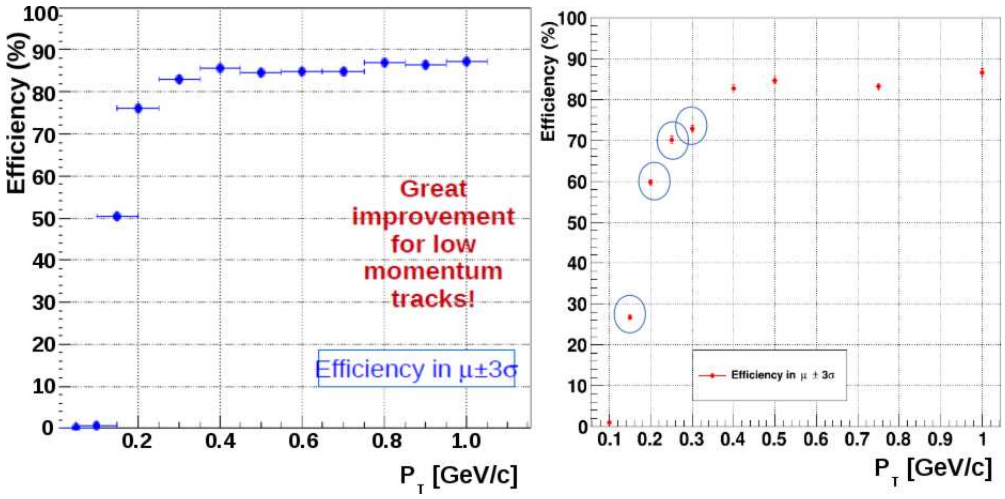

(a)

Figure 2: Efficiency vs transverse momentum, for pions generated using the Box MC Generator, at a fixed polar angle equal to 60°. The left plot shows the $genfit2$ improved performance for low momentum tracks, compared to the standard PandaRoot release tool, especially for p_T <350 MeV/c. The left plot is produced in the PandaRoot trunk revision 28747; the plot at right shows the performance of an old PandaRoot release, using the old version of $genfit$ [3].

References

[1] J. Rauch and T. Schlüter, arXiV: 1410.3698 [physics.ins-det].

[2] D. Bertini *et al*, Journal Phys. of Conf. Series 119 (2008) 032011.

[3] S. Costanza, $https://panda-wiki.gsi.de/foswiki/pub/Computing/Minutes23Jul2014/$

Search for polarization effects in the antiproton production process

D. Grzonka for the P349 collaboration

The availability of a polarized antiproton beam includes a large potential for interesting experiments in various fields. Several possibilities for the preparation of a well defined polarized antiproton beam have been proposed and are still under discussion, see e.g. [1], [2], [3]. The most simple one is the production process itself if the antiproton production process creates some polarization.

In order to study a possible polarization of produced antiprotons an experiment has been performed at the CERN PS test beam area [4]. The PS test beam lines at CERN are feed by reaction products of the 24 GeV/c proton beam of the CERN/PS accelerator hitting a production target. For the experiment the T11 beam line was chosen which accepts particles at a production angle of about 150 mrad which is sufficiently large to include not only s-wave production. The beam line was adjusted to a momentum of 3.5 GeV/c for negatively charged particles which corresponds to the antiproton momentum used at the CERN AD and foreseen at the future FAIR facility for the preparation of antiproton beams. The expected particle composition is dominated by pions with a ration of 1:5:100 for $\bar{p}$: K^- :π^-.

For the measurement of the polarization of produced antiprotons the elastic antiproton-proton scattering is analyzed in the Coulomb-nuclear interference (CNI) region. The analyzing power in the CNI region, which corresponds to a scattering angle around 20 mrad, is rather small, in the order of 0.45 %, but its well known which is a prerequisite to determine the polarization from the scattering asymmetry. In the experiment about $5 \cdot 10^5$ particles/spill were delivered with a spill length of about 400 ms. The detector arrangement for the measurement is shown in Fig. 1.

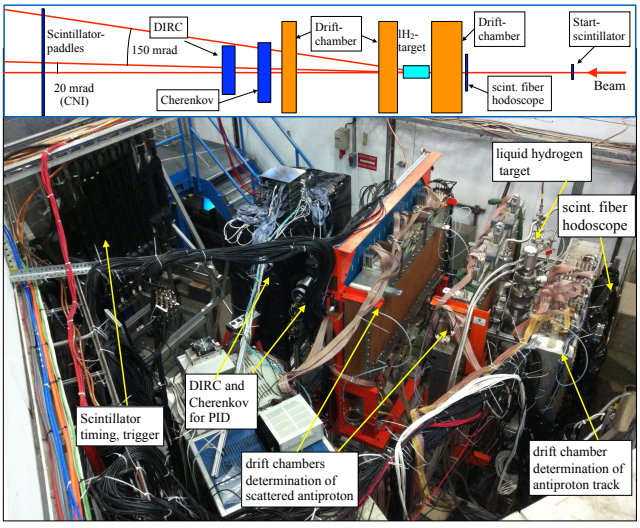

Fig. 1: The detector arrangement at the T11 beam line. A schematic sketch is shown in the upper part and below is a photo of the setup.

In order to determine the polarization of elastic $\bar{p} - p$ scattering the particle id and its scattering angle has to be determined. The beam particles first pass through a start scintillator used for trigger signal generation and a scintillating fiber hodoscope to adjust the beam. The primary particle track is measured with a first drift chamber before it enters the liquid hydrogen target with a length of 15 cm and a diameter of about 7 cm. The scattered particles pass through a package of two drift chambers to measure the scattering angle, an aerogel Cherenkov detector, a DIRC and finally a scintillator hodoscope as stop detector for a time of flight measurement. The aerogel Cherenkov detector with n $\sim$ 1.03 gives a signal for a pion but no signal for a $\bar{p}$ with 3.5 GeV/c momentum and is used for the online discrimination of the large pion background. The DIRC includes Plexiglas and gives Cherenkov light for all particles and is used for offline particle identification by the Cherenkov angle. A trigger signal is generated for a coincidence of start and stop scintillator vetoed by a Cherenkov signal. The selection of a scattering event is based on a single track in each drift chamber with a reconstructed reaction vertex in the target area.

Two beam times have been approved by the CERN SPSC, one measurement was done end of 2014 and a second measurement in summer 2015. All individual detectors worked well. The Cherenkov detector veto reduced the trigger rate by a factor of 10-15 which allowed an acquisition of the data with a low dead time and rates of about 20 000 events/s. With the DIRC a clear separation of $\bar{p}$ and π^- is achieved as shown in Fig. 2 for the 2015 data.

The data are presently under evaluation with focus on the track reconstruction procedure. The analysis needs a careful calibration of the distance to drift time relation and good background rejection procedure before scattering events can be selected.

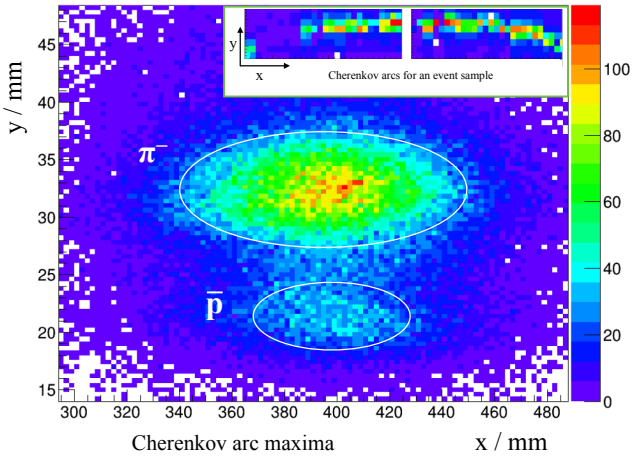

Fig. 2: Cherenkov arcs maxima reconstructed from the measured photon distribution of individual events. Antiprotons are located at a lower y-value which is proportional to the Cherenkov angle.

References:

[1] A. D. Krisch, *AIP Conf. Proc.* **145**, 207 (1986)
[2] E. Steffens, *AIP Conf.Proc.* **1008**, 1-5 (2008), *AIP Conf.Proc.* **1149**, 80-89 (2009)
[3] H. O. Meyer, *AIP Conf.Proc.* **1008**, 124-131 (2008)
[4] D. Grzonka et al., *Acta Phys.Polon.* **B46**, 191-201 (2015)

Commission of a Magnetostatic Beam Position Monitor

F. Hinder[a,b], H. Soltner[c] and F. Trinkel[a,b] for the JEDI collaboration

For the planned measurement of Electric Dipole Moments (EDMs) of charged hadrons, like the proton or deuteron, a new RF-Wien Filter will be installed at the COoler SYnchrotron (COSY). To control the beam position to the magnetic and electric center of the Wien Filter two new Beam Position Monitors (BPMs), using so called Rogowski coils, will be installed downstream and upstream of the Wien Filter [1]. These BPMs measure the magnetic field induced by the particle beam flux. The beam position is calculated out of this measured magnetic field. In November and December of 2015 first test measurements with a deuteron particle beam were performed. The first results of these measurements are presented.

Each BPM consists of a torus which is wound by one layer of a 150 µm copper wire. The radius of the torus is $R = 40\,\text{mm}$. The radius of the tube amounts to $a = 5\,\text{mm}$. The winding is divided in four segments. Each covers an azimuth angle range of 90°, starting at 0°. The number of windings for each segment is 255. A sketch of such a Rogowski coil is shown in Fig. 1.

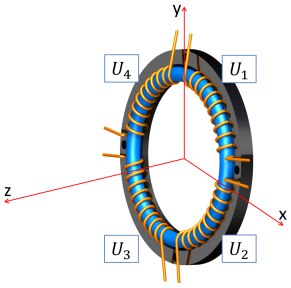

Fig. 1: Sketch of a Rogowski Coil, which detects the horizontal and vertical beam position. The radius of the torus is $R = 40\,\text{mm}$ and the radius of the tube amounts to $a = 5\,\text{mm}$.

The position can be calculated by combining the induced voltages (U):

$$x = \frac{\pi\sqrt{R^2 - a^2}}{2} \frac{U_1 + U_2 - (U_3 + U_4)}{U_1 + U_2 + U_3 + U_4} \tag{1}$$

and

$$y = \frac{\pi\sqrt{R^2 - a^2}}{2} \frac{U_1 + U_4 - (U_2 + U_3)}{U_1 + U_2 + U_3 + U_4}. \tag{2}$$

The combinations of the induced voltages for the x- and y-plane are illustrated in Fig. 2.

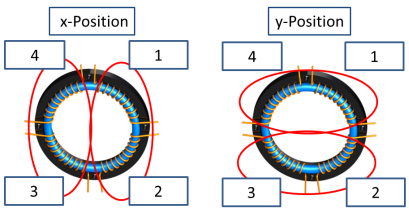

Fig. 2: Position determination: Voltage combination for the x- (left Fig.) and y-direction (right Fig.).

For the test of the functional principle, two of such BPMs were installed inside the PAX chamber at COSY. One at a x-y table, the second one fixed. Figure 3 displays the arrangement of the experimental setup. This setup enables a calibration of the first BPM relative to the x-y table. The second BPM can be calibrated against the movable one. All needed measurements are done with the particle beam and not with a laboratory setup, where a live wire is used. The calibration of the fixed BPM is done by moving the particle beam with local orbit bumps at the position, where both BPMs are installed. Figure 4 shows the readout scheme for one Rogowski coil. Each segment of the Rogowski coil is connected to a Lock-In amplifier after pre amplification. Two Lock-In amplifiers measure the induced voltage at the revolution frequency. The COSY RF signal is used to lock the two Lock-In Amplifiers to the beam revolution frequency of COSY. An other Lock-In amplifier converts the COSY RF signal into a TTL pulse as lock frequency. The measured voltages are sent for data acquisition to a local computer. The experimental method and first, preliminary, results of these measurements are discussed in the following.

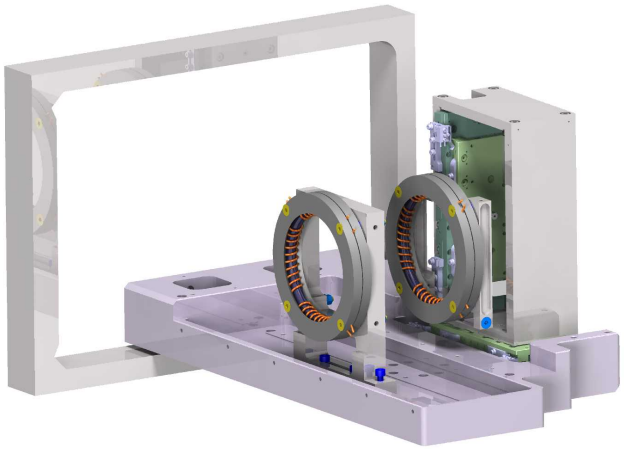

Fig. 3: Sketch of the Rogwoski Coil arrangement. The fixed Rogowski Coil is shown in the front. The second coil is installed on a Piezo-table, which allows to move the BPM to different positions.

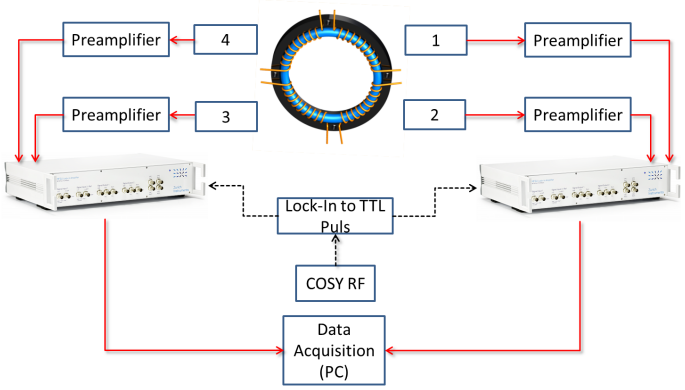

Fig. 4: Readout scheme for one Rogowski coil.

The measurements were performed with a bunched deuteron beam with 10^9 particles per fill. The momentum was 970 MeV/c. The corresponding revolution frequency is 750 kHz. The beam was injected, bunched, accelerated and electron cooled for 15 s. After switching off the e-cooler, a local horizontal and vertical orbit bump, using four steerer magnets, was performed. A schematic sketch of the beam preparation for one cycle in the horizontal and vertical plane is illustrated in Fig. 5. The beam was injected and stays at the initial orbit for 60 s. Next the orbit bumps in horizontal and vertical direction were performed. The bumps were active for 30 seconds. After the bumps were deactivated, the beam moved to the incoming position. The variation of the horizontal orbit bump was adjusted from $-2\,\%$ to $2\,\%$ in $0.1\,\%$ steps and for the vertical orbit bump fixed to the value $1\,\%$.

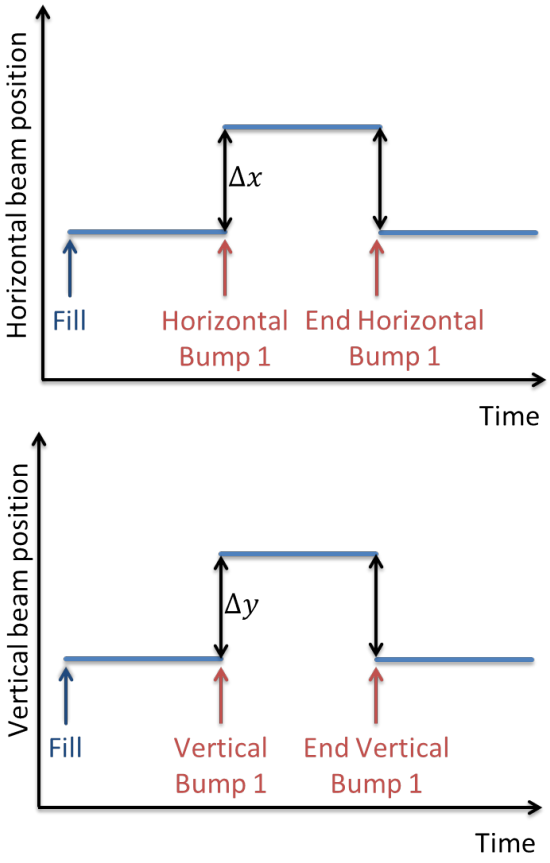

Fig. 5: Timing of the applied orbit bumps.

The measured beam position before and after the bump is described by two straight line fits $g1_{x,y}$ and $g2_{x,y}$ for each plane. These fits take into account the drift of the particle beam position over the cycle length. To the measured position of the beam during the bump time, a liner function with the same slope as the one used to describe the drift, is fitted (Eq. 3). The difference in the offset of both functions $p1_{x,y}$ and $p2_{x,y}$ is the beam movement induced by the local orbit bump (Eq. 4). This measurement was done for 20 different bump strengths. The bump strength is specified in % of the maximum current of the magnet. The magnet strength is calculated by using the COSY mad8 model. In this calculation 1 mm beam movement corresponds to 1 % in the COSY control interface. The described procedure is exemplary shown in Fig. 6 for the horizontal beam position, where $g1$ is the linear fit for the initial orbit and $g2$ is the position after the bumps are applied. This procedure is performed for all different horizontal steerer settings.

$$\begin{aligned} g1_x(t) &= p_{0,x}\cdot t + p_{1,x},\ 20s < t < 65s\ ,170s < t < 210s \\ g2_x(t) &= p_{0,x}\cdot t + p_{2,x},\ 95s < t < 135s \\ g1_y(t) &= p_{0,y}\cdot t + p_{1,y},\ 20s < t < 65s\ ,170s < t < 210s \\ g2_y(t) &= p_{0,y}\cdot t + p_{2,y},\ 95s < t < 135s \end{aligned} \tag{3}$$

$$\Delta x = p_{2,x} - p_{1,x} \quad \text{and} \quad \Delta y = p_{2,y} - p_{1,y} \tag{4}$$

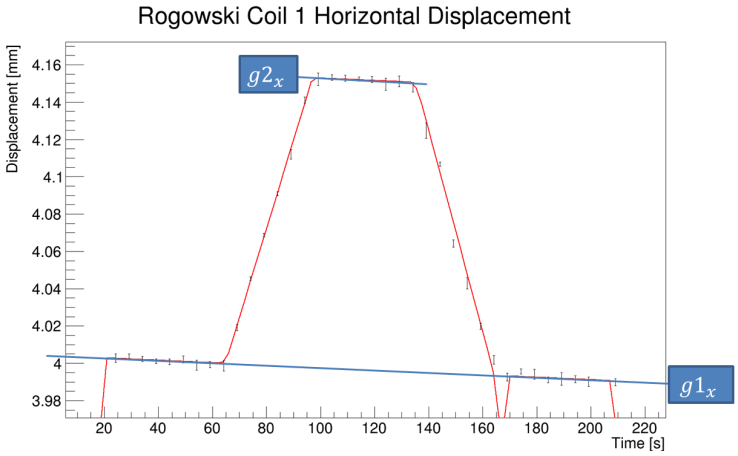

Fig. 6: Exemplary analyse procedure for position determination. The definition of the straight line fits and the range of the fits are shown in eq. 3.

The results of this measurement for both coils are shown in the Fig. 7 and 8 for the horizontal beam displacement and 9 and 10 for the vertical displacement. In the Fig. 7 and 8 the adjusted steerer strength is displayed against the measured horizontal displacement Δx for each coil. The measurement with both coils shows the expected linear behaviour for varying the horizontal steerer strength. The results confirm also the assumption that 1 mm beam movement corresponds to 1 %. In figure 9 and 10 the run number is plotted against the measured vertical displacement Δy for the two coils. The run numbers displays the progress over time. It is expected that the vertical displacement stays constant in both coils by varying the horizontal steerer strength. Only the measured displacement Δy shows that the beam does not stay constant in the vertical plane. The reason for this could be a tilt of the coils or a change in the horizontal plane also causes a change in the vertical plane. The vertical displacement change is in the order of 0.3 mm for horizontal steerer changes from $-2\,\%$ to $2\,\%$. With the standard BPM-system of COSY this small changes are not detectable.

[a] Institute for Nuclear Physics, FZ Jülich, Germany
[b] Physics Institute III B, RWTH Aachen University, Germany
[c] Zentralinstitut für Engineering, Elektronik und Analytik-1, FZ Jülich, Germany

References:

[1] Slim, D. Heberling, Towards a High-Accuracy RF Wien Filter for Spin Manipulation at COSY Jülich, in: XVIth International Workshop in Polarized Sources, Targets, and Polarimetry, 2015, p. PoS(PSTP2015)033

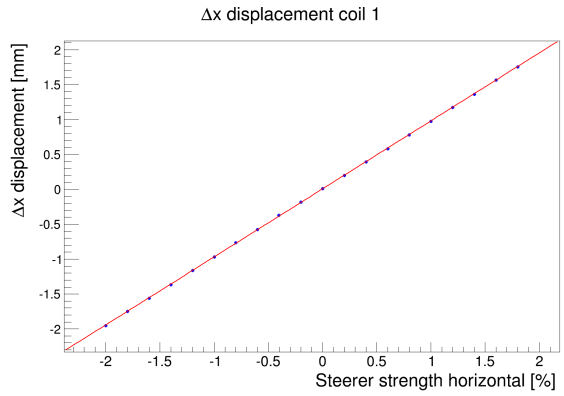

Fig. 7: Measured horizontal displacement with the movable BPM.

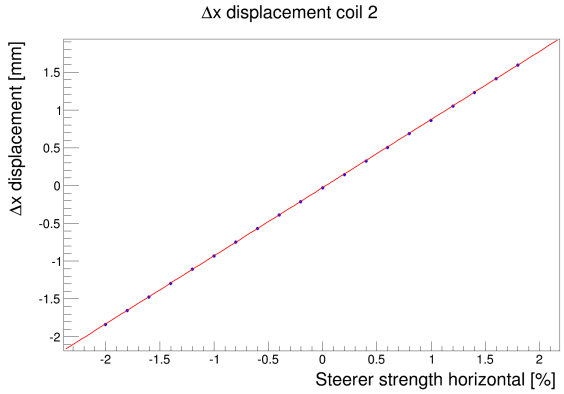

Fig. 8: Measured horizontal displacement with the fixed BPM.

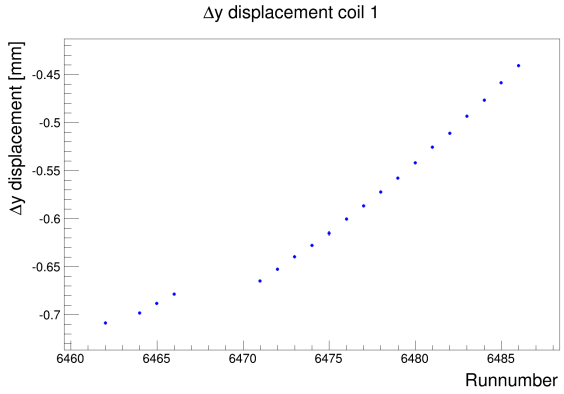

Fig. 9: Measured vertical displacement with the movable BPM.

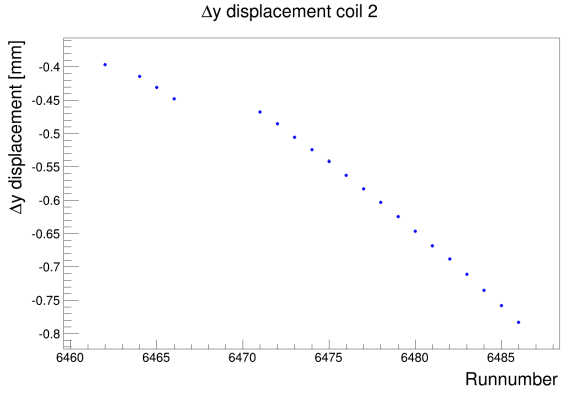

Fig. 10: Measured vertical displacement with the fixed BPM.

Spin Tune Determination using Fourier Transform

D. Eversmann[a]

In this report the new approach of determining the spin tune ν_s by performing a discrete Fourier Transform to the data obtained by the EDDA polarimeter is presented. For this purpose data from the beamtime in May/June 2015 is used. The spin tune is defined as the number of idle spin precessions of the particle spins per turn of the particle bunch in the COSY storage ring $\nu_s = \frac{\omega_s}{\omega_{cyc}}$. Thus, the spins of the initially vertical polarized deuteron beam of a momentum $p_d = 0.97\,\mathrm{GeV/c}$ were tilted by mean of a resonant rf-solenoid into the horizontal plane.

Given the beam momentum of $p_d = 0.97\,\mathrm{GeV/c}$ the angular cyclotron frequency becomes approximately $w_{cyc} \approx 2\pi \cdot 750\,\mathrm{kHz}$ which leads to a spin precession of

$$\omega_s = \nu_s \omega_{cyc} = \gamma G_d \omega_{cyc} \approx 2\pi \cdot 120\,\mathrm{kHz}, \tag{1}$$

where $\gamma = 1.125$ is the relativistic Lorentz factor and $G_d \approx -0.143$ denotes the anomalous magnetic moment of deuteron. The relation $\nu_s = \gamma G$ is only valid for a particle on the closed orbit circulating in horizontal plane of a pure magnetic ring.

Since the detection rate of the EDDA detector is of the order of several thousand events per second it is not possible to unfold the spin precession by a direct least squares fit. Therefore a dedicated algorithm was developed to determine the spin tune with a precision better than 10^{-10} within a 100 s cycle. The topic of this report is to demonstrate that using the discrete Fourier Transform leads to the same results.

The general principle of the discrete Fourier Transform is to transform a sequence of N complex numbers $x_0, x_1, \ldots, x_{N-1}$ into a N-periodic sequence

$$X_k = \sum_{n=0}^{N-1} x_n \cdot e^{-2\pi i k n/N} \tag{2}$$

$$= \sum_{n=0}^{N-1} x_n \left[\cos(-2\pi k n/N) + i \sin(-2\pi k n/N)\right] \tag{3}$$

whereas the Euler's formula is used and $k \in [0, N-1]$ denotes the number of cycles per N samples.

The time stamping system connected to the EDDA detector assigns each event to a turn number of the particle bunch in the ring n_{turn}, which is given by a real value. Thus, the symmetry $X_{N-k} = X_k$ leads to $N/2 - 1$ Fourier coefficients and the coefficients in Eq. 3 x_n are defined as

$$x_n = \begin{cases} 1 & \text{for } n = n_{turn} \\ 0 & \text{else .} \end{cases} \tag{4}$$

Consequently, the summation is given by the sequence of the total events $n_{ev} \in [1, N_{ev}]$ and the term kn/N can be substituted by $\nu_s n_{turn}(n_{ev})$. The real and imaginary part of X_{ν_s} are formed

$$a_{\nu_s} = \Re(X_{\nu_s}) = \sum_{n_{ev}=1}^{N_{ev}} \cos(2\pi \nu_s n_{turn}(n_{ev})) \tag{5}$$

$$b_{\nu_s} = \Im(X_{\nu_s}) = \sum_{n_{ev}=1}^{N_{ev}} -\sin(2\pi \nu_s n_{turn}(n_{ev})) . \tag{6}$$

to determine the amplitude ε_{ν_s} and the phase φ_{ν_s} of the spin precession, which are given by

$$\varepsilon_{\nu_s} = \frac{1}{N_{ev}} \sqrt{a_{\nu_s}^2 + b_{\nu_s}^2} \tag{7}$$

$$\varphi_{\nu_s} = \mathrm{atan2}(b_{\nu_s}, a_{\nu_s}) . \tag{8}$$

The turn depending spin tune consists of an assumed spin tune ν_s^0 selected by the user and a part, which represents the deviation between the true value $\nu_s(n_{turn})$ and ν_s^0. The second term can be expressed by the turn derivative of the phase obtained from the Fourier Transform φ_{ν_s}

$$\nu_s(n_{turn}) = \nu_s^0 + \frac{1}{2\pi} \frac{d\varphi_{\nu_s}(n_{turn})}{dn_{turn}} . \tag{9}$$

In Fig. 1 the phase distributions φ_{ν_s} and the statistical error of the Fourier Transform and the mapping method are shown. One observes a parabolic behaviour, which indicates a linear spin tune drift regarding to Eq. 9. This corresponds to the

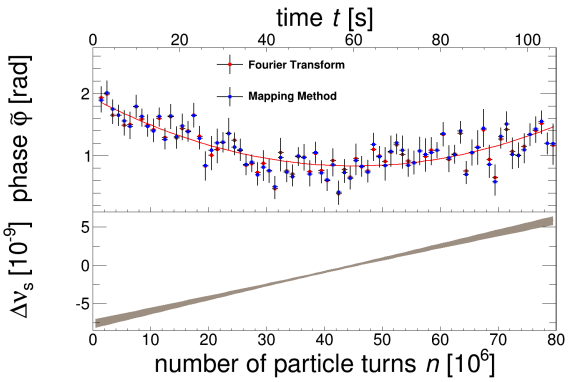

Fig. 1: In the upper plot the phase distributions φ_{ν_s} are shown for the Fourier Transform (red) and the mapping method (blue). The lower plot shows the spin tune deviation from the assumed spin tune.

lower plot of Fig. 1, where the deviation from the true spin tune $\nu_s(n_{turn})$ and the assumed one ν_s^0 is shown.

The phase distributions are not matching perfectly which each other. This is due to the fact, that the number of bins in the asymmetry fit used for the phase and amplitude determination yields one additional source of a systematic error. The spin tune determination based on the Fourier Transform

provides just one systematic error, namely the selection of the assumed spin tune ν_s^0.

Further discussion of systematic effect

[a] RWTH Aachen University, Germany

Development of the electrostatic deflector for JEDI

K. Grigoryev[a] for the JEDI collaboration

Search for the permanent electric dipole moments (EDM) of the proton or deuteron at COSY require significant improvements of the measurement accuracy of existing devices at the storage ring. Future upgrade may require building a dedicated ring with electric and magnetic or purely electrostatic elements. Ongoing JEDI precursor experiments at COSY will help to figure out how strong the electric field of the individual electrostatic deflector should be. The highest electric field gradient of about 17 MV/m (foreseen for 30 m storage ring with electrostatic components only) was taken as reference value for building the prototype of the electrostatic deflector.

Theoretically, a few meters long flat deflector, designed for several centimeters spacing between two capacitor plates, should not differ much from its small scaled version, made with the same accuracy and the electrode profile. Moreover, the minimization of the prototypes affects the following factors:

- the weight is not more a problem. A small-scaled deflector can be built from a bulk peace of material without special support,
- the laboratory-scale high voltage power supply is capable to produce the same field gradient at small distances between the electrodes,
- the safety restrictions for the laboratory room will be lower in case of smaller high voltage,
- cables, feedthroughs and flashover detection is much simpler.

Complementary requirements to perform these tests were ultra-high vacuum and the lack of dust inside the vacuum chamber. To achieve these conditions the test bench (shown in Fig. 1) for electrostatic deflector prototypes, build using UHV CF components, was assembled in ISO7[1] class clean room.

Fig. 1: The test bench for electrostatic deflectors.

Pumping of the vacuum chamber with one scroll pump, as fore pump, and one turbo-molecular pump allows reaching pressure level of 10^{-9} mbar in a reasonable time. After activation of the ion-getter pump, directly connected to the vacuum chamber, with simultaneous backing out the whole setup to get rid of the water from the walls, the main chamber must be isolated from the turbo-molecular pump using the UHV gate-valve. During the measurements and the rest of the time pressure in the chamber is kept by the ion-getter pump only at 10^{-10} mbar. It minimizes additional vibrations of the system caused by the scroll and turbo-molecular pumps.

Numerical simulations (see Fig. 2) show that there is no difference between field gradients in the flat region of the electrodes in case both of them have the same potential with the different sign or one of the electrodes powered with double voltage and another is grounded. Furthermore, the option with one grounded electrode is more attractive, because it will not require another high voltage power supply and all electronic devices will have the common ground. In this case, measurements of the dark current between the electrodes do not need to hang-up a picoammeter at the negative potential.

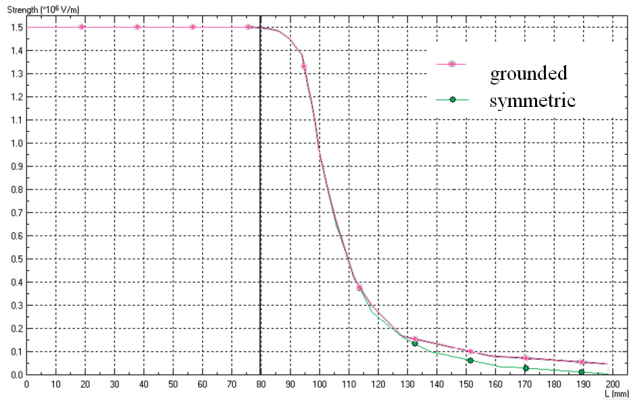

Fig. 2: The electric field strength along the central plane of deflector (green – both electrodes are powered, pink – one electrode is grounded).

The deflector prototypes (see Fig. 3) were made in two different sizes from stainless steel and aluminum. After machining they were mechanically polished. The small electrodes have ideal half-sphere shape with 10 mm radius. The large electrodes have additional flat region of 20 mm diameter (stainless steel) or 30 mm (aluminum) in the center with similar round edges. To increase the accuracy of measuring the distance between the deflectors, every new measurement procedure starts from positioning electrodes on top of each other; using a linear drive with precision of 0.01 mm.

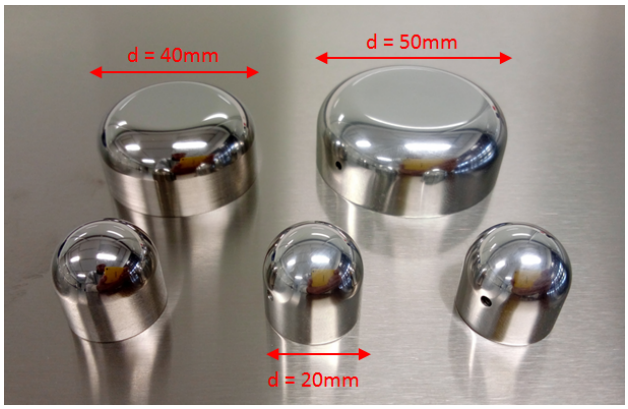

Fig. 3: Test electrodes made from the stainless steel (on the left) and from aluminum (on the right).

First high voltage tests were made with the stainless steel half-sphere electrodes in the wide range of distances from 30 mm to 0.05 mm. Varying the spacing between them, the discharge, if at all, happens in a smallest gap region, as it should be for the electrodes with spherical surface. The dark current at different distances between the electrodes behaved similarly (see Fig. 4) and, taking into account the field enhancement factor, could be scaled. This is another measure of the quality of surface polishing.

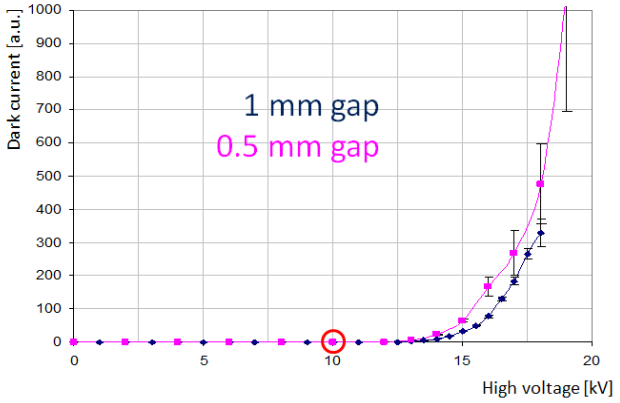

Fig. 4: Dark current during the measurements at different distances between the stainless steel electrodes (high voltage is scaled). Red circle stands for the field strength of 10 MV/m.

Similar tests were performed after exchange one of the electrodes to the largest stainless steel version. The measured field strength at 0.05 mm distance was about 200 MV/m which is the maximum possible in the vacuum.

A second material for electrodes tests was aluminum. The polishing procedure was not very well established and the breakdown at smallest distances during measurements with two half-spheres happened not in the region of the minimum gap, but on the side. It could happen because of the strongest impact on field inhomogeneity at such short distances caused by the roughness of the surface. The maximum field strength, achieved in that configuration, was about 30 MV/m.

Measurements at the small distances showed a good agreement with theoretical predictions of the breakdown conditions and will require further tests with different materials. Special attention should be paid to the measurements at larger distances and higher voltages.

[a] Physikalisches Institut III B, RWTH Aachen University, 52074 Aachen, Germany

[1] Class ISO7 is the level of the clean room contamination by 10^7 particles of 0.1 mkm in one cubic meter, or 352 000 particles of 0.5 mkm in the same volume.

Investigation of spin coherence time for the quasi-frozen spin method

S. Chekmenev[a] for the JEDI collaboration

1 Introduction to the quasi-frozen spin (QFS) method

The quasi-frozen spin (QFS) method [1] introduces a new idea, in which the spin oscillates around the momentum direction and after one revolution stays parallel to the momentum. Due to the low value of the anomalous magnetic moment of deuteron, an effective contribution to the expected EDM effect is reduced only by a few percent compared with the frozen spin method.

The lattice (Fig. 1) is created by two parts: two magnetic arcs with bend magnets, rotating the particle by an angle $\Phi^B = (\pi + 2\alpha)$ per arc and providing the MDM spin rotation in the horizontal plane relative to the momentum by an angle $\Phi_s^B = \nu_s^B \Phi^B$, and two electrostatic arcs with electric deflectors with negative curvature, rotating the beam by an angle $\Phi^E = -2\alpha$ per arc and providing the MDM spin rotation in the horizontal plane relative to the momentum in opposite direction by an angle $\Phi_s^E = \nu_s^E \Phi^E$. To realize the quasi-frozen spin concept, it is necessary to fulfil that condition and ensure $\Phi_s^E = -\Phi_s^B$. Since in the electrostatic deflector the spin is rotated with the frequency, which is by the factor of $K = \nu_s^E/\nu_s^B$ faster than in magnetostatic structure, we have the basic relation for two different arcs

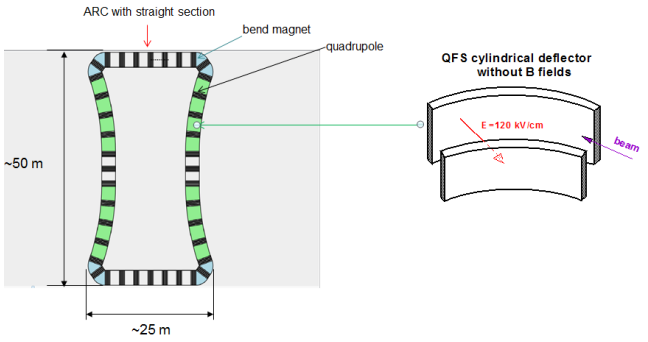

Fig. 1: The lattice for the quasi-frozen spin method

$$\nu_s^B \cdot (\pi + 2\alpha) = \nu_s^E \cdot 2\alpha$$
$$\alpha = \frac{0.5 \cdot \pi}{\nu_s^E/\nu_s^B - 1}. \quad (1)$$

As a result, the total EDM signal, which can be obtained in that ring, grows by $-3.5 \cdot 10^{-15}$ per turn (Fig. 2), and in order to get the total EDM signal to be $\sim 10^{-6}$, one has to keep the beam in the ring for the duration of $N_{turn} \sim 10^9$ turns or ~ 1000 s to measure the EDM of the order of 10^{-29} e $\cdot$ cm

2 Spin coherence time for QFS method

As it was mentioned in the previous section, the time, which is needed to observe an EDM signal is ~ 1000 s. During this time the spin vectors of the particles in a bunch must be aligned. This time is called the spin coherence time (SCT).

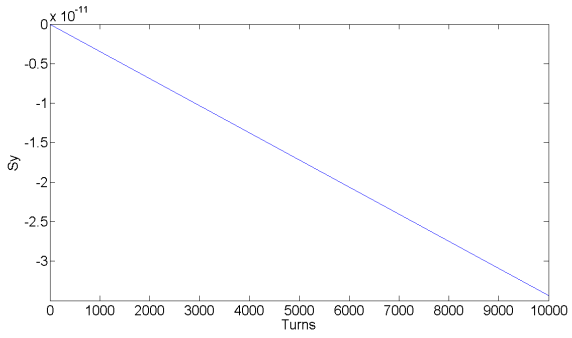

Fig. 2:

One can assume that if there is a difference more than 1 rad between the direction of the spin of the reference particle and other particles in the bunch, the polarisation is almost lost and the bunch is no longer suitable for the EDM experiment because the build-up speed of the EDM signal would start to decrease.

The number of simulations on the SCT maximization was performed. It was shown that the SCT may be prolonged by sextupole correction and beam cooling. Figure 3 demonstrates the value of S_x component after 10^4 turns for different sextupole settings. This value should not exceed 1 rad after 10^9 turns. This can be expressed as the spin coherence time. The SCT obtained is of the order of 150 s for the beam that has a horizontal size of 5 mm and 1500 s for the beam with 1 mm horizontal size.

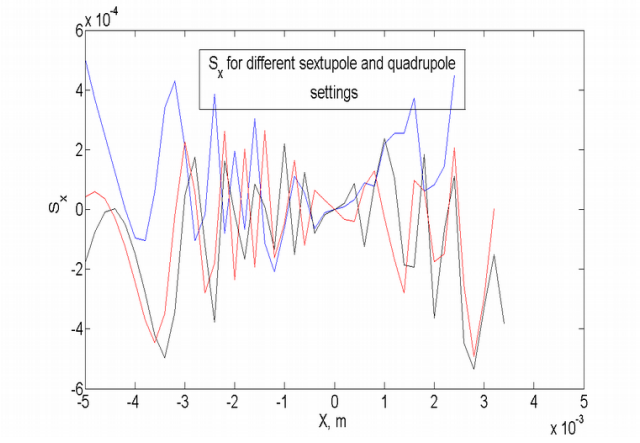

Fig. 3:

[a] III. Physikalisches Institut, RWTH Aachen

References:

[1] Yu. Senichev, quasi-frozen spin method for EDM deuteron search, in *Proc. 6th Int. Particle Accelerator Conf. IPAC2015*, eds. S. Henderson (ANL), E. Ayers (Jlab), T. Satogata (Jlab), V. RW Schaa (GSI), Richmond, VA, USA (2015), p. 213

Preparation of First Beam Tests of LYSO Modules for JEDI polarimetry

F. Müller[a,b], D. Mchedlishvili[a,c], I. Keshelashvili[a] and A. Kacharava[a] for the JEDI collaboration

Introduction

As the polarimetry detector for the EDM measurement will consist of modules containing LYSO crystals, the first step is to investigate the fundamental properties of these crystals. One of the most crucial properties of a LYSO crystal is the efficiency in identifying deuterons (ε_d). Especially, we need to analyze how break-up reactions of deuterons ($d \rightarrow p+n$) influence our ability to detect them. As the deuteron is a very weakly bound nucleus, such reactions are expected to take place inside the crystal [1]. The crystals are going to be hit by the deuteron beam on six symmetric points on the front face in order to explore the amplitude sensitivity dependence on the position. We are going to test LYSO crystals from two different companies. From Saint-Gobain, we have two crystals with dimensions of 30 x 30 x 100 mm^3 as well as two crystal with dimensions of 15 x 30 x 100 mm^3 and one from Epic Crystals with dimensions of 30 x 30 x 100 mm^3.

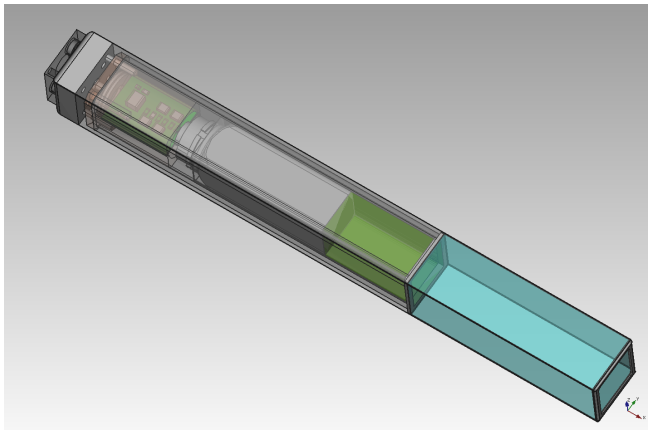

Fig. 1: Model of a LYSO crystal module with light guide, PMT and high voltage divider.

Further on, we want to test two different types of modules with the LYSO crystals: One module will consist of a LYSO crystal that is attached to a light guide. The light signal will then be converted into a charge signal using a dual channel PMT (R1548), see Fig. 1. The usage of a PMT has the advantage of long term stability - one of the main requirements of the detector [2]. A second module will contain a LYSO crystal directly coupled to a four arrays of 2x2 SiPMs (Sensl C-Series, 6 mm [3]). Table 1 summarizes the four modules. With this setting, there will be no need for a light guide and the whole module will be more compact than the first one, i.e. less than 15 cm instead of more than 30 cm. Furthermore, no high voltage source is needed for this module since the SiPMs need a supply voltage of only around 30 volts.

Both modules will be tested for their linearity over the whole signal chain and their energy resolution. First, we are going to test the modules with a proton beam of $E_{kin} = 150$MeV. Then with a deuteron beam with five different beam energies (100 MeV, 150 MeV, 200 MeV, 250 MeV and 270 MeV [2]) and investigate how precisely these energies can be reconstructed by the modules.

Module	Company	Size [mm]	Sensor
1	Saint-Gobain	30x30x100	SiPM
2	Saint-Gobain	30x30x100	PMT
3	Epic Crystals	30x30x100	PMT
4	Saint-Gobain	15x30x100 x2	PMT

Table 1: Overview of the crystals and sensors for the four detector modules.

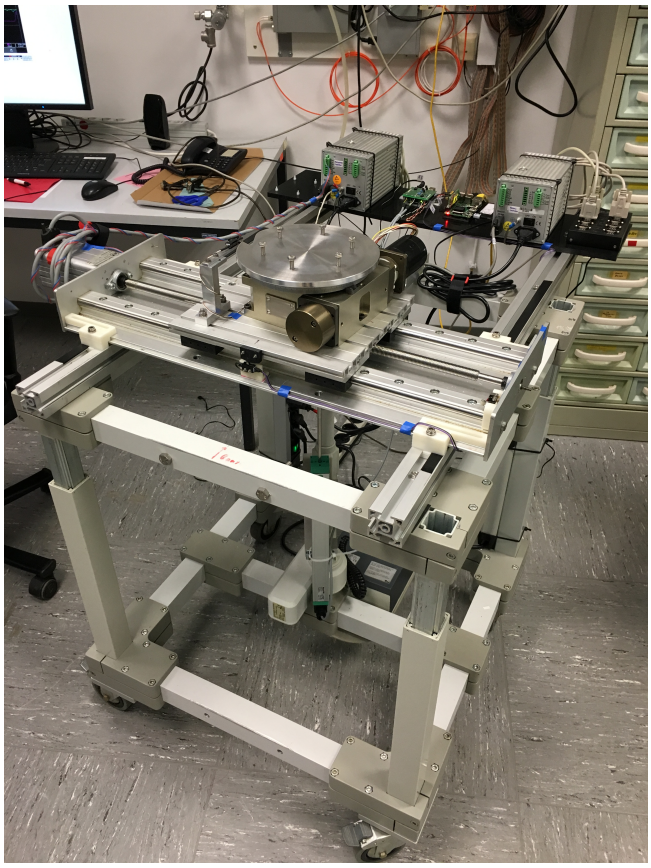

Fig. 2: Positioning table without LYSO crystal modules.

Eventually we are going to explore the position of the Bragg-peak inside the LYSO crystals. This position can be found by placing the crystals in a row and rotating them at different angles. Doing this will allow us to measure the deposited energy of the deuterons in the crystal relative to different path lengths and therefore, to reconstruct the Bragg-peak. A list of all properties which are to be measured are given below:

- Energy calibration E_{dep} vs. E_{kin}
- Energy resolution $\frac{\Delta E}{E}$
- Deuteron identification efficiency ε_d
- Linearity of the whole module

All the measurement described above require a table that can move the crystal modules in horizontal and vertical directions and rotate them to a specific angle in a horisontal plane.

Veto Modules for the LYSO Crystals

A veto scintillator is needed for two reasons: Firstly, in order to identify events where a deuteron escapes the LYSO crystal and secondly to detect break-up reactions, in which a proton escapes the crystal. For this task we are going to enclose the LYSO modules with four plastic scintillators with dimensions of 6 x 67 x 12 mm^3. All four edges are slanted which allows the attachment of a SiPM. These SiPMs are connected through coaxial cables with an amplifier circuit board that is attached directly to the scintillator. The circuit consists of individual operational amplifiers for each SiPM. Their outputs are summed by an inverting operational amplifier which acts as a line driver. The final output can be connected via a standard LEMO cable to our FADC DAQ system (SIS3316 [4]). The amplifier circuits were developed by Luca Barion and Simone Basile from the university of Ferrara, Italy.

Table and Vertical Movement

During the measurements mentioned above, LYSO modules will be exposed to the extracted COSY beam and expositions with different angles and positions will be measured. In order to achieve this, modules will be mounted on a table capable of positioning vertically, horizontally and also rotating in a horizontal plane. For these purposes the table with a manual vertical control was obtained, operated by a DC motor, and substantial modifications were performed in order to make it remotely controllable via the local area network connection.

Originally, the vertical movement system of the table did not include any feedback. In order to achieve the precise vertical positioning a linear potentiometer (LRW-M-300-S [5]) was attached to the table. It is read out by Arduino UNO board [6] which also controls the vertical movement, as shown schematically in Fig. 3. A special shield was developed and assembled for Arduino to perform the connection to the original manual controller of the table. Besides, for better positioning and also to reduce the stress on the mounted modules during start and stop operation of the vertical movements, a speed control has been also implemented. This is performed using a PWM control from one of the Arduino pins and a power MOSFET transistor (IRL2505). Due to this some modifications were introduced in the DC motor controller. However, the ability of the original (manual) control has been preserved.

The Arduino board was programmed to receive positioning commands from RaspberryPi [7] via a serial interface and adjust the vertical position of the table respectively. When the movement starts, the PWM control increases the average current through the DC motor linearly from some minimum to the maximum value in a predefined amount of time. Furthermore, when the requested position is being approached, if the distance from the final position gets less than a predefined value, speed begins to decrease linearly with the distance. The accuracy of the vertical positioning is limited by the resolution of Arduino's ADCs and is around 0.5 mm, which is more than sufficient for these measurements. When the position is reached the actual position is continuously monitored by Arduino and adjustments are performed if needed. This can be helpful in cases when the weight of the equipment, put on the table, changes. Another useful feature implemented in the Arduino code is the self-calibration procedure, which locates the minimum and maximum reachable vertical positions and the minimum PWM duty factor at which the table can still move. The latter parameter is sensitive to the table load and also the voltage of the DC motor supply (battery pack). The self calibration procedure can be initiated remotely by sending an appropriate command or locally, using the push button on the Arduino shield. Once the calibration is finished, parameters are saved in the EEPROM memory of Arduino's micro controller chip and are initialised every time the board restarts.

Horizontal Movement and Rotation

A bench with a sleigh for vertical positioning is mounted on top of the table. The sleigh is moved by screw shaft that is attached to a stepper motor. A rotatable platform that can be turned by another stepper motor is mounted on the sleigh. Each motor is managed by a stepper motor controller (Isel [8]). Neither the position of the sleigh nor the angle of the rotation platform is measured by an additional device as in the case of the vertical movement. Therefore, the position or angle are determined by counting the steps of the dedicated stepper motor. As the crystal modules mounted on top of the rotatable platform are rather lightweight, test have shown that no steps will get lost and we will be able to maintain an accuracy of less than 1 mm horizontally and 1° rotationally. The zero position of both devices is defined by a reference switch and must be found after the stepper motor controllers were powered on. For the rotation, this zero position is fixed but for the horizontal sleigh it can be adjusted by moving the ramp that presses the reference switch. The zero position of the horizontal sleigh was chosen to be at the center of the bench. This feature cannot be implemented using only the stepper motor controller and was therefore done by reading the reference switch directly by the RaspberryPi [7] which controls the whole table.

Control Hardware

Both stepper motor controller as well as the Arduino UNO [6] that manages the vertical position are controlled by a RaspberryPi. This micro-computer manages the stepper motor controller over a USB-to-serial converter hub. Arduino board is connected directly to the Pi's serial port. A level converter is needed as the RaspberryPi runs on 3.3 volts but the Arduino needs 5 volts. Furthermore, two dual-channel high voltage supplies (Iseg, NHQ206M [9]) are also connected to the serial hub and one six-channel high voltage supply (Iseg, NHS [10]) is connected directly to a USB port of Pi. These high voltage sources are needed to supply the PMTs in the detection modules.

Two laser line devices are attached to the beam pipe next two the output window. As they are mounted perpendicular to each other, the interception of both lines will indicate the position of the deuteron beam. These lasers can be turned off and on by RaspberryPi.

A second RaspberryPi is used to run a webcam software called Motion [11]. Two USB webcams are connected to this Pi in order to have visual control over the whole table system as the experimental hall will not be accesible during the beam time. A schematic overview of the control hardware is given in Fig. 3.

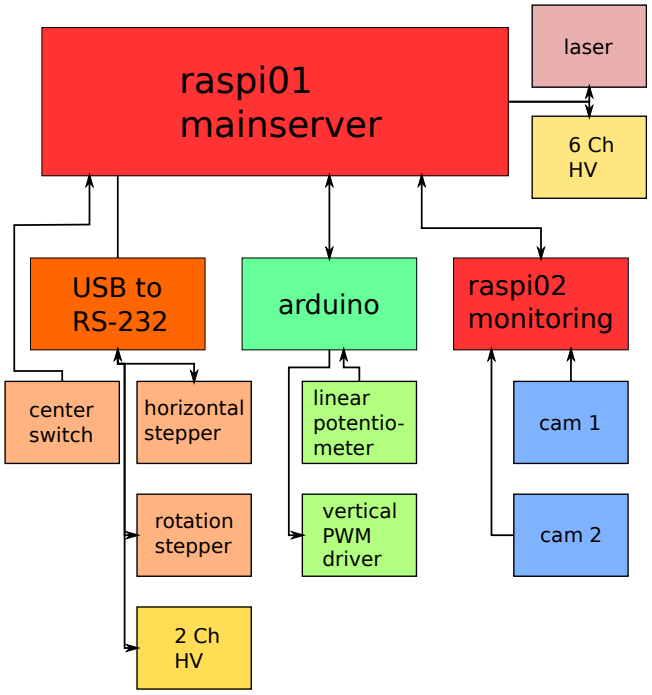

Fig. 3: Schematic figure of the hardware arrangement for the positioning table.

Slow Control Software

The slow control software consists of two main parts: A server that runs on RaspberryPi and a password protected UI which runs in a browser on any computer that has access to the internal network.
The server control is written in python. Each position controller is managed with an individual class containing all communication commands. Each command is mapped to a member function of this class and the communication with the hardware is done using the PySerial library [12]. The high voltage supplies are managed in the same way. The hardware pins on the RaspberryPi used to read the center switch of the horizontal sleigh and control the line lasers are addressed using the wiringPi library [13].
The main server program that provides the web interface for the UI implements all the controller classes and creates wrapper functions that connects button events from the UI with the communication functions of the controller classes. The main server uses the Flask micro framework [14] which provides a simple WebApp environment. A bi-directional communication between the server and the client UI is established using the Socket.IO library [15]. All position changes are broadcasted to a MQTT broker using paho-mqtt library [16]. The MQTT broker will transmit the position information to the DAQ system which will embed it in the binary files together with the data taken from the detection modules.
The client UI is done using a html structure that is styled with CSS. The functionality of the UI is written in javascript with heavy use of the JQuery library [17]. Again the event based communication with the server is done using Socket.IO. The whole UI is designed with the goal to provide a simple way to control the positioning table without any need to use the commandline. Another advantage of the web interface consist of the fact, that it can be restarted without the need of restarting the server as well.

[a] IKP FZJ, Jülich, Germany
[b] RWTH Aachen University, Germany
[c] HEPI TSU, Tbilisi, Georgia

References:

[1] http://pos.sissa.it/archive/conferences /243/026/PSTP2015_026.pdf
[2] http://collaborations.fz-juelich.de/ikp/jedi/public_files /proposals/JEDI_Polarimetry_2015_Final.pdf
[3] http://sensl.com/products/c-series/
[4] http://www.struck.de/sis3316.html
[5] http://www.waycon.de/
[6] https://www.arduino.cc/
[7] https://www.raspberrypi.org/
[8] https://www.isel.com/
[9] http://iseg-hv.com/en/products/detail/NHQ
[10] http://iseg-hv.com/en/products/detail/NHS
[11] http://www.lavrsen.dk/foswiki/bin/view/Motion/WebHome
[12] http://pyserial.readthedocs.org/en/latest/index.html
[13] http://wiringpi.com/
[14] http://flask.pocoo.org/
[15] http://socket.io/
[16] https://www.eclipse.org/paho/clients/python/
[17] https://jquery.com/

Systematic studies of spin dynamics in preparation for the precursor EDM experiment with the RF Wien filter at COSY*

A. Saleev[a] for the JEDI collaboration

The electric dipole moment (EDM) is a sensitive probe of the possible CP violation beyond the standard model. A signal of the EDM is a rotation of the spin in the electric fields which, for the charged particles, is only possible when they are confined in the storage rings. A special care must be taken to eliminate spurious signals from the rotation of the magnetic dipole moment (MDM) in the background imperfection, radial and longitudinal, magnetic fields in a ring, which is especially troublesome in the radio-frequency Wien filter (RF WF) approach to a search for the EDM at COSY.

RF Wien-filter exerts a vanishing Lorentz force on the beam and produce MDM RF spin kick with amplitude χ_{wf}. Under the resonance condition, $\nu_{wf} = \nu_s$, the RF modulation of the spin tune by RF WF would couple to the EDM interaction with the motional $\vec{E}$-field in the ring and the EDM-driven spin resonance will have a strength

$$\varepsilon = \frac{1}{2}\chi_{wf}|\vec{c}\times\vec{w}| = \frac{1}{2}\chi_{wf}\sin\xi_{edm}\,. \qquad (1)$$

Here $\vec{c} = (\sin\xi_{edm}, \cos\xi_{edm}, 0)$ is a stable spin axis which is uniform all over the ring and $\vec{w} = (0,1,0)$ is an axis of the magnetic field of the WF[1].

The misalignment of $\vec{w}$ from vertical can interfere with EDM signal and this issue is a separate task. What comes as a more substantial problem is that MDM-induced imperfection spin rotation produces a change in stable spin axis and its direction becomes location-dependent:

$$\vec{c} = c_y\vec{e}_y + (c_x(MDM) + \sin\xi_{edm})\vec{e}_x + c_z(MDM)\vec{e}_z\,, \quad (2)$$

The measurement of c_z has been done at COSY by using compensation solenoids of two e-coolers, located opposite to each other at straight sections. When the solenoids in one of the coolers are set up on a specific current J_k, they produce a spin kick $\chi_k = f_k J_k$ around longitudinal axis and create a shift of the spin tune. Calibration factors f_k are calcuated for each solenoid from measured field integrals. The spin tune can be resolved[2] with the precision of up to 10^{-10}. The experiment setup is following: vertically polarized deuterons are accelerated to $T = 270$ MeV and stored; during the beam cycle, polarization was put into the horizontal plane where it starts precessing with the spin tune $\nu_S = -0.160971917$; 20 seconds later the solenoids were switched on. In the data analysis of the spin tune, the relative shift of the spin tune $\Delta\nu_S$ has been registered, which is given by:

$$\begin{aligned}\cos\pi(\nu_S + \Delta\nu_S) = \qquad\qquad (3)\\ \cos\pi\nu_S\cos\tfrac{\chi_1}{2}\cos\tfrac{\chi_2}{2} - c_z^*\sin\pi\nu_S\sin\tfrac{\chi_1}{2}\cos\tfrac{\chi_2}{2}\\ -E\sin\tfrac{\chi_1}{2}\sin\tfrac{\chi_2}{2} - c_z\sin\pi\nu_S\cos\tfrac{\chi_1}{2}\sin\tfrac{\chi_2}{2}\end{aligned}$$

where c_z^* is longitudinal projection of spin closed orbit at location of solenoid 1 (2 MeV e-cooler), c_z at location of solenoid 2 (100 KeV e-cooler), $E \simeq 1$. The set of measurements for fixed spin kick by sol. 1 w.r.t. different spin kicks by sol. 2 is shown in Fig. 1. The mesh of $i \times j$ points when the solenoids are set up on different currents gives a spin tune map $\Delta\nu_s(\chi_1^i, \chi_2^j)$. Fitting the data points to function (3) gives the values of $c_z^* = -0.002691978 \pm 6.09 * 10^{-7}$ and

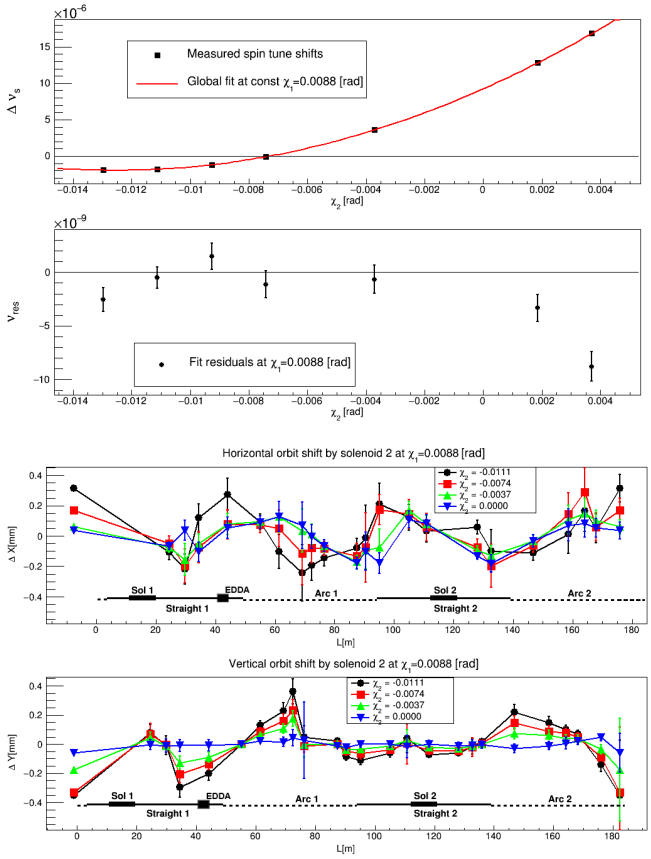

Fig. 1: Top to bottom: spin tune shifts $\Delta\nu_s(\chi_1,\chi_2)$ and global fit (red); fit residuals $\nu_{res} = \nu_s^{fit} - \nu_s^{data}$; horizontal and vertical orbit shifts alolng the ring w.r.t. spin kick χ_2.

$c_z = -0.002244980 \pm 6.30 * 10^{-7}$, with fit χ-sqrd $\simeq 13$. In the fit we also make an allowance for the mis-calibration of the spin kick in the solenoid, $\chi \to g_k\chi_0$, which guages the initially assumed field integral and corresponding f_k. Fit gives $g_1 = 0.9962245 \pm 3.45 * 10^{-5}$, $g_2 = 0.9943927 \pm 6.98 * 10^{-5}$. Analysis of possible systematic effects coming from the changes of closed orbit (see Fig. 1, bottom) produced by the solenoids in both vertical and horizontal planes is ongoing. The orbit shift and resulting changes in the configuration of imperfection fileds all over the ring contributes to the deviation of each measured $\Delta\nu_s(\chi_1^i, \chi_2^j)$ from the fit function (see residuals ν_{res} in Fig 1.). During JEDI beamtime at September 2014, two spin tune maps have been measured, with time span 24 hours. The values c_z, c_z^* are consistent for both maps.

References:

[1] F. Rathmann et al., *J. Phys.: Conf. Ser.* **012011**, 447 (2013).

[2] D. Eversmann et al. (JEDI), *Phys. Rev. Lett.***115**, 094801 (2015).

[a] Institut für Kernphysik, Forschungszentrum Jülich, Germany, and Landau Institute, Chernogolovka, Russia.

* supported by the COSY–FFE program under contract number COSY-125.

Closed orbit influencing effects at COSY

V. Schmidt[a,b] and A. Lehrach[a,b,c] for the JEDI collaboration

With regard to the precursor experiments [1] at the Cooler Synchrotron (COSY), a precise measurement and control of the orbit of the particle beam is necessary. Since misalignments of the quadrupoles in the ring affect not only the particle motion but also the spin motion due to additional radial fields, they play a major role in the search of an EDM[1]. To distinguish between these fake signals and real EDM contributions, the fake signals caused by positioning misalignments have to be smaller than the actual contribution of the EDM. The smaller the misalignments and therefore the RMS[2] of the vertical orbit displacements, the smaller fake EDM signals are produced. Gaussian distributed misalignments with a standard deviation of 0.1 mm lead to an RMS of vertical displacement of around 1 mm which corresponds to an EDM of $d \approx 5 \cdot 10^{-19}$ e·cm[2]. With the current set-up of COSY, a vertical orbit displacement in the order of 2 mm [3] is measured. To achieve a decrease of the deposition of the particle beam, external influences on the beam have to be investigated and changes of the current orbit control system have to be considered. Analysis of the influence of several sources of misalignments give indication of the required set-up for the precursor experiments.

The expected positioning accuracy of the elements of COSY is a misalignment within 0.1 mm in each direction and a rotation of 0.1 mrad around each axis.

Taking the current lattice of COSY and implementing the expected positioning errors to all quadrupoles and dipoles leads to a RMS of the vertical closed orbit in the order of 1 mm. The errors are gaussian distributed for every element and different random seeds where used in the simulation. Figure 1 shows the uncorrected orbit in x and y direction.

After the performance of the orbit correction implemented in MAD-X [4], the orbit reduces to a RMS in the order of 0.1 mm (Figure 2). The orbit correction was achieved using the method of Singular Value Decomposition (SVD)[5].

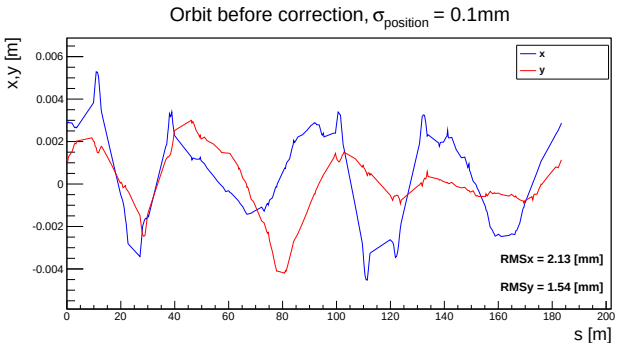

Fig. 1: Simulated vertical orbit before orbit correction with gaussian positioning errors of 0.1 mm/0.1 mrad; RMS in x:2.1 mm, RMS in y: 1.5 mm

After correction the RMS of the vertical displacement has decreased by one order of magnitude. Comparing the simulation results with the measured orbits at COSY, there is a large discrepancy between the sizes of the vertical orbits. The

[1] Electric Dipole Moment

[2] Root Mean Square

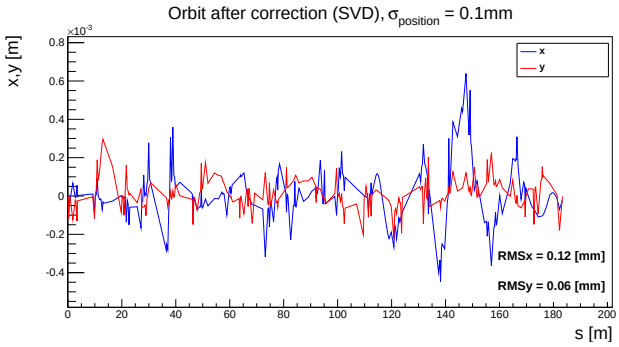

Fig. 2: Simulated vertical orbit after orbit correction; RMS in x: 0.12 mm, RMS in y: 0.06 mm

RMS of the orbit deviation of the measured orbit after correction is still in the order of 1 mm. One possible explanation for the difference between simulation and measurement are larger positioning errors of the elements than expected. The expectation of having all elements positioned within 0.1 mm (and 0.1 mrad respectivley) is based on the minimum achievable value when doing a full survey of the ring. To ensure a positioning accuracy in the expected range, a survey at COSY is planned to be done soon.

Besides the positioning accuracy of the elements in the ring, there are other effects influencing the beam which have to be analysed as a next step. As the fields of all magnets are directly influenced by the ripple [3] of their power supplies, an estimate has do be done for the use of the current power supplies in the precursor experiment and the need of changes in the orbit control system have to be investigated.

References:

[1] A. Lehrach, B. Lorentz, W. Morse, Precursor Experiments To Search For Permanent Electric Dipole Moments (EDMs) of Protons and Deuterons at COSY, 2011

[2] M. Rosenthal, A. Lehrach, Spin Tracking Simulations Towards Electric Dipole Moment Measurements at COSY, in Proceedings 6th International Particle Accelerator Conference, IPAC15, Richmond, VA, USA (2015), http://jacow.org/IPAC2015/papers/thpf032.pdf

[3] F. Hinder, M. Rosenthal, F. Trinkel, Beam Position Monitors at COSY, 2015

[4] Methodical Accelerator Design, http://mad.web.cern.ch/mad/

[5] Y. Chung, G. Decker, K. Evans, Closed Orbit Correction Using Singular Value Decomposition of the Response Matrix, 1993

[a] Institute for Nuclear Physics IV , FZ Jülich, Germany

[b] Physics Institute III B, RWTH Aachen University, Germany

[c] JARA-FAME

[3] Residual oscillation

Beam and Spin Dynamics in an RF Wien-Filter

Sebastian Mey*† and Ralf Gebel* for the JEDI Collaboration

1 Setup of the RF Wien-Filter

For measurements of permanent EDMs (**E**lectric **D**ipole **M**oments) of charged, light hadrons in dedicated storage rings, a technique, which requires a spin tune modulation by an RF Dipole without inducing any coherent beam oscillations, has been proposed [1].
In the course of 2014 and 2015, a prototype RF (**R**adio-**F**requency) Dipole with perpendicular electric and magnetic fields has been successfully commissioned and tested at COSY [2][3]. With careful adjustments of the amplitudes of the radial magnetic and vertical electric field, a field configuration, where the *Lorentz* force onto the revolving particles in the synchrotron ring cancels out, can be achieved. The desired field configuration forms a velocity filter named after its inventor, *Wilhelm Wien* [4].
The magnetic dipole field for the desired *Wien*-Filter field combination is generated by means of a coil wound lengthwise around a ceramic part of the beam-pipe. Ferrite blocks bundle the field lines and flatten the transverse field distribution. To generate an oscillating field, the coil is connected to an adjustable, parallel resonance circuit with a quality factor of $Q \approx 20$. A similar, but separate resonance circuit drives the electric RF Dipole. The electric field is generated by the potential difference between two stainless steel electrodes inside the vacuum chamber, spanned over glass rods held by a frame inside the flanges of the ceramic beam-chamber. For details see Fig.1.

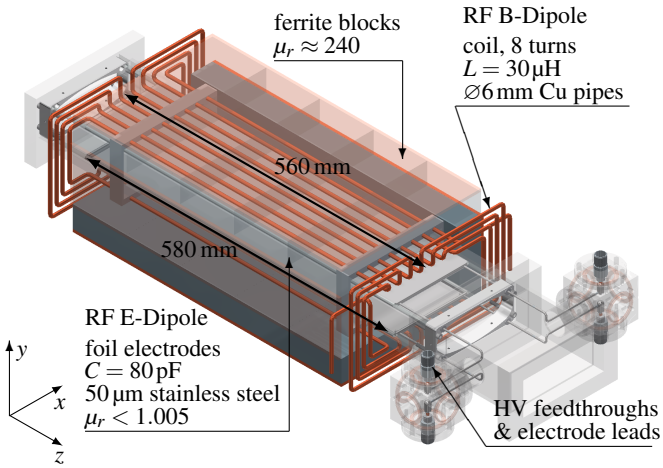

Fig. 1: A view inside the RF ExB-Dipole.

The coil itself is water cooled and fans dissipate the remaining lost power. Therefore, it is possible to run the system up to 90 W input power in continuous, long term operation. The corresponding operating parameters have been collected in Table 1.

2 Beam Dynamics

Figs. 2a and 2b show that the transverse distribution of the main field components is flat across the center of the beam chamber. But due to different drop-off rates of the electric and magnetic field, particles will encounter a down-up kick at the entrance and a corresponding up-down kick at the exit of the *Wien*-Filter. The geometry has been optimized insofar that particles with the reference momentum of 970 Mev/c, entering the system on axis, won't get any vertical excursion, as shown in Fig. 2c. Particles off momentum will probe different *Lorentz* forces, leading to a slight spread in vertical beam size in the order of 20 nm for an energy spread of $\Delta\gamma/\gamma = 10^{-4}$. The main field asymmetry stems from the feeds to the coil and the electrodes. They give a small horizontal kick, which steers the particles ≈ -40 nm off axis 1 m behind the device center.
For comparison, Fig: 3 shows the phase space distribution of particles at the location of the RF Wien-Filter, calculated using the beam optics functions from the September 2014 and May 2015 JEDI beam-times. Considering a normalized

	RF B-Dipole	RF E-Dipole
$\hat{U}$		2 kV
$\int \hat{E}_y \, dl$		24.1 kV
$\hat{I}$	5 A	
$\int \hat{B}_x \, dl$	0.175 T mm	
f_{RF} range	630 kHz to 1170 kHz	630 kHz to 1060 kHz

Table 1: The RF ExB-Dipole at 90 W RMS input power.

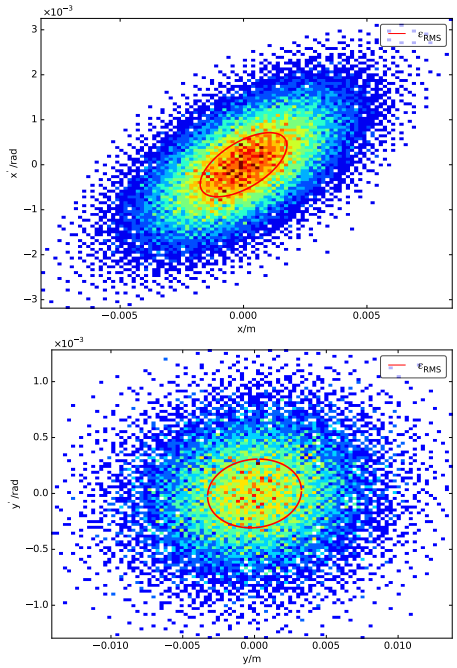

Fig. 3: Horizontal and vertical phase-space distribution in the center of the RF Wien-Filter with the RMS emittance ellipse.

R.M.S. emittance of $\varepsilon \approx 1\,\pi$mm mrad, which is typical for a well cooled deuteron beam at COSY, one gets an estimate for the beam size at the location of the RF ExB-Dipole.

$$\beta_x = 4.1\,\text{m} \;\Rightarrow\; \langle x \rangle = \sqrt{\varepsilon \beta_x} = 2.0\,\text{mm} \tag{1}$$

$$\beta_y = 21.1\,\text{m} \;\Rightarrow\; \langle y \rangle = \sqrt{\varepsilon \beta_y} = 3.9\,\text{mm}. \tag{2}$$

*IKP, Forschungszentrum Jülich GmbH, Germany
†III. Physikalisches Institut B, RWTH Aachen, Germany

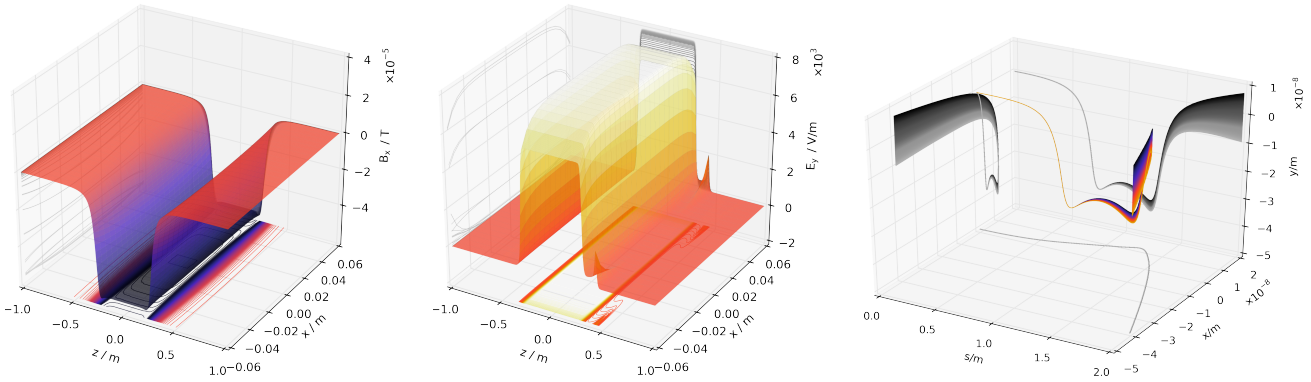

(a) $\hat{B}_x$ across the center of the beam-pipe. (b) $\hat{E}_y$ across the center of the beam-pipe. (c) Trajectories for deuterons passing through the ExB field distribution.

Fig. 2: Simulation of the main field components generated by the RF ExB-Dipole, normalized to an RF B current amplitude of 1 A. The right panel shows the result of particle tracking through these fields. The Deuterons have been initialized on the reference orbit ($x_0 = y_0 = 0\,\mathrm{mm}$, $x'_0 = y'_0 = 0\,\mathrm{rad}$).

Since the field strengths are small in the first place and the *Lorentz* force onto the particles is canceled out in average, the beam disturbance of the RF *Wien*-Filter is 5 orders of magnitude below these beam size estimates.

3 Spin Dynamics

The system has been tested with spin manipulation on a vertically polarized deuteron beam. Plugging the *Lorentz* force cancellation into the *Thomas-BMT* Equation [5] yields a simple formula for the spin precession frequency $\vec{\Omega}$ in an ideal *Wien*-Filter [6].

$$\vec{F}_\mathrm{L} = q\left(\vec{E} + c\vec{\beta}\times\vec{B}\right) \stackrel{!}{=} 0 \quad \Rightarrow \quad \vec{\Omega}_\mathrm{WF} = \frac{q}{\gamma m}\frac{1+G}{\gamma}\vec{B} \quad (3)$$

The particles sample the localized RF field distribution (see Figs. 2a,2b) once every turn n. Its contribution can be approximated by the integrated field along the particles path assigned to a point-like device at an orbital angle θ:

$$b(\theta) = \int \hat{B}_x \mathrm{d}l \cos\left(\frac{f_\mathrm{RF}}{f_\mathrm{rev}}\theta + \phi\right) \sum_{n=-\infty}^{\infty} \delta(\theta - 2\pi n). \quad (4)$$

The field integrals of a deuteron beam as used during the JEDI beam-times are shown in Fig. 4. For a realistic beam with momentum and velocity spread as shown in Fig. 3, each particle will sample slightly different field strengths but, for the main field components $\hat{B}_x$ and $\hat{E}_y$, the resulting distribution of the field integrals is very narrow with a standard deviation three orders of magnitude of its mean value. The particles spread out across the phase space will mainly pick up different fringe field components. Since the unwanted field components are small, two orders of magnitude below the main field in case if the magnetic field and tree orders of magnitude below for the main electric field component, equation 4 is a good approximation for the determination of the spin motion in the RF *Wien-Filter*.

The resonance strength ε of this field configuration is given by the amount of spin rotation inside the device per turn. In the absence of RF induced coherent beam beam motion, it solely depends on the strength of the RF field. In this case, it can be calculated by the *Fourier* integral for spin kicks in many consecutive turns [7, 8]:

$$\begin{aligned}\varepsilon_K &= \frac{\Omega_\mathrm{WF}}{\Omega_\mathrm{rev}} = \frac{1+G}{2\pi\gamma}\oint \frac{b(\theta)}{B\rho} e^{iK\theta}\,\mathrm{d}\theta \\ &= \frac{1+G}{4\pi\gamma}\frac{\int \hat{B}_x\,\mathrm{d}l}{B\rho}\sum_n e^{\pm i\phi}\delta\left(n - K \mp \frac{f_\mathrm{RF}}{f_\mathrm{rev}}\right). \end{aligned} \quad (5)$$

If the RF *Wien*-Filter is operated on a harmonic of the spin tune in the storage ring, the spin kicks induced by the radial magnetic field add up and introduce an additional, continuously rotation of the particles' spins around the magnetic field's axis. For deuterons with a momentum of 970 MeV/c the spin tune is $\nu_S \approx \gamma G = -0.1609$. This gives resonance side-bands at

$$f_\mathrm{RF} = f_\mathrm{rev}|n - \gamma G| = \begin{cases} 630\,\mathrm{kHz\ for}\ n = 1 \\ 871\,\mathrm{kHz\ for}\ n = -1 \end{cases} \quad (6)$$

Both are available for studies inside the frequency range of the RF *Wien*-Filter. Resonance strength measurements have been performed during the September 2014 and May 2015 JEDI beam-times at COSY. The driven spin rotation was detected by observing the vertical component of a polarized deuteron beam as an left-right asymmetry in the angular distribution in $^{12}\mathrm{C}(\vec{\mathrm{d}},\mathrm{d})$ [9]. The resulting oscillation frequency of the rate-asymmetry in the four-quadrant polarimeter detector was measured[10] and is directly proportional to the resonance strength in Eq. 5.

Comparison measurements were performed between the RF ExB-Dipole in *Wien*-Filter-mode, the RF ExB-Dipole operated without compensating electric field as a pure RF B-Dipole and with only the electric field switched on as a pure RF E-Dipole and with an already installed RF Solenoid. By modifying the strengths of two of the main quadrupole families in the synchrotron, the fractional vertical betatron tune q_y is shifted and the betatron oscillation frequency is moved farther or closer to the frequency of the RF systems, thereby varying the degree of induced coherent beam oscillations.

Fig. 5 shows, that, as for an RF Solenoid, the RF *Wien*-Filter resonance strength is independent of the vertical betatron tune. In contrast, the resonance strength of the pure RF dipoles is dominated by the interference between the driven spin motion and the one induced by coherent beam oscillations. Experimentally, this effect was already observed by

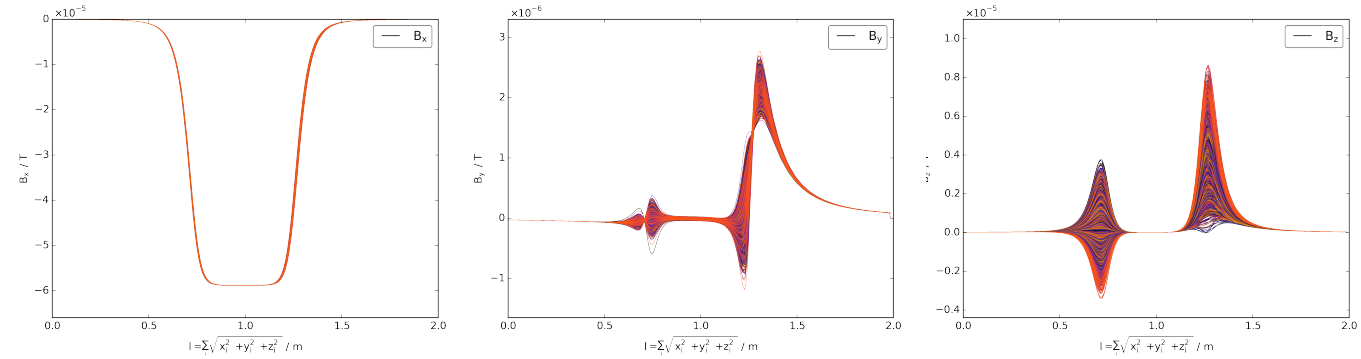

(a) $\int \hat{B}_x \mathrm{d}l = -3.479 \cdot 10^{-5}\,\mathrm{T\,m}$, $\sigma_{\int \hat{B}_x \mathrm{d}l} = 0.005 \cdot 10^{-5}\,\mathrm{T\,m}$

(b) $\int \hat{B}_y \mathrm{d}l = 4.14 \cdot 10^{-7}\,\mathrm{T\,m}$, $\sigma_{\int \hat{B}_y \mathrm{d}l} = 0.07 \cdot 10^{-7}\,\mathrm{T\,m}$

(c) $\int \hat{B}_z \mathrm{d}l = 7.2 \cdot 10^{-7}\,\mathrm{T\,m}$, $\sigma_{\int \hat{B}_z \mathrm{d}l} = 0.4 \cdot 10^{-7}\,\mathrm{T\,m}$

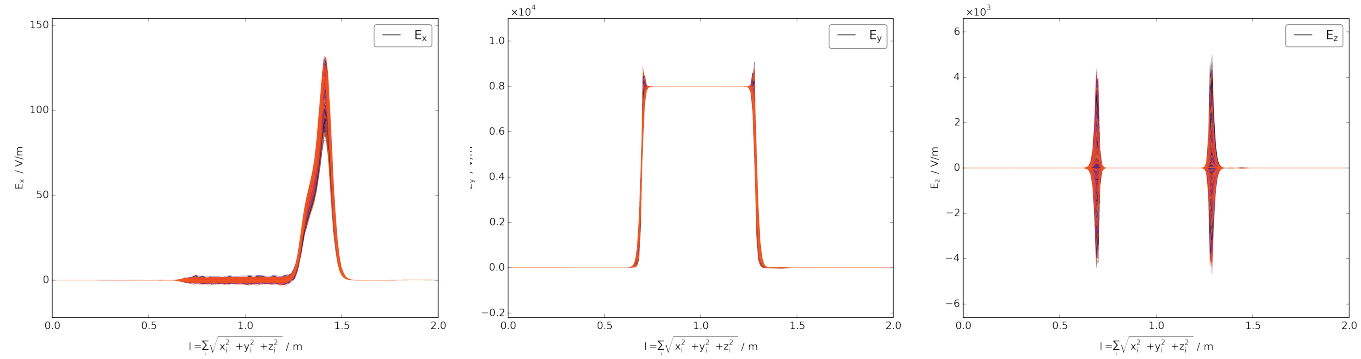

(d) $\int \hat{E}_x \mathrm{d}l = 13.0\,\mathrm{V}$, $\sigma_{\int \hat{E}_x \mathrm{d}l} = 0.6\,\mathrm{V}$

(e) $\int \hat{E}_y \mathrm{d}l = 4793\,\mathrm{V}$, $\sigma_{\int \hat{E}_y \mathrm{d}l} = 7\,\mathrm{V}$

(f) $\int \hat{E}_z \mathrm{d}l = 0.002\,\mathrm{V}$, $\sigma_{\int \hat{E}_z \mathrm{d}l} = 2.000\,\mathrm{V}$

Fig. 4: Amplitudes of the electromagnetic field components of the RF *Wien*-Filter, evaluated along each particles trajectory for a beam set up as shown in Fig. 3. The captions show the mean of all individually integrated trajectories and its standard deviation.

experiments with resonance strength measurements by the SPIN@COSY Collaboration [11]. A constant fit to the mea-

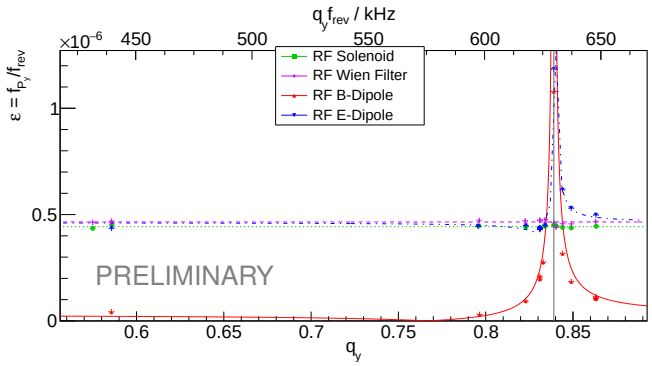

Fig. 5: Results of the resonance scans at the nominal tune of COSY at $q_y = 0.56$ and for a set of vertical betatron tunes with sideband frequencies around the spin resonance at, depicted by the vertical line at 629 777.3 Hz.

surements of the RF *Wien*-Filter gives a resonance strength of
$\varepsilon = (4.65 \pm 0.04) \cdot 10^{-7}$ for the measured current amplitude of $\hat{I} = (0.740 \pm 0.005)\,\mathrm{A}$. The resulting normalized effective field strength of the system agrees well with the estimate from the field simulations (see figure 4)

$$\frac{\int \hat{B}_x \mathrm{d}l}{\hat{I}} = \varepsilon \frac{4\pi\gamma}{1+G} \frac{B\rho}{\hat{I}} = (3.40 \pm 0.05) \cdot 10^{-5}\,\mathrm{Tm/A}. \quad (7)$$

4 Conclusion

As a preparation for future EDM experiments in storage rings, a first prototype of an RF *Wien*-Filter has been commissioned at COSY. We have shown, that this device generates a configuration of RF dipole fields which allow spin manipulation in a storage ring without beam disturbance.

References:

[1] W. M. Morse, Y. F. Orlov and Y. K. Semertzidis, *Phys. Rev. ST Accel. Beams* **16**, 114001 (2013).

[2] Institut für Kernphysik/ COSY *Juel-4381* (2013).

[3] Institut für Kernphysik/ COSY *Juel-4367* (2014).

[4] W. Wien, *Annalen der Physik* **301.6** 440-452 (1998).

[5] V. Bargmann, L. Michel, and V. L. Telegdi, *Phys. Rev. Lett.* **2**, 435 (1959).

[6] N. N. Nikolaev, `http://www.bnl.gov/edm/files/pdf/NNikolaev_Wien_RFE.pdf`*D*uality of the MDM-transparent RF-E Flipper to the EDM transparent RF Wien-Filter at all Magnetic Storage Rings (2012).

[7] M. Bai, W. W. MacKay, and T. Roser, *Phys. Rev. ST Accel. Beams* **8**, 099001 (2005).

[8] S. Y. Lee, *Phys. Rev. ST Accel. Beams* **9**, 074001 (2006).

[9] G.G. Ohlsen and P.W. Keaton, Jr., *NIM* **109**, 41-59 (1973).

[10] Z. Bagdasarian et al., *Phys. Rev. ST Accel. Beams* **17**, 052803 (2014).

[11] A. D. Krisch, *Phys. Rev. ST Accel. Beams* **10**, 071001 (2007).

Extension of COSY Toolbox for the Analysis of the Final Electric Dipole Moment Storage Ring

A. Skawran[a,b] and A.Lehrach[a,b,c] for the JEDI Collaboration

The investigation of the permanent electric dipole moment (EDM) of charged subatomic particles requires a new storage ring. The plan is to use a horizontal polarised beam where the motion of the spin is described by the Thomas-Bargmann-Michel-Telegdi equation [1]:

$$\frac{d\vec{s}}{dt} = \vec{s}\times\vec{\Omega}_{MDM} + \vec{s}\times\vec{\Omega}_{EDM} \tag{1}$$

$$\vec{\Omega}_{MDM} = \frac{q}{\gamma m}\left[(1+G\gamma)\vec{B} - \frac{G\gamma^2}{\gamma+1}\vec{\beta}(\vec{B}\cdot\vec{\beta}) - \left(G\gamma+\frac{\gamma}{\gamma+1}\right)\vec{\beta}\times\vec{E}\right] \tag{2}$$

$$\vec{\Omega}_{EDM} = \frac{\eta}{2\gamma m}\left[\vec{E} - \frac{\gamma}{\gamma+1}\vec{\beta}(\vec{\beta}\cdot\vec{E}) + \vec{\beta}\times\vec{B}\right]. \tag{3}$$

Where $\vec{\Omega}_{MDM}$ describes the angular frequency of a magnetic dipole moment and $\vec{\Omega}_{EDM}$ the counterpart for the EDM. One lattice concept is the so called frozen-spin method [2] where the contribution of $\vec{\Omega}_{MDM}$ is eliminated to zero by a matching set up of the magnetic and electric fields inside electro magnetic deflectors (E×B deflectors). An existing EDM would be measured by a vertical build-up of the polarisation.
Thus spin tracking simulations must be executed to determine the influences of the ring parameter on the desired frozen-spin condition and the sources of misleading artificial build-ups of vertical polarisation.
COSY Toolbox (COTOBO) [3] is a C++ based framework which enables the powerful interaction between COSY INFINITY [4] and ROOT [5] to handle efficient spin tracking simulations and analysis. Some extensions have to be included to exploit the available COTOBO for the frozen-spin simulations.

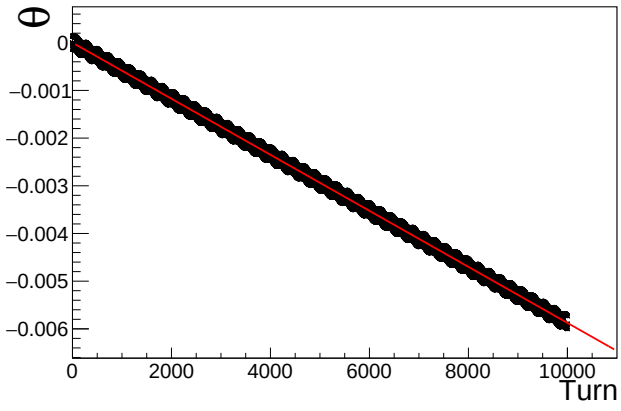

Fig. 1: Change of the polarisation orientation θ depending on the turn number n for a sample ring with $r = 30\,\mathrm{m}$ and deuterons with $p = 1\,\mathrm{GeV}$. In this example $\nu = -5.9\times10^{-7}$.

At first E×B deflectors are needed. Thus the element Wien Filter from COSY INFINITY, containing the desired properties, is included in the class Wien for E×B deflectors with homogeneous fields and in WienMultipole for inhomogeneous fields. Furthermore classes are developed to calculate automatically the parameters for the lattice design. The required parameters for the calculations are the desired energy, bending radius of the ring and the particle properties mass, charge and the anomalous magnetic moment G.
Two main quantities characterize the fulfilment of the frozen-spin conditions. At first the spin tune ν and furthermore the spin coherence time τ_{SCT} [6]. The spin tune for the reference particle can be calculated by COSY INFINITY but not for the simulated phase space distribution.
Therefore the mean polarisation orientation in the horizontal plane of the simulated beam for each turn is calculated. Assuming a linear change of the orientation θ with respect to the beam direction depending on the turn number n results in

$$\theta(n) = \theta_0 + \nu\cdot n \tag{4}$$

as displayed in Fig. 1. Similar is the description of the spread σ of the distribution of the polarisation orientation in the horizontal plane (compare Fig. 2).

$$\sigma(t) = \sigma_0 + \alpha\cdot t. \tag{5}$$

Defining a maximum acceptable spread $\sigma_{SCT} = 1\,\mathrm{rad}$ for the

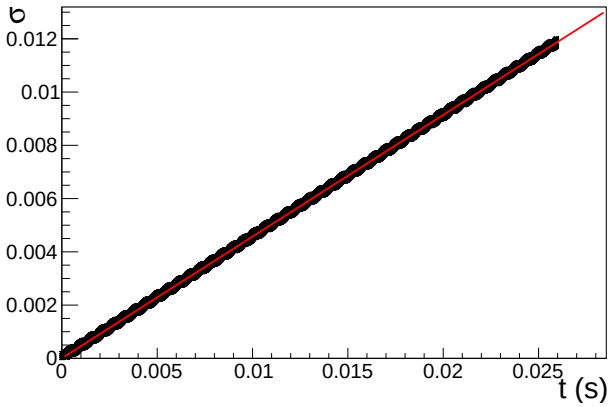

Fig. 2: Development of the polarisation spread σ depending on the beam time for a sample ring with $r = 30\,\mathrm{m}$ and deuterons with $p = 1\,\mathrm{GeV}$. In this example $\tau_{SCT} = 2.2\,\mathrm{s}$.

distribution the spin coherence time can be calculated by

$$\tau_{SCT} = \frac{\sigma_{SCT} - \sigma_0}{\alpha} \tag{6}$$

Thus COTOBO includes now new tools to analyse and to optimise the desired lattice and can support the decision for the final structure of the lattice.

[a] Institut fur Kernphysik 4, FZ Jülich, Germany
[b] Physics Inst. III B, RWTH Aachen University, Germany
[c] JARA-FAME

References:

[1] Fukuyama, T., et al. "Derivation of generalized Thomas-Bargmann-Michel-Telegdi equation for a particle with electric dipole moment." International Journal of Modern Physics A 28.29 (2013): 1350147.

[2] Pretz, J., and JEDI collaboration. ”Measurement of permanent electric dipole moments of charged hadrons in storage rings.” Hyperfine Interactions 214.1-3 (2013): 111-117.
[3] Rosenthal, M. IKP Annual Report, (2014)
[4] Makino, K., et al. ”COSY INFINITY version 9.” Nuclear Instruments and Methods in Physics Research Section A: Accelerators, Spectrometers, Detectors and Associated Equipment 558.1 (2006): 346-350.
[5] Brun, R, and Rademakers, F.. ”ROOT - an object oriented data analysis framework.” Nuclear Instruments and Methods in Physics Research Section A: Accelerators, Spectrometers, Detectors and Associated Equipment 389.1 (1997): 81-86.
[6] Anastassopoulos, V., et al. ”A storage ring experiment to detect a proton electric dipole moment.” arXiv preprint arXiv:1502.04317 (2015).

A candidate layout for the JEDI polarimeter

P. Maanen[a] for the JEDI Collaboration

The proposed method for a search for an Electric Dipole Moment of charged particles consists of storing the particles in a storage ring and letting the charged particles interact with a radial electric field. Starting with a horizontally polarized beam, the EDM signal would be a vertical polarization build-up. If the EDMs of deuteron and proton are in the order of 10^{-29}e·cm, the polarization build-up due to the EDM is in the order of nrad/s. Assuming a horizontal polarization lifetime of 1000 s, this means the vertical polarization to be detected is in the order of 10^{-5}.
For the polarization measurement, nuclear scattering which uses spin-dependent asymmetries in the nuclear scattering cross section to measure the beam polarization was chosen. A vertical polarization is associated with a left-right asymmetry in the scattering cross section while a longitudinal polarization leads to an up-down asymmetry.

Polarimeter design goals

To achieve the necessary precision, the EDM polarimeter should achieve the following goals:

- Large statistical figure of merit
- Minimal influence on the beam
- High sensitivity to systematic effects
- Good long term stability and reproducibility
- Simple concept

The statistical figure of merit of a polarimeter is defined as $\mathcal{F} = \sigma \cdot A_y^2$ which means to maximize the statistical accuracy of a polarimeter one has to simply choose the process with the highest possible cross section and analyzing power. The influence on the beam should be minimal because even the slightest pertubation can influence the beam on a noticeable level. In the past it has been demonstrated that it is possible to control the systematic uncertainties to the 10^{-6} level by calibration of the detector by inducing large errors in the beam and measuring the variation of the output [1].

Target material

Different target materials have been evaluated for their applicability as a polarimetry target. Carbon has been chosen as the most suitable candidate. Figure 1 the differential FOM for Deuteron-Carbon and Proton-Carbon elastic scattering are shown. As one can clearly see, the differential Figure of Merit for both the deuteron-carbon and proton-carbon scattering is heavily concentrated in the forward direction. This should allow one to use the same polarimeter for both proton and deuteron EDM measurements.

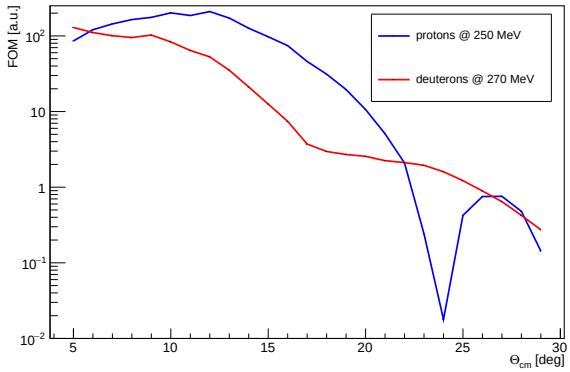

Figure 1: red: Differential FOM for Deuteron-Carbon scattering at $T_d = 270$ MeV [2] blue: The same quantity for Proton-Carbon scattering at $T_p = 250\,\mathrm{MeV}$[3].

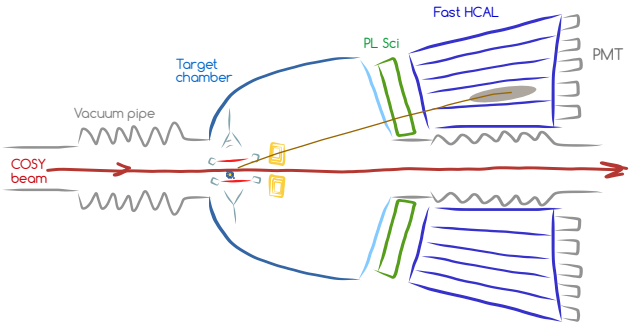

Figure 2: The current JEDI candidate detector concept.

Target type

In principle, many different target types are available for use. Solid State Targets in general are easier to handle than cluster and gas targets and target densities in the order of magnitude of $10^{20}\,\mathrm{cm}^{-2}$ are easily achievable. Cluster targets can achieve target densities of up to $10^{14}\,\mathrm{cm}^{-2}$ - $10^{15}\,\mathrm{cm}^{-2}$. The target currently used for R&D measurements is a carbon slab with several cm in thickness. For extraction the beam is placed close to the target and then heated by application of white noise [4]. Recently, a research has begun to develop a new type of target that uses small diamond pellets to continuosly extract the beam without needing external electrical fields [5].

Detector concept

The current candidate concept is shown in figure 2. It envisions a segmented plastic scintillator to measure the direction of the outgoing particles and a fast hadronic calorimeter to stop the particles and provide a accurate energy measurent of the particle to select only elastically scattered particles. The material cur-

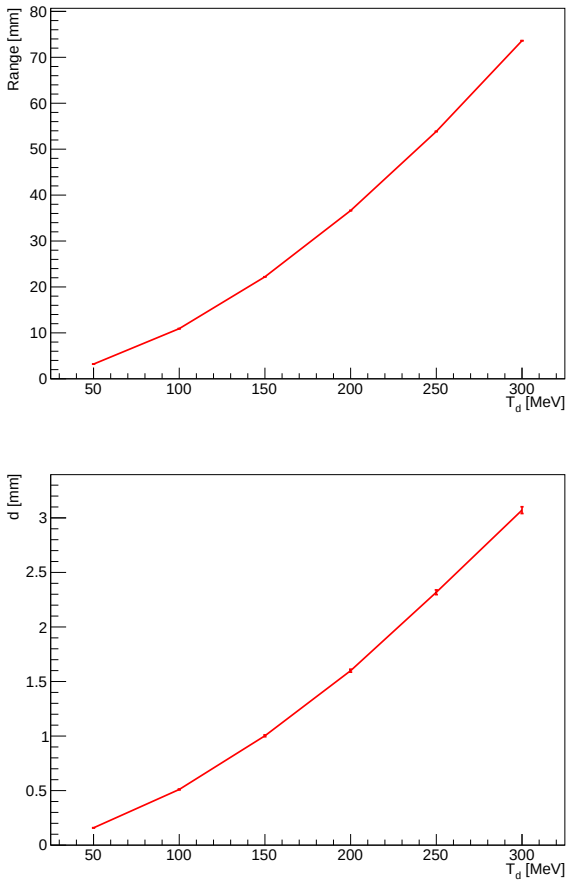

Figure 3: top: Range of deuterons in LYSO for different deuteron kinetic energies. bottom: Average displacement in x-direction of deuterons for the same energies.

rently under evalution is the anorganic scintillator LYSO $Lu_{1.8}Y_{0.2}SiO_2(Ce)$. Figure 3 shows the range and lateral displacement of an incoming deuteron beam in LYSO for different deuteron energies. As can be seen, a crystal of around 100 mm length and 10 mm − 30 mm width is able to completely absorb an incoming deuteron beam. Accordingly, LYSO crystals of the sizes $30\times30\times100\,\mathrm{mm}^3$ and $15\times30\times100\,\mathrm{mm}^3$ have been ordered and are unter investigation. Hardware tests with cosmic muons have demonstrated an energy of $\mathcal{O}(20\%)$ are achievable [6].

Conclusion

A detector concept has been chosen and Monte-Carlo simulations and prototype measurements are ongoing to further refine the components for the polarimeter. First test measurements with deuterons are planned for the March 2016 beam time.

[a]RWTH Aachen University, Germany
[b]IKP FZJ Germany

References

[1] BRANTJES, N. et al., Nuclear Instruments and Methods in Physics Research Section A: Accelerators, Spectrometers, Detectors and Associated Equipment **664** (2012) 49 .
[2] SATOU, Y. et al., Phys. Lett. B **549** (2002) 307 .
[3] MEYER, H. O. et al., Phys. Rev. C **37** (1988) 544.
[4] EVERSMANN, D. et al., Phys. Rev. Lett. **115** (2015) 094801.
[5] KESHELASHVILI, I., Jülich ballistic diamond pellet target for storage ring edm measurements, 2016.
[6] DZIWOK, C., Characterisation of a lyso scintillation detector for the jedi project, fz jülich, Bachelor's thesis, RWTH Aachen, 2015.

Automation of the Orbit Response Matrix Measurement at COSY

F. Hinder[a,b], B. Lorentz[a], M. Rosenthal[a,b] and M. Simon[a]
for the JEDI collaboration & the COSY Beam-Instrumentation-Group

The ambitious goal of a measurement of Electric Dipole Moments (EDMs) of elementary particles at the storage ring COSY (COoler SYnchrotron) requires a precise and reliable closed orbit correction. Simulations of the planned measurement method using an radio frequency Wien filter show, that a closed orbit correction is a crucial tool to lower systematic errors of an EDM measurement [1]. A model independent orbit correction is possible by using an Orbit Response Matrix (ORM). Such an ORM describes the linear response of the closed orbit at each Beam Position Monitor (BPM) to a change of each corrector magnet. A new measurement method, developed for COSY, is presented.

The ORM M is defined by:

$$\begin{pmatrix} \vec{x} \\ \vec{y} \end{pmatrix} = M \cdot \begin{pmatrix} \vec{\theta}_x \\ \vec{\theta}_y \end{pmatrix}, \tag{1}$$

where $\vec{x}, \vec{y}$ are the measured beam positions at the horizontal and vertical BPMs, respectively. The variables $\vec{\theta}_x, \vec{\theta}_y$ are the deflection angles at the horizontal and vertical correctors. For an uncoupled linear machine the ORM simplifies to a block diagonal matrix . The matrix entries for the vertical (y) block are given by [2]:

$$M_{ij} = \frac{\sqrt{\beta_i \beta_j}}{2\sin(\pi\nu)} \cos\left(\left|\phi_i - \phi_j\right| - \pi\nu\right). \tag{2}$$

These matrix entries are defined by the beta functions β at the elements i and j, the difference of the phase advance ϕ between both elements and the tune ν. The corresponding entries for the horizontal block matrix have to be modified by a dispersion term:

$$M_{ij} = \frac{\sqrt{\beta_i \beta_j}}{2\sin(\pi\nu)} \cos\left(\left|\phi_i - \phi_j\right| - \pi\nu\right) + \frac{D_i D_j}{\eta L_0}, \tag{3}$$

where D_i is the dispersion at element i, η denotes the phase slip factor and L_0 is the orbit length. The additional term has to be included, since the cavity has to be switched on during the closed orbit measurement. For an unbunched, coasting beam the additional dispersion term vanishes. On one hand, the terms can be calculated by knowing all twiss parameters. On the other hand, a method of evaluating the ORM is to measure the entries of the matrix by applying small corrector changes and measuring the variation of the beam position at each BPM.

Up to now the measurement of the ORM was done manually by setting up a corrector magnet to three different magnetic fields. For each of these fields the closed orbit was measured and saved to a data file. This procedure was repeated for all corrector magnets. All resulting measurements were analyzed and the matrix was calculated. The complete, manual measurement took roughly eight hours. Besides the time consumption, this method was error-prone since all settings were done by hand.

To have a faster and reliable method to measure the ORM a software application is beeing developed. This application applies all settings and measures the ORM automatically. It establishes network connections to all BPMs, the timing system of COSY and all corrector magnets. In addition the application accesses a database, where calibration factors for the currents of the corrector magnets are stored. A schematic overview of the mentioned connections is given in Fig. 1.

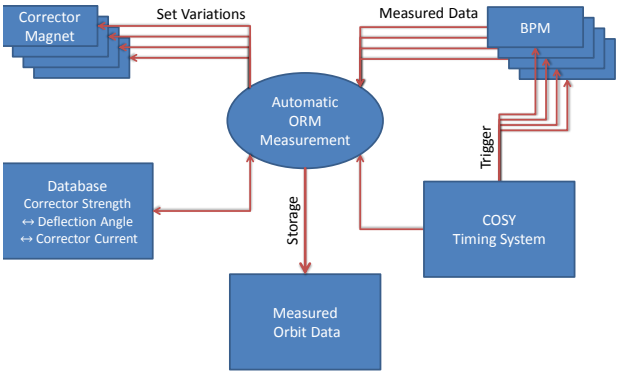

Fig. 1: Scheme of the network connections between the ORM measurement application and the used subsystems of COSY.

The application measures the ORM in the following way: It creates an adjustable number of orbit variations for each corrector magnet. Each variation lasts typically five seconds. All these variations are done after each other in one cycle of COSY. If the complete cycle time is used up, the remaining corrector magnet changes are distributed in the upcoming cycles until all of them for all correctors are done. All BPMs are triggered by the timing system, which enables a synchronization to the deflection angle, introduced by the correctors. Due to the fact that the maximum repetition rate of the BPMs is 1 Hz, each variation is measured typically five times. The measured data are sent to the application and are stored with the corresponding corrector strength. The synchronization of the BPM measurement, the corrector setting and the data storage is done by the COSY timing system, which triggers the used devices. All the measured data are stored in the ROOT [3] tree format to provide a simple use of the ROOT framework for further analysis. With this measurement scheme, a complete ORM measurement takes typically 30 minutes. Thus, the new method gains a factor of 16 in measurement time. In addition the application controls all systems needed, reduces the error-proneness and does not need any additional controlling of the shift crew.

To calculate the ORM, the measured beam displacement at each BPM is plotted against the change of the current in the corrector. The slope of a linear fit to these data points is one entry in the ORM. As an example the measured beam displacements for the corrector SV32 and the BPM bpmy08 is shown in Fig. 2. For the measurement shown, eleven different deflection angles were used. The beam position for each deflection angle is measured five times and averaged.
The fit shown results in the matrix entry:

$$M_{\mathrm{SV32,\,bpmy08}} = -0.197\,\mathrm{mm}/\Delta I\,[\%I_{\mathrm{max}}]. \tag{4}$$

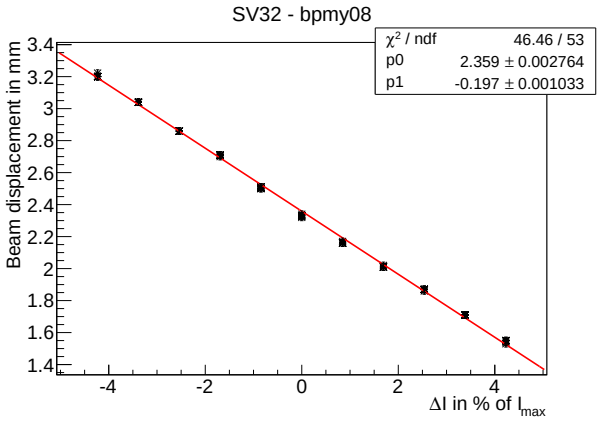

Fig. 2: The measured orbit response at bpmy08 for a change of the corrector magnet SV32. The corrector strength is expressed in the technical current through the magnet.

By calculating the fit parameters for all combinations of corrector magnets and BPMs the ORM is calculated.

In addition to the automated ORM measurement application, a tool to calculate the ORM, to analyse the ORM and to correct the closed orbit is developed.
The orbit correction is done by pseudo inverting the ORM. Multiplying the inverted matrix by the measured, uncorrected orbit results in corrector currents which can be used to correct the closed orbit towards an orbit with a smaller RMS[1]:

$$\begin{pmatrix} \vec{\theta}_{x,\mathrm{cor}} \\ \vec{\theta}_{y,\mathrm{cor}} \end{pmatrix} = M^{-1} \begin{pmatrix} \vec{x} \\ \vec{y} \end{pmatrix}, \tag{5}$$

Since the ORM M is not a square matrix, the pseudo inversion is done by using the Singular Value Decomposition (SVD), algorithm provided by the linear algebra library armadillo [4]. By choosing the number of used singular values, the required corrector strength and the resulting RMS value of the corrected orbit can be calculated. Figures 3 and 4 depict the calculated RMS values in both planes depending on the number of used singular values. The red points depict the measured RMS values after the corresponding correction.

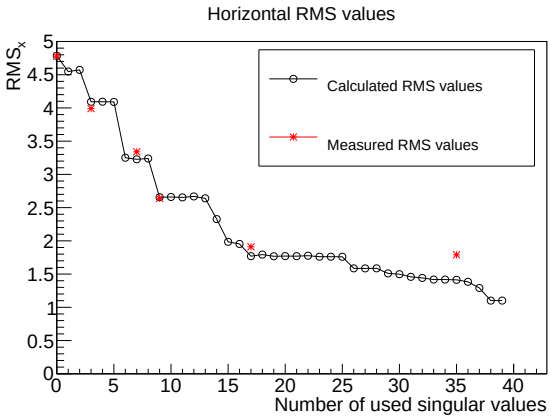

Fig. 3: Calculated horizontal RMS values for different numbers of singular values (black). The red points indicate the measured RMS values.

[1]Root Mean Square

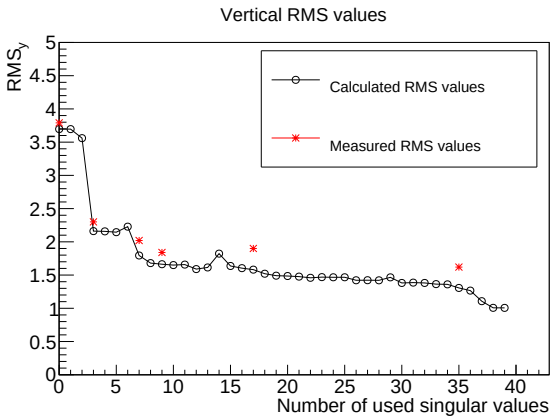

Fig. 4: Calculated vertical RMS values for different numbers of singular values (black). The red points indicate the measured RMS values.

The comparison of the measurement with the theoretical prediction shows good agreement for low numbers of singular values. For a higher number of singular values, which correspond to a higher corrector currents, the measured RMS value is larger than the calculated one. Until now, this effect is not understood and under investigation by using simulations, including realistic models of the BPM resolution and magnet misalignments.

In addition to the orbit correction the measured ORMs can be used to improve the MAD[2] model of COSY by using the Linear Optics from Closed Orbits (LOCO) algorithm [5]. The implementation of this algorithm is under development.
In summary, the new developed tools, namely ORM measurement and orbit correction, work and improve the daily work of the accelerator crew. Additionally the measured ORMs can be used to get an improved understanding of the COSY model, which is crucial to simulate the spin evolution during the storage time for an EDM measurement.

Acknowledgment The authors would like to thank the COSY beam instrumentation group for their efforts of maintaining the BPM electronics and their support during the measurements.

References:

[1] M. Rosenthal, Spin Tracking Simulations Towards Electric Dipole Moment Measurements at COSY, in Proceedings 6th International Particle Accelerator Conference, IPAC15, Richmond, VA, USA (2015). http://jacow.org/IPAC2015/papers/thpf032.pdf

[2] H. Wiedemann, "Particle Accelerator Physics 3rd ed.", Berlin, New York, Springer. (2007)

[3] R. Brun, F. Rademakers, "ROOT An Object Oriented Data Analysis Framework", Nuclear Instruments and Methods in Physics Research Section A: Accelerators, Spectrometers, Detectors and Associated Equipment, Volume 389, Issues 12, 11 April 1997, Pages 81-86, ISSN 0168-9002, http://dx.doi.org/10.1016/S0168-9002(97)00048-X.

[2]The MAD-X Program (Methodical Accelerator Design) http://madx.web.cern.ch

[4] Conrad Sanderson ”Armadillo: An Open Source C++ Linear Algebra Library for Fast Prototyping and Computationally Intensive Experiments”, Technical Report, NICTA, 2010. http://arma.sourceforge.net/armadillo_nicta_2010.pdf

[5] J. Safranek, ”Experimental Determination of Storage Ring Optics using Orbit Response Measurements”, Nuclear Instruments and Methods in Physics Research Section A: Accelerators, Spectrometers, Detectors and Associated Equipment, Volume 388, Issues 12, 21 March 1997, Pages 27-36, ISSN 0168-9002, http://dx.doi.org/10.1016/S0168-9002(97)00309-4.

a Institut für Kernphysik 4, FZ Jülich, Germany
b Physics Institute III B, RWTH Aachen University, Germany

Systematic Limitations of EDM Measurements at COSY due to Magnet Misalignments

M. Rosenthal[a,b] for the JEDI Collaboration and the IKP-4 Accelerator Physics Group

Electric Dipole Moment (EDM) measurements bear the potential to disentangle CP violating sources in the Standard Model and beyond [1]. The JEDI collaboration aims for a first direct measurement of the deuteron EDM in the existing storage ring COSY at Jülich. The deuteron EDM is assumed to be aligned to the particle spin $\vec{S}$ as follows:

$$\vec{d} = \eta_{\mathrm{EDM}} \cdot \frac{q}{2mc} \vec{S} \tag{1}$$

Here, η_{EDM} denotes a dimensionless scaling parameter and q and m are the deuteron charge and mass, respectively. A powerful simulation framework is required to model the measurement method and explore the systematic limitations. The developed framework combines the existing beam and spin tracking algorithms of COSY INFINITY [2] with the analysis functionality of the ROOT framework [3]. This has been illustrated in [4]. Subsequently a follow-up report is presented.

The spin motion for relativistic particles in constant electromagnetic fields is theoretically described by the Thomas-BMT equation [5, 6]

$$\frac{d\vec{S}}{dt} = \vec{\Omega} \times \vec{S}, \tag{2}$$

which can be extended for an permanent particle EDM [7]. Here, $\vec{S}$ denotes the spin vector in classical representation, while $\vec{\Omega}$ is the spin rotation axis. Its magnitude amounts to the angular precession frequency. The particular form of $\vec{\Omega}$, depending on the electromagnetic fields, is given in [7]. Considering an ideal magnetic storage ring, the reference trajectory is defined by the location of the bending dipole magnets. Due to the particle magnetic dipole moment the spin vector precesses around the vertical axis $\vec{e}_y$. A non-vanishing EDM introduces a tilt of the spin rotation axis towards the radial direction $\vec{e}_x$. This is illustrated in Figure 1. In the misalignment-free lattice, the spin rotation axis in each of the bending dipoles defines the orientation of the spin closed orbit $\vec{n}_c$.

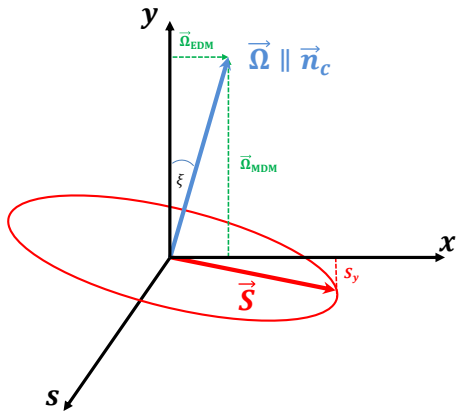

Fig. 1: Tilt ξ of the spin closed orbit $\vec{n}_c$ due to spin interaction in the guiding fields of a magnetic storage ring. The contributions of MDM and EDM to the spin rotation axis $\vec{\Omega}$ are perpendicular to each other. The tilt induces an oscillation of a vertical spin component. (similar to [8])

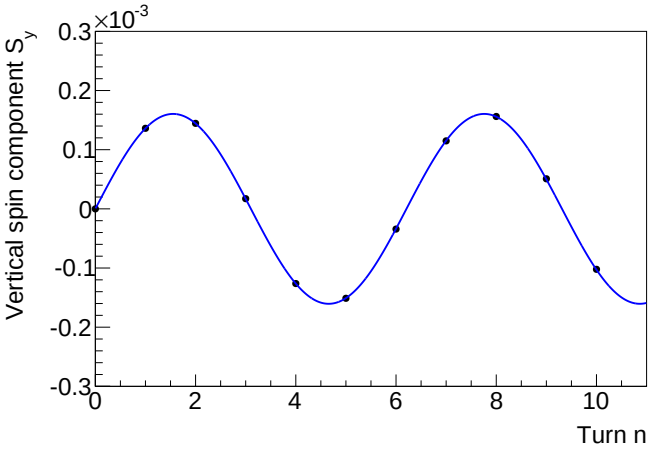

Fig. 2: Fast oscillation of the vertical spin component of a reference deuteron with an initial spin vector precessing in the plane perpendicular to the spin closed orbit. An EDM of $\eta_{\mathrm{EDM}} = 10^{-4}$ is assumed, which causes a tilt of the spin closed orbit. The solid line is a fit of a sinusoidal function. (similar to [8])

A spin vector initially perpendicular to the spin closed orbit possesses an oscillating vertical spin component, whose amplitude depends on the tilt angle ξ. Deuterons with a momentum of 970 MeV/c are currently under investigation. Assuming an EDM corresponding to $\eta_{\mathrm{EDM}} = 10^{-4}$, the oscillation amplitude $\hat{A}$ is given by:

$$\hat{A} \approx \left| \frac{\eta_{\mathrm{EDM}} \cdot \beta}{2G} \right| = 0.16 \cdot 10^{-3} \tag{3}$$

Here, G denotes the anomalous magnetic moment. The calculated amplitude estimate is reproduced in associated spin tracking simulations as illustrated in Figure 2. The spin tune for the given configuration amounts to $\nu_s \approx -0.161$. This amounts to about 6.2 turns per oscillation period. A precise time resolution would be required to extract the desired signal. Furthermore only a tiny signal amplitude can be expected. To enhance the amplitude, a different measurement method based on an radiofrequency Wien filter is proposed [9, 10]. The Wien filter is designed to have a vertical magnetic and radial electric field, whose strengths are adjusted to minimize the Lorentz force. Simulations have been performed assuming a Wien filter device length of 0.8 m and a magnetic field amplitude of $\hat{B} = 0.1$ mT. In the ideal case, the resulting spin rotation axis in this device is vertically oriented and independent of a potential EDM. The Wien filter frequency needs to be adjusted to the spin precession frequency (plus multiples of the revolution frequency) to excite a resonant spin signal. In case of a non-vanishing EDM, this signal shows up as a slow oscillation of the average vertical spin component, which can be approximated by a linear function as illustrated in Figure 3. The slope scales linearly with the tilt angle of the spin closed orbit $\vec{n}_c$ at the Wien filter location. In ideal case, this tilt is proportional to the EDM magnitude and provides the desired signal in this measurement method. An important relation between the phase of the precessing spin as shown in Figure 1 and the phase of the

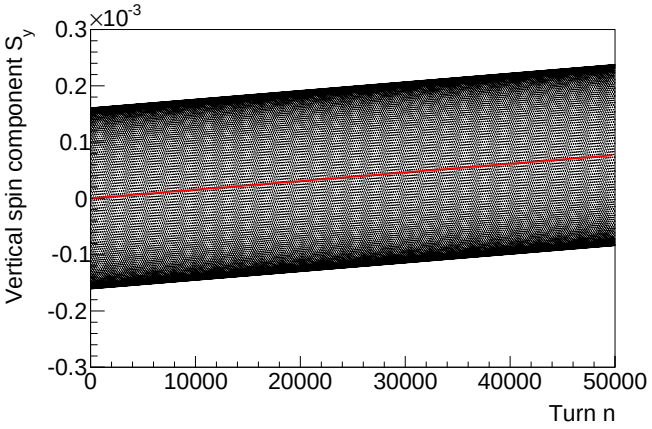

Fig. 3: Behaviour of the vertical spin component in presence of an EDM and the radiofrequency Wien filter with a vertical magnetic field. The same conditions as described in the caption of Figure 2 were applied. The initial phase of the Wien filter field oscillation is set to $\phi = 0°$. The solid lines are linear fits used to extract the average change. (similar to [8])

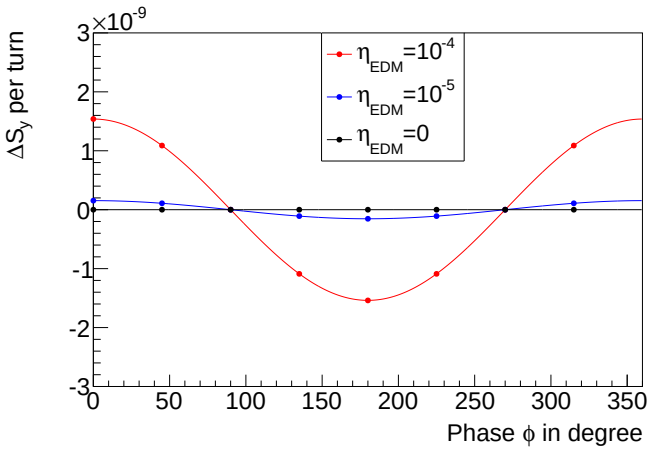

Fig. 4: Extracted average change of the vertical spin component as shown in Figure 3 for different initial phases of the Wien filter fields with respect to the initial spin orientation. Different magnitudes for an EDM are investigated. The solid lines correspond to the theoretical expectation. A Wien filter magnetic field of $1 \cdot 10^4$ mT and the corresponding electric field and its length of about 0.8 m are used. (similar to [8, 11])

Wien filter fields is observed. This is depicted in Figure 4. Assuming an initially longitudinal spin direction at the Wien filter location, a maximum slope is obtained for a Wien filter phase corresponding to the maximum field amplitude. This situation is further referred to as $\phi = 0°$.

As previously discussed, the tilt angle of the spin closed orbit is directly connected to the EDM signal. Misalignments of the storage ring magnets can introduce radial and longitudinal magnetic fields on the reference trajectory. These fields infer tilts of the spin closed orbit and can introduce a change of the vertical spin component mimicing a deuteron EDM. The order of magnitude of these false signals is investigated in the following study. For this purpose the quadrupole magnets of the storage ring are randomly shifted in vertical direction. Normal distributions with different Gaussian widths σ_y are applied in subsequent simulation runs. Besides the

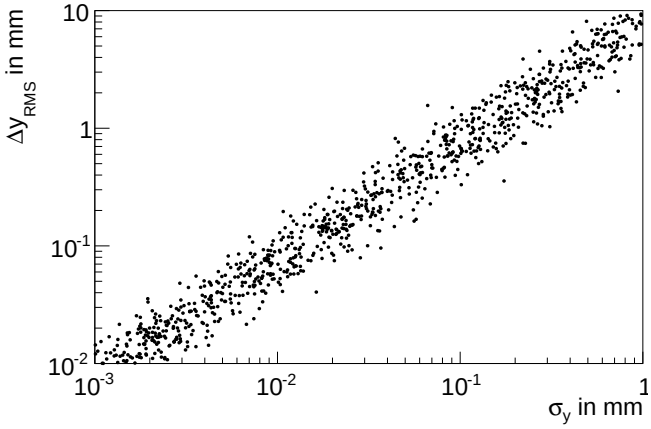

Fig. 5: Simulated RMS value of the vertical orbit deviations Δy_{RMS} in presence of misaligned quadrupole magnets. Gaussian distributed shifts in vertical direction have been assumed for the misaligned quadrupole magnets. The misalignments were diced assuming different Gaussian widths σ_y. (similar to [8])

spin motion, also the beam motion is affected by those fields, leading to vertical orbit deviations. The RMS[1] of the vertical orbit deviations Δy_{RMS} at the locations of the quadrupoles is used as a measure of the underlying misalignments. Figure 5 illustrates the proportionality between σ_y and Δy_{RMS} for 1000 different randomization seeds and magnitudes of σ_y. The resulting slope of the vertical spin component for two different misalignment seeds is shown in Figure 6. The tilt angle and tilt direction of the spin closed orbit depends on the misalignment location in the storage ring. The magnitude and relation of the radial and longitudinal component of the

[1] Root Mean Square

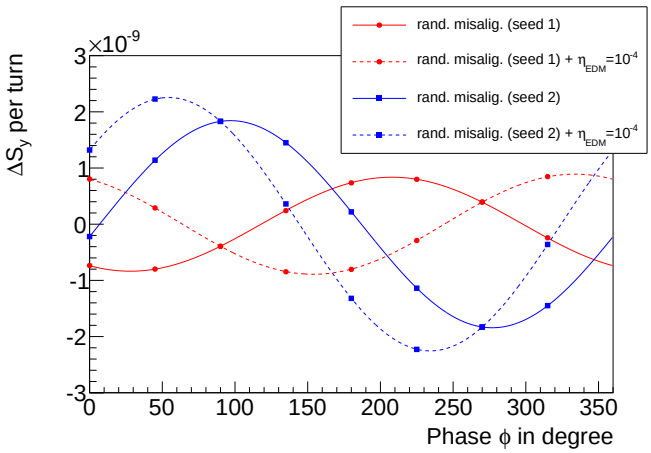

Fig. 6: Extracted average change of the vertical spin component for different initial phases of the Wien filter fields with respect to the initial spin orientation. The superposition of the false signal due to misaligned quadrupole magnets ($\sigma_y = 0.1$ mm) and different magnitudes of the EDM has been investigated. Two different randomization seeds are illustrated. The solid and dashed lines correspond to the theoretical expectations. A Wien filter magnetic field of $1 \cdot 10^4$ mT and corresponding electric field is used. The length of the Wien filter is about 0.8 m. (similar to [8, 11])

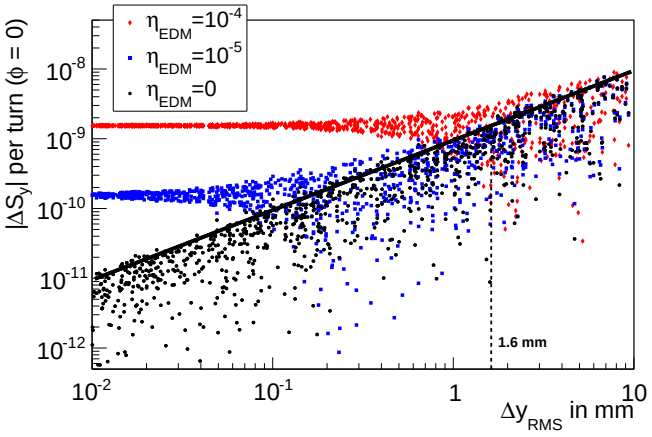

Fig. 7: Absolute average change of the vertical spin component $|\Delta S_y|$ per turn with respect to different Δy_{RMS} and an initial Wien filter phase $\phi = 0°$ in the simulation. The different Δy_{RMS} have been generated by randomized vertical quadrupole shifts assuming Gaussian distributed misalignment errors. Furthermore different EDM magnitudes are considered. The solid line shows the 90% upper confidence limit for pure misalignments. The dashed line refers to the location for which the false signal by misalignments is equal to an EDM signal corresponding to $\eta_{\mathrm{EDM}} = 10^{-4}$. (similar to [8])

spin closed orbit determines the phase ϕ, for which a maximum polarization buildup is observed. In case the false signal due to misalignments is superimposed by a non-vanishing deuteron EDM, the phase relation is modified towards increasing slopes for $\phi = 0°$. This reflects that the slope measured at $\phi = 0°$ is most sensitive to a potential EDM. The superposition of EDM signal and false signals have been systematically investigated for different EDM magnitudes and misalignment seeds. For each setting, the absolute value of the slope at $\phi = 0°$ was retrieved. The results are shown in Figure 7. Towards smaller values of the vertical orbit RMS Δy_{RMS} the EDM related signal and the false signal are distinguishable, while an EDM related signal may hide for larger orbit deviations introduced by misalignments. According to the conducted study for vertically shifted quadrupoles, the 90% upper confidence limit of the false signal at $\Delta y_{\mathrm{RMS}} \approx 1.6\,\mathrm{mm}$ is of equal magnitude as a pure EDM signal corresponding to $\eta_{\mathrm{EDM}} = 10^{-4}$. This sets a stringent limit to the sensitity of EDM measurements at COSY for the proposed measurement method. The results for different misalignment sets, the contribution for imperfections of the Wien filter itself and more details on the performed studies will be given in [8]. A similar phase behaviour as shown in Figures 4 and 6 (but not scaling linearly with the deuteron EDM) can be observed using a radiofrequency solenoid instead of the Wien filter. A successful experimental confirmation was carried out in the most recent beam time end of 2015.

References:

[1] W. Dekens et al., JHEP 7, (2014), p. 69
[2] K. Makino and M. Berz, Nucl. Inst. & Meth. in Phys. Res. A 558 (2006), p. 346-350
[3] R. Brun and F. Rademakers, Nucl. Inst. & Meth. in Phys. Res. A 389 (1997), p. 81-86
[4] M. Rosenthal, IKP Annual Report (2014)
[5] L. H. Thomas, Phil. Mag. 3, 1 (1927)
[6] V. Bargmann, L. Michel, V. L. Telegdi, Phys. Rev. Lett. 2 (1959), p. 435-436
[7] T. Fukuyama and A. J. Silenko, Int. Journal of Modern Physics A 28 (2013), 1350147
[8] M. Rosenthal, PhD thesis in preparation
[9] F. Rathmann, A. Saleev and N. N. Nikolaev, Journal of Physics: Conference Series 447 (2013), p. 012011
[10] W. Morse, Y. Orlov, Y Semertzidis, Phys. Rev. ST Accel. Beams 16 (2013), p. 114001
[11] M. Rosenthal and A. Lehrach, Proceedings of IPAC'15 (2015), THPF032

[a] Institut für Kernphysik 4, FZ Jülich, Germany
[b] Physics Inst. III B, RWTH Aachen University, Germany

Automation of Rogowski Coil Test Bench and Data Acquisition System

D. Shergelashvili[a,b], F. Hinder[c,d], H. Soltner[a] and F. Trinkel[c,d] for the JEDI collaboration

1 Motivation

Technical development at COSY is a very important issue in the frame of the JEDI project. One of them is the development of the Beam Position Monitoring system (BPM). The idea of the new BPM is different from the old one. The new measurement principle is based on measuring the magnetic flux of the particle beam to determine the beam position. For picking up, a toroidal Rogowski coil is used. A Rogowski coil is an electrical device for measuring alternating current (AC) or high speed current pulses. Generally, it consists of a helical coil of wire with the lead from one end returning through the centre of the coil to the other end so that both terminals are at the same end of the coil (see Fig. 1). This makes the coil more flexible for noninvasive measurements. In our case, the coil is divided into four equal parts, one covers $1/4$ arc of the total circumference. This makes it possible to measure position in two dimensions of the current flow inside the torus. The winding density, the inner and outer diameter of the coil and the rigidity of the winding are important to increase sensitivity and linearity of the coil for position determination.

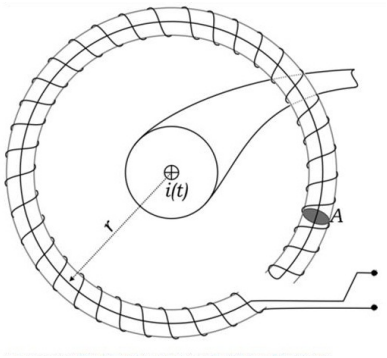

Fig. 1: The generic Rogowski coil.

The induced voltage for a full covered Rogowski coil can be calculated by Eq. 1

$$U_{ind} = \frac{\partial I_0}{\partial t} N \mu_0 \left(r - \sqrt{r^2 - A^2} \right) \tag{1}$$

$$\frac{\Delta U}{\Sigma U} = \frac{\sqrt{2}}{\pi \sqrt{r^2 - A^2}} x_0, \tag{2}$$

where N is number of windings and r is radius of torus with winding radius A. The induced voltage is proportional to the change of a fast current (I_0) and to the distance of the between the current source and the coil itself. The mathematical calculation, presented in Eq. 2, describes the induced voltage depending on the position for ideally manufactured windings. In reality, four coils parameters are always different from theoretical prediction. Due to this common problem, it is very useful to check the manufactured coil on the test bench first (see Fig. 2).

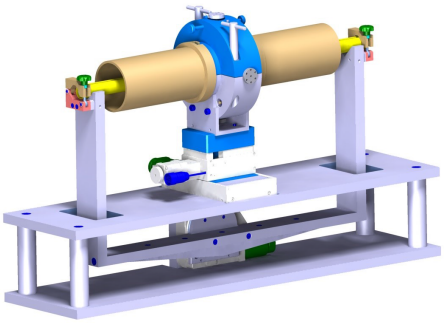

Fig. 2: Test bench for Rogowski coil Measurment.

2 Devices at the Test Bench

The test bench consists of universal positioning control system and two lock-in amplifiers. The positioning systems include a movable table with stepper motors and their corresponding driver unit PS90 (Fig. 3). The table can be controlled using three stepper motors with 10 µm step size. Two motors move the attached coil in X (horizontal) and Y (vertical) planes. The third motor is responsible for angular movement of the copper wire. This thin wire goes through the torus and simulates the particle beam. The PS90 is an electrical device which creates a bridge between the computer or the server and the motors systems. The PS90 has several communication ports: USB 2.0, RS-232 and optional Anybus®interface.

The measurement devices are the lock-in amplifiers from Zurich Instruments, model: HF2LI. The HF2 series is a product line comprising an impedance spectroscope and a digital lock-in amplifier covering advanced requirements for laboratory equipment. It provides Numerical, Sweeper, Spectroscope, Zoom FFT and Oscilloscope tools. Each device has two differential inputs and two outputs. The signal to be measured is connected to one of the two high-frequency analog inputs where it is amplified to a defined range, filtered and digitized at a very high speed. The resulting samples are fed into the digital signal processing block for demodulation by means of up to 8 dual-phase demodulators. Working frequency range is 0-100 MHz. It has Digital I/O ports for signal triggering and additional Auxiliary ports, too. This device does not have user interface itself, and it can be controlled by the server computer, where special software is running. The test bench requires two lock-in amplifiers to readout a quartered coil. These devices contain synchronization I/O ports for simultaneous polling the data with equal time stamps from all the input channels. The signal input range, AC/DC coupling, 50 ohm internal resistor and lots of other options can be set via commands.

3 Software Development

During the experiment, all the devices need control and communication to the computer . The PS90 listens only ASCII commands over the COM port. Zurich Instruments devices

use a server-based connectivity methodology. Server-based means that all communication between the user and the instrument takes place via a computer program called a server, the LabOne Data Server. The Data Server recognizes available instruments and manages all the communication between the instruments and the host computer on one side, and communication to all the connected clients on the other side. Herewith, the software package serving the test bench is developed using the Python programming language. The Python script manages all the devices and it is responsible for recording and analysing of the data. Figure 3 shows the architecture of the test bench system.

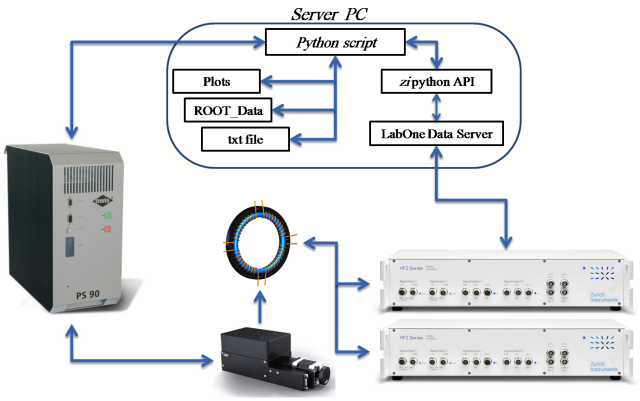

Fig. 3: Architecture of test bench.

The Python code, which was written specially for this test bench, runs on both operating systems, Windows and Linux. At the beginning, the code establishes the communication to the PS90 and the lock-in amplifiers. Then it sets all the necessary parameters for the stepper motors. Last command during initialization is calibration of the table and linear measurement system. The calibration described is a selectable option. Variable parameters such as travel distance, measured in dots in whole distance, frequency, sample per second, type of analyzing can be set by the user before starting the script. When the experiment starts the computer sends the destination coordinates in the PS90 driver. The PS90 drives the motors before the table reaches the correct place and then switch them in auto place correction mode. After reaching the XY coordinates, the script automatically starts sending commands for polling all necessary data from the H2LI devices, sorts them and saves in a ROOT file. It is very important to poll the data with equal time stamps which is also implemented in the new script package. After one measurement, it sends new coordinates to the PS90 and starts polling again. When all data are collected and saved, the script starts the analysing process and displays the results. For each measurement series, four figures are created. Two figures for the movement along one axis. Each of these figures shows the measured voltage depending on the position of the wire, relative to the coil. Additional analysing steps can be done, by using the raw data, saved in the ROOT files. At the end of the measurement the devices are sent into standby mode and the stepper motors are switched off.

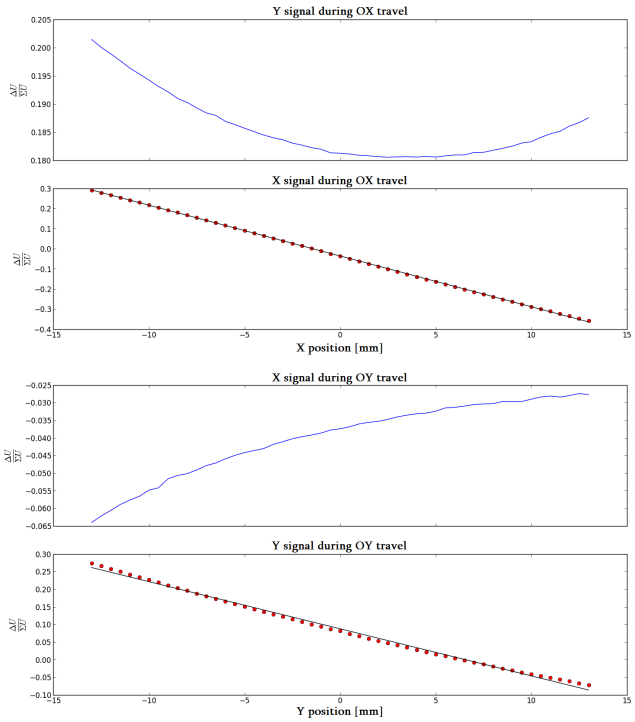

Fig. 4: New Python Script Results.

4 Measurements and Results

For the experiment, discussed, the new Python script was used. Measurement was done according to these parameters: x travel and y travel distances is 26 mm (-13 to +13 mm), 53 points per travel (106 total), 10000 samples for each point, lock in frequency - 750 kHz. The whole experiment took about 15 minutes. The experiment results is shown on Fig. 4. The first two plot describes position measurements along horizontal axis. The induced voltage in the vertical plane ($U_{up} - U_{down}$) is changing during the horizontal travel, that nonlinear correlation indicates to uneven distributed windings. In case of linear shape it will indicates rotated coils against to XY plane. For the same reason on the forth plot, the signal from the vertical plane is curved and dots are out of linear function. The second plot on Fig. 4 shows that linear function fits the points fairly well, which corresponds the signal from the horizontal plane ($U_{left} - U_{right}$) during travel along X axis. It was expected because on the third plot, the voltage is increasing during whole experiment unlike from first one.

5 Conclusion

The new Python script is very useful and comfortable to analyze the Rogowski coil. The script manages all necessary processes for the whole test bench system. It automatically drives the XY tables and takes data from the lock-in amplifiers. The script generates the output files, holding plots for fast online analysis as well as raw data for detailed offline analysis. Most important improvement of the script is that the measurement time is almost ten times less than it was and the measurement process is fully automated.

References:

[1] F. Hinder, F. Trinkel. Rogowski coil Mathematical Calculation. (2015)

[2] P. Forck, P. Kowina, D. Liakin. Beam Position monitors: Principle and Realization. (2008)

[3] R. Brun, F. Rademakers, ROOT An Object Oriented Data Analysis Framework", Nuclear Instruments and Methods in Physics Research Section A: Accelerators, Spectrometers, Detectors and Associated Equipment, Volume 389, Issues 12, 11 April 1997, Pages 81-86, ISSN 0168-9002,

[4] Hans Petter Langtangen, Python Scripting for Computational Science, Third Edition.

[5] LabOne Programming Manual. Revision 31421, 8-Jul-2015

[6] HF2 User Manual. Revision 30817, 19-Jun-2015

[7] Universal Position Control Unit user manual, OWIS GmbH

a ZEA-1, Forschungszentrum Jülich GmbH, Germany
b Georgian Technical University, Tbilisi
c IKP, Forschungszentrum Jülich GmbH, Germany
d RWTH Aachen University, Germany

Differential cross section of the $d^{12}C \to pX$ reaction at 270 MeV

Yu. N. Uzikov[1] for the JEDI collaboration.

Search for EDM of charged particles requires measurement of the polarization of the particle after its circulation in a ring with special configurations of electromagnetic fields [1]. For the deuteron case, it is suggested to measure the left-right asymmetry in the elastic scattering of the polarized deuteron on the carbon target ^{12}C. Vector analyzing power A_y of the reaction $d+^{12}C \to d+^{12}C$ is rather large at energies of the dedicated experiment with the deuteron beam energy about $T_d = 200-300$ MeV. For this reason the $d^{12}C$- elastic scattering can be used in the discussed polarimetry measurements. For better understanding of the efficiency of the detector system in such a measurement it is necessary to know the relative ratio of the inelastic $d^{12}C$ interaction cross section with deuteron breakup $d^{12}C \to p+X$ to the elastic one. For our knowledge, the corresponding data are absent at present.

The main aim of the present study is to give an estimation of the cross section of reaction $d^{12}C \to p+X$ at a momentum of the final proton close to the half of the initial deuteron beam momentum. Within the Glauber theory the cross section of the reaction $d+A \to p+X$ was considered in Ref.[2]. This cross section contains i) the contribution from the deuteron breakup with elastic rescattering of the proton and neutron from the deuteron, ii) the neutron absorption cross section, when the neutron participates in inelastic collisions only, while the proton scatters elastically. After some approximations to this scheme the invariant cross section can be written in a form corresponding to the impulse approximation [3]. Within the Relativistic Hamiltonian Dynamics [4] it can be written as

$$E_p \frac{d^3\sigma}{d^3p_3} = K[u^2(q)+w^2(q)]\sigma_{tot}(nA \to X), \qquad (1)$$

where $\sigma_{tot}(nA \to X)$ is the total inelastic cross section of nA-interaction, $u(q)$ and $w(q)$ are the deuteron S and D-waves, respectively, in momentum space, q is the relativistic internal momentum; K is a kinematical factor.

The results of numerical calculations for zero angle of the final proton θ_p^l (in respect to the direction of the deuteron beam) are shown in Fig. 1 for the beam momentum p_d=9.1 GeV/c and for $p_d = 1.042$ GeV/c (i.e. $T_d = 270$ MeV) as function of the modulus of the 3-momentum of the final proton p_L in the laboratory system. The total cross section $\sigma_{tot}(p^{12}C \to X)$ is taken from Ref.[5] assuming that it is equal to the neutron $\sigma_{tot}(n^{12}C \to X)$ cross section. The results for $\theta_p^l \neq 0$, are shown on Fig. 2. One can see that for the spectator mechanism the cross section quickly decreases with increasing θ_p^l. The *pn*-rescattering in the final state, not considered in this approach, may change this behavior.

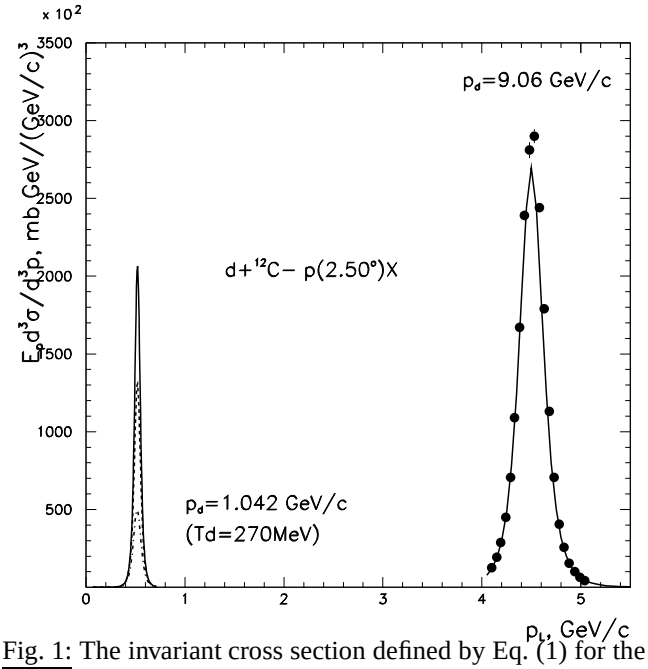

Fig. 1: The invariant cross section defined by Eq. (1) for the $d^{12}C \to p(0)+X$ reaction versus the laboratory momentum of the final proton at $p_d = 9.1$ GeV/c (data points are taken from [6]) and 1.042 GeV/c

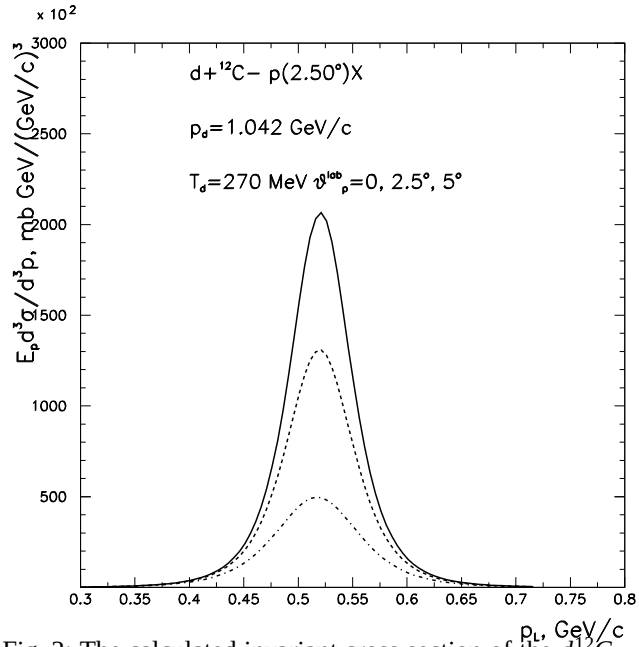

Fig. 2: The calculated invariant cross section of the $d^{12}C \to p(0)+X$ reaction at $p_d = 1.042$ GeV/c ($T_d = 270$ MeV) for differnt proton emission angles in the laboratory system $\theta_p^l = 0, 2.5^\circ$ and 5°.

References:

[1] JEDI Proposal
[2] L.Bertocchi, D. Treleani, Nuovo Cim. 36 A, 1 (1976)
[3] A.P. Kobushkin, L. Vizireva, J Phys. G8, 893 (1982)
[4] B.L.G.Backer, L.A. Kondratyuk, M.V. Terentjev, Nucl.Phys. B 158, 497 (1979)
[5] B.Abu-Ibrahim et al., Phys.Rev. C 77, 034607 (2008)
[6] V.G. Ableev et al. JETP Lett. 47, 649 (1988).

1 JINR, 141980 Dubna, Russia

First Results of the Upgraded Low Energy Polarimeter Read-Out

N. Hempelmann for the JEDI collaboration

Low Energy Polarimeter Read-Out The Low Energy Polarimeter (LEP) [1] is the polarimeter in the injection beam line of COSY. The polarization is measured using elastic scattering at a carbon or polyethylene (CH_2) target. Fig. 1 shows the basic design. The beam enters the polarimeter from the left and hits the target at the center. The outgoing particles are detected using twelve plastic scintillators installed in groups of three above, below, to the left and to the right of the beam. The scintillators in each group are spaced 10° of polar angle apart and can be moved as a rigid unit to select a scattering angle.

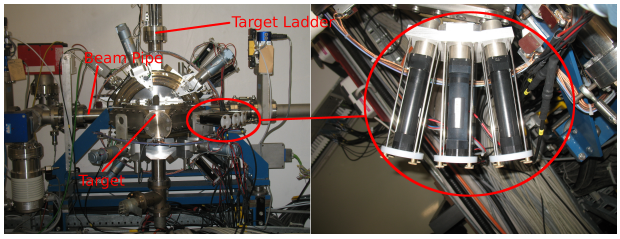

Fig. 1: Low Energy Polarimeter (left). Close-up of a group of detectors (right)

.

The present detector read-out uses analog NIM modules. It is able to select elastic scattering events using pulse height discrimination. Apart from that it can detect kinematic coincidences in deuteron proton scattering with a time resolution of about 2.5 ns.
To facilitate a faster online measurement of the beam polarization a new system using field-programmable gate arrays (FPGA) was tested. The detectors are read out using a GANDALF VME-board [2], which was developed for the COMPASS experiment at the University of Freiburg. The GANDALF module provides an FPGA for signal processing and an eight channel analog to digital converter (ADC) with a resolution of 12 bits and a sampling rate of 1 GHz.
The firmware of the module was modified for this application. The amplitude and time of each incoming pulse is measured using a constant fraction discriminator implemented on the FPGA. The precision of the time measurement is about 50 ps.
In addition to the pulse height and coincidence measurements that were possible with the old electronics the new system can also measure the time of flight for each particle. One of the ADC channels is connected to a signal from the radio amplifier of the cyclotron. The time between this signal and the arrival of a particle is the time of flight. This method only measures the relative time of flight for different particles as the exact run time of the signals and the time the beam takes from the cyclotron to the polarimeter are not taken into account.

Results During the beam times in June and December 2015 the first successful measurements with the new read-out were taken [3]. The experiment used polarized deuterons at an energy of 75 MeV. Fig. 2 shows the distribution of the amplitude and the time of flight for particles registered at a scattering angle of 40°. As indicated in the plot, several different reactions can be identified. There is a clear peak corresponding to elastic scattering, which is used for the polarization measurement. There is also a broad continuum from deuteron breakup reactions and another peak from the reaction ^{12}C(d,p)^{13}C, both lead to protons in the final state.
The observed time distribution is broadened by the difference in time at which particles from the cyclotron arrive at the polarimeter. In the cyclotron, particles from more than one turn are extracted simultaneously, leading to a spread in energy.

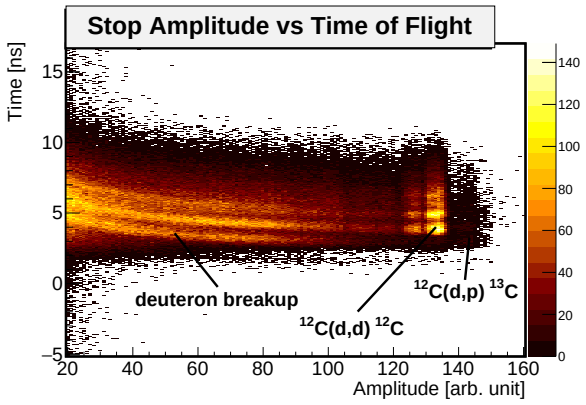

Fig. 2: Plot of the amplitude and time of flight of particles detected at a scattering angle of 40° using a carbon target

.

Conclusion A new read-out system for the Low Energy Polarimeter was tested successfully. In 2015, amplitude and time of flight spectra were measured as well as the beam polarization. The new read-out is available as a routine tool for calibrating the polarized source in upcoming beam times.

References:

[1] M. Eggert: *Entwicklung eines gepulsten Cäsium-Ionenstrahls fur die Quelle polarisierter Ionen an COSY/Jülich*, Ph.D. Thesis
[2] S. Schopferer et al. : *Development and Performance Verification of the GANDALF High-Resolution Transient Recorder System*, IEEE Transactions on Nuclear Science, vol. 58, no. 4, pp. 1456-1459, Aug. 2011
[3] N. Hempelmann: *FPGA-Based Upgrade of the Read-Out Electronics for the Low Energy Polarimeter at COSY/Jülich*, Presentation at PSTP Bochum, 2015, Proceedings PoS(PSTP2015)025

* Institut für Kernphysik, Forschungszentrum Jülich, Germany

Improvements in Barrier-Bucket Signal Shaping

B. Breitkreutz, F.J. Etzkorn, G. Schug , R. Stassen

Abstract

A prototype of the HESR barrier-bucket (BB) cavity is installed at COSY and used to compensate the mean energy loss provoked by experiments. Unfortunately, its bucket is not completely flat. In combination with stochastic cooling, the particles don't distribute uniformly but concentrate in local minima. Therefore, efforts have been made to further reduce the ripple of the gap voltage.

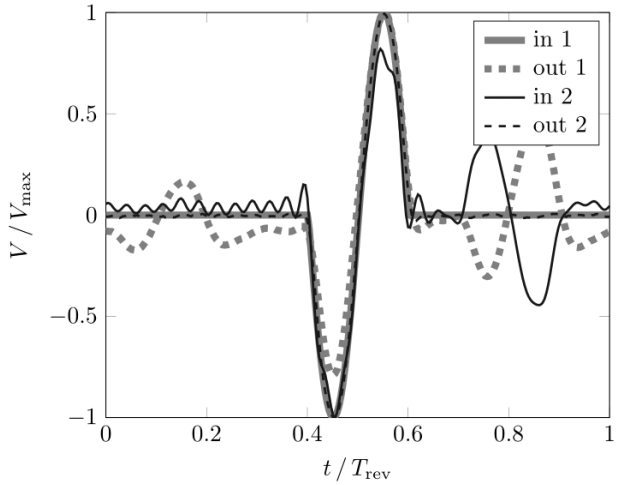

Fig. 1: Measurement of the system response on an ideal sine burst (gray), and on the pre-distorted signal (black) at 500 kHz. Due to the small amplitude of approx. 4 Vpp, the signal is corrected almost perfectly after one single iteration.

Pre-distortion

The bucket signal is generated with an arbitrary waveform generator (AWG). It ideally consists of a single sine burst, building a time gap of μ=10—20% (Fig. 1, "in 1"). It is, for one revolution interval $0 \leq t < T_{\mathrm{rev}}$:

$$v(t) = \hat{V} \sin\left(2\pi \frac{t}{\mu T_{\mathrm{rev}}}\right) \Pi_{\mu T_{\mathrm{rev}}}(t - T_{\mathrm{rev}}/2).$$

Due to long cables, the amplifier and the water-cooled transformer rings inside the cavity, the gap voltage $\tilde{v}(t)$ is heavily distorted ("out 1"). It is necessary to correct this distortion.

Since v and $\tilde{v}$ are periodic with f_{rev}, they have discrete spectra $\underline{c}_k$ and $\underline{\tilde{c}}_k$, each element corresponding to $k f_{\mathrm{rev}}$. Therefore, the frequency response $\underline{g}_k$ of the system is discrete as well and can be calculated for every single harmonic by dividing the Fourier coefficients of the output signal by those of the input signal.

$$\underline{g}_k = \frac{\underline{\tilde{c}}_k}{\underline{c}_k}$$

The pre-distorted input signal ("in 2") is calculated by simply dividing the wanted coefficients $\underline{c}_k$ by $\underline{g}_k$.

Although it is possible to use any test signal with non-zero coefficients for the measurement of $\underline{g}_k$, it is reasonable to use the desired signal $\underline{c}_k$. The system contains non-linear elements; therefore, the system response depends on the spectral power distribution of the input signal. Furthermore, it is beneficial to start with a small input power in order to calculate an initial $\underline{g}_k$ in the linear range. Subsequently, the power can be enhanced successively, always using an input signal which was corrected by the prior response. This is a sufficiently robust way to obtain a well-shaped gap voltage with the desired amplitude despite the non-linear behavior of the system.

This approach was already implemented in the past [1] and successfully used to improve the voltage profile of the BB at COSY. However, the bucket part of the signal still had a ripple in the order of 5—7% of the magnitude of the barrier. This turned out to be disadvantageous especially in combination with stochastic or electron cooling, since the particles tend to collect in the resulting local minima.

The procedure was now re-implemented in order to challenge the causes of the ripple.

First of all, the signal analysis was improved. Well measured Fourier coefficients are critical for the correction process, since higher harmonics are of little amplitudes, hence small numbers are divided by small numbers. The influence of noise often led to instabilities, and the correction did not converge. The main source of noise is the 8-bit ADC of the oscilloscope, resulting in a staircase approximation of the signal with only 256 levels maximum. Therefore, a time span of at least 16 periods is measured and cross-correlated with the reference signal. This way, it is possible to detect every single period with a minimal phase error. The distorted signal $\tilde{v}(t)$ is found by averaging over all detected periods.

Ripple Reduction

The ripple is caused by the low-pass characteristic of the power amplifier. By design it is supposed to have a constant gain up to 12 MHz. Above approximately 15 MHz the gain is almost zero. The spectrum of the rectangular window function consists of slowly decaying harmonics, since the borders of the window are angular. The suppression of high harmonics leads to the observed ripple.

This problem was approached in two ways. The first one is to replace the rectangular window function by a raised-cosine-window.

$$\Pi_{\mu T_{\mathrm{rev}}}(t) \leftrightarrow \Pi_{\mu T_{\mathrm{rev}}}(t) \cos^2\left(\pi \frac{t}{\mu T_{\mathrm{rev}}}\right)$$

The effective width of the sine burst is reduced by the round shape of the raised-cosine-window. A larger value for μ has to be chosen in order to roughly match the shape of the two signals. In Fig. 2, the influence on the spectrum is shown. The signal has hardly any power above the 10$^{\mathrm{th}}$ harmonic. Consequently, a truncation of the spectrum leads to a much smaller ripple than in the case of a rectangular window.

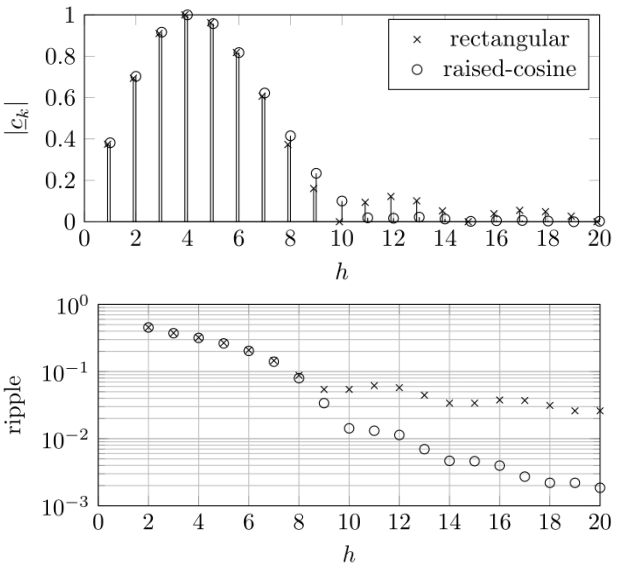

Fig. 2: *top*: Fourier coefficients of a BB-signal with rectangular window (μ=20%) and raised-cosine window (μ=26%). *bottom*: resulting ripple when spectrum is truncated after the h^{th} harmonics.

The second approach is a computer aided optimization process. After an initial pre-distortion of the signal, an optimizer routine tries to minimize the ripple of the gap voltage by varying amplitude and phase of the single harmonics. The goal function is chosen to be the ratio of the amplitudes of the highest ripple and the wanted pulse. This definition lacks of some important constraints, e.g. a constant pulse width and a symmetric shape, but it turned out to be sufficient in this simple form. The width increased by a few percent during the optimization process, which can be compensated by reducing the initial value for μ.

Measurement results

Measurements were made at f_{rev}=1.52 MHz, which is the revolution frequency at COSY of protons with β=0.93. The highest reasonable harmonic is H=10. This is not sufficient to represent a pulse with of μ=10%. For μ=20% however, the analytical ripple is 5.4% with a rectangular window. With a gap voltage amplitude of approx. 200 volts, a ripple of 5.6% was achieved with the new implementation of the iterative pre-distortion process (the old version had 7.5%). After 182 iterations of the optimizer, the value was further reduced to 2.5%. The highest achieved peak voltage was 435 volts, using a rectangular window.

Table 1: BB signal path elements

Arbitrary Waveform Generator	Tektronix AWG5012
Oscilloscope	R&S RTE1024
Amplifier	2 kW solid state
Transformer material	VitroPerm 500F

Additional measurements were made at 500 kHz, a typical revolution frequency of HESR. Due to the small frequency, it was possible to take 30 harmonics and therefore shorter pulses. With μ=20%, a ripple of 1.84% (analytical value: 1.74%) was achieved with a rectangular window. It was reduced to 0.8% (0.05%) by a raised-cosine window. The optimizer could reduce this value even further to 0.6%. For a barrier width of μ=10%, values around 2% could still be realized.

References

[1] R. Stassen, K. Bongardt, F.J. Etzkorn, H. Stockhorst, S. Papureanu, A. Schnase, The HESR RF-System and Tests in COSY, Proceedings of EPAC08, pp. 361-363

Development of MAD-X based LOCO algorithm for COSY optics measurement as well as model improvement

C. Weidemann, M. Bai, F. Hinder

COSY's diverse capabilities of phase space cooling and the flexibility of its lattice with respect to ion-optical settings makes COSY an ideal test facility for accelerator technology developments [1, 2]. High demands on beam control and beam based measurements have to be fulfilled for future experiments such as the proposed precursor experiment for a direct measurement of the electric dipole moment of the deuteron (see [3] and references within).

One major task toward reaching this goal is the improvement of the model of COSY, which currently reaches a precision for $\Delta\beta/\beta$ of 30 to 50 %. A technique called linear optics from closed orbit (LOCO) [4] has succesfully been employed on light sources and storage rings to calibrate and correct linear optics. Therefore, a LOCO algorithm in C++ framework using MAD-X[1] for optics calculation is currently under development.

LOCO is based on the analysis of a measured orbit response matrix (ORM), which contains thousands of data points reflecting the focussing structure of the ring ([4], equations in [5]) . A typical ORM at COSY contains about 2400 entries, representing the orbit deviations caused by a change in the deflection strength of each of the ≈ 40 correction-dipole magnets measured with the ≈ 60 beam position monitors (BPMs) (30 horizontal, 30 vertical) along the ring. An automated ORM measurement system was implemented in the past year allowing to collect a full data set within 30 minutes [5].

In addition, an ORM based on the existing COSY model can be calculated using MAD-X. LOCO now adjusts the parameters of the lattice model in order to minimize the χ^2 difference between the model (M_{mod}) and the measurement (M_{meas})

$$\chi^2 = \sum_{\mathrm{i,j}} \frac{\left(M_{\mathrm{mod,ij}} - M_{\mathrm{meas,ij}}\right)^2}{\sigma_{\mathrm{i,j}}^2} = \sum_{\mathrm{k=i,j}} E_{\mathrm{k}}^2, \tag{1}$$

where σ_{ij} are the errors of the linear fits to the beam displacement at each BPM(i) plotted against the current in each steerer magnet(j). The model parameters under investigation so far are listed in Tab.1. By varying these, $dE_{\mathrm{k}}/dK_{\mathrm{l}}$ can be determined for every parameter:

$$-E_{\mathrm{k}} = \frac{dE_{\mathrm{k}}}{dK_{\mathrm{l}}} \cdot \Delta K_{\mathrm{l}}. \tag{2}$$

Applying a singular value decomposition (SVD) of this non square matrix allows for the determination of its pseudo inversion and the direct recalculation of the correct parameter settings using

$$\frac{dE_{\mathrm{k}}}{dK} = USV^{\mathrm{T}} = \sum \vec{u}_{\mathrm{l}} s_{\mathrm{l}} \vec{v}_{\mathrm{l}}^{\mathrm{T}} \quad \text{and} \tag{3}$$

$$\Delta K = -\sum \vec{v}_{\mathrm{l}} \frac{1}{s_{\mathrm{l}}} \vec{u}_{\mathrm{l}}^{\mathrm{T}} \cdot E_{\mathrm{k}}. \tag{4}$$

Since the response matrix is not linear to most of the parameters LOCO must be iterated until it converges to the best set of parameters.

[1]The MAD-X Program (Methodical Accelerator Design) http://madx.web.cern.ch

Table 1: Parameters under investigation.

parameter name	number
BPM calibration	60
BPM roll, position (s)	2×60
Steerer calibration	40
Steerer roll, position (in s)	2×40
Quadrupole gradients	56
Quadrupole rolls and misalignments	6×56

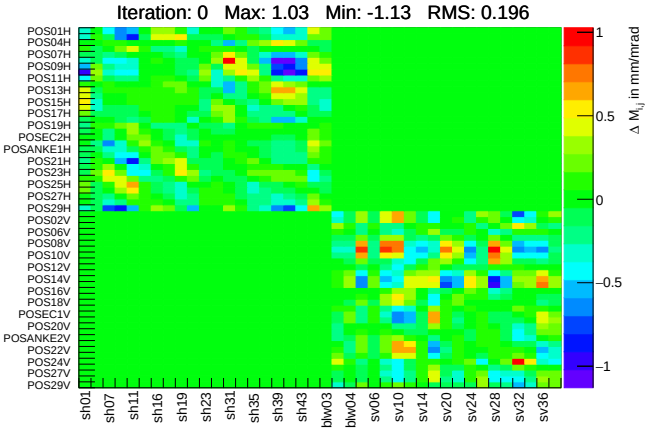

Fig. 1: Comparison of the measured and calculated ORM ($\Delta M_{\mathrm{i,j}} = M_{\mathrm{mod,ij}} - M_{\mathrm{meas,ij}}$) before applying LOCO. Here, the measurement was simulated by randomly dicing the gradient of all 56 quadrupole magnets.

For developing and benchmarking the LOCO algorithm the measured ORM is for the moment simulated by dicing parameter errors in a realistic range. The comparison of this "measured" ORM to the model ORM using the existing COSY lattice without parameter errors forms the reference E_{k} for the first iteration (see Fig. 1). Subsequently one parameter is modulated in three to five steps and a new ORM is calculated for every step. The change of every ORM entry with respect to the "measured" entry is plotted in a separate graph as function of the parameter change. The slope of a linear fit to these data points yields the entries of the so-called error vector $dE_{\mathrm{k}}/dK_{\mathrm{l}}$. This procedure is repeated for every parameter and the error vectors are combined to one matrix dE_{k}/dK. The pseudo inverse of that matrix is than multiplied to the reference ORM E_{k} (see Eq. 4) yielding the new parameter settings ΔK. These settings are then used to calculate the new model ORM for the next iteration. This procedure is repeated several times, where the program allows to adjust different parameters within individual iterations.

The example shown in Fig. 1 is the ORM comparison for a Gaussian distributed change of the quadrupole gradients with $\sigma = 1\,\%$ of k. As one can see only the diagonal matrix elements are significantly affected, meaning that the applied variations do not introduce phase-space coupling, but change the beam response in one plane to a kick in the same. Figure 2 displays in the top panel the root mean square (RMS) deviation of the reconstructed parameter setting with respect to the measurement ($\Delta\mathrm{Par} = \mathrm{k_{mod}} - \mathrm{k_{meas}}$) and in the bottom panel the β-beat ($[\beta_{\mathrm{mod}} - \beta_{\mathrm{meas}}]/\beta_{\mathrm{meas}}$) for three iterations. As vis-

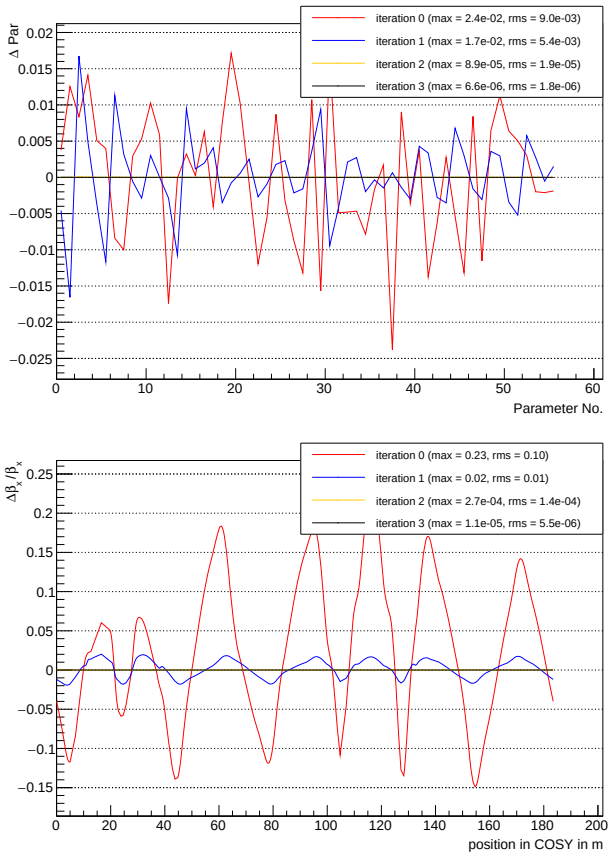

Fig. 2: Top panel: $\Delta\mathrm{Par} = \mathrm{k_{mod}} - \mathrm{k_{meas}}$ for the 56 quadrupole gradients for the starting conditions (red curve) and after up to three iterations.
Bottom panel: The $\Delta\beta/\beta_{\mathrm{meas}}$ in the horizontal plane can be improved by about four orders of magnitude assuming almost perfect BPMs.

ible ΔPar is improved from $9.0 \cdot 10^{-3}$ to $1.8 \cdot 10^{-6}$ meaning that the diced variations are very well detected. The β-beat of initially 0.1 was decreased to $5.5 \cdot 10^{-6}$. The resulting ΔORM after three iterations is displayed in Fig. 3 showing average (rms) deviations of only $1.4 \cdot 10^{-5}$ mm/mrad. These numbers were achieved assuming an error of 10^{-9} m for the position measurement of the BPMs. The effect of the error of the position measurement on the reconstruction of different model parameters is currently under careful investigation. In Fig. 4 the resulting $\Delta\beta_x/\beta_x$ for the variation of quadrupole gradients is plotted as function of the iteration number assuming BPM errors from 1 nm up to 1 mm. Summarizing this graph the optical functions can still sufficiently be reproduced for $\Delta x = 10^{-5}$ m. The reconstruction of the parameter settings is usually a bit worse.

Besides studying the effect of the BPM error on the parameter reconstruction as well as the corresponding optics further investigations are ongoing. Namely, the study of the sensitivity of the LOCO algorithm to different machine parameters, the sensitivity to the step size of the parameter variation, the sensitivity to the cut value of the SVD analysis, and the distribution of individual parameter variations on different iterations. In addition, alternative minimization algorithms will be investigated.

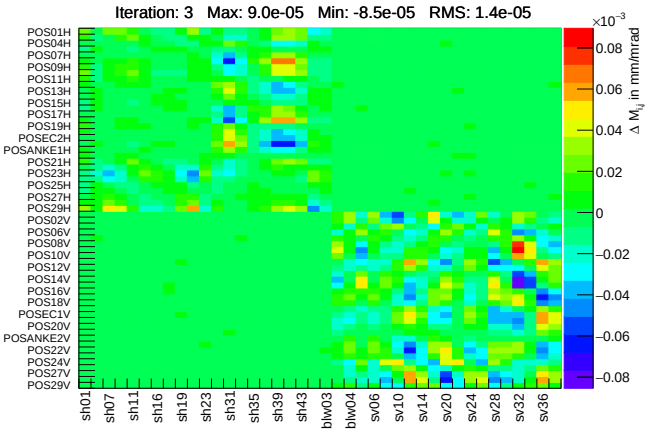

Fig. 3: $\Delta M_{\mathrm{i,j}}$ after applying LOCO for three iterations. The assumed BPM error is 1 nm.

After finalization and robust benchmarking of the LOCO algorithm it is planned to exchange the ORM, which was derived using diced parameter settings, by ORMs measured at COSY. A set of orbit response matrices was recorded in a dedicated beam time in November 2015, where only quadrupole gradients have been changed. The goal is to reconstruct these changes. In a second step the measured ORMs are supposed to be utilized for improving the existing COSY model using LOCO.

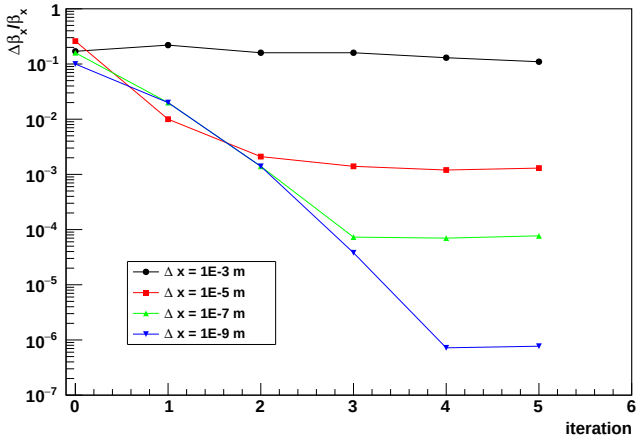

Fig. 4: For the variation of the gradient of all 56 quadrupole magnets the $\Delta\beta_x/\beta_x$ is plotted as function of the iteration number of the LOCO algorithm. The resulting precision clearly depends on the error of the beam position measurement, which is varied from 1 nm up to 1 mm.

References:

[1] R. Maier, Nucl. Instrum. Meth. A **390**, 1 (1997).
[2] C. Weidemann *et al.*, Phys. Rev. ST Accel. Beams **18** 020101 (2015).
[3] D. Eversmann *et al.* [JEDI Collaboration], Phys. Rev. Lett. **115**, no. 9, 094801 (2015).
[4] J. Safranek, Nucl. Instrum. Meth. A **388**, 27 (1997).
[5] F. Hinder *et al.* This annual report: "Automation of the Orbit Response Matrix Measurement at COSY".

Measurement of the Harmonic Content of the HESR Dipoles with a Single 3D Hall Probe

J. Hetzel*

For the upcoming facility of antiproton and ion research (FAIR) in Darmstadt, IKP is responsible for the construction of the High Energy Storage Ring (HESR) [1]. In December 2014 the series production of the bending sector dipoles has started. For beam dynamics calculations the field description of these dipoles is included as one source of non-linear particle motion. This is done in terms of so called harmonic content or multipole components $\mathcal{A}_n$ and $\mathcal{B}_n$ [2], as defined in

$$B_\theta(r,\theta) + \mathrm{i}B_r(r,\theta) = \sum_{n=1}^{\infty} (\mathcal{B}_n + \mathrm{i}\mathcal{A}_n) \left(\frac{r}{r_{\mathrm{ref}}}\right)^{n-1} \cdot \mathrm{e}^{\mathrm{i}\theta}. \quad (1)$$

Here B_r and B_θ are the magnetic field strength' in radial and polar direction averaged over the length of the magnet. r and θ are the polar coordinates of a point inside the aperture of the magnet with origin at the reference trajectory. r_{ref} is a fixed reference radius. In previous calculations (e.g. [3]) the utilized harmonic content is based on model assumptions. As the first dipoles are available now, these assumptions can be replaced by a harmonic description based on measurements.

Different techniques can be applied to measure the harmonic content. In straight magnets the most common techniques are rotating coils and vibrating wires. As the sector dipole is curved in the transversal direction, rotating coil technology with a coil along the whole trajectory[1], cannot be used. Alternative approaches with shorter coils [4] used at different positions along the trajectory or a modified description of the harmonic content along with vibrating wire technology[5] are subject to current research and development. To measure the multipoles of the HESR dipoles a different approach based on hall probes is used[2]. The current work serves as a prove of concept for an automated device for the measurement of the dipoles which is currently developed in cooperation with ZEA Jülich.

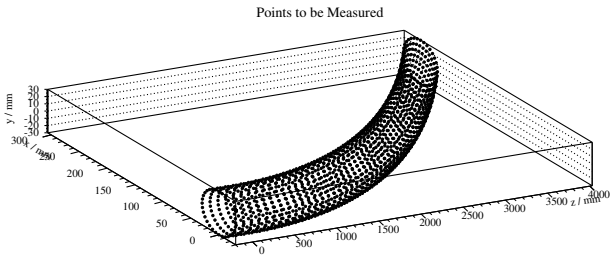

Fig. 1: Sketch of points at which a measurement is performed. The magnet is located such that the center of the entrance face is at $(0.,0.,0.)$.

The principle of the topical measurement is the following: The hall probe is located at equidistant points at a circle with fixed radius with respect to the main trajectory. This circle is in the plane normal to the main trajectory. The radial component as well as the polar component are then measured at each point. Afterwards the circle is moved along the trajectory and further measurements are carried out. This procedure is repeated until the mesh of measured points describes the surface of a bend cylinder through the whole dipole (cf. fig. 1). These measurements also include the fringe field outside the geometric boundaries of the element. The measured values for each polar coordinate are then averaged along the trajectory. Afterwards the harmonic content is estimated via a Fourier transform of the measured and averaged data.

In comparison to the other measurement methods mentioned above, a hall probe based measurement has the advantage of being able to resolve the field locally. On the other hand this results in the necessity to calibrate the orientation of the probe with high accuracy. For the current measurement a single 3D Hall probe [7] attached to a computer driven translation stage is used. The probe used in this setup is measuring in horizontal, vertical as well as in longitudinal direction with fixed orientation with respect to the translation stage. Therefore the measured field in radial and azimuthal direction (cf. eq. 1) as well as the influences caused by bending in longitudinal direction have to be calculated by rotational transformations from the measured data.

Prior to the measurement the position of the probe with respect to the dipole as well as the orientation of the axes of the translation stage is measured by a laser tracker. A possible roll α or pitch angle β cannot be identified by the laser tracker measurement. Therefore the first step is to identify these quantities based on field measurements within the magnet.

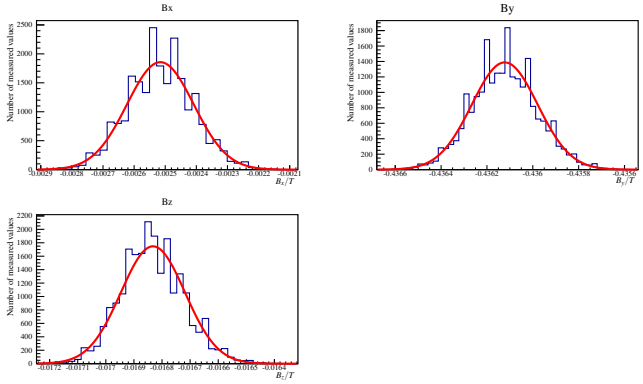

Fig. 2: Measurement of magnetic field inside the dipole to identify roll and pitch angle of the probe. The binned part is the measurement while the continuous line is a Gaussian fit to the data.

As the field well inside the dipole is constant in the vertical direction and vanishes in the longitudinal and horizontal directions, only the subpart of the probe oriented in y direction should measure values differing from zero. A non-vanishing value in either x or z direction can directly be interpreted as caused by a non-zero roll or pitch angle. To correct for these angles a measurement on a circle at $z = 150\,\mathrm{mm}$ inside the magnet to ensure the absence of effects from the fringe field is taken. All values are averaged and the pitch and roll angles are identified. For the present setup a roll angle of $\alpha = 5.8\,\mathrm{mrad}$ along with a pitch angle of $\beta = -42.3\,\mathrm{mrad}$ are identified by this method (non vanishing B_x and B_z in figure 2). In all succeeding steps these angles are taken into account

[1] And therefore it is averaging over the whole magnet as desired.

[2] Similar measurements have been successfully tested at Alba University[6]

by multiplying a rotation matrix to the measured data B_{meas}

$$\vec{B}' = \begin{pmatrix} \sin(\alpha) & \cos(\alpha) & 0 \\ \cos(\alpha)\cos(\beta) & -\sin(\alpha)\cos(\beta) & \sin(\beta) \\ -\cos(\alpha)\sin(\beta) & \sin(\alpha)\sin(\beta) & \cos(\beta) \end{pmatrix} \cdot \vec{B}_{\mathrm{meas}}.$$

The curvature of the magnet is taken into account by multiplying another rotation around the vertical axis by the yaw-angle $\gamma(z)$. This angle depends on the longitudinal position z.

$$\vec{B} = \begin{pmatrix} \cos(\gamma(z)) & 0 & \sin(\gamma(z)) \\ 0 & 1 & 0 \\ -\sin(\gamma(z)) & 0 & \cos(\gamma(z)) \end{pmatrix} \cdot \vec{B}'.$$

The achieved values are then averaged along the longitudinal path according to

$$\bar{B}_i(x,y) = \int_{-\infty}^{\infty} \frac{B_i(x,y,z)dz}{L_{\mathrm{eff}}} \approx \frac{\sum_{n=1}^{N} B_i(x,y)_n \Delta z_n}{L_{\mathrm{eff}}}, \quad i \in x,y$$

where N is the number of measured circles, Δz_n is the medium distance of the n-th circle to the adjacent circles, and L_{eff} is the effective length of the magnet at the reference trajectory. At present $\bar{B}_z$ is not calculated as it should cancel out due to the symmetry of the magnet. In future one could use this fact as cross check for the validity of the measurement. The values for $\bar{B}_x$ and $\bar{B}_y$ are transformed to the desired values by

$$B_r = \frac{\bar{B}_x x + \bar{B}_y y}{\sqrt{x^2+y^2}}, \qquad B_\theta = \frac{\bar{B}_y x - \bar{B}_x y}{\sqrt{x^2+y^2}}.$$

As the positions on the measured circle are equidistant,

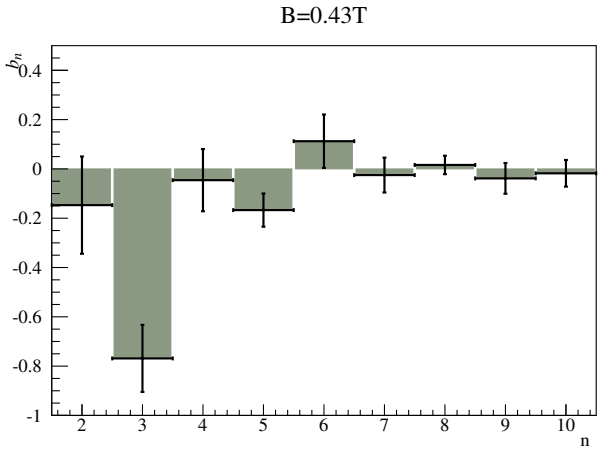

Fig. 3: Normal components of the dipole in units (cf. text, eq. 2). The vertical error bars show the variance over repeated measurements.

the desired multipoles from eq. 1 can be found directly via Fourier transform over B_r and B_θ. The result is shown in figure 3 for the so-called upright harmonics b_n and shown in figure 4 for the so-called skew harmonics a_n. Following a common convention the shown values are normalized to the main component $\mathcal{B}_1$:

$$b_n = \frac{\mathcal{B}_n}{\mathcal{B}_1} \times 10^4, \qquad a_n = \frac{\mathcal{A}_n}{\mathcal{B}_1} \times 10^4. \tag{2}$$

As indicated by the relatively large error bars in figs. 3 and 4, reproducibility is still an issue. However the actual setup

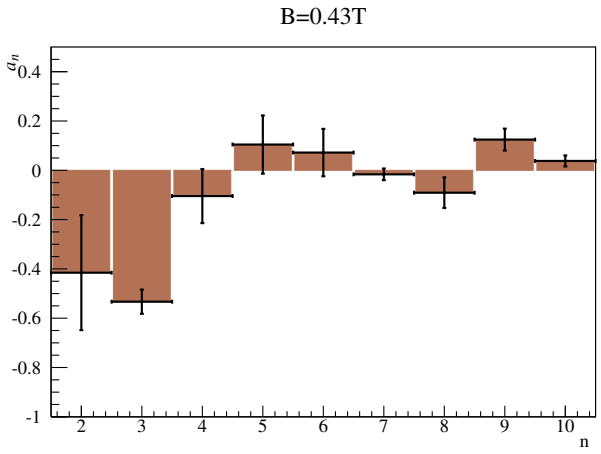

Fig. 4: Skew components of the dipole in units (cf. text, eq. 2). The vertical error bars show the variance over repeated measurements.

has known flaws, such as missing temperature stabilization or a huge incertainty of positioning the probe due to a vibrating connection between probe and traslational stage during movements. Considering, that the results shown here are inline with previous simulations [8] as well as the fact, that even with those flaws some components could be reproducibly resolved, the actual setup serves as prove of concept for further developments of the hall probe based system. As well this is the first confirmation that the simulated and the actual magnetic field of the dipole are in good agreement.

References:

[1] IKP, "High energy antiproton physics, hadron structure and quark-gluon dynamics", `http://www.fz-juelich.de/ikp/EN/Forschung/Beschleuniger/_doc/HESR.html`

[2] S. Russenschuck, "Electromagnetic Design and Mathematical Optimization Methods in Magnet Technology", Version 3.2 (2006), ISBN: 92-9083-242-8

[3] D. M. Welsch, A. Lehrach, B. Lorentz, R. Maier, D. Prasuhn, R. Tölle, "Investigation and Optimization of Transverse Non-linear Beam Dynamics in the High-energy Storage Ring HESR", Proceedings of IPAC'10 (2010), Kyoto, Japan, p. 4659-4661

[4] P. Schnizer, E. Fischer, A. Mierau, K. Sugita "Superconducting Magnet Testing for FAIR", IEEE Transactions on Applied Superconductivity, vol. 24, no. 3 (2014)

[5] M. Buzio, "Magnetic measurement techniques and systems for small and curved aperture magnets", oral presentation at Beam Dynamics Meets Magnets Workshop II (2014)

[6] J. Campmany, J. Marcos, V. Massana, "Determination of Magnetic Multipoles Using a Hall Probe", Proceedings of IPAC'14 (2014), Dresden, Germany, p. 4025-4027

[7] Metrolab, "Three-axis Magnetometers THM1176 and TFM1186", manual, version 1.3 (2014)

[8] H. Soltner, "3D-Dipol-Berechnungen März 2012", internal presentation (2012)

* Institut für Kernphysik 4, FZ Jülich, Germany

Development of an automatic adjustment of the transport channal of the 2 MeV electron cooler at COSY

A. Halama

The 2 MeV electron cooler has been installed in the COSY ring in 2013 for cooling the proton and deuteron beams in the entire energy range of the machine and to gather knowledge for a proposed 4/ 8 MeV cooler at the HESR (FAIR) [1].

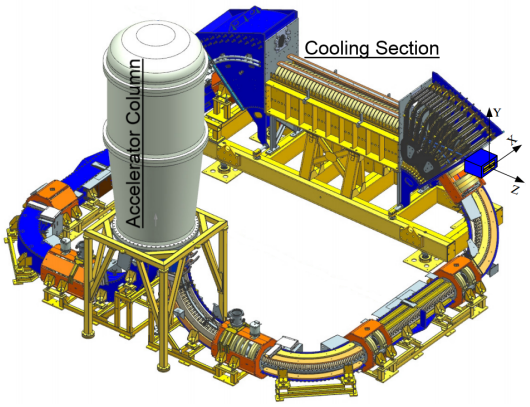

Fig. 1: Cooler magnetic system layout. Edited from [2]

Beam transport and beam parameters

The electron beam is guided by a longitudinal magnetic field through the entire beamline. This allows a lossless transport while maintaining the low electron beam temperature. The wide energy range of 25 keV to 2 MeV[1] and the given geometry make manual adjustments of the beam line time consuming. A cool beam, i.e. an electron beam with low transverse and longitudinal velocitiy spread is crucial for a high cooling efficiency. For this and for suitable recuperation conditions, the beam parameters of interest are the orbit and the dipole and quadrupole motion, informally called larmor and galloping motion. The cooling efficiency also scales with electron current. The beam is easier partially or totally lost having a higher beam current with unsuitable beam parameters. For this reason a precise beam transport setup is of great importance.

Larmor motion

This kind of motion occurs as a superposition of cyclotron motion due to a velocity component perpendicular to the magnetic field and the beam's inherent longitudinal motion. It manifests itself as a helical spiral trajectory. The profiles of the dipole bending field and the longitudinal guiding field of the bending sections do not match exactly therefore larmor rotation occurs within the bending section. Given the condition of an integer number of oscillations inside the bending section[2], the dipole motion will stop at the exit. This is the case, because the beam propagates without any phase advance and gains therefore no larmor amplitude. The longitudinal magnetic field integral varies for some bending sections because adjacent magnetic elements cannot be matched due to limited current ranges and/ or limited knowledge about the magnetic profiles. Therefore the condition of an integer number of oscillations cannot be fulfilled to a satisfying extend by manual adjustment of the magnet currents within a reasonable amount of time. The beam passes through three bending sections of 90° and one bending section of 45° to reach the cooling section halfway of the transport channel. As mismatches are present, the oscillation past each passage of the bending sections sums up. The larmor rotation is dealt with using short dipole magnets to transmit a kick that counteracts the resulting rotation within the cooling section. A suitable setting for the short dipoles can be found using an automatized larmor response procedure. This procedure can only be used to measure and compensate the larmor rotation for one straight section with an individual longitudinal field setting, like the cooling section. Although a beam, suitable for cooling can be delivered as the oscillation may be compensated for the cooling section, the beam gains again larmor amplitude propagating downstream towards the collector. This way an acceptable collector efficiency cannot be guaranteed. Another symmetrically located pair of short dipoles can be used to compensate the larmor rotation shortly before deceleration, but because there is no chance to implement a direct larmor response procedure, there is little chance to assure manually a high collector efficiency. Till now there is only an indirect measurement for the larmor rotation. The electric current for the longitudinal magnetic field in the beam line of interest is varied. Since the magnetic wave number of the larmor oscillation changes accordingly, the phase of the oscillation will change at a stationary BPM downstream. Position changes are logged and used as a curve to fit and yield the amplitude, i.e. the larmor radius.

Galloping motion

Magnetic gradient fields between adjacent elements cause beam heat up. Although this can be seen as incoherent local larmor oscillations with changing phase and amplitude for every electron, it is still a symmetric effect with respect to the magnetic axis. The term galloping growth can be applied here, as the individual larmor radii increase linearly with distance to the axis. As a result the beam starts seemingly to wobble and maintains this motion due to the magnetic lensing of the longitudinal magnetic field. The transverse velocity distribution and therefore the beam tempreture is increased. As such a heated beam is not suitable for cooling, one tries to avoid gradient fields. At two particular locations a gradient field is inevitable. There is a weaker magnetic field within the accelerator column and the stronger adjacent longitudinal field at the first and last bending section. To reduce the heating effect a matching section is installed to shape the magnet field, such that the integrated gradient field effect throughout the passage is decreased. Finding a solution for an appropriate magnetic setting manually proved time consuming and most delicate. To quantify the galloping growth, the larmor radius of the electron beam is measured several times with various parts of the beam made visible to the beam position monitors. The electron beam is superimposed with an intensity-modulation, because the beam would be invisible to the BPM system as a pure DC beam. A separate modulation by quadrant is possible to only highlight a quarter of the beam. If the larmor oscillation coefficients of the center of charge are subtracted from each quarter beam's coefficients

then the galloping motions remains. This is possible as the larmor motion is coherent and fully determined by the center of charge measurement. The obtained resulting radius is the galloping radius per unit of distance between the absolute center of charge and the center of a single quadrant .

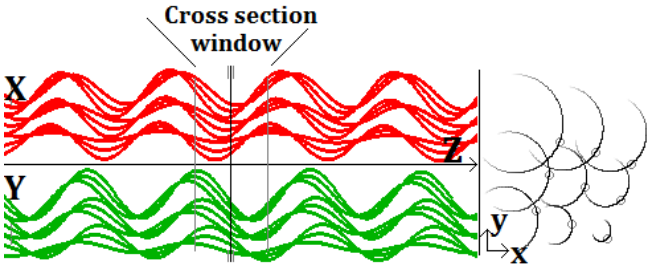

Fig. 2: 9 trajectories in the cooling section are shown. Larmor and galloping motion are superimposed.

Model based adjustment motivation

Till now the orbit is adjusted manually using a set of dipole corrector magnets distributed along the beam line. The settings for the magnets are derived empirically by known energy settings and adjusted one magnet after another for optimal operation. The mentioned short dipoles for larmor rotation compensation do also affect the orbit as well as any changed orbit, using correctors, results into a changed accumulation of larmor amplitudes. Therefore the orbit adjustment and the larmor respone procedure have to be performed sequentially multiple times until the wanted beam properties converge. For the reason of time saving and gaining more knowledge about the beam's behavior, a model basis is called for. This would allow for the prediction of the electron beam behavior for various settings and can be used for fast optimization. For this reason a model is under development for the automatic model based adjustment of the 2 MeV electron cooler. The implementation of the model based adjustment will result in a cold and well controlled beam transport to achieve high cooling efficiency and suitable recuperation conditions. It allows then higher beam current as well as fast and save operation in the upper energy range.

Model description of the 2 MeV Electron Cooler

The model consist mostly of magnetic field maps obtained using COMSOL Multiphysics 5.0 and the underlying implemented physics of electron motion. Other than many commonly used models the magnetic elements are not simplified and translated to transfer functions, because the magnet density is considered very high and there are small upstream influences onto the electron beam. Magnetic assemblies of all magnetic elements were constructed and simulated in reasonable sets with each 1 A of current. Field maps of magnetic assemblies as plain coils in vacuum and those situated within their magnetic shielding were individually simulated. This serves the preparation for the inclusion of saturation effects. During development COMSOL delivered magnetic field data as data point clouds according to the vertices of the mesh. For performance enhancement the fields have been parsed into equidistant grids for fast indexed referencing. Approximated magnetic field values for any point are given by linear interpolation of the eight vertices of the surrounding data grid cube. The accelerating electric field was implemented using a homogeneous static field which scales with the chosen high voltage. Trajectories of an electron beam are obtained by logging an electrons path, which represents the center of charge, driven by its equation of motion. Firstly the magnetic field influence is considered as follows: Given the starting conditions as known position in three-space, $\vec{x}$,the magnetic flux density, $\vec{B}_{(x)}$, at this location and absolute velocity,$\vec{v}$, one obtains derived from $\vec{F}_{cent} = \vec{F}_{lorenz} = q(\vec{v} \times \vec{B})$, where $\vec{v} = \vec{v}_{\perp} + \vec{v}_{\parallel}$ and $\vec{v} \parallel \vec{B}$:

$$\Delta\vec{v}_{lorenz} = \Delta t\,\vec{a}_{lorenz} = \Delta t \frac{q(\vec{v}\times\vec{B})}{\gamma m_0}, \quad \vec{v}'_{new} = \vec{v}_{old} + \Delta\vec{v}_{lorenz}$$
$$\vec{v}_{new_B} = \vec{v}'_{new}\frac{|\vec{v}_{old}|}{|\vec{v}'_{new}|}, \qquad \vec{x}_{new} = \vec{x} + \Delta t\,\vec{v}_{new_B}$$

For reasons of simplexity the velocity, $\vec{v}'_{new}$, is scaled down accordingly. The differential time step has to be kept as small as reasonably possible, for example 1 picosecond. Some additional steps to satisfy physical behavior are implemented but not mentioned. In case of the applied electrostatic field, during acceleration and deceleration respectively, a second step is carried out:

$$\vec{a}_{el} = \frac{q\vec{E}}{\gamma m_0}, \qquad \Delta E_{kin} = (v_{\parallel}\Delta t + \tfrac{1}{2}|\vec{a}_{el}\Delta t^2|)q\vec{E}$$
$$E_{kin_{new}} = E_{kin_{init}} + \Delta E_{kin}, \qquad \gamma_{new} = 1 + \frac{E_{kin_{new}}}{E_0}$$
$$\beta_{new} = \sqrt{1 - \frac{1}{\gamma^2_{new}}}, \qquad |\vec{v}_{new}| = \beta_{new} c$$
$$|\vec{v}_{\parallel}| = \sqrt{|\vec{v}_{new_E}|^2 - |\vec{v}_{\perp}|^2}, \qquad \vec{v}_{new_E} = \vec{v}_{\parallel} + \vec{v}_{\perp}$$
$$\vec{x}_{new} = \vec{x} + \Delta t\,\vec{v}_{new_E}$$

For this step, one convention changes, where now $\vec{v} \parallel \vec{E}$. $\vec{E}$:= electrical field;$\vec{B}$:= magnetic flux density; β := speed of light ratio;γ := Lorenz factor; E_{kin} := kinetic Energy; q := electrical charge; m_0 := rest mass.; $\vec{a}$:= acceleration

Magnetic influence throughout most magnetic elements is steady. This allows for simple trajectory fits according to: $x_{(z)} = x_0 + z\frac{dx}{dz} + A_x sin(k_m z) + B_x cos(k_m z)$ and $y_{(z)} = y_0 + z\frac{dy}{dz} + A_y sin(k_m z) + B_y cos(k_m z)$ respectively. Where it turns out that: $A_x = -B_y$ and $A_y = B_x$ as the phase advance between the x and y coordinate is $\frac{\pi}{2}$. The magnetic wave number km is given by$k_m = \frac{\int Bdl}{\gamma\, m_0\, \beta\, c\, l_{total}}$ as the number of oscillation per unit of length times 2π. The geometric sum of A and B yields the larmor radius. $r_{Larmor} = \sqrt{A^2 + B^2}$

Within the first development stage, the model does not cover saturation and hysteresis effects. Since the transport channel of the 2 Mev electron cooler contains no yoke but only magnetic shielding surrounding the beam line, applying a linear model seemed reasonable. Nevertheless future plans foresee usage of the magnetic field data obtained in vacuum and appropriate scaling factors to cover saturation and hysteresis as follows:

Linear model: $B_{(I)_{total}} = (\frac{dB_{vac}}{dI} + \frac{dB_{shield}}{dI})I$

Saturation model: $B_{(I)_{total}} = \frac{dB_{vac}}{dI}I + B_{0\,shield}(1 - e^{-kt})$

Hysteresis model: $B_{(I)_{total}} = \frac{dB_{vac}}{dI}I + B_{0\,shield}(1 - e^{-kt}) + B_{rem}$, where $B_{rem} = aB_{shield}$ and a being a factor and B_{shield} is not a function of applied electric current. As measurements are ongoing, appropriate constants and factors for those elements where those effects become visible are looked for.

Automatic adjustment

The described model embedded within a control GUI delivers 3D electron trajectories corresponding to the chosen electric currents applied to the magnetic elements. Any beam responses can be obtained by varying currents of magnetic

elements and comparing the former trajectory with the resulting new one. These responses are used for a sequential orbit adjustment as well as larmor rotation compensation. Since more information about the beam's behavior is available, compared to the 12 distributed pairs of BPMs, effects of higher order can be quantified. The fulfillment of the condition of an integer number of larmor oscillations renders feasible, using a model basis. Furthermore, a simulation of a distribution of electrons yields information about galloping growth in various magnetic sections. This way it is possible to set up the matching section between accelerator column and the first and last bending section to result in more favorable beam conditions. A planned automatic procedure will firstly set up the main magnetic fields allowing the most favorable beam transport without using corrector magnet. The matching section will be set up to yield minimal galloping growth firstly within a straight section, which replaces the first bending section and thereafter within the first actual line section. The orbit and larmor rotation will be corrected iteratively. Finally there will be a check for disturbing gradient fields, which would induce the galloping effect. At this point the process might repeat from correcting the orbit and larmor rotation in case those were affected previously.

Current development stage

The Model is coded in Java. Magnetic fields with a satisfying degree of accuracy have been simulated and parsed to be fed into the control GUI. Simulated electron dynamics reflect the expected physical behavior. Trajectory fits resulting from semi-automated response determinations have been used to correct the larmor rotation in the cooling section and the overall orbit. Galloping growth can be decreased using a simulated straight replacement of the first bending section for the setup of the matching sections. The matching section consists of 7 independent solenoidal coils to shape the gradient transition between two different field strengths. Since all coils affect the galloping growth, a simple gradient response optimization was implemented. Iteratively every coil current is slightly varied. This setting with a decreased galloping growth will be kept. Within the simulation, this procedure led to significant beam performance increase. There are ongoing measurements to compare the magnetic field influence of the 2 MeV electron cooler to its model and rescale magnetic profiles if necessary.

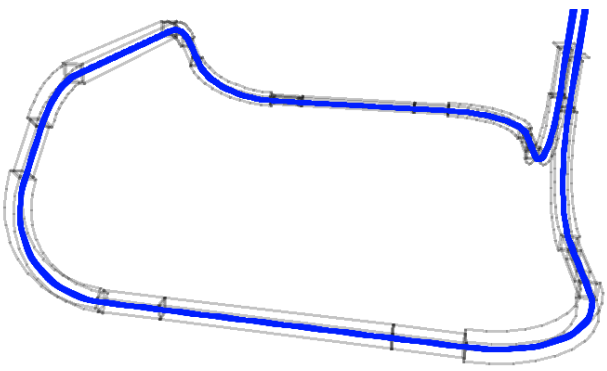

Fig. 3: 3D trajectory representation of the electron beam through the entire magnetic structure.

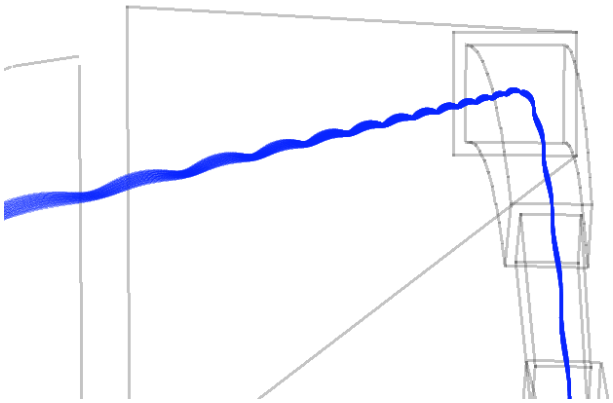

Fig. 4: 3D trajectory representation of the electron beam zoomed through the cooling section.

Outlook

The field maps will be refined to accurately reflect strongly varying gradients. COMSOL simulations for this task are ongoing. When scaling factors for the magnetic profiles agree with the manual response measurements, the model will be tested to predict accurate electron beam behavior. Deviations will indicate where and how to rescale certain magnetic field maps. An Ethernet connection from the control software to the power supply and BPM system will be implemented for remote control and direct fast feedback. Procedures for the automatic adjustment will be implemented and tested on the 2 MeV electron cooler. As soon as long term reliability is ensured, the software will be integrated into the control system of the cooler.

Acknowledgement: The author is thankful for the regular advice and help from the members of the Budker Institute of Nuklear Physics M. Bryzgunov and V. Reva, Novosibirsk and from his supervisor V. Kamerdzhiev.

References:

[1] Alinovskiy, N. et al., "2MeV Electron Cooler for COSY and HESR - First Results", IPAC2014

[2] M. Bryzgunov et al., "Magnetic System of Electron Cooler for COSY," BINP SB RAS, Novosibirsk, Russia MAGNETIC SYSTEM OF ELECTRON COOLER FOR COSY

Comparative numerical study of two BPM designs for the HESR

A. Halama, C. Böhme and V. Kamerdzhiev

Beam position monitors (BPM) are mostly passive devices to measure the transverse beam position of a charged particle beam. The following results were obtained, considering the HESR antiproton injection beam with parameters as follows: kinetic energy of 3 GeV, 6 σ bunch length of 150 m, at least 10^7 particles.[1]

Diagonally cut cylindrical design

The design corresponds to the commonly known cylindrical diagonally cut capacitive BPM pickup. The key feature to this design is the constant linearity across the entire aperture.

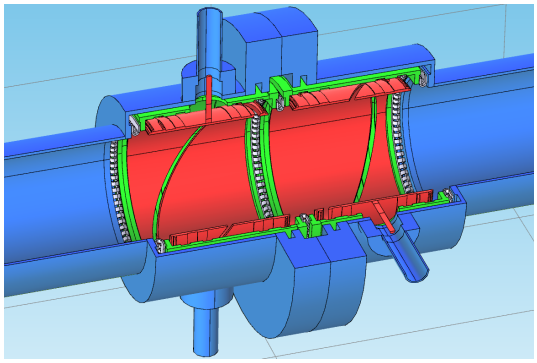

Fig. 1: The image shows the diagonally cut cylindrical BPM design. The pickup electrodes are highlighted in red. The grounded holder cylinders are shown in green. The beam pipe is shown in blue.

The 3D model of the pickup was analyzed using COMSOL 5.0 Multiphysics and LTSpice. The first analysis allowed for capacitance determination for any pair of independent electrode, as voltage was applied between two electrodes and the electric field was simulated. A necessary byproduct is the capacitance. All involved capacitances have been determined such as electrode against ground and electrode against any other electrodes. These results were used for the simulation of the electrical equivalent circuit. The signal shape of the image current source is gaussian and given by $I_{im}(t) = -\frac{N\,e\,t\,L_{BPM}}{2\sqrt{2\pi}\,\sigma^3\,\beta\,c} e^{-\frac{1}{2}(\frac{t}{\sigma})^2}$ [2]. The voltage drop resistor, i.e. the input impedance of the following preamplifier was chosen to be 500 kΩ. This sets the cut off frequency with an estimated capacitance against ground of 20 pF to about $f_{cut} = \frac{1}{2\pi\,5{\cdot}10^5\,\omega 2{\cdot}10^{-11}pF} \approx 16\,kHz$. The characteristic frequency is 1.86 MHz and equals the σ-width in the frequency spectrum.

$$I_{im}(t) = -\frac{N\,e\,t\,L_{BPM}}{2\sqrt{2\pi}\,\sigma^3\,\beta\,c} e^{-\frac{1}{2}(\frac{t}{\sigma})^2}$$

In order to obtain a signal response as voltage drop proportional to the longitudinal beam shape, the following condition must be fullfilled; the cut of frequency is much smaller than the characteristic frequency content of the beam shape. Capacitances of the diagonally cut cylindrical design were determined as follows: Cel-ground = 19 pF and Cel-el = 7.6 pF. Capacitances between both measurement planes were not considered at this stage. Given the image current and the capacitive and resistive values for the equivalent circuit, an output voltage for a centered beam was obtained as $V_{output} \approx 49\,\mu V$. This values can also be obtained using the following formula: $U_{img} \approx \frac{3}{\sqrt{2\pi}} \frac{L_{BPM}}{L_{Bunch}} \frac{N\,e}{C_{el}}\, e^{-\frac{1}{2}(\frac{6\,t\,\beta\,c}{L_{Bunch}})^2}$, as long as the mentioned condition is fulfilled.

Position dependent parameters

The signal yield and sensitivity distributionof the BPM were determined. For this, the entire equivalent circuit had to be used.

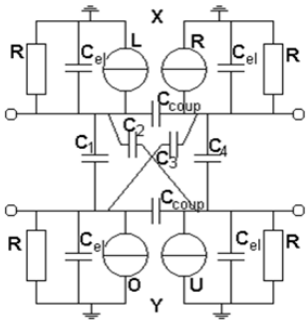

Fig. 2: Entire equivalent circuit, containing each electrode as image current source with parallel capacitance towards ground and all coupling capacitances between all electrodes.

Appropriate scaling factors for the image current sources to reflect the positional response correctly and the missing capacitances were included. Those contained the capacitances of each electrode to any other and all electrodes towards ground. For the diagonally cut cylindrical design two electrodes are situated closer together, two are further apart and two pairs have an intermediate distance to one another. This leads to an asymmetric capacitance distribution. As a result of that, the electrical center and the mechanical center do not coincide. The displacement is approximately 0.1 mm for both axes. The characteristic linearity could be verified. But due to the asymmetric distribution of cross capacitances the sensitivity changes slightly for any other position. A prototype of this design is expected to be available soon for characterization and comparison to verify the simulation results.

Design utilizing four straigt symmetrical electrodes

Following the recomendation given in [3], another possible design was investigated. This design is characterized by its symmetry and smaller capacitive coupling between the electrodes.

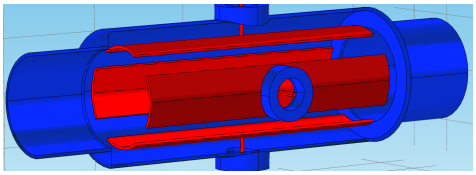

Fig. 3: The image shows the initial BPM design. The pickup electrodes (red) and the beam pipe (blue) is shown.

Manufacturing tolerances will result only in little deviation from the expected behavior. As the length and angular coverage was open for discussion different sized BPMs were simulated and compared to the first design.

	Capacitance in pF		
BPM Design	diag. cut	sym. straight	
Dimensions	77 mm	27 cm; 60°	27 cm; 82.5°
electrode - ground	19	18.6	21.8
$elec_{x+}$ - $elec_{x-}$	7.6	3.1	3.6
$elec_x$ - $elec_y$	2.3	4.3	7.4
$elec_x$ - $elec_{y\ alt2}$	1.3	–	–
$elec_x$ - $elec_{y\ alt3}$	0.9	–	–

Table 1. Exemplanary summary of capacitance values.

These lead to the voltages such as:

	Output voltage in µV		
BPM Design	diag. cut	sym. straight	
Dimensions	77 mm	27 cm; 60°	27 cm; 82.5°
electrode - ground	49	61	72

Table 2. Exemplanary summary of peak to peak output voltage at electrode for a centered beam.

Noise and signal-to-noise ratio

The spectral noise density is given by the thermal noise of the input impedance filtered by the intrinsic capacitance with the low pass cut-off frequency $f_{cut} = \frac{1}{2\pi RC}$. For that reason, the rms noise level is different for any other capacitance that is given with a different geometry. Three bandwidths have been looked at for that in particular.

	signal-to-noise ratio		
BPM Design	diag. cut	arc-like	
Dimensions	77 mm	27 cm; 60°	27 cm; 82.5°
$full_{quasi}$ bandwidth	1.39	1.78	2.36
broad band filter 200 kHz - 1200 kHz	4.50	5.81	8.45
narrow band filter 480 kHz - 520 kHz	1.44	1.94	2.82

Table 3. Signal-to-noise ratio for the different BPM types and sizes. Determined by rms ratio resulting upon sharp-edge filter fourier transformed frequency spectrum.

Sensitivity

Another point of interest is the sensitivity distribution of the BPMs. For this, an array of beam positions was simulated to yield signal levels for all electrodes at these locations. These beam positions reflect a pencil beam behavior as the relative influence of a longitudinal line like charge. This influence towards each electrode is used to scale the image current source in the equivalent circuit appropriately. Upon calculation of the difference over sum signal value, this obtained value has to be scaled using the sensitivity to yield the position. Unlike as the diagonally cut BPM, the capacitive arc-like BPM shows no constant sensitivity across the transverse plane. Therefore one is free to select from a variety of position yielding formulas, as common digital post processing has to be perform in any given case. Possible formulas are for example [2]:

$$(1) \quad y = b\frac{U_{up} - U_{down}}{U_{up} + U_{down}},$$

$$(2) \quad y = b\frac{U_{up} - U_{down}}{U_{up} + U_{down} + U_{left} + U_{right}},$$

$$(3) \quad y = b\, ln(\frac{U_{up}}{U_{down}})$$

or with a 45° arrangement

$$(4) \quad y = b\frac{(U_1 + U_2) - (U_3 - U_4)}{U_1 + U_2 + U_3 + U_4} \quad or$$

$$(5) \quad y = b\, ln(\frac{U_1 + U_2}{U_3 + U_4})$$

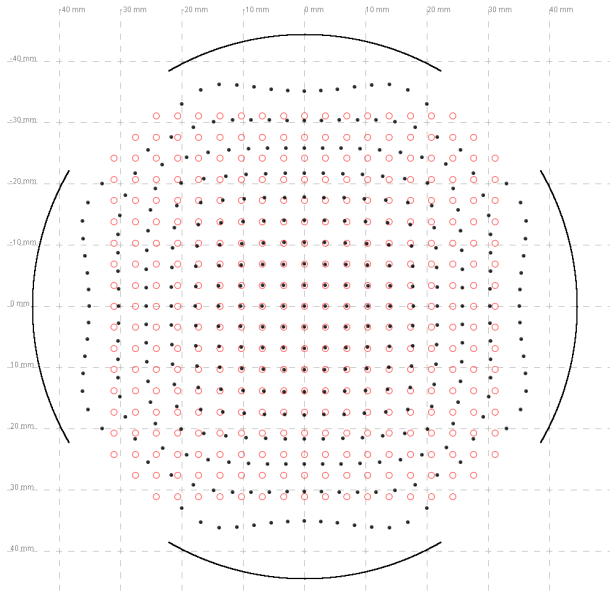

Fig. 4: The projection of a pencil beam resulting from formula (3).

The sensitivity of the diagonally cut BPM was determined to be 0.9 %/mm. The center sensivity of the proposed design varies for every applied position determination formula. Formula (1) through (5) lead to higher center sensitivities, ranging from 1.21 %/mm to 4.8 %/mm for the 60° pickup. Where this drops off to the range of 0.67 %/mm to 3.36 %/mm for a beam at half aperture position. The values for the 82.5° pickup are about 5 % lower.

A decision regarding the manufacturing and testing of a prototype of the proposed design will be made as soon as the error analysis is completed.

References:

[1] C. Böhme et al., "Beam Position Monitors for the HESR," IKP Annual Report 2014, Forschungszentum Jülich

[2] Peter Forck, Piotr Kowina, Dmitry Liakin, "Beam Position Monitors," GSI, Darmstadt, Germany

[3] M. Bozzolan, M. Gasior, R. Jones, M. Wendt, CERN, P. Kowina, M. Schwickert, GSI, and K. Wittenburg, DESY "Review of COSY Beam Diagnostics", Jülich, November 19th - 20th, 2015

Design of a test bench to characterize BPMs for the HESR

S. Srinivasan, N. Giese

A test bench is a virtual environment with tools for measurement and manipulation to manually verify the correctness of a device under test (DUT), here, beam position monitors (BPMs). The test bench that will characterize the BPMs for the HESR will be stimulus type, containing the stimulus driver and the DUT. This will eventually provide a conditioned response elicited by the stimulus.

BPMs are beam diagnostic devices implemented to precisely measure the transverse beam position. However, prior to beam operation, it is necessary to characterize the BPM which involves establishing a relationship between beam position and sensitivity, developing a look-up table and determining its electrical center. This will be achieved with the help of a standalone test bench using stretched wire method.

Stretched wire test bench at COSY

The fundamental design concept is the in-tower mounting of the BPM along with its main stand elements within two BPM reference boxes made of aluminum. This aids in realization of the stretched wire passing through the hollow center of the BPM, thus avoiding any wire bending due to gravity. The whole setup will be rested on a granite slab of surface flatness smaller than 9 µm. This will aid in precise mounting of BPM reference box on to the BPM as well as damping the ground vibrations.

With the BPM fixed on the BPM reference box from either ends, the stretched wire is moved by micro-mover stages to yield wire-BPM relative displacement through their position readout. Moving the wire instead of the BPM is preferred as the calculated weight of the BPM assembly exceeds the normal load capacity of the translation stages. Figure 1 represents the front, isometric and side view of the test bench setup.

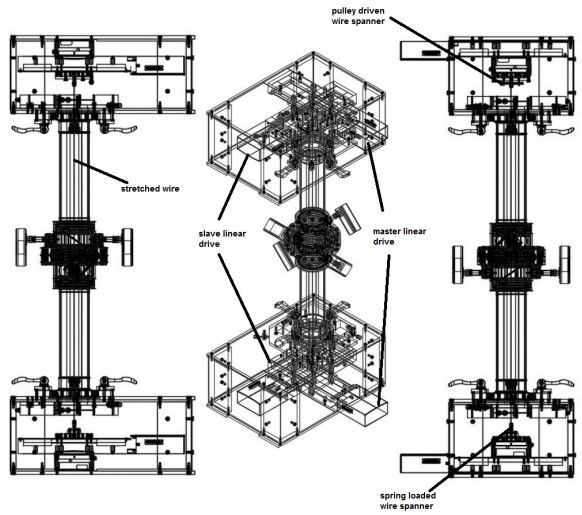

Fig. 1: Front, Isometric and Side view of the test bench

The test bench that will be assembled on the granite slab will have the following components:

BPM and its assembly: The design for the HESR BPMs has been chosen as per the technical demands of HESR. The BPM chosen is a capacitive pick-up with a cylindrical geometry [1]. Figure 2 shows the 3D view of the HESR pickup electrodes.

Two electrode pairs (*i.e.* pickup), which are galvanically isolated, are held in place (one each in X and Y plane) by a grounded supporting cylinder.

The BPM assembly, Fig. 3, housing the grounded cylinder at its centre, has its one end fixed with a non-rotatable flange and the other with a rotatable flange. Moreover, the vacuum surface on these flanges house two reference pins (each on X and Y plane in gold, Fig. 4), at 10° offset in CW direction. These guide through slots are provided on the vacuum surface of BPM reference box, to precisely measure the mechanical center of the BPM.

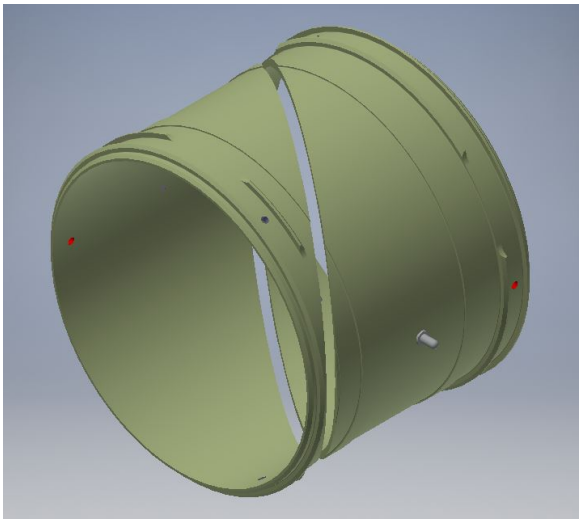

Fig. 2: Isometric view of the pickup electrodes

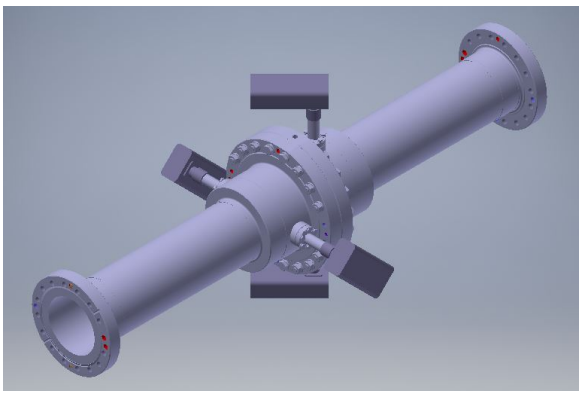

Fig. 3: Isometric view of the BPM assembly

BPM reference box: Two reference boxes (same dimensions) made of aluminum will be used to house the BPM assembly. The reference box, as shown in Fig. 4, is provided with precisely machined reference edges (marked) to initially mount the assembly from either ends, on its vacuum surface, in horizontal plane. Such a strategy is chosen for the as-

sembly, primarily to minimize mechanical deviations as one end of the BPM assembly has a rotatable flange and also to zero the mechanical aberrations on the vacuum surface while mounting. The reference box also entails press clamps (in red) to secure the BPM assembly.

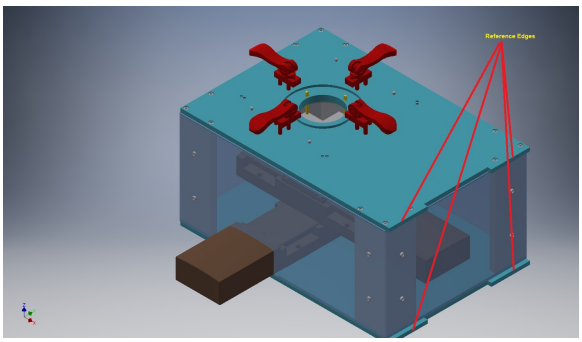

Fig. 4: BPM reference box

Optical micrometer: Two RF656-25[2] optical micrometers, from Riftek, will be mounted in *XY* assembly, as shown in Fig. 5, from the inside of the top plate of the BPM reference box. The two reference pins, mentioned earlier, will fall within the micrometer's measurement range, 4.5 mm from its receiver's end. Such an arrangement is prioritized, as the positional information of the beam analogue *i.e.* the stretched wire will be measured with respect to the reference pins.

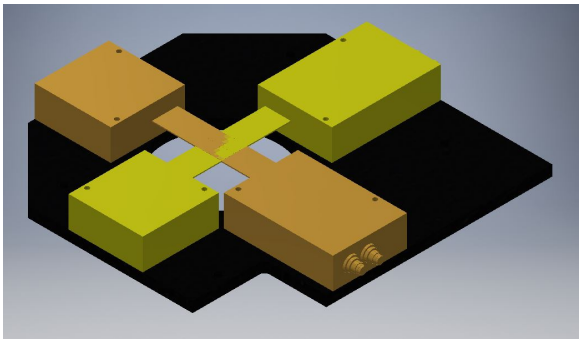

Fig. 5: *XY* assembly optical micrometer

Micro-mover stage: The two linear stages will be orthogonally mounted (master-slave) on the base plate of the BPM reference box, providing the wire-BPM relative displacement in (*X*,*Y*) direction. The M-ILS150HA[3], as shown in Fig. 1 (*XY* assembly), will be chosen for each translation stage, being a high performance precision micro-mover driven by DC motors from Newport. The maximum linear travel range is 150 mm with an on-axis accuracy of $\pm 2\,\mu$m and the smallest incremental linear motion of 0.3 µm. The maximum normal load capacity is 250 N (25.5 kg) which can withstand the weight considerations of the wire elements in the test bench.

Wire elements: The selected wire will be stretched through the BPM assembly, from the upper BPM reference box to the bottom BPM reference box. This will be achieved by fixing it between the wire spanners and allowing it to pass through the BPM assembly, thereby one spanner acting as a hanging weight, employing gravity. In the bottom BPM reference box, the wire spanner will be mounted on a spring load to compensate for tension loss whereas in the upper BPM reference box, the wire spanner will be mounted on the pulley platform to provide easy access, as shown in Fig. 1. The wire elements, will then be mounted on the slave linear drive at both ends.

RF matching networks: The RF matching networks will be used to provide undisturbed excitation signal and measure S-parameters via a network analyzer).

Metrology of the stretched wire test bench

For the design of the test bench, we have decided a target accuracy of 50 µm in positional measurement of the BPM. Therefore, the uncertainties that can be introduced by the test bench should be minimized, as it is required for linearity and offset characterization tests. This is critical for such high precision measurements as the misalignments of the wire in the test bench can adversely affect the accuracy of the HESR BPMs. In such sense, the typical misalignments that will be considered in this metrology test includes mechanical fabrication, linear drive positioning uncertainties, and the assembly of the test bench elements. Moreover, the concern that the test bench could be deformed under load conditions was eased by FEA stress analysis simulation, giving maximum displacement in nanometer ranges.

Wire tilt: The inclination of the wire with respect to the BPM cross-sectional plane will be measured by the *XY* assembly of optical micrometer RF656-25 on either ends of the BPM assembly. Deviations in the positional information from the micrometer assembly will imply the wire tilt. This can be rectified by correcting the positions of the linear drives until same measurements are observed in micrometer assemblies.

Coplanar linear drive and micrometer assembly: The coplanar arrangement of the linear drive assembly and the micrometer assembly aids in reducing positional uncertainties. Such uncertainties can be rectified by the usage of micrometer screws on the optical micrometer platform.

Wire Offset: Followed by the wire tilt correction, the wire is positioned at the BPM mechanical center with the help of linear drives. The BPM mechanical center will be measured at ZEA metrology section i.e. a 3D CMM (Coordinate-Measuring Machine) with a linear measuring tolerance of 2.8 µm. This positional information will be used to reference the measured electrical center to its mechanical fiducial and provides the reproducibility of the test bench. The optical micrometer platform will be placed coaxially, as such an arrangement would mean on-plane observation of the BPM cross-section. After positioning the wire at the BPM mechanical center with the linear drives and verifying with optical micrometers, this position will be referenced as the home position for further measurements.
In this test bench, the uncertainties due to wire rotation on the wire center is minimum as the arrangement of the test bench restricts these. This is determined by the readings of the linear drives provided the optical micrometer reading remains unchanged in the cross-sectional plane. This is an important parameter as by definition wire center is the only point which does not change its position under rotation or torsion.

Orthogonality and parallelism of wire trajectories: As per manufacturer's specifications, the relative orthogonality between linear drives mounted in *XY* configuration is $\pm 2.9^\circ$.

This might change the trajectories followed by the wire in XY plane. Nevertheless, the wire trajectory deviation will be measured with the help of optical micrometers on either ends for a wire travel within the optical micrometer's measurement range, obtaining much smaller deviations. The pitch and yaw of the linear drive is $\pm 75\,\mu$rad ($\pm 0.0043^\circ$) and $\pm 50\,\mu$rad ($\pm 0.0029^\circ$). Corresponding to these deviations (pitch is responsible for non-parallelism), the slope of the X and Y coordinate is $0.0875\,\mu$m/mm. Hence, for a linear travel of $\pm$45mm in either X or Y coordinate will result in a deviation (both ends) of $3.9375\,\mu$m.

Future Works

Followed by the construction of the test bench, we consider the stretched wire signal excitation as the primary method to detect BPMs electrical center and characterize it. This can be achieved by using fixed pulse shapes to generate a look-up table at fixed frequencies.

Acknowledgement

The authors would like to thank Vsevolod Kamerdzhiev, Christian Boehme, Arthur Halama and Maike Maubach for their valuable efforts in realising the conceptual design and steering us in the right direction whenever needed.

References:

[1] **A. Halama**, *Comparative numerical study of two BPM designs for the HESR*, IKP Annual Report 2015, FZJ, Germany.

[2] **Riftek**, *RF656 User Manual*, Available at `https://riftek.com`.

[3] **Newport**, *ILS User Manual*, Available at `http://assets.newport.com/`

GAN-BASED HIGH POWER AMPLIFIER FOR THE HESR MAIN STOCHASTIC COOLING SYSTEM

R. Stassen, B. Breitkreutz, N. Shurkhno, H. Stockhorst

Abstract

The stochastic cooling system for the HESR consists of various broadband, active devices like low noise amplifier or programmable delay-lines. Most critical parts of the active elements are the high power amplifiers. The stochastic cooling power amplifiers for the HESR will be based on new GaN devices. Nonlinearities of these devices necessitate a dedicated analysis of the use in stochastic cooling systems.

HIGH POWER AMPLIFIERS

One of the most critical parts in the active chain of the stochastic cooling system will be the high power amplifiers. Different concepts have been analysed to find the best high power, broadband amplifiers. Several decades ago GaAs (gallium-arsenide) was the first choice to build high power solid-state amplifiers in the GHz-range. Since some years GaN (gallium-nitride) technology became very attractive not only for expensive military applications [1]. Higher voltages and higher heat-densities allow much higher power with better efficiencies.

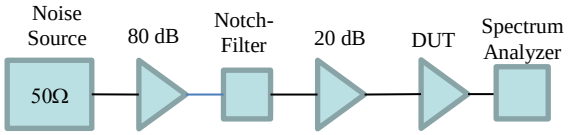

Figure 1: Setup to determine intermodulation products due to non-linearities with the aid of a notch-filter.

Stochastic cooling is mostly dominated by highly amplified noise. Noise-peaks can easily drive amplifiers into saturation. Due to non-linearities intermodulation products (IMD) will always occur even far below the 1 dB compression point (P_{1dB}). Normally, these IMD products are not visible, but with a notch-filter (comb-filter) - which is already in use in the longitudinal cooling system – these products can be measured. Noise will be filtered by the notch-filter in the same way as sinusoidal signals and the notch-depth can be directly measured with a spectrum analyser when highly gained noise is used. IMDs will reduce the notch-depth they will fill up the notch-depths. Figures 1 and 2 show a corresponding measurement. Starting with a 50 Ω load as noise-source, two low-noise preamplifiers boost the noise level (blue curve) to about -80 dBm. After the notch-filter one can clearly see the noise reduction by the notch (notch-depth: about 35 dB). The insertion loss of the notch-filter can be compensated by an additional medium power amplifier (green curve). After the high-power amplifiers (DUT: device under test) the notch-depths are reduced. The results of one 50 W GaAs amplifier and an 80 W GaN based prototype already optimized for the HESR cooling system are shown.

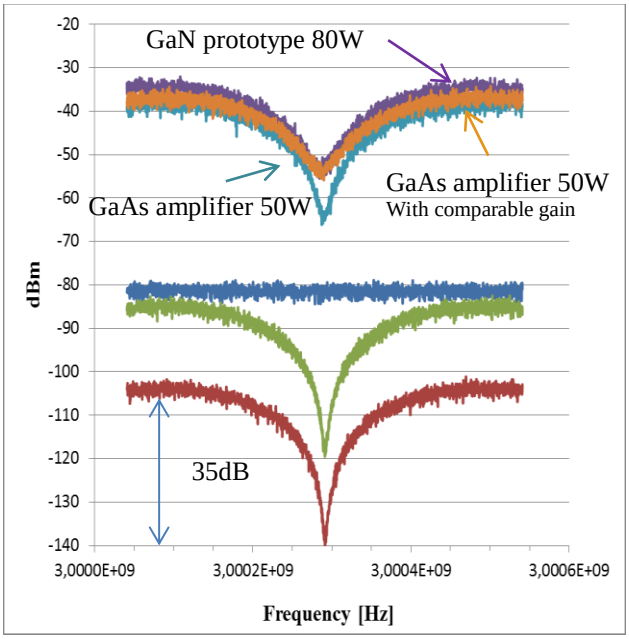

Figure 2: Filling up the notches due to IMDs-products of noise by non-linearities of power-amplifiers.

In a first view the GaAs amplifier looks better than the GaN prototype. But when the input level was increased to a comparable gain regarding the 1 dB compression point, no great difference could be realized. One has to keep in mind here that the noise level is far away from the 1dB compression point. Although GaN devices are not as linear as GaAs

High notch-depths in the whole frequency-range are essential for a good stochastic filter cooling. IMD products will create additional noise which acts as an additional heating term to the beam particles. The cooling time and particularly the equilibrium momentum spread will be increased. The existing stochastic cooling system of COSY was used to demonstrate this [2]. The notch-depth of the optical notch-filter can be easily changed to demonstrate the influence of a finite notch-depth. Figure 3 shows the normal longitudinal cooling of 5×10^8 protons at 2.6 GeV/c with the initial momentum distribution (yellow) and the final distribution (blue). The average notch-depth was in the order of 30 dB and better.

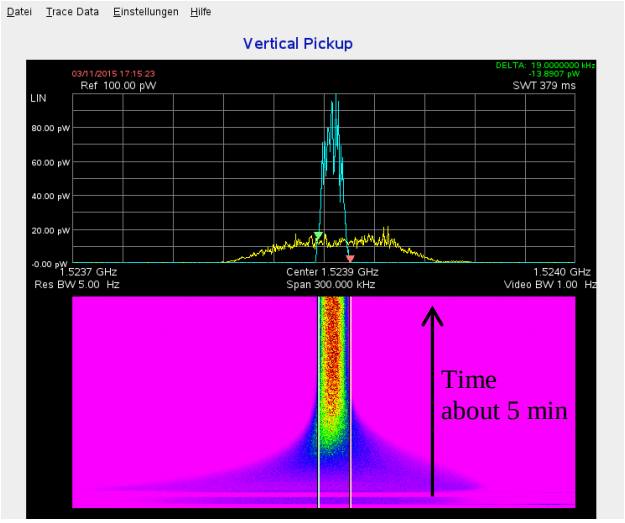

Figure 3: Starting and final beam distribution with a notch-depth of more than 30 dB.

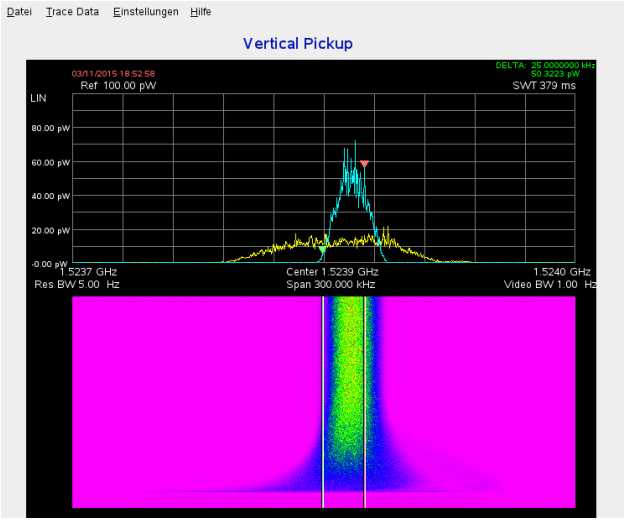

Figure 4: Starting and final beam distribution with a notch-depth of about 15 dB.

The equilibrium momentum spread was reached after about 200 seconds. After changing the notch-depth to about 15 dB the equilibrium value was doubled (Fig. 4).

The same behaviour can be found in the simulations as demonstrated in Figure 5 [3]. Further simulations have shown that notch-depths higher than 30 dB will no longer improve the cooling time and equilibrium value.

Still not solved is the discrepancy of the equilibrium with high notch-depths. The larger measured equilibrium emittance cannot be explained with residual gas scattering and IBS (Intra Beam Scattering) plays no role at this energy.

Beside the IMD with highly gained noise several additional requirements are important for a successful stochastic cooling system.

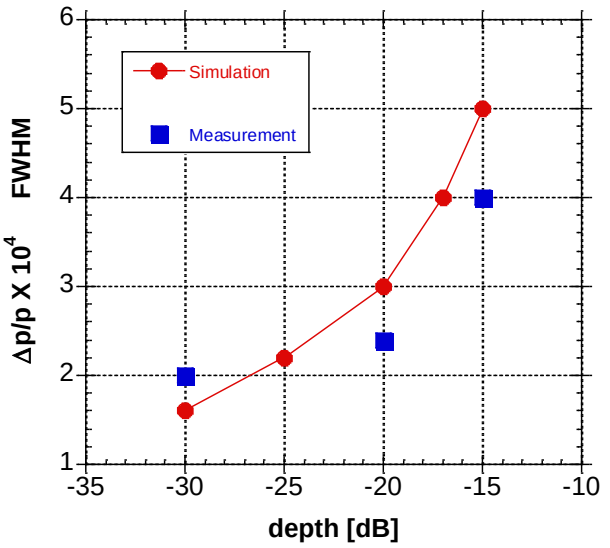

Figure 5: Simulated and measured beam equilibrium as function of different notch-depths.

Not only a flat gain and phase response but also flat group-delay behaviour over the entire frequency band allows an optimized stochastic cooling. The good experience at the COSY stochastic cooling system - to build each active element in the cooling chain as good as possible – led to a required gain variation smaller than 1dB, phase-change less than +/-10° and a group-delay within +/- 100ps. The output power is in the order of 80W.

The signal delay from pickup to kicker in the stochastic cooling system is limited. Highly integrated technologies like LTCC will be mandatory to build compact and electrical short amplifiers. After several years of prototyping and market validation all high power amplifier of the main system (2-4 GHz) have been ordered now at the Canadian company Nanowave. Here all necessary technologies to build such amplifier are in-house.

REFERENCES

[1] P. Saad et al., “Design of a Highly Efficient 2-4GHz Octave Bandwidth GaN-HEMT Power Amplifier”, IEEE Transactions on Microwave Theory and Techniques, Vol. 58, No7, July 2010

[2] R. Stassen et al., “COSY as ideal Test Facility for HESR RF and Stochastic Cooling Hardware”, proceedings of PAC09, Vancouver, BC, Canada, 2009

[3] H. Stockhorst, R. Stassen, “Stochastic Beam Cooling”, 2nd CBAC meeting, IKP, FZ-Juelich, 2015

Status of the HESR BPM

C. Böhme, A. Halama and V. Kamerdzhiev

1 Introduction

The HESR, part of the FAIR project in Darmstadt, Germany, is dedicated to the field of antiproton and heavy ion physics. The envisaged momentum range is 1.5 GeV/c to 15 GeV/c. The racetrack shaped ring will be 575 m long.

2 BPM system

The BPM system is designed to measure the beam position throughout the ring. 22 BPMs are located in each arc of the ring and will be co-located to sextupole magnets. An illustration of the elements between two dipoles in the arc sections is given in Figure 1. 32 BPMs are planned to be located in the straight sections, giving a total number of 76.

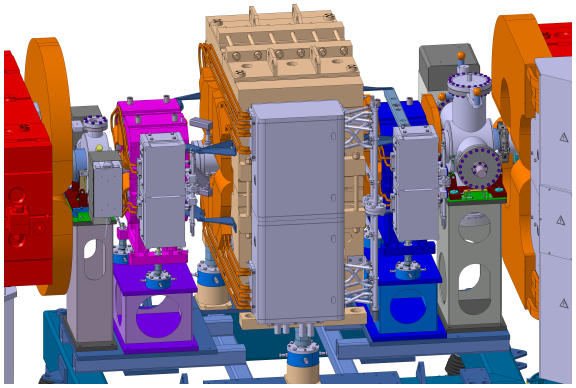

Fig. 1: Illustration of the elements between two dipole magnets in the arc. From left to right: Dipole magnet (red), pumping vessel, sextupole magnet (purple), BPM, quadrupole magnet (ocher), steerer (blue), pumping vessel, dipole (red). Magnetic coils are in orange.

The BPMs consist of two cylindrical diagonally-cut pickups. Both sets are rotated by 90° towards each other in order to measure the location in both plains. The setup is shown in Figure 3. The inner diameter of the pick-ups is 89 mm and the length 77 mm with a cut of 3 mm between the pickups using an angle of 55.5°. The expected signal levels depend on the ion charge, the amount of ions, and the bunch length and can be calculated using

$$U_{img}(t) = \frac{1}{\beta c C_{el}} \frac{A}{2\pi r_{BPM}} I_{beam}(t) \quad (1)$$

$$= \frac{1}{\beta c C_{el}} \frac{L_{BPM}}{2} I_{beam}(t) \quad (2)$$

The capacitance was calculated using COMSOL Multiphysics 5.0 software. For the lowest case, the first injection of antiprotons with 10^7 particles in the ring, the signal level was calculated to 49 μV, and the highest case, again antiprotons with 10^{11} particles stored, the signal level is 390 mV.

The achievable resolution ε is dependent on the capacitance between the pick-up electrodes:

$$\varepsilon = \frac{1}{b} = \frac{\alpha}{r_{BPM}} \quad (3)$$

$$\alpha = \frac{1 - \frac{CD}{C_{ges}+CD}}{1 + \frac{CD}{C_{ges}+CD}} \quad (4)$$

with CD the capacitance between the pick-up electrodes and C_{ges} the capacitance to ground. The CD value was determined to be 7.6 pF. With this value $\alpha = 0.0146 mm^{-1}$.

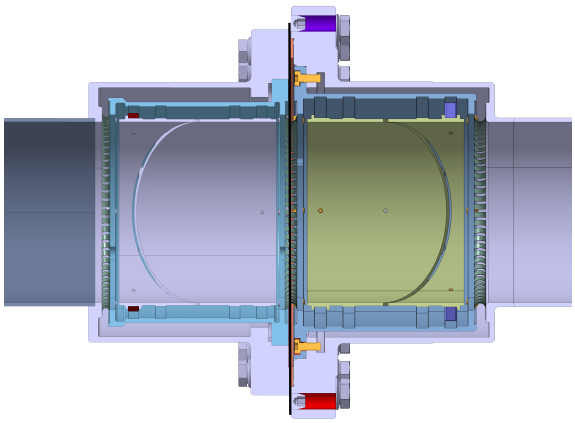

Fig. 2: Comparison between the design of the COSY BPM (left) and the current HESR design (right). Pictures have been scaled to fit the inner diameter of both BPMs. The distances between the BPM pick-ups and the carrier tube on ground potential have been widened in order to reduce the capacitance and so increase the signal level.

The pick-up design is based upon the COSY BPMs [1]. The length and diameter is shrunk by a common factor in order to keep the length to diameter ratio. As can be seen in Figure 3 the electrodes are mounted into a carrier tube which is then inserted into the beam pipe. In order to enhance the signal level, which is proportional to the capacitance to ground, efforts were made to increase the distance from the beam pipe to the carrier tube without changing the inner diameter of the BPM nor the outer diameter of the beam pipe as shown in Figure 2. In detail:

- Increasing the gap between carrier cylinder and electrodes.
- Shorten all screws to the minimum length.
- Increasing the diameter of holes in the carrier cylinder for the signal connections.
- Introducing bevels on the small edges of the pick-up cylinder.
- Removing all unnecessary holders of the carrier cylinder, left from production.
- increasing the gap between the two electrodes to 3 mm.

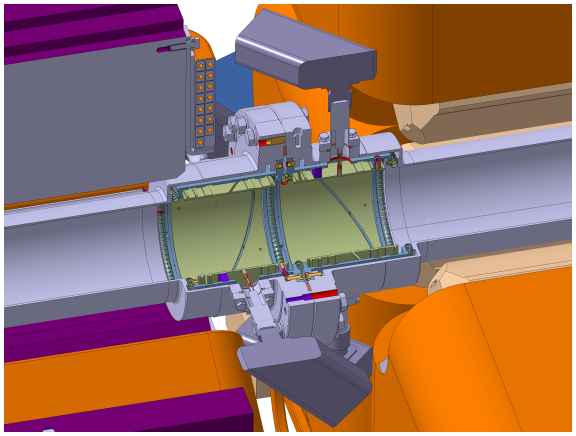

Fig. 3: Illustration of the BPM between a sextupole magnet (left) and a quadrupole magnet (right).

These efforts lead to an increase of about 50 % in signal level shown in simulation.
Furthermore, the influence of the coupling of the pick-ups of one plain to the other was examined. The coupling effects the sensitivity of one plain if the beam moves in the other plain. Also the electrical center is shifted in one plain by the movement in the other plain. Simulations showed, that by moving the beam by 1 mm in e.g. Y direction, the offset in X direction shifts by 2.6 μm.
A prototype of the HESR BPM is being manufactured in the central machine shop of the Research Center. It is expected to be ready for testing by February 2016 . A test bench for testing the prototype and later on the entire series, is under construction [2].

3 BPM Redesign

In November 2015 a COSY beam instrumentation review was performed, where, although not in the main scope of the meeting, the design of the envisaged HESR BPM was discussed [3]. This lead to a recommendation from the review committee to use a pickup utilizing four straight symmetrical electrodes instead of the cylindrical diagonally-cut style. The benefit is, that the electrodes can be longer resulting in a higher signal level. Such a design can be made very symmetrical eliminating the systematic errors associated with the inherent asymmetries of the diagonally-cut pickup. The disadvantage is the non-linear behavior. However, the modern readout electronics, directly digitizing the signals and performing all calculations afterwards, is capable of correcting for these effects. Initial simulations concerning the dimensions and the resulting signal level and sensitivity have been performed and are presented in [4].

4 Ion Clearing

For antiprotons clearing of residual gas ions trapped within the beam is regarded crucial [5]. Therefore a constant voltage should be applied to clearing electrodes distributed at critical locations throughout the ring. The required field strength has been calculated to be $\geq$500 V/m. Simulations showed that a voltage of $\pm$ 100 V will be sufficient to fulfill this request, depending on the shape and size of the electrodes. Therefore

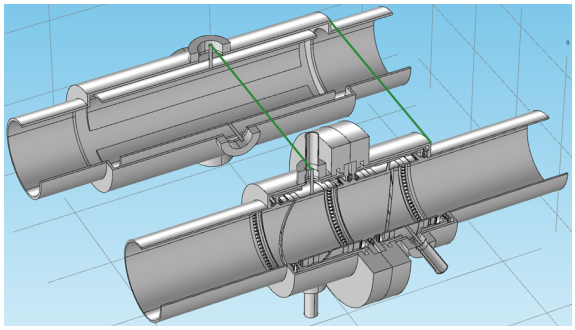

Fig. 4: Overview of the old design with cylindrical diagonally-cut electrodes and the proposed design utilizing four straight symmetrical electrodes. Taking the outer boundaries like the position of the quadrupole and sextupole magnets into account, and keeping the electrical feedthrough in the center of the pickups, the electrodes can be roughly 25 cm long compared to a total length of roughly 15 cm before. [4]

higher voltages might have to be applied in order to effectively clear the ions out of the antiproton beam.
In a first approach the BPM electrodes have been envisaged to be used for ion clearing as well. The advantage is, that the system is already distributed throughout the ring. But this way the electrode locations may not be optimum in respect to the β-functions. Another disadvantage is, the injection of the HV to the electrodes comes with adverse effects like a bigger capacitance and the power supply noise. These effects will disturb the measurements possibly up to a point where a BPM can no longer be used for position measurements but exclusively for ion clearing. Therefore a modified approach based on the installation of dedicated clearing electrodes is preferred.

References:

[1] R. Maier et. al., “Non-Beam Disturbing Diagnostics at COSY-Jülich,” EPAC’90, Nice, France, June 1990, p. 800.
[2] S. Srinivasan, “Design of a test bench to characterize BPMs for the HESR,” IKP Annual Report 2015, Forschungszentum Jülich
[3] R. Jones et. al., “Review of COSY Beam Diagnostics,” Jülich, November 19th - 20th, 2015
[4] A. Halama, “Comparative numerical study of two BPM designs for the HESR,” IKP Annual Report 2015, Forschungszentum Jülich
[5] F. Hinterberger, “Ion Trapping in the High-Energy Storage Ring HESR,” Berichte des Forschungszentrums Jülich 4343, ISSN 0944-2952, October 2011.

Upgrade of the BPM Readout Electronics at COSY

C. Böhme and V. Kamerdzhiev

1 Overview

The measurement of the ion beam position is one of the standard beam instrumentation tasks. At COSY the original BPM system commissioned in the early 90's is still in operation. It is based on analog processing with 8 bit digitization. The position data transfer is done through a shared 10 Mbit coaxial cable Ethernet, preventing the fast transfer of measurements of the distributed BPM. Therefore the system is currently limited to less than one measurement every 2 seconds of all BPMs in closed orbit, or showing the turn-by-turn data of one BPM.

The aging processing modules introduce additional problems. The drifts of parameters like gains and offsets are quite big, making it necessary to calibrate the system quite often. As there are no in-situ calibration signals the calibration can only be done by taking the modules out of the system and performing manual adjustments on the bench. Furthermore, the capabilities of the position processing CPU modules (VXI form factor), do not allow for post-processing using a calibration table. Moreover, an increased failure rate of the analog modules is being observed.

To be able to fulfill the requirements of the future experiments e.g. driven by the JEDI-collaboration, requesting a better control of the beam, it is crucial that systematic uncertainties associated with the current system are minimized. Therefore several upgrade paths were examined.

2 Current Status

COSY is equipped with 32 cylindrical and rectangular diagonal-cut style BPMs. During commissioning 28 BPMs of two types were installed, a cylindrical type with 150 mm diameter and a rectangular type 150 mm · 60 mm [1]. The selection was made to fit into the beam pipe, which is round in the straight sections and rectangular in the arcs in order to fit into the dipole magnets. Later on 4 BPMs were added, with special geometries to fit within the beam pipe of a different diameter close to experiments, giving a total number of 32. Two of them are installed within the recently added 2 MeV electron cooler [2] and use their own electronics for readout, which is different from the others. The other two at the ANKE experiment, use the standard readout hardware.

All the BPMs excluding the ones installed in the 2 MeV electron cooler are read out by the same type of electronics [3], whose concept is shown in Figure 1. The readout electronics for each BPM (except for the pre-amplifiers) consisting of 2 analog modules, 2 digital modules, one CPU, and one timing receiver board is housed in one VXI crate. The pre-amplifiers are directly connected to the N-type vacuum feedthrough of the pick-ups. This low noise pre-amplifier has a fixed gain of 13.5 dB with an input impedance of 500 $k\Omega$ and a bandwidth of 100 MHz. The gains and offsets of pre-amplifiers have to be exactly matched pairwise for one plane of one BPM in order to avoid incorrect measurements. The preamplified signals are fed into an analog module, where sum and delta signals are produced using a hybrid. These signals are then treated separately and can be further amplified in 6 dB steps from 0 dB to 66 dB. Furthermore, both the sum and the delta branches have two signal paths. A narrowband path features 3 possible filter settings with bandwidths of 10 kHz, 100 kHz, or 300 kHz and an additional amplifier that can be set from 0 dB to 18 dB in 6 dB steps. The broadband path with 10 MHz bandwidth can be used for turn-by-turn measurements while the narrowband signals are used for closed orbit measurements. The analog outputs are unipolar, the sign of the narrowband delta signal is detected separately and the information is transmitted by a separate TTL signal line. After the analog signal processing the signals are digitized in a digital module. This is done using 20 MHz 8 bit ADCs. For the narrowband signal the sampling frequency is lowered to 1 MHz or 100 kHz, depending on the selected analog bandwidth. For the sum signal only 7 of the 8 bits of the ADC are used, the 8th bit is used to indicate the polarity of the delta signal. The digital module generally has the possibility to buffer 4096 data points, while few modules can store up to 32768 data points for turn-by-turn measurements. The CPU of the VXI crate then calculates out of the narrowband signal the beam position using a scaling factor for the specific BPM geometry. It is also possible to transfer the raw data to the control system, display and export it.

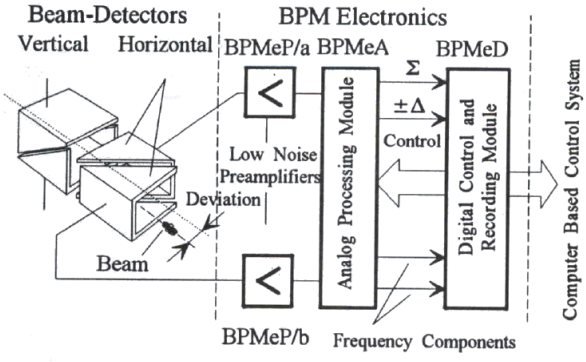

Fig. 1: Current Beam Position Monitor electronics assembly [3].

3 Upgrade Scenarios

Several upgrade scenarios were explored. This included the replacement of only the digital part, keeping the analog processing in place and allowing it to digitally correct for the drifts introduced by the analog parts. Because of the decreasing reliability of analog modules currently being observed, this scenario was ruled out and a complete upgrade of the readout electronics was decided. Three scenarios were taken into account:

3.1 LIBERA

The LIBERA system is a commercially available system from Instrumentation Technologies d.d. It consists of a μTCA 4.0 crate with up to 4 BPM readout cards, each for 4 channels, thus a complete BPM. The BPM signals are directly digitized using 250 MHz 16 bit ADCs. The signals are after-

wards processed using an FPGA. The FPGA is responsible for almost all processing within the unit. Within the system a PC is included to take care of the interaction with the user and the control system. The system has a free-running algorithm to detect the bunch. An RF reference signal is fed into the system for error detection only, if the bunch is longer than the RF reference, a failure is assumed and the detection is reset.

3.2 Spectrum Digitizer

The company Spectrum is offering a PCIe digitizer card with basically the same specifications as the LIBERA system: 250 MHz 16 bit digitizer with 4 channels. Drivers for a.o. LabView and C++ are provided. Although the card features a FPGA, this is not foreseen to be programmed by the user. Therefor the computation of the beam position would be done in software on the PC processor afterwards.

3.3 CERN Open Hardware

CERN OPEN hardware repository allows excessing current electronics designs potentially leading to significant reduction of development time and cost compared to an in-house development. This option is being considered.

3.4 μTCA

This standard is adopted from the telecom industry and modified according to scientific needs. The main feature is that boards can be inserted from both sides into a crate, separating an analog signal processing from the digital one, minimizing digital noise on the analog part. Several vendors supply components needed for the construction of a possible BPM readout solution. In this case the whole programming would have to be done in house, although several other labs like DESY, ESS or SLAC have solutions based on this standard in operation or planned, so that collaborations would be possible.

3.5 Control System Adaption

For all upgrade solutions, significant effort related to the integration of the new BPM readout electronics into the existing control system is necessary. The COSY control system was developed in house in the early 90's and does not include sufficient DAQ functionality to ensure efficient operation of a turn-by-turn BPM system. Evaluations are made if a modern control framework like Control System Studio (CSS) or FESA based could be used as a mediator between the new electronics and the current control system to minimize the effort extending the existing control system. Within the current control system only features already existing for the old hardware would be available, while the full set of features would become available using the new framework. With this approach other accelerator sub-systems undergoing an upgrade in the future could as well use the new framework as mediator, replacing the control system currently in operation completely in a medium to long time frame.

4 Next Steps

In November 2015 a review of the BPM upgrade plans was performed at the IKP by the experts invited from DESY, CERN and the GSI. The recommendation given was, that the LIBERA Hadron system appears to be the most suitable candidate for the upgrade due to limited time and man power available for the project [4]. The recommendation is also based on the fact, that the COSY team is responsible for the construction of the HESR where the Libera system will be used for the BPM readout. Choosing the same technology for COSY ensures the most efficient use of resources available. For detailed testing one LIBERA unit was ordered and is expected to arrive in February 2016. One Spectrum digitizer was ordered as well, which was delivered in November 2015. Based on the results of the tests a decision will be made in 2016 regarding the choice of the BPM readout electronics. The implementation and commissioning is foreseen in early 2017.

References:

[1] R. Maier et. al., "Non-Beam Disturbing Diagnostics at COSY-Jülich," EPAC'90, Nice, France, June 1990, p. 800.

[2] V. B. Reva et. al., "Cosy 2 MeV Cooler: Design, Diagnostic and Commissioning," IPAC2014, Dresden, Germany, MOPRI075.

[3] J. Biri et. al., "Beam Position Monitor Electronics at the Cooler Synchrotron COSY Jülich," Eigth Conference on Real-Time Computer Applications in Nuclear Physics, Vancover, June 1993.

[4] R. Jones et. al., "Review of COSY Beam Diagnostics," Jülich, November 19th - 20th, 2015

Prototype of DAQ for commercial stand-alone devices with Ethernet interface

Sergey Trusov, Sergey Mikirtytchiants, Leonid Eltcov, and Yury Valdau

In the experiments at an accelerator it is often necessary to continuously control some parameter of the installation with high precision. It is very convenient to use for this purpose commercial stand-alone measurement devices available on the market. Often, in such applications there is no need for the permanent control over all the device parameters, which is usually available at the device front panel or via the web interface. Hence, such equipment is usually configured at the beginning of operation and perform a measurement either on a command from operator at remote host or as a reaction on the external trigger.

Nowadays, almost all the companies which produce test and measurement equipment offer software solutions for the readout and remote control of their devices. Unfortunately, in most cases, solutions from different producers are not compatible with each other. The National Instruments [1] (NI) is, essentially, the only company which offer hardware and software for almost all the commercially available devices on the market. But LabVIEW software and hardware from the NI is rather expensive and often exceeds the needs of a particular experiment.

Recently, large international consortium of test and measurement equipment producers have started to develop and implement in to their products a support for the common opened LXI standard [2] (LAN Extension for Instrumentation). It has many important features, in particular, it uses industrial Ethernet interface for communication and affords a possibility to supply a common trigger signal to the different devices. Unfortunately, many devices support LXI standard only to the very limited extend and hence the major advantages of the standard can not be used in the DAQ with these instruments. Nevertheless, most of the modern devices have Ethernet interface and support telnet communications over TCP/IP protocol. Hence, it is possible to unify a readout of such equipment in one DAQ using standard industrial Ethernet. Devices with serial or GPIB interfaces can be implemented into this system by using commercially available Serial to Ethernet or GPIB to Ethernet converters [3]. In such a system, synchronisation and triggering can be done either over the network using a server which is running on the readout PC (software trigger), or using a dedicated triggering scheme (hardware trigger) which is connected to the device. A scheme of this kind of DAQ for the TRIC experiment [4] is shown in Fig. 1. The purpose of this system is to readout, calibrate, and control a Fast Current Transformer (FCT) [5] - the new sensor for the bunched beam, using commercially available high precision measurement devices. A set of front-end electronics located close to the FCT (shown in green) transmit a signal over the coaxial lines to the measurement devices (shown in blue). The temperature sensors on a 1-wire bus are readout using a serial-to-Ethernet adapter [3]. Dedicated calibration scheme together with an arbitrary wave form generator is used for calibration of the FCT readout scheme both in the laboratory and at COSY.

Measurement devices from different vendors (Agilent, Keythley, and Stanford Research) are readout, and controlled over the Ethernet using server, written in C. The new Ethernet base device can be implemented relatively easily into the DAQ readout using only one configuration file and dedicated

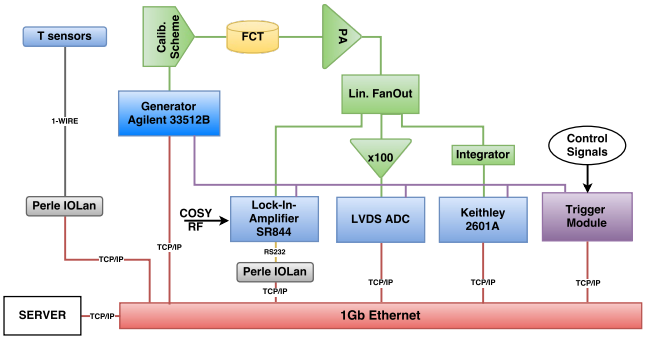

Fig. 1: Prototype of the DAQ for the TRIC experiment. The Fast Current Transformer (in yellow) is readout and calibrated using custom build front-end electronics (in green) and commercially available stand-alone devices (in blue), which are triggered and synchronised using dedicated triggering scheme (in violet), which gets external control signals from COSY and other experimental installations. All the devices are configured and readout over Ethernet (in red) by a server running on one of the PC connected to this network segment.

readout function. Experimental data from all the devices together with the corresponding time-stamp information from every system are stored in a text or binary file on a readout PC running under the Debian Linux OS. The data stream from the FCT readout system can be easily included into the data stream from the standard DAQ from ZEA, usually used for other experiments at COSY.

External synchronisation and hardware triggering for the TRIC experiment is done by using the functionality from the most advanced LXI device available in our system (Keithley 2601A) and the dedicated FPGA-based trigger module. The trigger module gets control signals from COSY and other experimental installations and produces a hardware trigger signal. Devices get trigger signals and perform measurements (or other actions) according to preloaded during initialisation procedures.

The first tests in the laboratory have shown that this FCT readout scheme allows one to reach the precision in averaged beam current measurement better than 10^{-4} for 1 mA using the available lock-in amplifier. The FCT readout system together with a trigger scheme, which is under preparation now, will be used for the beam current measurement during the TRIC beam time scheduled for summer 2016.

References:

[1] `http://www.ni.com/labview/d/`
[2] `http://www.lxistandard.org/Default.aspx`
[3] Perle Systems Limited, IOLAN SDS/SCS/STS/MDC Users Guide, Ver. 4.1, 2014.
[4] Yury Valdau, Dieter Eversheim and Bernd Lorentz, CBAC proposal E006, 2015.
[5] Bergoz Instrumentation, User Manual Fast Current Transformer, Rev. 3.1, 2015.

Feasibility study on muon production with laser-accelerated protons or ions

P.Fedorets[a,b], M.Büscher[c], H.Glückler[d]

Muons are used as probes to investigate properties of a various types of materials. Muons for solid-state research are currently available at four facilities: PSI in Switzerland, ISIS in England, J-PARC in Japan and TRIUMF in Canada. Here we present a simulation study on the use of laser-accelerated protons and ions for the generation of muons and give an estimate of the muon rates that can be achieved with state-of-the-art high-power lasers.

Muons are generally produced from charged pion decays which, in turn, are generated in nuclear interactions of accelerated protons with the nucleons in a secondary scattering target. The typical threshold for pion production is 280 MeV in the laboratory frame. This still is a serious challenge for laser-acceleration technologies since the maximum proton energies currently amount to 130 MeV [1]. However, due to the rapid progress of laser technology one expect that the required energy can be achieved in a few years from now. For our estimate we use an extrapolation [2] based on available DRACO data at FZ Dresden/Rossendorf [3] for the amount of produced protons at energies of 300, 400 and 500 MeV. Figure 1 shows the energy spectra of protons for the data and the extrapolation.

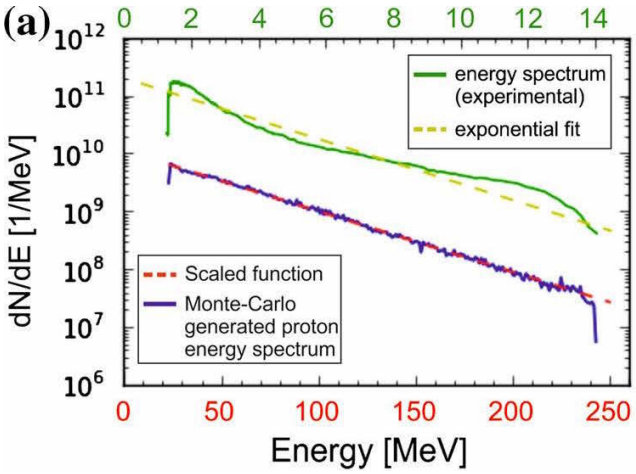

Fig. 1: Averaged measured proton energy spectrum from DRACO (green-line, upper energy axis). The dashed yellow line is an exponential fit to the data. The scaled function predicts the proton spectrum in the higher energy range (dashed red-line, lower energy axis) and the blue line is the spectrum of a proton bunch generated with a Monte-Carlo code. The figure has been taken from Ref. [2].

The pions that are produced from laser-accelerated protons have a broad energy distribution. The low energy fraction is stopped and decays inside the target, the others leave the target and decay in flight. Muons produced near the surface of the target from pion decay at rest are called surface muons. They have a fixed energy of 4.1 MeV and are fully polarised.

Ref. [4] presents a Geant-4 simulation for the ISIS target

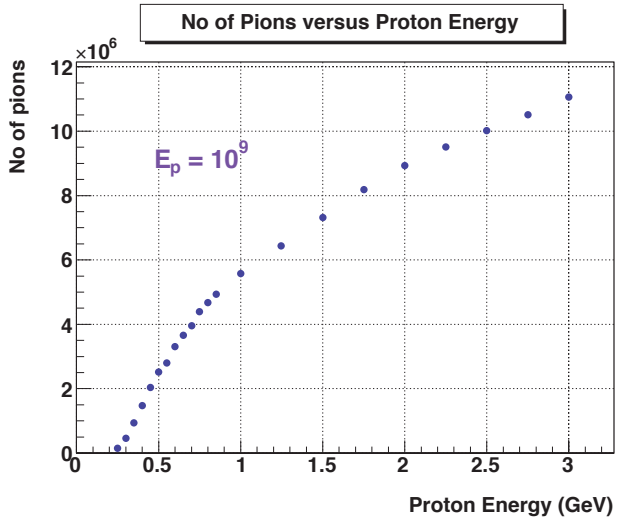

Fig. 2: Simulated variation of the pion yield with proton energy for an incoming beam of 10^9 protons [4].

geometry (graphite target with a thickness of 0.7 cm). Here most of the protons ($> 96\%$) pass through the target without interacting. The pion-production cross section increases rapidly with proton energy, as shown in Fig. 2. Figure 3 presents the result of a simulation for the muon yield for 10^9 primary protons. The spectrum shows a peak from surface muon production around 450 MeV proton energy. For higher proton energy a higher fraction of energetic pions can leave the target and decay in flight outside.

Based on Fig. 3 the yield of muons has been recalculated for the extrapolated amounts of laser-accelerated protons at energies of 300, 400 and 500 MeV. The results are presented in Table 1. Despite of the increasing pion production for higher proton energies, the surface muon output drops by about one order for each 100 MeV. This drop is due to the decrease of the laser-proton yield per laser bunch for the higher proton energy. The absolute numbers of surface muon production from the laser driven protons are significantly below the typical yield of $10^7 - 10^9$ muons/s at PSI and J-PARC.

T_{proton}, MeV	300	400	500
$\frac{dN}{dT_p}$, MeV^{-1}	$1.6 \cdot 10^7$	$1.9 \cdot 10^6$	$2.25 \cdot 10^5$
N_μ, total/shot	~ 150	~ 30	~ 4
N_μ, surface/shot	~ 130	~ 25	~ 3

Table 1: Simulated count rates for muon production with laser-accelerated protons.

An alternative approach is pion production through

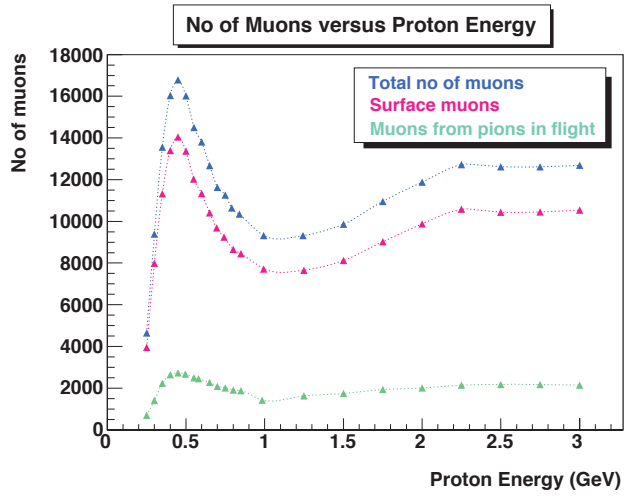

Fig. 3: Simulated variation of the muon yield with proton energy for the incoming beam of 10^9 protons [4].

heavy-ion collisions. Figure 4 shows data for laser driven C^{6+} ion production at the Trident laser facility, Los Alamos [5]. The maximum carbon-ion energies are in excess of 1 GeV (or >83 MeV/nucleon). The absolute ion numbers with energies above 900 MeV were estimated to be in the order of 10^7 ions per shot. Figure 5 shows the double differential cross sections for pion production in collisions of C ions with Li, C, and Pb targets, at a beam energy of 85 MeV/nucleon.

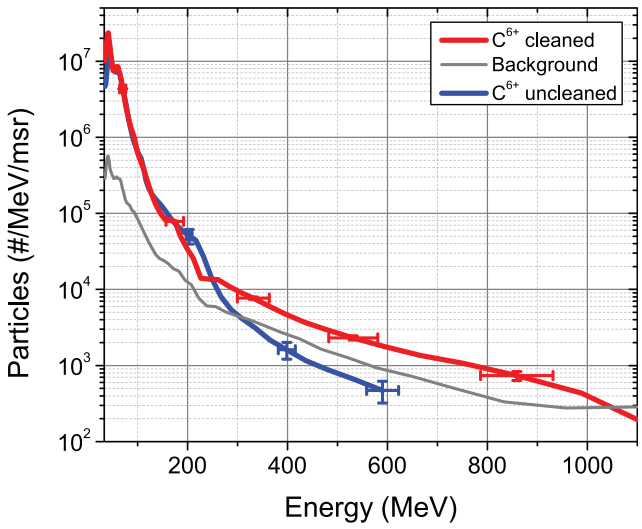

Fig. 4: Carbon C^{6+} energy distribution from the Trident experiment [5].

The count rate of the pion production from C+Pb interactions can be estimated as

$$\mathrm{d}N/\mathrm{d}E = L \cdot \frac{\mathrm{d}\sigma}{\mathrm{d}E} \quad ,$$

where $\mathrm{d}\sigma/\mathrm{d}E$ is the double differential cross section averaged over 4π. From the cross-section data at $27°, 90°, 120°$ [6] $\mathrm{d}\sigma/\mathrm{d}E$ was assumed to be 0.5 of $4\pi \cdot \left(\mathrm{d}^2\sigma/\mathrm{d}\Omega\mathrm{d}E\right)$.
For the calculation of the effective target areal density, full overlap of the ion beam with the target was assumed

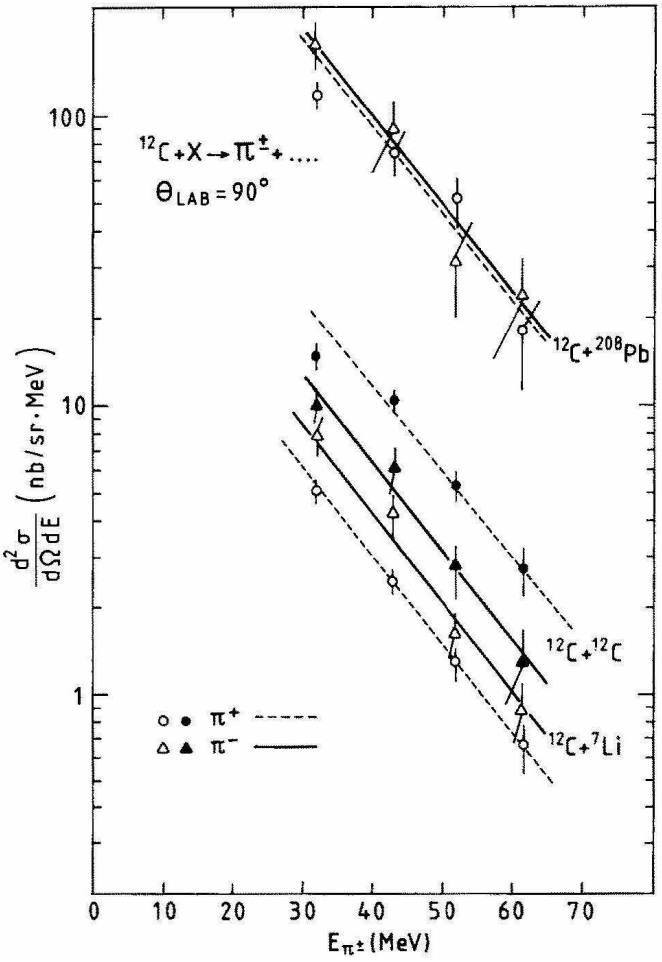

Fig. 5: Double differential cross sections $\left(\frac{d^2\sigma}{d\Omega dE}\right)$ for π^+ and π^- emission at 90^0 from C+Li, C+C and C+Pb interactions at 85 MeV/nucleon [6].

and a target thickness of 1 cm was used. It is important to check that the C ions are not stopped in the Pb target before they reach the rear surface at 1 cm. Since it is very difficult to find data on the range of the C ions in Pb, we used those for the range of α particles. The stopping power of α particles and C ions per amu in Pb is very similar [7]. According to the Bethe formula the particle range is proportional to its kinetic energy and inversely proportional to the mass multiplied by the squared charge of particle. Therefore, at equal kinetic energies (12·85=1020 MeV) the range of C ions can be calculated from the α range from the ratio of masses and squared charges. The range for alphas with $T = 1020$ MeV then is 77 g/cm^3 [8] and the range for C ions in Pb amounts to $R \sim 9$ cm for charge 1 and 0.25 cm for charge 6, which is assumed in most papers of laser driven C ion acceleration. That means the assumption of a Pb target thickness of 1 cm is not valid and C ions with energy 1020 MeV will stop earlier. We therefore reduce the effective target density by a factor 4:

$$L = N_{\mathrm{carbon}} \cdot \rho_{\mathrm{eff}} \cdot 1/4 = 0.825 \cdot 10^{29}\ (\mathrm{cm}^2\ \mathrm{shot})^{-1} \quad ,$$

where $N_{\mathrm{carbon}} = 10^7$ is the assumed yield of laser-accelerated carbon ions, and ρ_{eff} the effective Pb target density,

$$\rho_{\mathrm{eff}} = \rho_{\mathrm{Pb}} \cdot \frac{N_{\mathrm{A}} \cdot n_{\mathrm{a}}}{\mathrm{GMW}} \cdot l_{\mathrm{target}} = 3.3 \cdot 10^{22}\ \mathrm{atoms/cm}^2 \quad ,$$

where $\rho_{\mathrm{Pb}} = 11.34$ g/cm^3, GMW = 207.2 g/Mol is the Gram-Molecular Weight, $N_{\mathrm{A}} = 6.022 \cdot 10^{23}$ molecules/mole the Avogadro constant, and $n_{\mathrm{a}} = 1$ the number of atoms per molecule.
The estimated count rate for pion production from C+Pb interactions then is:

$$\mathrm{d}N/\mathrm{d}E = L \cdot \frac{\mathrm{d}\sigma}{\mathrm{d}E} = (5-1) \cdot 10^{-2}\ (\mathrm{shot} \cdot \mathrm{MeV})^{-1}$$

at an energy of ∼50 MeV (cf. Fig. 5).
The total pion yield in an energy interval of ΔE=50 MeV is around 1 pion/shot. Simulations on the ratio of the pion and muon production rates from Ref. [4] give a value of $\sim 10^{-2}$ (for a C target). With this number we expect an absolute muon count rate in C+Pb interactions of 10^{-2} muons/shot.
Our estimate on the possibility of muon production with laser driven protons and ions shows that the muon yield is at least a factor of 10^7 below that of dedicated muon facilities. Therefore, the realization of a laser-based muon source would require significant progress of laser performance (pulse power, repetition rate) and/or target technology (for example mass-limited cryogenic targets like clusters or pellets).

References:

[1] M. Roth, Review of recent advances in laser driven ion acceleration and applications. The 16th Advanced Accelerator Concepts Workshop (AAC 2014), July 13 – 18, 2014, San Jose, USA
[2] U. Masood et al., A compact solution for ion beam therapy with laser accelerated protons. Appl. Phys. B 117 (2014) 41
[3] K. Zeil et al., The scaling of proton energies in ultrashort pulse laser plasma acceleration. New J. Phys. 12 (2010) 045015
[4] A. Bungau et al., Impact of the energy of the proton driver on muon production. Proceedings MOPEA079 of IPAC'10, Kyoto, Japan
[5] D. Jung et al., Laser-driven 1 GeV carbon ions from preheated diamond targets in the break-out afterburner regime. Phys. Plasmas 20 (2013) 083103
[6] V. Bernard et al., Production of charged pions in intermediate-energy heavy-ion collisions. Nucl. Phys. A 423 (1984) 511
[7] SRIM - The Stopping and Range of Ions in Matter. http://www.srim.org/index.htm
[8] NIST - Physical Measurement Laboratory. Stopping-Power and Range Tables for Electrons, Protons, and Helium Ions. http://www.nist.gov/pml/data/star/
[9] B.M. Hegelich et al., Laser-driven ion acceleration from relativistically transparent nanotargets. New J. Phys. 15 (2013) 085015

[a]ITEP, Moscow; [b]IKP, FZJ; [c]PGI-6, FZJ; [d]ZEA-1, FZJ

SEU Tests with the STS-XYTER Version 1 ASIC

J. Lehnert[1] *and P. Kozcon*[1]
[1]GSI, Darmstadt, Germany

The sensors of the CBM Silicon Tracking System (STS) are connected to 8 STS-XYTER frontend ASICs with 128 channels each developed at AGH Cracow [1]. The ASICs are located just outside of the active area of the STS and exposed to high charged particles rates and total integrated doses over the full lifetime up to 100 kRad. In order to ensure proper functionality in this environment and to reduce single event upsets (SEU) which manifest as bit flips, the ASIC design implements a DICE (Dual Interlocked Storage) cell architecture for the configuration settings of each channel as well as for critical global settings.

SEU Testing of DICE Cells at COSY

During the CBM electronics beam test at COSY Jülich[1] in October 2015, the first version of the STS-XYTER frontend ASIC, produced in a UMC 180 nm process, was characterized for the first time with respect to single-event effects in its DICE cell architecture. Goal was the quantitative assessment of SEU cross sections for the DICE cells, which may strongly depend on the actual cell architecture, and the comparison to the regular flip flops in the design [2]

Tests were performed in a dedicated high-intensity proton beam used in parallel for multiple irradiation studies within CBM, which allowed running at rates up to 3×10^9 protons per spill on the setup, which provided a good compromise between sufficient statistics for the SEU investigations and a stable (not fully DICE protected) readout interface. Device under test was a single STS-XYTER version 1 ASIC bonded to a prototype frontend board (FEB). The ASIC was centered in the proton beam. The FEB was connected to a standard readout and control chain with a SYSCORE3 readout board and a data aquisition PC with a HTG-K7 board and a FLESnet based readout. For the purpose of the test only the control functionality of the system was used, i.e. reading and writing to ASIC registers. The test used 32240 bits each of DICE cells and flip flops respectively, arranged in a two-dimensional structure of 8bit DICE discriminator threshold values and 8bit flip-flop counters for 130 channels with 31 discriminators each. The test procedure consisted in a continuous readback of a predefined pattern from the DICE cells and of fixed random values from the read-only counters and a check for bit flips in the expected register values. Repeated readback allows to distinguish SEUs from readout errors. An ionisation chamber from GSI detectorlab (B. Voss) with QFW based readout was placed behind the ASIC to provide an accelerator-independent and continuous measurement of beam intensities[2] .

SEU Test Results

The test was done for a total of 48 hours of effective irradiation. In this period, 3467 bit flips for the flip flops were observed and 116 bit flips for the DICE cells. These numbers provide a direct quantification of the relative SEU rate of the DICE cells with respect to flip flops. The factor of 29.9 is in the expected range for DICE cells. With a preliminary estimate of the proton fluence larger than $2 \times 10^7/\text{cm}^2/\text{s}$, the SEU counts translate in an SEU cross section below 1.1×10^{-15} cm^2/bit for the DICE cells which is consistent with literature values.

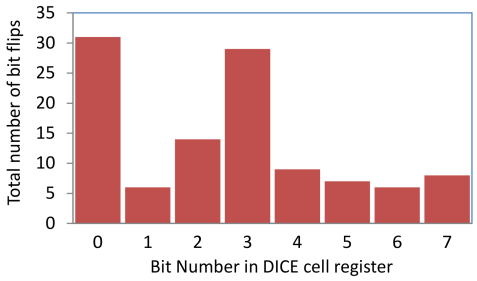

Figure 1: SEU counts for the individual bits of the DICE cell threshold registers

The DICE cells exhibit significant differences in bit flip count over the 8 bits of the individual DICE registers (see Fig. 1). This observation could be correlated with different distance from bulk/well contacts for the individual bits in the DICE cell layout. Consequently the upcoming revision 2 of the STS-XYTER ASIC [3] will implement an modified DICE cell layout. The expected improvement in DICE SEU rate by a factor of up to 3 will be verified in a forthcoming beam test.

References

[1] K. Kasinski et al., “STS-XYTER, a High Count-Rate Self-Triggering Silicon Strip Detector Readout IC for High Resolution Time and Energy Measurements”, IEEE NSS/MIC, 2014

[2] S. Löchner et al., “Radiation Studies on the UMC 180 nm CMOS Process at GSI”, RADECS 2009 Proceedings, p. 614

[3] K. Kasinski et al., ”STS-XYTER2, a prototype detector readout chip for the STS and MUCH”, CBM Progress Report 2015, Darmstadt 2016

[1]Various support by IKP, FZ Jülich is acknowledged.

[2]Various support by S. Löchner, GSI, is acknowledged.

Radiation hardness tests of electronic components for CBM-STS low voltage power supply

S. Löchner[1], *P. Koczoń*[1], *and A. Rost*[1]
[1]GSI, Darmstadt, Germany

Electronic components installed in the field of reaction products in future experiments at FAIR have to be radiation hard. At present, selected parts like DC/DC converters and LDO voltage stabilisers undergo exhaustive tests with use of intense minimum ionising particles' beams, mostly about 3 GeV protons at the COSY facility, Jülich[1].

Test setup

For components like DC/DC converters or LDO voltage stabilisers the output voltage level as well as the expected transient voltage spikes rate due to single event upsets have to be monitored during irradiation. Voltage level monitoring (input and output) requires relatively low readout frequency below 1 Hz and can be implemented on the inexpensive ARDUINO system [1]. Fast transients have been monitored on a 4-trace digital oscilloscope Rhode-Schwarz RTO1044 [2] . Measurement results have been recorded in nonvolatile memory and analysed.

Selected ASICs

For the radiation hardness tests several DC/DC converters have been chosen. Selection criteria like circuit efficiency, chip size, coreless inductivity, apropriate output voltage and sufficient output power as well as voltage setting flexibility have been applied.

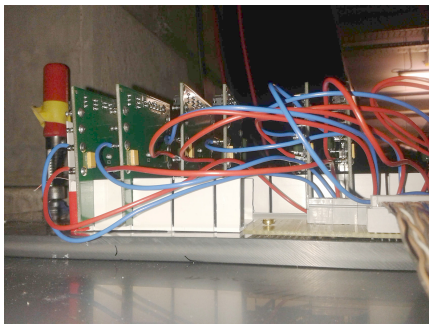

Figure 1: Base plate with PCB card holder and wiring.

Only one model of the LDO stabilizer produced in rad hard technology has been examined until now. Alltogether 10 test boards with LTC3605, 3 boards with LTC3610 (Linear Technology), 4 boards containing LM2596S (Texas Instruments) as well as 4 FEASTMP boards [3] have been tested in two beam times. All tested ASICs were powered on during the irradiation runs. The test boards were placed in a holder fixing their positions with respect to the proton beam during the measurement as shown in Fig. 1.

Test results

The PCBs with tested chips were placed in a row along the beam axis such that the irradiating beam punched through all of them. A small ionisation chamber placed on the beam axis behind tested chips was used to monitor the beam intensity (Fig. 2, left).

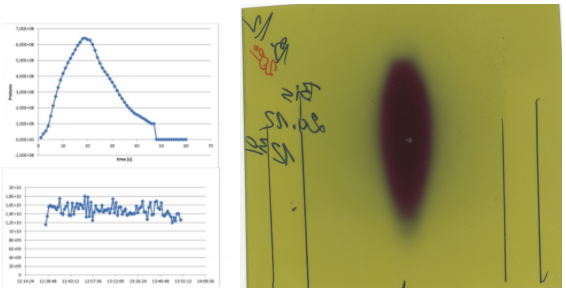

Figure 2: Beam intensity in one spill (upper left panel) and avarage proton current (lower left panel). Beam spot on Gafchromic self-developing dosimetric film (right panel).

The beam profile has been investigated with Gafchromic dosimetric film [4]. In the course of the irradiation the film developes a spot corresponding to the shape of the proton beam with the optical density corresponding to the integrated beam intensity (Fig. 2, right). The total dose is known from the measurement with the ionisation chamber and the position of the irradiated chips marked on the film. A fractional dose can be estimated for each point on the film by scanning the optical density. This allows to estimate precisely the beam intensity integral and - consequently - the dose at the ASICs' positions. Out of the tested DC/DC converters only FEASTMP survived more than 10^{13} protons which corresponds to a dose of 4×10^{12} cm^{-2}. No fast transients were observed on LDO voltage stabilisers.

References

[1] S. Löchner and P. Koczoń, GSI Annual Report 2014

[2] http://www.rohde-schwarz.de/de/Produkte/messtechnik-testsysteme/aerospace-and-defense/messtechnik/oszilloskope-fuer-ad/RTO.html

[3] http://project-dcdc.web.cern.ch/project-dcdc/public/Documents/FEASTMod_Datasheet.pdf

[4] http://www.ashland.com/products/gafchromic-radiotherapy-films

[1]Various support by IKP, FZ Jülich is acknowledged.